

UC Irvine

UC Irvine Electronic Theses and Dissertations

Title

Unraveling Mechanisms of Reactive Oxygen Species Formation from Secondary Organic Aerosols

Permalink

<https://escholarship.org/uc/item/8892v4d0>

Author

Wei, Jinlai

Publication Date

2022

Copyright Information

This work is made available under the terms of a Creative Commons Attribution License, available at <https://creativecommons.org/licenses/by/4.0/>

Peer reviewed|Thesis/dissertation

UNIVERSITY OF CALIFORNIA,
IRVINE

Unraveling Mechanisms of Reactive Oxygen Species Formation from Secondary Organic
Aerosols

DISSERTATION

Submitted in partial satisfaction of the requirements
for the degree of

DOCTOR OF PHILOSOPHY
in Chemistry

by

Jinlai Wei

Dissertation Committee:

Associate Professor Manabu Shiraiwa, Chair

Professor Sergey Nizkorodov

Professor James N. Smith

2022

Chapter 2 © 2021 American Chemical Society (USA)

Chapter 3 © 2022 American Chemical Society (USA)

Chapter 4 © 2021 American Chemical Society (USA)

All other materials © 2022 Jinlai Wei

DEDICATION

To my supportive parents, family, and friends.

Thank you.

TABLE OF CONTENTS

LIST OF FIGURES	vi
LIST OF ABBREVIATIONS	viii
ACKNOWLEDGEMENTS	ix
VITA	xii
ABSTRACT	xv
Chapter 1: Introduction	1
1.1 Ambient Primary and Secondary Particles	1
1.2 Laboratory Generation of SOA	2
1.3 Health Effects of SOA	5
1.4 Free Radical Characterization using EPR Spectroscopy	8
1.5 Outline of the Dissertation	9
Chapter 2: Superoxide Formation from Aqueous Reactions of Biogenic Secondary Organic Aerosols	11
2.1 Abstract	11
2.2 Introduction	11
2.3 Materials and Methods	13
2.3.1 SOA formation, collection and extraction	13
2.3.2 EPR measurements	15
2.3.3 H ₂ O ₂ fluorometric assay	15
2.3.4 Kinetic modeling	16
2.4 Results and Discussion	18
2.4.1 ROS formation efficiencies by SOA	18
2.4.2 Reaction mechanism	21
2.5 Implications	25
2.6 Chapter 2 Appendix	29
2.6.1 SOA chemistry	29
2.6.2 H ₂ O ₂ fluorometric assay	30
Chapter 3: Effects of Acidity on Reactive Oxygen Species Formation from Secondary Organic Aerosols	37
3.1 Abstract	37
3.2 Introduction	38
3.3 Materials and Methods	39

3.3.1 Preparation of SOA and Model Compounds	39
3.3.2 pH Control	40
3.3.3 EPR Analysis	41
3.3.4 H ₂ O ₂ Measurement.....	42
3.3.5 Diogenes Chemiluminescence Assay	42
3.4 Results and Discussion	43
3.4.1 Radical Formation from SOA at Different pH.....	43
3.4.2 Reaction Mechanisms	48
3.4.3 H ₂ O ₂ Formation from SOA at Different pH.....	50
3.5 Implications.....	52
3.6 Chapter 3 Appendix	54
3.6.1 Calibration of Diogenes Chemiluminescence Assay	54
3.6.2 Superoxide Measurement at Neutral pH by EPR and Chemiluminescence.....	54
Chapter 4: Iron-facilitated Organic Radical Formation from Secondary Organic Aerosols in Surrogate Lung Fluid.....	59
4.1 Abstract	59
4.2 Introduction.....	59
4.3 Materials and Methods.....	61
4.3.1 SOA formation, collection and extraction	61
4.3.2 EPR Measurements	62
4.3.3 Fe ²⁺ Measurement	63
4.3.4 Total Peroxide Measurement	63
4.3.5 DTT assay	64
4.3.6 Kinetic modeling.....	65
4.4 Results and Discussion	66
4.4.1 Radical formation from SOA and Fe ²⁺ in water and SLF	66
4.4.2 Reaction Mechanisms	68
4.5 Implications.....	73
4.6 Chapter 4 Appendix	75
4.6.1 Additional discussion on reaction mechanisms	75
4.6.2 Peroxide measurements.....	76
4.6.3 Additional information on experiments	77
Chapter 5: Impacts of Photoirradiation on Reactive Oxygen Species Generation by Secondary Organic Aerosols	88
5.1 Abstract	88

5.2 Introduction.....	88
5.3 Materials and Methods.....	90
5.3.1 Preparation of SOA.....	90
5.3.2 EPR Analysis	91
5.3.3 Characterization of spectral flux density.....	91
5.3.4 Total peroxide measurement.....	92
5.3.5 HR-MS analysis	93
5.4 Results and Discussion	93
5.4.1 Spectral flux of <i>in-situ</i> irradiation system.....	93
5.4.2 Photolytic generation of free radicals from SOA.....	94
5.4.3 Total peroxide fractions	97
5.4.4 Composition of organic radicals	99
5.5 Conclusions.....	100
Chapter 6: Conclusions, Limitations and Outlook.....	102
6.1 Conclusions.....	102
6.2 Contributions to co-authored papers	104
6.3 Limitations and Outlook	105
6.3.1 Complex nature of SOA.....	105
6.3.2 Future directions in photolytic ROS formation of SOA	106
6.3.3 Connecting exogenous ROS to endogenous ROS.....	107

LIST OF FIGURES

Figure 1.1. Schematic of PAM reactor...	4
Figure 1.2. Studies on health effects of aerosols with a wide range of length and time scales.....	5
Figure 1.3. Interaction of air pollutants and ROS in the ELF of the human respiratory tract	7
Figure 1.4. Schematic and principle of EPR spectroscopy	9
Figure 2.1. EPR spectra of BMPO-radical adducts from aqueous reactions of isoprene SOA	19
Figure 2.2. Relative and total yields of BMPO-radical adduct from aqueous reactions of SOA.....	20
Figure 2.3. Temporal evolution of molar yields of BMPO-OH and BMPO-OOH adducts from aqueous reactions of SOA	22
Figure 2.4. Implications of ROS formation by aqueous reactions of biogenic SOA.....	26
Figure 3.1. EPR spectra of aqueous extracts of isoprene SOA and α -terpineol SOA at different pH.....	44
Figure 3.2. Yields and relative abundance of different radical species from SOA at different pH.....	45
Figure 3.3. Initial superoxide production rates from SOA measured by Diogenes chemiluminescence assay at pH 7.4.....	46
Figure 3.4. Temporal evolution of concentrations of BMPO-OH adducts from UV-vis irradiation of the mixture of 1 mM H ₂ O ₂ and 10 mM BMPO at different pH.....	47
Figure 3.5. Yields and relative abundance of different radical species from model compounds at different pH.....	48
Figure 3.6. H ₂ O ₂ yields from aqueous reactions of SOA at different pH.	51
Figure 4.1. EPR spectra of isoprene SOA with or without Fe ²⁺ in water and SLF; Yields and relative abundance of different radical species from SOA in water and SLF with or without mM Fe ²⁺	67
Figure 4.2. EPR spectra of mixtures of Fe ²⁺ with model compounds in water or in SLF.....	69
Figure 4.3. Concentrations of Fe ²⁺ formed in the mixtures of ascorbate with Fe ³⁺ with and without PBS; EPR spectra of Fe ³⁺ and ascorbate with and without PBS.....	70
Figure 4.4. Temporal evolution of molar yields of BMPO-R and BMPO-OR from isoprene SOA and Fe ²⁺ in SLF; Yields of carbon- centered and oxygen-centered organic radicals from isoprene SOA in SLF as a function of [Fe ²⁺]/[ISO] molar ratios; Organic radical yields versus total peroxide molar fractions in SOA with or without Fe ²⁺	71
Figure 4.5. Implications of free radical formation by SOA and Fe ²⁺ in water and epithelial lining fluid.....	73
Figure 5.1. Spectral flux density of the 100 W Hg lamp, Los Angeles summer solstice maximum, and the 24-hour average Los Angeles solar flux.....	94
Figure 5.2. Temporal EPR spectra of BMPO-radical adducts from isoprene SOA with <i>in-situ</i> irradiation over 76.6 min.....	95

Figure 5.3. Temporal formation of BMPO-radical adducts from SOA under UV-Vis irradiation versus dark conditions.....	96
Figure 5.4. Total peroxide molar fractions from SOA in original extracts, under dark conditions and under UV-Vis irradiation.....	98
Figure 5.5. High-resolution ESI (+) mass spectra of α -pinene SOA with 10 mM BMPO under irradiated and dark conditions.....	100

LIST OF ABBREVIATIONS

AMS	aerosol mass spectrometer
α -HHs	α -hydroxyhydroperoxides
BMPO	5- <i>tert</i> -Butoxycarbonyl-5-methyl-1-pyrroline-N-oxide
CHP	cumene hydroperoxide
DHA	Dehydroascorbic acid
DTT	dithiothreitol
DTTm	DTT activity normalized by mass
ELF	epithelial lining fluid
ELVOC	extremely low volatility organic compounds
EPR	electron paramagnetic resonance
ESI	electrospray ionization
HOM	highly oxygenated molecules
HR-MS	high resolution mass spectrometry
HX	hypoxanthine
KM-SUB-ELF	kinetic multi-layer model of surface and bulk chemistry in the epithelial lining fluid
LC-MS	liquid chromatography-mass spectrometry
MCGA	Monte Carlo genetic algorithm
OFR	oxidation flow reactor
PAM	potential aerosol mass
PBS	phosphate buffer saline
PM	particulate matter
PTFE	polytetrafluoroethylene
ROOH	organic hydroperoxides
ROOR	organic peroxides
ROS	reactive oxygen species
SLF	surrogate lung fluid
SMPS	scanning mobility particle sizer
SOA	secondary organic aerosols
VOC	volatile organic compounds
XO	xanthine oxidase

ACKNOWLEDGEMENTS

My six years of graduate school have past like a blink of an eye. There are many people who have profoundly influenced my life and work during this period, and this dissertation would not have been possible without their help. First and foremost, I must thank my thesis advisor Dr. Manabu Shiraiwa. Manabu is an inspirational scientist and role model who I genuinely look up to. Manabu has always demonstrated innovation, hard work, persistence and promoted optimism, even when roadblocks appeared in the course of research. Personally, Manabu always cares about the development of students, postdocs and project scientists in his group, and makes sure we are on the right track by doing his best to support us to lead a successful career. Thank you, Manabu, for supporting me over the last four years, being a constant source of encouragement, and for making grad school so enjoyable and rewarding.

I also whole-heartedly thank Dr. Ting Fang for her constant mentorship, scientific insight and immense kindness and empathy. Ting joined the Shiraiwa group six months earlier than I as a postdoctoral scholar and has served as my co-mentor in science for the past four years. I am truly grateful for all the meaningful discussion with Ting that inspire new ideas, as well as her constructive feedback to solidify my experiments and findings. Thank you, Ting, for being a key co-author in each of my paper! My dissertation also would not have been realized without the support from Dr. Pascale Lakey. I was a 100% experimentalist before my PhD program and had this natural “fear” about modeling. It was Pascale’s patience and expertise that helped me overcome my fear and start coding which eventually resulted in significant contributions in Chapters 2 and 3. Thank you, Pascale, for proofreading my messy codes line by line and troubleshooting whenever there is an error!

I am also immensely grateful for Dr. Sergey Nizkorodov serving as my committee member as well as our collaborator. I had my first setback in PhD research during the first year when I could not reproduce consistent results with literature, which kept burning us for two months. After reaching out to Sergey, we started collaborating by using the SOA samples generated in Nizkorodov lab which immediately resolved our questions. Thank you, Sergey, for providing novel perspectives and incredible insights in SOA

formation and photochemistry! I also learned a lot from other members of Nizkorodov group including Cynthia Wong, Vahe Baboomian and Alex Klodt. Thank you for your wisdom and guidance in SOA formation, photochemistry and mass spec experiments and analysis!

I would also like to thank all other past and current members in Shiraiwa group: Dr. Ying Li, Dr. Brian Hwang, Dr. Tommaso Galeazzo, Dr. Meredith Schervish, Kasey Edwards, Sukriti Kapur and Lena Gerritz. Your presence alone makes it fun to be in the lab, and I appreciate all your support along the journey! I am also thankful for the AirUCI community for providing incredible resources to advance our careers. I learned a lot from external and internal seminars, AAAR student chapters and interactions with other PIs and students. Thank you, Dr. Jim Smith for serving as my doctoral committee member and your insights. Shoutout to Vero Perraud and Lisa Wingen for always willing to help troubleshooting with their expertise in instrumentation. It has been a rewarding journey to thrive in such an inclusive, supportive and resourceful environment.

I would also like to say special thanks to my research advisor at University of Illinois at Urbana-Champaign during my master program, Dr. Vishal Verma. Vishal is technically my first research advisor, who is an amazing environmental engineer and atmospheric scientist. He always leads by example, being original, hard-working and optimistic in research. His guidance truly helped me learn how to conduct research in an appropriate manner and seek the truth with relentless work ethic. My two years of research experience with Vishal really laid a strong foundation for my PhD program. Thank you, Vishal, for challenging me to think critically, teaching me how to approach science, and helping me become a better researcher.

Finally, I thank my family and friends who have been a constant source of love and support during the past six years. Largest thank you to my parents who sacrificed so much for me and have not seen me for almost three years because of the pandemic. I miss you so much and I hope I can see you soon as a doctor. Thank you especially to my girlfriend, Anran, who has supported me through highs and lows unconditionally, and has put up with many moments of stress. Thank you for listening to me rant about all

things including science, basketball and job hunting, and encouraging me to have more work-life balance.

Thank you, Mimi, for meowing and waking me up 6 am every day to push me to work.

VITA

Jinlai Wei

Education:

- 2018-2022 Ph.D. in Chemistry, University of California, Irvine
2016-2018 M.S. in Environmental Engineering, University of Illinois at Urbana-Champaign
2012-2016 B.E. in Environmental Engineering, Tianjin University, China

Publications:

Peer-reviewed

Wei, J., Fang, T., & Shiraiwa M. (2022) Effects of Acidity on Reactive Oxygen Species Formation from Secondary Organic Aerosols. *ACS Environmental Au*. <https://doi.org/10.1021/acsenvironau.2c00018>.

Wei, J., Fang, T., Wong, C., Lakey, P. S. J., Nizkorodov, S., & Shiraiwa M. (2021) Superoxide Formation from Aqueous Reactions of Biogenic Secondary Organic Aerosols. *Environmental Science & Technology*, 55(1), 260-270.

Wei, J., Fang, T., Lakey, P. S. J., & Shiraiwa M. (2021) Iron-facilitated Organic Radical Formation from Secondary Organic Aerosols in Surrogate Lung Fluid. *Environmental Science & Technology*. <https://doi.org/10.1021/acs.est.1c04334>

Wei, J., Yu, H., Wang, Y., & Verma, V. (2019). Complexation of Iron and Copper in Ambient Particulate Matter and Its Effect on the Oxidative Potential Measured in a Surrogate Lung Fluid. *Environmental Science & Technology*, 53(3), 1661-1671.

Yu, H., **Wei, J.**, Cheng, Y., Subedi, K., & Verma, V. (2018). Synergistic and Antagonistic Interactions among the Particulate Matter Components in Generating Reactive Oxygen Species Based on the Dithiothreitol Assay. *Environmental Science & Technology*, 52(4), 2261-2270.

Xiong, Q., Yu, H., Wang, R., **Wei, J.**, & Verma, V. (2017). Rethinking Dithiothreitol-based Particulate Matter Oxidative Potential: Measuring Dithiothreitol Consumption versus Reactive Oxygen Species Generation. *Environmental Science & Technology* 51(11), 6507-6514.

Hwang, B., Fang, T., Pham, R., **Wei, J.**, Gronstal, S., Lopez, B., Frederickson, C., Mendez-Jimenez, D., Galeazzo, T., Wang, X., Jung, H., & Shiraiwa, M. (2021) Environmentally Persistent Free Radicals, Reactive Oxygen Species Generation, and Oxidative Potential from Highway PM_{2.5}. *ACS Earth and Space Chemistry*, 5(8), 1865-1875.

Huang, Y., Fang, Ting., **Wei, J.**, Monterrosa Mena, J. E., Lakey, P. S. J., Digman, M. A., Kleinman, M. T., & Shiraiwa, M. (2022) Phasor Approach FLIM as an Indicator for NADPH Oxidase during Exposure to Secondary Organic Aerosols. *Biophysical Journal*, 121(3), 415a.

In Revision

Fang, T., Huang, Y., **Wei, J.**, Monterrosa Mena, J. E., Lakey, P. S. J., Digman, M. A., Kleinman, M. T., & Shiraiwa, M. (2022) Cellular Superoxide Release Overwhelms Chemistry upon Lung Deposition of Particulate Matter.

In Preparation

Wei, J., Fang, T., Wong, C., Nizkorodov, S., & Shiraiwa M. (2022) Impacts of Photoirradiation on Reactive Oxygen Species Generation by Secondary Organic Aerosols.

Edwards, K., Klodt, A. L., Galeazzo, T., Schervish, M., **Wei, J.**, Fang, T., Aumont, B., Nizkorodov, S., & Shiraiwa M. (2022) Nitrogen oxide influences on the production of reactive oxygen species from alpha-pinene and naphthalene secondary organic aerosols.

Conference Presentations:

- Platform **Wei, J.**, Fang, T., Lakey, P., & Shiraiwa M. Iron-facilitated Organic Radical Formation from Secondary Organic Aerosols in Surrogate Lung Fluid. *ACS 2021 Fall National Meeting, Atlanta, GA, August 21-25, 2021.*
- Platform **Wei, J.**, Fang, T., Lakey, P., & Shiraiwa M. Iron-facilitated Organic Radical Formation from Secondary Organic Aerosols in Surrogate Lung Fluid. *39th Annual conference of American Association for Aerosol Research (AAAR), Virtual, October 18-22, 2021.*
- Platform **Wei, J.**, Fang, T., Wong, C., Lakey, P., Nizkorodov, S., & Shiraiwa M. Superoxide Formation from Aqueous Reactions of Biogenic Secondary Organic Aerosols. *38th Annual conference of AAAR, Virtual, October 5-9, 2020.*
- Poster **Wei, J.**, Fang, T., Wong, C., Nizkorodov, S., & Shiraiwa M. Comparison of Secondary Organic Aerosols from Dark Ozonolysis and OH-initiated Oxidation in Generating Reactive Oxygen Species. *37th Annual conference of AAAR, Portland, OR, October 14-18, 2019.*
- Poster **Wei, J.**, Fang, T., Wong, C., Nizkorodov, S., & Shiraiwa M. Comparison of Secondary Organic Aerosols from Dark Ozonolysis and OH-initiated Oxidation in Generating Reactive Oxygen Species. *3rd Inhaled Aerosol Dosimetry Conference, Irvine, CA, October 10-12, 2019.*
- Poster **Wei, J.**, Yu, H., & Verma V. Complexation State of Iron and Copper in Ambient PM and its Effect on the Oxidative Potential. *35th Annual conference of AAAR, Raleigh, NC, October 16-20, 2017.*

Teaching and Working Experience:

07/2019-03/2021	Graduate Research Assistant	Chemistry, University of California, Irvine
07/2021-Present		Advised by Dr. Manabu Shiraiwa
10/2018-06/2019	Teaching Assistant	Chemistry, University of California, Irvine
03/2021-06-2021		General Chemistry 1LD; General Chemistry 1C Chemistry Honor H2C
08/2016-05/2018	Graduate Research Assistant	Environmental Engineering University of Illinois at Urbana-Champaign Advised by Dr. Vishal Verma
07/2015-08/2015	Research Intern	Chinese Research Academy of Environmental
07/2014-08/2014		Sciences (CRAES), Beijing, China.

Awards and Honors:

04/2021	C. Ellen Gonter Graduate Student Paper Award	<i>American Chemical Society (ACS)</i>
10/2020	Student Poster Competition Award	38 th Annual conference of AAAR
10/2017	Student Poster Competition Award	35 th Annual conference of AAAR
10/2014	Anxin Group Scholarship	Tianjin University, China

10/2013	E-TECH Scholarship	Tianjin University, China
10/2013	Merit Student	Tianjin University, China

ABSTRACT

Unraveling Mechanisms of Reactive Oxygen Species Formation from Secondary Organic Aerosols

By

Jinlai Wei

Doctor of Philosophy in Chemistry

University of California, Irvine, 2022

Reactive oxygen species (ROS), including the hydroxyl radical ($\bullet\text{OH}$), superoxide ($\text{O}_2^{\bullet-}$), hydroperoxyl radical (HO_2^{\bullet}) and hydrogen peroxide (H_2O_2), play a central role in chemical transformation and health effects of atmospheric aerosols. Respiratory deposition of secondary organic aerosols (SOA) and transition metals may lead to the generation of ROS to cause oxidative stress, but the underlying mechanism and formation kinetics of ROS are not well understood. Using electron paramagnetic resonance (EPR) spectroscopy coupled with a spin trapping technique, the ROS formation is characterized from aqueous reactions of SOA involving transition metals, lung antioxidants, reaction media with different pH as well as photoirradiation.

First, we demonstrate dominant formation of superoxide ($\text{O}_2^{\bullet-}$) with molar yields of 0.01 – 0.03% from aqueous reactions of biogenic SOA generated by $\bullet\text{OH}$ photooxidation of isoprene, β -pinene, α -terpineol, and d-limonene. The temporal evolution of $\bullet\text{OH}$ and $\text{O}_2^{\bullet-}$ formation is elucidated by kinetic modeling with a cascade of aqueous reactions including the decomposition of organic hydroperoxides, $\bullet\text{OH}$ oxidation of primary or secondary alcohols, and unimolecular decomposition of α -hydroxyperoxyl radicals. Relative yields of various types of ROS reflect relative abundance of organic hydroperoxides and alcohols contained in SOA. In addition, we observed substantial formation of organic radicals in surrogate lung fluid (SLF) by mixtures of Fe^{2+} and SOA generated from photooxidation of isoprene, α -terpineol and toluene. The molar yields of organic radicals by SOA are measured to be 0.03 – 0.5% in SLF, which are 5 – 10 times higher than in water. We observe that Fe^{2+} enhances organic radical yields dramatically by a factor of 20 – 80, which can be attributed to Fe^{2+} -facilitated decomposition of organic peroxides, consistent

with a positive correlation between peroxide contents and organic radical yields. Ascorbate mediates redox cycling of iron ions to sustain organic peroxide decomposition, as supported by kinetic modeling reproducing time- and concentration-dependence of organic radical formation as well as additional experiments observing the formation of Fe^{2+} and ascorbate radicals in mixtures of ascorbate and Fe^{3+} . $\bullet\text{OH}$ and superoxide are found to be scavenged by antioxidants efficiently.

Furthermore, we find highly distinct radical yields and composition at different pH in the range of 1 – 7.4 from SOA generated by oxidation of isoprene, α -terpineol, α -pinene, β -pinene, toluene and naphthalene. We observe that isoprene SOA have substantial hydroxyl radical ($\bullet\text{OH}$) and organic radical yields at neutral pH, which are 1.5 – 2 times higher compared to acidic conditions in total radical yields. Superoxide ($\text{O}_2^{\bullet-}$) is found to be the dominant species generated by all types of SOA at lower pH. At neutral pH, α -terpineol SOA exhibit a substantial yield of carbon-centered organic radicals, while no radical formation is observed by aromatic SOA. Further experiments with model compounds show that the decomposition of organic peroxide leading to radical formation may be suppressed at lower pH due to acid-catalyzed rearrangement of peroxides. We also observe 1.5 – 3 times higher molar yields of hydrogen peroxide (H_2O_2) in acidic conditions compared to neutral pH by biogenic and aromatic SOA, likely due to enhanced decomposition of α -hydroxyhydroperoxides and quinone redox cycling, respectively.

Finally, we identify that photoirradiation can induce efficient formation of organic radicals from SOA with radical yields up to 1.5%, ~ 100 times higher compared to dark conditions. Further experiments show that total peroxide fractions in SOA decrease 50 – 70% after irradiation, indicating organic peroxides as a probable source of organic radical formation. High resolution mass spectrometry (HR-MS) confirms the substantial formation of organic radicals by identifying BMPO-organic radical adducts, which may provide insights into the chemical structures of these organic radicals and subsequently their formation mechanisms. These findings and mechanistic understanding have important implications on the atmospheric fate of SOA and particle-phase reactions of highly oxygenated organic molecules as well as oxidative stress upon respiratory deposition.

Chapter 1: Introduction

1.1 Ambient Primary and Secondary Particles

During the past decades, urban air pollution has been recognized as one of the key contributors to global burden of disease.¹⁻³ Fine particle ($PM_{2.5}$, particulate matter less than 2.5 μm in diameter) pollution is estimated to cause about 0.8 million premature deaths and 6.4 million lost life years.⁴ Ambient PM originate from emissions from both natural and anthropogenic sources. The former constitutes dust, sea salt, volcanic ash, pollens, the products of wildfires and the oxidation of biogenic volatile organic compounds (VOCs), whereas the anthropogenic sources include fossil fuel combustion, industrial processes, construction work and wood stove burning.⁵ Based on how particles are introduced into the atmosphere, they can be divided into primary and secondary. Primary particles are directly emitted from their sources, such as road transport, industrial combustion, and soil/marine aerosol particles.⁵ In comparison, secondary particles are generated from a series of chemical reactions, forming low-volatility products that subsequently condense into solid or liquid phase, thus becoming PM. For example, sulfur dioxide (primarily from industrial combustion) and nitrogen dioxide (primarily from vehicular and industrial emissions) can be oxidized in the atmosphere to form sulphates and nitrates, which can be neutralized by ammonia mainly from agricultural sources. In addition, secondary particles consist of a major fraction of carbonaceous particulates,⁶ also known as secondary organic aerosols (SOA), originating from VOC oxidation. Secondary particles can persist in the atmosphere longer than primary particles because the chemical processes involved in the particle formation are relatively slow as well as the smaller sizes compared to primary particles thus slower deposition. The complex processes involved in the formation and chemical transformation of secondary particles, particularly SOA, are still under investigation worldwide.

SOA represent a substantial fraction of ambient PM and have significant impacts on global climate, air quality, and public health.⁷⁻⁹ Organic compounds by mass constitute on average $\sim 50\%$ of ambient fine particles in the urban-impacted Northern Hemisphere,¹⁰ while SOA contribute to 65% - 95% of this organic mass from urban to remote regions.¹¹ SOA are generated from oxidation of anthropogenic and biogenic

VOCs followed by nucleation and condensation of semi- and low-volatile oxidation products.¹² These VOCs, also known as SOA precursors, include volatile and semi-volatile alkanes, alkenes, aromatic hydrocarbons and oxygenated compounds.¹³ Anthropogenic VOCs consist of ~40% alkanes, ~10% alkenes, and ~20% aromatic compounds with the rest being oxygenated and unidentified compounds.^{13, 14} Biogenic VOCs are mostly alkenes, consisting of ~50% isoprene, ~15% monoterpene, ~3% sesquiterpene, and other reactive and unidentified precursors.¹⁵ Overall, the non-methane VOC emissions are dominated by biogenic VOCs which contribute to ~90% globally, while anthropogenic emissions play a more significant role in urban regions.¹⁶ Upon formation, SOA can affect global climate by both direct and indirect radiative forcing. Organic aerosols can directly absorb or scatter solar radiation, which alters the radiative balance of the atmosphere,¹⁷ while hydrophilic aerosols can modify cloud properties by acting as cloud condensation nuclei (CCN) thus exerting indirect effect on climate.¹⁸ In addition, SOA can significantly impact the air quality around the globe. Biogenic SOA originating from isoprene and monoterpenes have been identified as a major contributor to ambient PM mass in Southeastern US,¹⁹ Europe,²⁰ and Amazon,²¹ while urban pollution may largely enhance the aerosol formation from these biogenic VOCs.²² Furthermore, a growing number of studies have linked SOA to health effects. Cell exposure studies indicated that SOA may induce intracellular formation of reactive oxygen species (ROS),²³ inflammatory responses²⁴ and cell death.²⁵ SOA are also capable of generating ROS through aqueous chemical reactions which can cause oxidative potential.^{26, 27} Understanding the properties of SOA is important due to their huge impact in various environmental processes. Therefore, it is essential to apply a suitable method to obtain SOA that is representative of ambient SOA.

1.2 Laboratory Generation of SOA

The major oxidants that initiate VOC oxidation and SOA formation are ozone (O₃) and hydroxyl radical (•OH) during daytime, whereas nitrate radical (NO₃•) is the most important oxidant at nighttime.²⁸ Numerous studies have investigated SOA generated by ozonolysis and •OH photooxidation of isoprene,^{29, 30} monoterpenes,^{31, 32} sesquiterpenes,^{33, 34} and aromatic compounds (only •OH photooxidation).^{35, 36}

Different SOA properties have been widely studied including their oxidation states,³⁷ hygroscopicity,³⁸ CCN activity,³⁹ viscosity,⁴⁰ and optical properties.⁴¹ A vital tool to obtain laboratory-generated SOA, since the first generation by Haagen-Smit,⁴² is environmental chambers (or smog chambers). Chambers have been extensively used in atmospheric research to study kinetics of gas-phase reactions,⁴³ VOC oxidation and SOA formation,⁴⁴⁻⁴⁶ atmospheric multiphase chemistry,⁴⁷ new particle formation,⁴⁸ ice nucleation⁴⁹ and many other atmospheric topics. A main advantage of environmental chambers is the atmospheric relevance. The light sources in chambers usually use wavelengths $> \sim 300$ nm which are similar to the wavelengths of actinic radiation in the troposphere. Photon absorption can then initiate photochemistry and radical formation (primarily $\bullet\text{OH}$) as oxidants.⁴⁵ With similar range of wavelength and intensity compared to tropospheric solar radiation, chambers are often found with $\bullet\text{OH}$ levels similar or slightly higher than the ambient conditions ($10^6 - 10^7$ molecules cm^{-3} vs. 1.5×10^6 molecules cm^{-3} on average).⁵⁰ As implied by this feature, the integrated exposure of the chemical species in chambers to oxidants and radiation is also similar to that in the troposphere, which leads to a comparable “photochemical age”.⁵¹ Despite the atmospheric relevance, wall effects of environmental chambers have been identified as a major limitation in the past decade. Reactive gaseous and particle-phase compounds can be adsorbed substantially to Teflon chamber walls (also known as wall losses) within 15 minutes,^{52, 53} which can also take place due to reactive losses,⁵⁴ diffusion, and electrophoresis.⁵⁵ Overall, wall losses may limit chamber experiments to be no longer than 1 day (i.e. photochemical ages ≤ 1 day), while many atmospheric oxidation processes have much longer lifetimes such as benzene photooxidation¹³ and chemical aging of SOA.⁵⁶

In addition to the use of traditional chambers, the use of oxidation flow reactors (OFR) has been growing exponentially in recent years.⁵¹ OFR are defined as flow reactors using oxidants with significantly higher (multiple orders of magnitude) concentrations compared to ambient conditions which vastly accelerates the oxidation chemistry.^{57, 58} As the most popular form of OFR, potential aerosol mass (PAM) reactors are often found with $\bullet\text{OH}$ concentrations at $10^8 - 10^{10}$ molecules cm^{-3} ,^{51, 59} which can be translated into integrated $\bullet\text{OH}$ exposure (OH_{exp}) up to $\sim 10^{12}$ molecules cm^{-3} s, assuming a few minutes of residence

time in the reactors. Such high levels of OH_{exp} are equivalent to photochemical ages from days to weeks under tropospheric $\bullet\text{OH}$ levels, with the advantages of short residence time (minutes) hence reduced wall losses.⁶⁰ Furthermore, OFR are often much smaller compared to chambers (volume in L vs. volume in m^3). Thus, OFR can be applied beyond laboratory work due to their portability, which have been deployed to field,^{61, 62} aircraft,⁶³ and source studies.^{64, 65} Indeed, concerns about OFR mostly center on their extremely high oxidative capacity and photolysis processes that are irrelevant to tropospheric solar radiation. However, PAM-generated SOA have been found to have similar characteristic with ambient and chamber-generated SOA in terms of mass yield, oxidation state, hygroscopicity, and chemical composition with similar mass spectra measured by an Aerodyne ToF AMS.⁶⁶⁻⁶⁸ Therefore, a PAM reactor was adopted in our work to obtain ambient-relevant SOA and to subsequently study ROS formation from aqueous reactions of SOA.

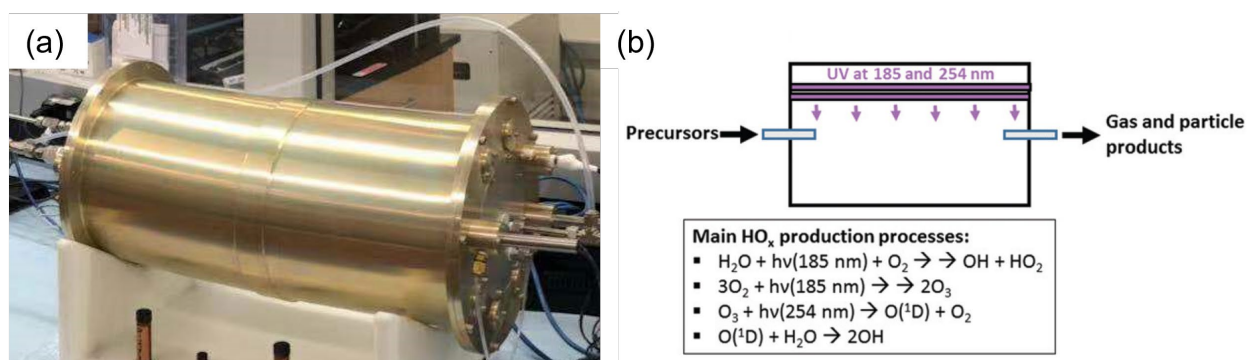


Figure 1.1. (a) PAM reactor in Shiraiwa Lab. (b) Schematic of OFR185 mode for PAM reactor adapted from Peng and Jimenez.⁵¹ Figure 1.1(a) shows the PAM reactor used in our work which operated at OFR185 mode as shown in Figure 1.1 (b). Two of the most commonly used modes for PAM reactor are OFR254 and OFR185, where “254” and “185” represent 254 nm and 185 nm UV light as the photochemistry initiator.⁵¹ For OFR254, low-pressure Hg lamps provide UV radiation at 254 nm which photolyzes external generated O_3 to form $\text{O}(^1\text{D})$ and react with H_2O to form $\bullet\text{OH}$.⁵⁷ For OFR185, UV at 185 nm is also provided in addition to 254 nm. As shown in Figure 1.1(b), 185 nm photons have energy strong enough to directly photolyze H_2O molecules into H^\bullet (which reacts with O_2 to form HO_2^\bullet) and $\bullet\text{OH}$ and to dissociate O_2 into $\text{O}(^3\text{P})$.⁶⁹ Thus, no external O_3 is needed for $\bullet\text{OH}$ generation, while $\text{O}(^3\text{P})$ can also combine with O_2 to

generate O_3 , which can provide additional $\bullet OH$ source under UV 254 nm. Figure 1.1(b) shows the main reactions for the HO_x ($\bullet OH$ and $HO_2\bullet$) production in the PAM reactor.

1.3 Health Effects of SOA

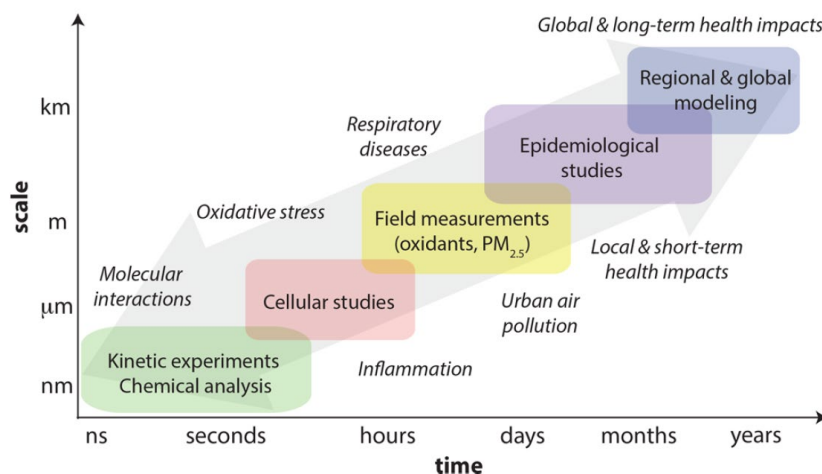


Figure 1.2. Studies on health effects of aerosols cover a wide range of length and time scales as adapted from Shiraiwa et al.⁸ Different physicochemical and biological approaches (colored boxes) are necessary to elucidate the complex nature of aerosol health effects.

Understanding the health effects of SOA is highly complex which requires collective efforts from interdisciplinary studies as shown in Figure 1.2. As the foundation of these studies, epidemiological studies have mostly focused on the impacts of exposure to ambient PM.⁷⁰⁻⁷³ In comparison, the epidemiological outcomes of SOA exposure have been relatively understudied. Chowdhury et al.⁷⁴ recently estimated 260,000 excess deaths due to exposure to anthropogenic SOA globally. More strikingly, Pye et al.⁷⁵ reported that SOA contributed by both biogenic and anthropogenic sources are associated with 6.5 times higher rate of cardiorespiratory mortality than $PM_{2.5}$ in the United States. Due to smaller range and time scales required, more studies investigated the toxicological impacts of SOA both *in vivo* and *in vitro*. Cardiopulmonary response and vascular diseases were identified for mice exposed to biogenic and anthropogenic SOA.⁷⁶⁻⁷⁸ Cognitive function, maternal behavior and social behavior of mice can be also significantly affected with exposure to SOA from diesel engine exhaust.^{79, 80} Meanwhile, *in-vitro* studies demonstrated that isoprene-

and monoterpene-derived SOA may induce increased level of expression of oxidative stress response genes.⁸¹⁻⁸³ Inflammatory responses were also found in cell lines exposed to biogenic and traffic-related SOA.^{24, 84, 85}

In addition to epidemiological and toxicological studies, oxidative potential (OP) is an emerging metric to assess the health effects of ambient PM in the past decade or two. OP is known as catalytic generation of ROS by PM components such as organic compounds and transition metals, as well as simultaneous depletion of antioxidants.⁸⁶ While OP studies initially focused on ambient aerosols and traffic-related particles,⁸⁷⁻⁹⁰ a growing number of studies have applied OP measurements to SOA. SOA derived from isoprene,^{91, 92} monoterpenes^{23, 93} and polycyclic aromatic hydrocarbons⁹⁴ may lead to significant OP as shown by their capacity to consume dithiothreitol (DTT), a widely used surrogate for *in-vivo* antioxidants. Besides the consumption rate of DTT (also known as DTT activity), OP can be also assessed through direct measurement of ROS generated by intracellular mechanisms and chemical reactions. Liu et al.⁹⁵ proposed that hydrogen peroxide (H₂O₂) formation from naphthalene SOA may diffuse rapidly into cells and trigger intracellular ROS formation. A recent study reported higher cellular ROS production and lower cell viability from naphthalene SOA than β -pinene SOA.⁹⁶ As for the characterization of chemically generated ROS by aerosols, electron paramagnetic resonance (EPR) spectroscopy has received increasing attention as a vital tool since the pioneering work by Dellinger et al.⁹⁷ Tong et al.²⁶ demonstrated that hydroxy radical (\cdot OH), the most reactive ROS, can be formed through decomposition of organic hydroperoxides in monoterpene SOA. More recent studies observed formation of other free radicals including superoxide (O₂ \cdot^-) and organic radicals from aqueous reactions of isoprene SOA,⁹⁸ naphthalene SOA⁹⁹ and cooking aerosols.¹⁰⁰ However, the underlying mechanism for the free radical formation is still poorly understood. Therefore, the major objective of this dissertation is to facilitate mechanistic understanding of ROS formation from SOA.

ROS play a central role in atmospheric oxidation processes and oxidative stress. Figure 1.3 shows the interaction of air pollutants and ROS in the epithelial lining fluid (ELF) of the human respiratory tract

and the mechanism to induce oxidative stress. Under most atmospheric conditions, $\bullet\text{OH}$ radicals govern the oxidative capacity through numerous mechanisms including addition to a $\text{C}=\text{C}$ bond, aromatic ring

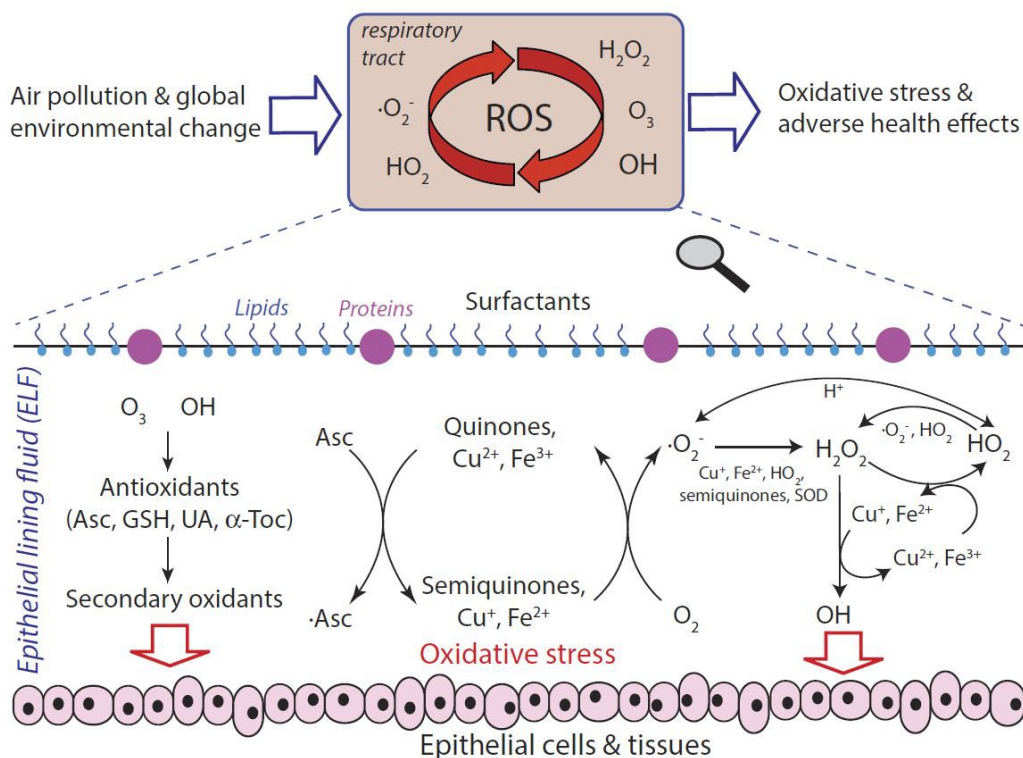


Figure 1.3. Interaction of air pollutants and ROS in the ELF of the human respiratory tract adapted from Lakey et al.¹⁰¹ ELF can be considered as an interface between atmospheric and physiological chemistry induced by air pollution. Atmospheric O_3 and $\bullet\text{OH}$ can react with surfactants and antioxidants (ascorbate, uric acid, reduced glutathione, α -tocopherol) and form secondary oxidants. Redox-active components of ambient PM, including quinones, transition metals and SOA can trigger ROS formation and induce oxidative stress.

substitution, hydrogen abstraction and monoelectronic oxidation.¹⁰² *In-vivo* formation of $\bullet\text{OH}$ is known to induce drastic toxicological effects such as lipid oxidation¹⁰³ and DNA strand breaking,¹⁰⁴ which can ultimately lead to cell apoptosis and death.^{105, 106} $\text{O}_2^{\bullet-}$ and its protonated form, hydroperoxyl radical (HO_2^{\bullet}) are also important atmospheric oxidants. HO_2^{\bullet} is essential for the termination of radical propagation reactions by forming organic hydroperoxides,¹⁰⁷ which can contribute to formation of highly oxygenated organic molecules (HOM) and low volatility organic compounds and ultimately condense into particle

phase.^{108, 109} Formation of H₂O₂ and O₂^{•-} in epithelial lining fluid have been linked to oxidative stress and adverse health effects upon inhalation and deposition of ambient SOA in the human respiratory tract.^{110, 111} Low levels of O₂^{•-} modulate various kinases or directly activate transcription factors to affect gene regulation in the nucleus;¹¹² however, excess O₂^{•-} formation is cytotoxic and induces a variety of diseases.¹¹³ Superoxide is also known as a crucial precursor of H₂O₂, which can be further converted via Fenton (-like) reactions into •OH as shown in Figure 1.3.^{111, 114} Organic radicals, such as alkyl, alkoxy and peroxy radicals can be interconverted during propagation steps and are thus crucial to chemical transformation of SOA.¹⁰⁷ Meanwhile, organic radicals in ELF usually have long lifetimes compared to •OH and O₂^{•-}.¹¹⁵ Therefore, they may initiate lipid radical formation and subsequent lipid peroxidation, which are central to many pathological processes.¹¹⁶ Given the atmospheric and physiological importance of ROS, it is critical to quantify kinetics and elucidate chemical mechanisms of the formation of different types of radicals from SOA in the aqueous phase.

1.4 Free Radical Characterization using EPR Spectroscopy

The method used in this dissertation for free radical characterization is EPR spectroscopy coupled with a spin-trapping technique. Free radicals can be measured by EPR spectroscopy as shown in Figure 1.4. Free radicals contain unpaired electrons. When placed between an electromagnet in an EPR spectrometer, the unpaired electrons line up to be either parallel or antiparallel to the magnetic field (Figure. 1.4 (b)), thus splitting into two energy states. The difference in the two energy states is denoted by Zeeman effect:¹¹⁷

$$\Delta E = g\mu_B B_0$$

Where g represents a dimensionless magnetic moment, μ_B represents Bohr magneton, and B_0 represents the magnetic field strength of the EPR spectrometer. When a microwave energy (Figure 1.4. (a)) is applied to the sample which equals to ΔE , an EPR signal can be generated, with the fundamental equation of EPR spectroscopy as follows:

$$\Delta E = h\nu = g\mu_B B_0$$

Since free radicals are generally short-lived and are very difficult to be directly quantified within the timescales of an EPR measurement, it is coupled with a spin-trapping technique in this dissertation. A spin trap, BMPO (5-*tert*-Butoxycarbonyl-5-methyl-1-pyrroline-N-oxide), is employed to react with highly reactive radical species such as $\bullet\text{OH}$, $\text{O}_2\bullet$ and organic radicals to form stabilized BMPO-radical adducts. Such adducts have much longer lifetimes compared to the free radicals thus can be better quantified using EPR spectroscopy.

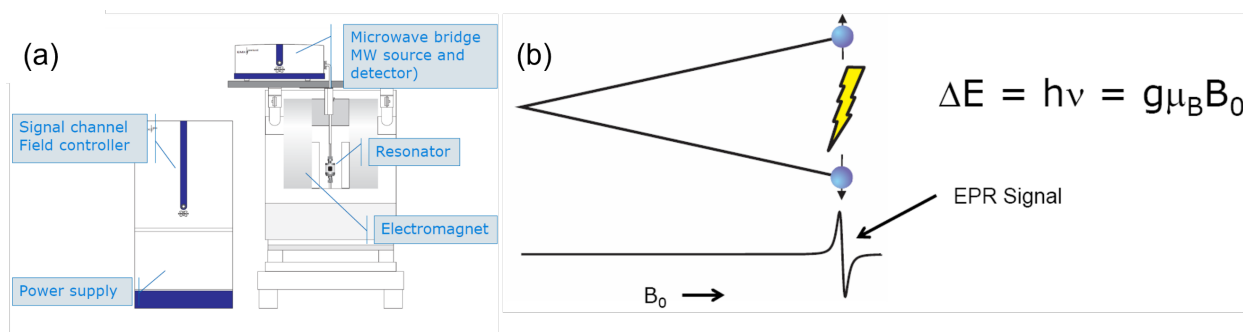


Figure 1.4. (a) Components of an EPR spectrometer. (b) Working principle of EPR spectroscopy. Adapted from Bruker EPR training materials.

1.5 Outline of the Dissertation

This dissertation applies EPR spectroscopy coupled with a spin-trapping technique to characterize the ROS formation from aqueous reactions of SOA involving reaction media with different pH, transition metals, lung antioxidants, and photoradiation. In Chapter 2, we aim at understanding the superoxide formation from biogenic SOA and the underlying mechanism. We observed substantial formation of $\text{O}_2\bullet$ by SOA formed by $\bullet\text{OH}$ photooxidation of biogenic SOA. We found that the oxidation pathways and chemical composition of SOA play a critical role in determining ROS composition. Using a combination of laboratory experiments and kinetic modeling, we successfully established the $\text{O}_2\bullet$ formation mechanisms from aqueous reactions of biogenic SOA. The goal of Chapter 3 is to elucidate the effects of acidity (pH) on ROS formation from SOA. We characterized ROS formation from laboratory-generated SOA under

highly acidic, moderately acidic, and neutral conditions. We observed that pH impacts yields, and composition of ROS depending on SOA types and provide mechanistic discussion using model compounds.

In Chapter 4, we focus on radical formation from interactions among transition metals, SOA and lung antioxidants. We characterized radical formation from laboratory-generated SOA and Fe^{2+} in water and in surrogate lung fluid (SLF). We observed major formation of $\cdot\text{OH}$ and $\text{O}_2\cdot^-/\text{HO}_2\cdot$ in water, but dominant formation of organic radicals in SLF with significant enhancement effects by Fe^{2+} . Kinetic modeling elucidated the central role of Fe^{2+} -facilitated decomposition of organic peroxides and iron redox cycles mediated by antioxidants. In Chapter 5, we combined an *in-situ* UV-Vis irradiation system with EPR to characterize the photolytic formation of ROS from laboratory-generated SOA. We observed substantial organic radical formation upon irradiation, which can be partially due to photolytic decomposition of organic peroxides. High-resolution mass spectrometry elucidates the chemical composition of the organic radicals, which can be essential to understand the formation mechanisms. Finally, Chapter 6 summarizes the main conclusions and limitations of this work and outlines potential areas of future research.

Chapter 2: Superoxide Formation from Aqueous Reactions of Biogenic Secondary Organic Aerosols

This chapter was published in *Environmental Science & Technology* in 2021:

Wei, J.; Fang, T.; Wong, C.; Lakey, P. S. J.; Nizkorodov, S. A.; Shiraiwa, M., Superoxide Formation from Aqueous Reactions of Biogenic Secondary Organic Aerosols. *Environ Sci Technol* **2021**, 55(1), 260-270. <https://doi.org/10.1021/acs.est.0c07789>

2.1 Abstract

Reactive oxygen species (ROS) play a central role in aqueous-phase processing and health effects of atmospheric aerosols. While hydroxyl radical ($\bullet\text{OH}$) and hydrogen peroxide (H_2O_2) are regarded as major oxidants associated with secondary organic aerosols (SOA), the kinetics and reaction mechanisms of superoxide ($\text{O}_2^{\bullet-}$) formation are rarely quantified and poorly understood. Here we demonstrate dominant formation of $\text{O}_2^{\bullet-}$ with molar yields of 0.01 – 0.03% from aqueous reactions of biogenic SOA generated by $\bullet\text{OH}$ photooxidation of isoprene, β -pinene, α -terpineol, and d-limonene. The temporal evolution of $\bullet\text{OH}$ and $\text{O}_2^{\bullet-}$ formation is elucidated by kinetic modeling with a cascade of aqueous reactions including the decomposition of organic hydroperoxides, $\bullet\text{OH}$ oxidation of primary or secondary alcohols, and unimolecular decomposition of α -hydroxyperoxyl radicals. Relative yields of various types of ROS reflect relative abundance of organic hydroperoxides and alcohols contained in SOA. These findings and mechanistic understanding have important implications on the atmospheric fate of SOA and particle-phase reactions of highly oxygenated organic molecules as well as oxidative stress upon respiratory deposition.

2.2 Introduction

Secondary organic aerosols (SOA) constitute a major fraction of ambient particulate matter and have significant impacts on global climate, air quality and public health.^{7, 8} Biogenic volatile organic compounds (VOC), including isoprene and monoterpenes, have been identified as the primary precursors of SOA around the globe⁹, including the Amazon region,¹¹⁸ China,¹¹⁹ and southeastern United States.¹²⁰

Formation of SOA is initiated by multi-generational oxidation of VOC and subsequent condensation of semi-volatile oxidation products.^{9, 12} Recent studies have revealed that highly oxygenated organic molecules (HOM) and low volatility organic compounds generated by autoxidation substantially contribute to new particle formation and SOA growth.^{108, 109} These compounds are found to be labile in the particle phase¹²¹ and a recent study suggested that particle-phase reactions need to be considered for a full understanding of the atmospheric fate of HOM.¹²² Particle-phase chemistry and aqueous-phase processing involving oxidants and water-soluble organic compounds in cloud and fog droplets are very efficient pathways for chemical transformation of SOA.¹²³⁻¹²⁵ These aging processes can lead to the change of particle properties including cloud condensation nuclei activity¹²⁶ and absorption coefficient due to the formation of light-absorbing compounds.¹²⁷

Reactive oxygen species (ROS), including the hydroxyl radical ($\bullet\text{OH}$), superoxide ($\text{O}_2^{\bullet-}$), hydroperoxyl radical (HO_2^{\bullet}) and hydrogen peroxide (H_2O_2), play a central role in chemical transformation of organic and inorganic compounds in the atmosphere.¹²⁸ Substantial amounts of H_2O_2 were detected in ambient and laboratory-generated SOA resulting from the hydrolysis of hydroxyhydroperoxides and peracids.^{129, 130} $\bullet\text{OH}$, the most reactive form of ROS, was found to be released by decomposition of organic hydroperoxides,²⁶ peracids,¹³¹ and HOM.¹³² While $\bullet\text{OH}$ and H_2O_2 have been traditionally considered as the most important oxidants in aqueous droplets and thus studied extensively, additional oxidants have received growing attention. Singlet oxygen and organic triplet excited state have emerged as new oxidants produced from dissolved organic compounds in atmospheric water.^{133, 134} Redox reactions of quinones contained in aromatic SOA can lead to the formation of $\text{O}_2^{\bullet-}$.^{98, 135} Previous studies have observed superoxide formation from biogenic ozonolysis SOA as a minor component;^{26, 98, 99, 136} however, the mechanism and kinetics of $\text{O}_2^{\bullet-}$ formation are poorly understood and rarely quantified.

Ambient SOA are found to have a significant oxidative potential,^{8, 23} which can be correlated with formation of H_2O_2 and $\text{O}_2^{\bullet-}$ in epithelial lining fluid,¹³⁷ inducing oxidative stress and adverse health effects upon inhalation and deposition in the human respiratory tract.^{8, 110, 111} ROS can exert drastic effects on

biological tissues and cell components, subsequently causing acute airway inflammation and cardiopulmonary illnesses.^{110, 138} Low levels of $O_2^{\bullet-}$ modulate various kinases or directly activate transcription factors to affect gene regulation in the nucleus;¹¹² however, excess $O_2^{\bullet-}$ formation is cytotoxic and induces a variety of diseases.¹¹³ Superoxide is also known as a crucial precursor of H_2O_2 , which can be further converted via Fenton (-like) reactions into $\bullet OH$.^{111, 114} Given the atmospheric and physiological importance of ROS, it is critical to quantify kinetics and elucidate chemical mechanisms of the formation of different types of ROS from SOA in the aqueous phase. In this study, we observe substantial formation of $O_2^{\bullet-}$ by SOA formed by $\bullet OH$ photooxidation of isoprene, β -pinene, α -terpineol, and d-limonene with the highest formation efficiency by α -terpineol SOA. We found that the oxidation pathways (e.g., ozonolysis vs. $\bullet OH$ photooxidation) and chemical composition of SOA play a critical role in determining ROS composition. Using a combination of laboratory experiments and kinetic modeling, we demonstrate that $O_2^{\bullet-}$ formation is caused by a cascade of aqueous reactions of biogenic SOA involving the decomposition of organic hydroperoxides, $\bullet OH$ oxidation of primary or secondary alcohols, and unimolecular decomposition of α -hydroxyperoxyl radicals. To the best of our knowledge, this is the first study that explicitly addresses the mechanisms and kinetics of $O_2^{\bullet-}$ formation from biogenic SOA involving aqueous chemistry. These results have significant implications on chemical transformation of organic compounds in the atmosphere and adverse aerosol health effects in the human respiratory tract.

2.3 Materials and Methods

2.3.1 SOA formation, collection and extraction

SOA particles were generated from dark ozonolysis and $\bullet OH$ photooxidation (referred as SOA_{O_3} and SOA_{OH} , respectively) of isoprene (Sigma-Aldrich, $\geq 99\%$), β -pinene (Sigma-Aldrich, $\geq 99\%$), α -terpineol (Arcos Organics, 97%), and d-limonene (Arcos Organics, 96%). Figure A1 shows the schematics of both oxidation systems. Briefly, SOA_{O_3} particles were produced in an oxidation flow reactor under dry and dark conditions. Prior to each experiment, the reactor was purged with zero air (Parker 75-62 purge gas

generator). Ozone was introduced into the reactor by flowing pure oxygen at 1 standard liters per minute (slm) through a commercial ozone generator (OzoneTech OZ2SS-SS). After the ozone concentration stabilized, pure isoprene, β -pinene, α -terpineol and d-limonene were injected into 5 slm of purge air flow separately using a syringe pump at a rate of $\sim 2 \mu\text{L}$ per minute. High concentrations ($2.2 \times 10^{15} \text{ cm}^{-3}$ for isoprene and $1.4 \times 10^{15} \text{ cm}^{-3}$ ppm for β -pinene, α -terpineol and d-limonene) of precursor and ozone ($1.8 \times 10^{14} \text{ cm}^{-3}$) were used to generate enough material for analysis.

SOA_{OH} particles were generated in a 19 L potential aerosol mass (PAM) reactor.⁵⁸ 100 – 500 μL of VOC precursors (isoprene, β -pinene, α -terpineol and d-limonene) were placed in an open 1.5 mL amber glass vial, which was kept inside a glass bottle prior to the PAM reactor. The precursors were then injected into the chamber by a 0.5 slm of carrier flow mixed with a 6 slm of humidified (Perma Pure humidifier, MH-110-12P-4) flow of purified air from a zero-air generator (Model 7000, Environics). The $\bullet\text{OH}$ radicals were generated through photolysis of water molecules by 185 nm UV radiation. The exposure time for the photooxidation of precursors in the PAM reactor was about three minutes with relative humidity around 30 – 40%. Despite the high $\bullet\text{OH}$ concentrations ($\sim 10^{11} - 10^{12} \text{ cm}^{-3}$) compared to ambient levels ($\sim 10^6 \text{ cm}^{-3}$), the PAM-generated SOA are found to be similar to ambient and chamber-generated SOA in terms of yield, oxidation state, hygroscopicity, and chemical composition.⁶⁶⁻⁶⁸ Additional advantages of the PAM reactor include shortened experimental timescales, ability to reach long photochemical ages, and minimized wall losses.⁶⁸

A scanning mobility particle sizer (SMPS, Grimm Aerosol Technik) was used to record the number concentrations and size distributions of SOA produced in the PAM reactor. The typical particle diameter of SOA_{OH} ranged from 30 nm to 500 nm, and the geometric mean diameter by mass varied from 70 – 120 nm. Particle sampling was initiated after the number concentrations stabilized. The SOA particles were collected on 47mm polytetrafluoroethylene (PTFE) filters (Millipore FGLP04700, 0.2 μm pore size) at a flow rate of 13 slm for 40 min and 5 slm for 3 hours for SOA_{O₃} and SOA_{OH}, respectively.

The filter samples were extracted in 1 mL spin trap solutions (10 mM) or Milli-Q (deionized, resistivity = 18.2 M Ω /cm) water for 7 min. The filter extracts were used for radical measurements or the H₂O₂ fluorometric assay, respectively. The mass difference before and after the extraction was regarded as SOA dissolved in reagents, and an average molar mass of 200 g mol⁻¹ was used for the calculation of SOA molar concentrations in filter extracts. The SOA_{O3} and SOA_{OH} concentrations were in the range of 1 – 16 mM and pH of SOA extracts varied between 4 – 6. At least three samples were prepared for each SOA_{O3} and SOA_{OH} for EPR analysis and H₂O₂ measurement, respectively.

2.3.2 EPR measurements

A continuous-wave electron paramagnetic resonance (CW-EPR) spectrometer (Bruker, Germany) coupled with a spin-trapping technique was used for free radical quantification. The spin trapping agent used to capture free radicals generated upon aqueous reactions of SOA is 5-*tert*-Butoxycarbonyl-5-methyl-1-pyrroline-N-oxide (BMPO) (Enzo, $\geq 99\%$). After extraction, the filter extracts were incubated at a room temperature of 20 °C, and a 50 μ L aliquot was loaded into a 50 μ L capillary tube (VWR) and inserted in the resonator of the EPR spectrometer at 10, 20, 60, 120 and 240 min from the start of aqueous reactions. The parameter set for EPR measurements was a center field of 3515.0 G, a sweep width of 100.0 G, a receiver gain of 30 dB, a modulation amplitude of 1.0 G, a scan number of 10 – 50, attenuation of 12 dB, a microwave power of 12.6 mW, a modulation frequency of 100 kHz, and a conversion time/time constant of 5.12 ms. After obtaining the EPR spectra, SpinFit and SpinCount methods embedded in the Bruker Xenon software were applied to quantify BMPO-radical adducts²⁶ at each time point.

2.3.3 H₂O₂ fluorometric assay

A modified protocol¹³⁹ was applied for the H₂O₂ measurement using a fluorometric H₂O₂ assay kit (MAK165, Sigma-Aldrich). 250 μ L DMSO and 1 mL assay buffer were added to the red peroxidase substrate and horseradish peroxidase for reconstitution, respectively. The reagents were divided into ten sets of aliquots (25 μ L red peroxidase substrate, 100 μ L horseradish peroxidase and 2 mL assay buffer each).

Prior to each analysis, one set of reagents was used to prepare 2 mL working solutions, consisting of 20 μL red peroxidase substrate, 80 μL horseradish peroxidase, and 1.9 mL assay buffer. All H_2O_2 measurements were conducted within two hours from the preparation of working solutions due to the high instability of the probe. A calibration was performed using H_2O_2 standards concentrations ranging from 0.05 – 1.5 μM , which were prepared by diluting 30 wt% H_2O_2 (Sigma-Aldrich). The reaction vials (3 mL) consisted of 2.94 mL solution (Milli-Q water + filter extracts) and 60 μL working solution. The H_2O_2 yields from different SOA samples varied significantly and dilution factors were adjusted, so that the final H_2O_2 concentrations in the reaction vial were below 1.5 μM . All H_2O_2 measurements were conducted with a filter blank, with the same dilution factor as the samples. The addition of working solution was considered as the start of reaction, and the reaction vials were incubated at the room temperature for 15 min until the measurement. The fluorescence of the reagents was measured by a spectrofluorophotometer (RF-6000, Shimadzu) at excitation and emission wavelengths of 540 and 590 nm, respectively.

2.3.4 Kinetic modeling

A kinetic model was applied to simulate the simultaneous formation of $\bullet\text{OH}$ and $\text{O}_2\bullet/\text{HO}_2\bullet$ by aqueous reactions of SOA using the reactions listed in Table A2. The reactions include chemical reactions of SOA components (R1 – R7), ROS coupling reactions (R8 – R16), and radical-trapping reactions by BMPO (R17 – R21). SOA chemistry includes decomposition of organic hydroperoxides (ROOH) generating $\bullet\text{OH}$ radicals (R1),^{26, 98} $\bullet\text{OH}$ oxidation of primary and secondary alcohols ($\text{R}_1\text{R}_2\text{CHOH}$) and subsequent reaction with O_2 to form α -hydroxyperoxyl radicals ($\text{R}_1\text{R}_2\text{C}(\text{O}_2)\text{OH}\bullet$) (R2), decomposition of $\text{R}_1\text{R}_2\text{C}(\text{O}_2)\text{OH}\bullet$ to generate $\text{HO}_2\bullet$ (R3),^{140, 141} $\bullet\text{OH}$ oxidation of ROOH (R4)¹⁴⁰, $\text{R}_1\text{R}_2\text{C}(\text{O}_2)\text{OH}\bullet$ (R5), and other SOA components (R6) and $\text{HO}_2\bullet$ termination of $\text{R}_1\text{R}_2\text{C}(\text{O}_2)\text{OH}\bullet$ (R7). The reaction yield of R3 (c_1) was also considered in the model. Rate coefficients of decomposition of ROOH and $\text{R}_1\text{R}_2\text{C}(\text{O}_2)\text{OH}\bullet$ as well as H-abstraction of $\text{R}_1\text{R}_2\text{CHOH}$ were assumed to be independent of the structures of R groups contained among different SOA, representing a major model assumption. This assumption is in line with the

CAPRAM 3.0 model¹⁴⁰, in which the rate constants of H-abstraction on alcohols vary within one order of magnitude regardless of carbon numbers and functionalities besides the hydroxy group. The radical composition profiles generated by different SOA are solely determined by the relative abundance of ROOH and R₁R₂CHOH groups in SOA. Potential variation of these rate constants depending on R structures can be partly translated into uncertainties in molar fractions of ROOH and R₁R₂CHOH as shown in Table A3.

The rate coefficients of ROS coupling reactions were obtained from literature values and the unknown rate coefficients and molar fractions of ROOH and R₁R₂CHOH contained in SOA were determined using the Monte Carlo genetic algorithm (MCGA) to reproduce experimental data.¹⁴² In the Monte Carlo search, input parameters were varied randomly within individual bounds: the boundaries of all reaction rate constants were generally constrained to within two orders of magnitude based on literatures, while the ROOH/R₁R₂CHOH molar fractions were constrained to between 0.1 – 80%. As discussed in the main text, the determined rate coefficients and molar fractions are reasonable and in line with previous experimental measurements and modeling studies. The uncertainty of the reaction rates in Table A2 and the ROOH/R₁R₂CHOH fractions in Table A3 were obtained by running the MCGA numerous times (~ 40), which resulted in 20 parameter sets which reasonably captured the temporal trends of the experimental data. The 20 parameter sets were then used to plot 20 traces for the temporal formation of the BMPO adducts by each SOA, and the highest and lowest traces were selected as the upper and lower boundaries shown in Figure 2.3 for each SOA, respectively. Note that these boundaries do not necessarily correspond to the boundaries of each parameter in Table A2 and A3. There is still relatively large uncertainty in the actual values of some parameters, as shown by the parameter ranges in Table A2; further measurements to quantify organic hydroperoxides and alcohols as well as dedicated kinetic studies would be required for determination of these parameters.

The relative abundance of O₂^{•-} and HO₂[•] in the aqueous solution is largely determined by pH. Tresp et al.¹⁴³ showed that at neutral pH (7.4), over 99.9% of BMPO-OOH was generated by BMPO reacting with O₂^{•-}. In contrast, the pH of the SOA aqueous solutions obtained in this study ranged from 4 to 6. According

to the Henderson-Hasselbalch equation with a pK_a value of 4.88 for HO_2^\bullet , HO_2^\bullet would dominate over O_2^\bullet when the pH approaches 4, while O_2^\bullet and HO_2^\bullet are in comparable amounts when $pH = \sim 5$. Therefore, BMPO trapping reactions of both O_2^\bullet and HO_2^\bullet to form BMPO-OOH are considered (R18, 19).¹³⁶ The BMPO radical adducts (BMPO-OH, BMPO-OOH) can decay by self-decomposition or reactions with other radicals. While self-decomposition half-life of BMPO-OH and BMPO-OOH in neutral solutions are known to be 30 min¹⁴⁴ and 23 min,¹⁴⁵ respectively, rate coefficients with radicals (e.g., $^\bullet OH$, O_2^\bullet , organic radicals) leading to adduct decay are unknown. Thus, in this study decay of BMPO-OH (R18) and BMPO-OOH (R21) are treated with pseudo-first-order rate coefficients. The estimated half-lives of BMPO-OH and BMPO-OOH are shorter than the literature values to be 14 – 24 min and 6–14 min, respectively, indicating that decay of adducts by radicals are non-negligible or lower pH may have impacted adduct stability.¹⁴⁶

2.4 Results and Discussion

2.4.1 ROS formation efficiencies by SOA

Biogenic SOA were generated by both dark ozonolysis and $^\bullet OH$ photooxidation (referred as SOA_{O_3} and SOA_{OH} hereafter) of isoprene, β -pinene, α -terpineol, and d-limonene. Particle water extracts were analyzed with electron paramagnetic resonance (EPR) spectroscopy coupled with a spin-trapping technique for detection of free radicals. Figure 2.1 shows the observed EPR spectra of isoprene (a) SOA_{O_3} and (b) SOA_{OH} . The observed spectra were simulated and deconvoluted into spectra for different BMPO adducts with radicals including $^\bullet OH$, O_2^\bullet/HO_2^\bullet , and carbon- and oxygen-centered organic radicals (BMPO-OH, BMPO-OOH, BMPO-R, and BMPO-OR, respectively). The EPR spectrum of isoprene SOA_{O_3} is dominated by a four-peak pattern, which can be attributed to BMPO-OH with a minor contribution from BMPO-OOH. In contrast, the major peaks in the EPR spectrum from isoprene SOA_{OH} represent BMPO-OOH with a minor contribution from carbon- and oxygen-centered organic radicals. Similar trends are observed for β -pinene and α -terpineol SOA, while d-limonene SOA mainly produces O_2^\bullet/HO_2^\bullet for both oxidation systems (Figure A2).

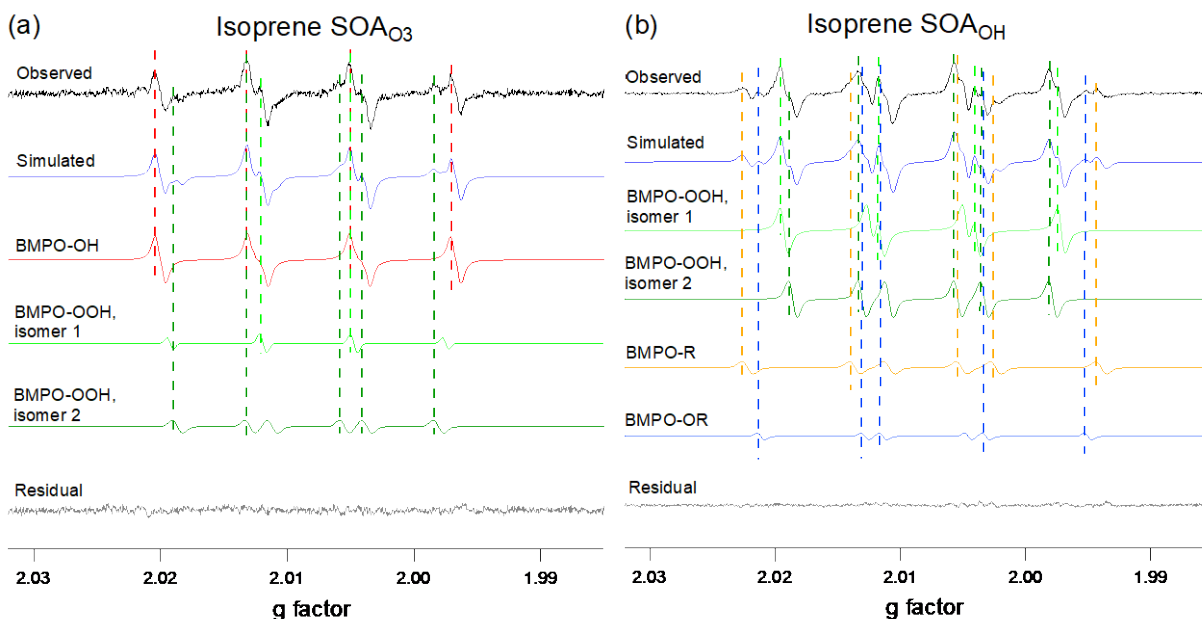


Figure 2.1. EPR spectra of BMPO-radical adducts from aqueous reactions of isoprene SOA generated from (a) dark ozonolysis and (b) $\bullet\text{OH}$ photooxidation. The observed spectra (black) are simulated (purple) and deconvoluted into BMPO-OH (red), BMPO-OOH isomer 1 (light green), BMPO-OOH isomer 2 (dark green), BMPO-R (yellow), and BMPO-OR (blue). Residual (grey) denotes the difference of observed and simulated spectra. Note that the two isomers of BMPO-OOH represent the trans or cis structures of the -OOH group.

Integration of deconvoluted spectra allows us to quantify contributions from each radical species. Figure 2.2 shows quantifications of different types of radicals in water extracts of SOA generated by ozonolysis or $\bullet\text{OH}$ oxidation of isoprene, β -pinene, α -terpineol, and d-limonene. Relative yields of BMPO-OH of isoprene and β -pinene SOA_{O_3} after 20 min of reactions are 44% and 52%, respectively (Figure 2.2(a)), both of which further increase to >70% after 2 hours (Figure A3a). This is in very good agreement with a previous study which demonstrated major OH formation from biogenic SOA formed by ozonolysis.⁹⁸ α -terpineol SOA_{O_3} generates $\bullet\text{OH}$ exclusively, while d-limonene SOA_{O_3} generates $\text{O}_2\bullet^-/\text{HO}_2\bullet$ dominantly (80%) with minor contributions from $\bullet\text{OH}$ (11%) and organic radicals (7%). In contrast to major $\bullet\text{OH}$ formation by most of SOA_{O_3} , more than 80% of radical species generated from SOA_{OH} are in the form of $\text{O}_2\bullet^-/\text{HO}_2\bullet$. Figures 2.2 (b) and (c) show the molar yields or formation efficiencies of $\bullet\text{OH}$ and $\text{O}_2\bullet^-/\text{HO}_2\bullet$.

(molar concentration ratios of BMPO-radical adduct to SOA) for SOA_{O3} and SOA_{OH}, respectively. α -terpineol SOA_{O3} has the highest \bullet OH formation efficiency with 0.06% followed by β -pinene and isoprene SOA_{O3}. All types of SOA_{OH} are found to have a similar O₂ \bullet /HO₂ \bullet formation efficiency of 0.018 - 0.03%.

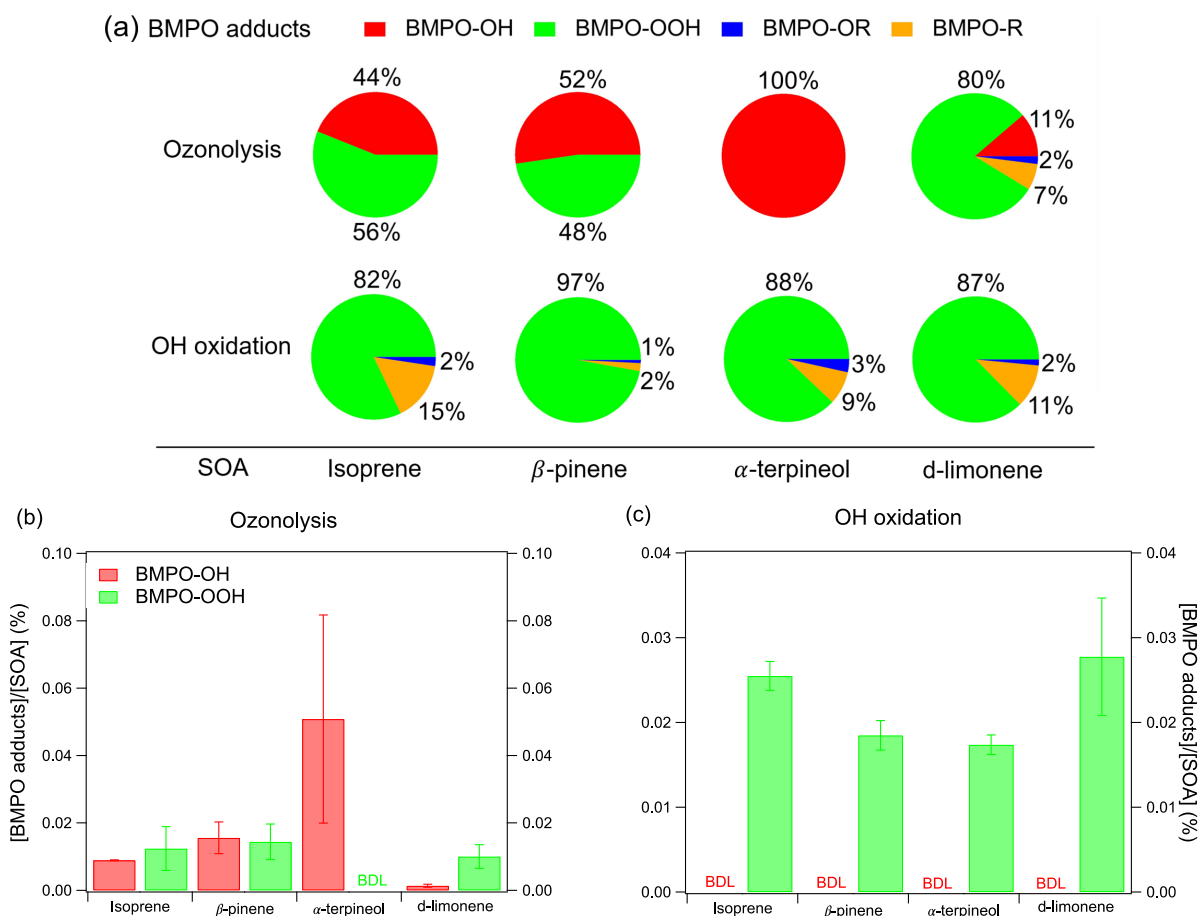


Figure 2.2. (a) Relative yields of BMPO-radical adduct from aqueous reactions of SOA generated by ozonolysis versus \bullet OH photooxidation of isoprene, β -pinene, α -terpineol and d-limonene. Molar yields of BMPO-OH (red) and BMPO-OOH (green) adducts generated by SOA from (b) dark ozonolysis and (c) \bullet OH photooxidation after 20 min of aqueous reactions.

The molar yields of H₂O₂ from SOA were also quantified using a fluorometric H₂O₂ assay (Table A1). Isoprene SOA generally yields higher H₂O₂ compared to other types of SOA. The H₂O₂ yield from β -pinene SOA_{O3} (1.8 \pm 0.3%) is comparable with results of Wang et al. (1.3 \pm 0.9%),¹²⁹ but around half of the amount reported by Tong et al. (3.2 \pm 0.7%).⁹⁸ Isoprene SOA_{O3} generally produce higher H₂O₂ (4.2 \pm 0.7%) compared to β -pinene SOA_{O3} (1.8 \pm 0.3%), which are comparable with Tong et al.⁹⁸ (8.0 \pm 0.8% for isoprene

SOA_{O3} and 3.2±0.7% for β-pinene SOA_{O3}). For both oxidation systems with various precursors, the production of O₂[•]/HO₂[•] is tightly correlated with H₂O₂ formation with *R*² greater than 0.9 (Figure A4), indicating that O₂[•] is an important precursor of H₂O₂, or O₂[•] and H₂O₂ have similar types of source compounds. For β-pinene, α-terpineol, and d-limonene SOA, the H₂O₂ yields from SOA_{O3} are about one order of magnitude higher than those from SOA_{OH}. This is consistent with the reaction mechanism of ozonolysis, in which stabilized Criegee intermediates hydrolyze to form α-hydroxyhydroperoxides that can readily decompose into carbonyls and H₂O₂.^{129, 147, 148}

The distinct profiles of ROS composition by SOA_{O3} and SOA_{OH} reflect differences in chemical compositions and functionalities caused by different oxidation pathways. Monoterpene SOA from ozonolysis generally contains higher fractions of organic peroxides (12 – 65%) compared to those from photooxidation (6 – 18%),^{149, 150} partly because organic hydroperoxides are decomposed with prolonged UV exposure.^{151, 152} As ROOH can be a primary source of •OH radicals through decomposition,^{26, 98} lower ROOH fractions should lead to minor contributions of •OH formation for SOA_{OH}. Detailed ROS formation mechanisms are discussed below to better understand how precursors and oxidation systems can affect ROS profiles.

2.4.2 Reaction mechanism

The temporal evolution of •OH and O₂[•]/HO₂[•] formation from the aqueous reactions of SOA was measured. As shown in Figure 2.3 (a), the molar yields of BMPO-OH adducts from SOA_{O3} increase over time to reach a steady state after approximately two hours. In contrast, the molar yields of BMPO-OOH adducts from SOA_{O3} (except α-terpineol SOA_{O3}, which was below detection limit) reach their maximum concentrations within a short period of time (< 30 min), followed by a slight decrease (Figure 2.3 (b)). For SOA_{OH}, O₂[•]/HO₂[•] yields reach their maximum within 40 min but decrease gradually over 4 hours (Figure 2.3 (c)). The BMPO-OH concentrations from all SOA_{OH} are below detection limit. The highly distinct time-dependent profiles of •OH and O₂[•]/HO₂[•] formation lead to an interesting evolution of radical composition

by SOA. For example, radical production from isoprene and β -pinene SOA_{O_3} is initially dominated by O_2^\bullet / HO_2^\bullet , while $^\bullet\text{OH}$ becomes dominant after 20 min (Figure A3a). In comparison, d-limonene SOA_{O_3} and all types of SOA_{OH} (Figure A3b) are consistently dominated by O_2^\bullet / HO_2^\bullet (> 70%) over 4 hours.

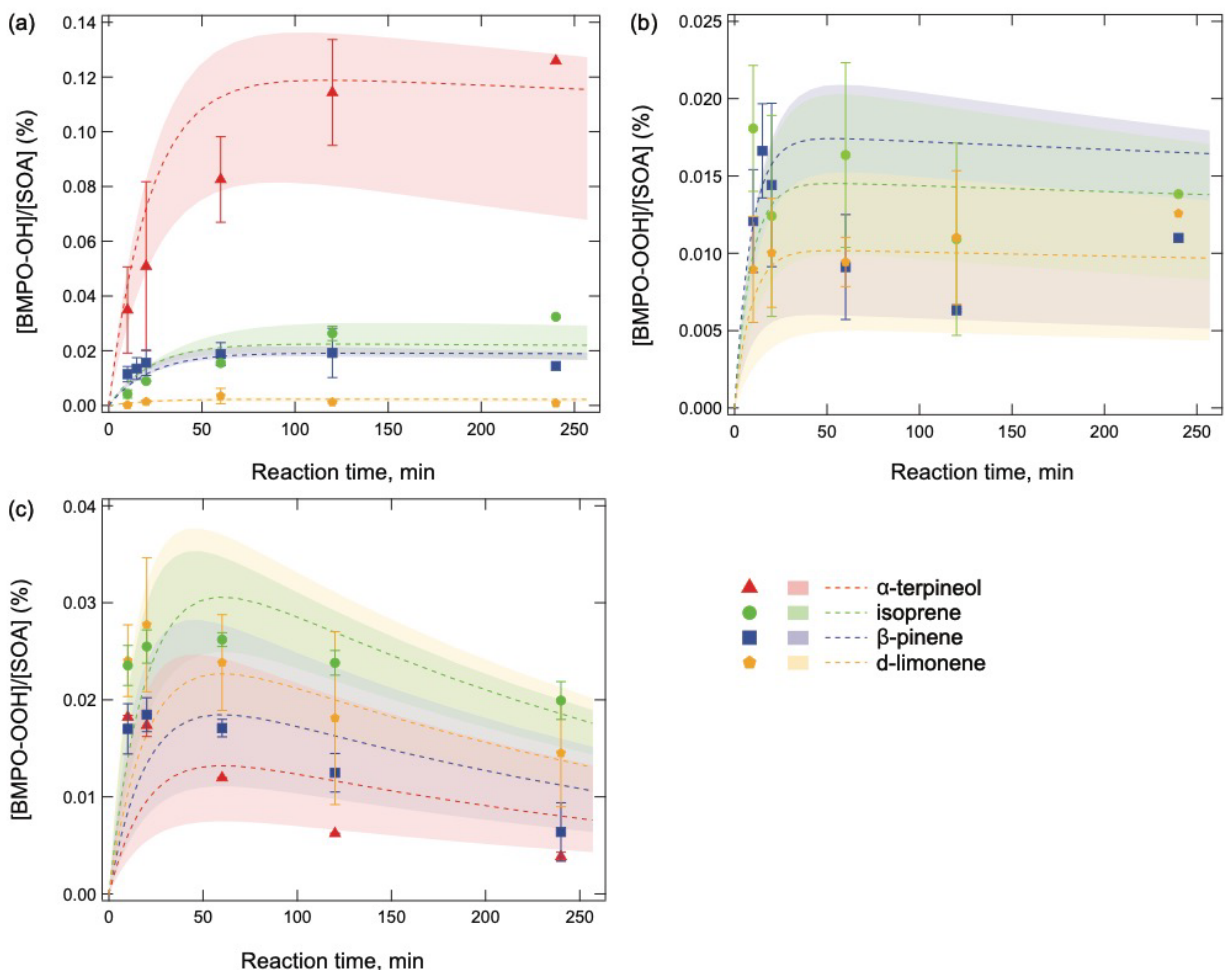
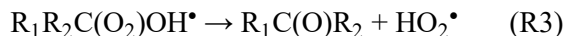
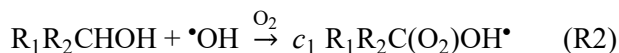
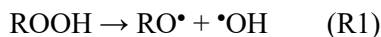


Figure 2.3. Temporal evolution of molar yields of (a) BMPO-OH and (b) BMPO-OOH adducts from aqueous reactions of SOA generated from dark ozonolysis (SOA_{O_3}) and (c) BMPO-OOH adducts from SOA generated from $^\bullet\text{OH}$ photooxidation (SOA_{OH}) of α -terpineol (red), isoprene (green), β -pinene (blue), and d-limonene (yellow). The markers are experimental data. The dashed lines represent the best fits of kinetic model with the shaded area denoting the modeling uncertainties. The O_2^\bullet / HO_2^\bullet formation from α -terpineol SOA_{O_3} and $^\bullet\text{OH}$ formation from all SOA_{OH} are below detection limit.

To further elaborate the reaction kinetics and mechanism, a kinetic model was developed and applied to simulate the temporal evolution of $\bullet\text{OH}$ and $\text{O}_2\bullet/\text{HO}_2\bullet$ radicals. The following reactions were implemented into the kinetic model for $\bullet\text{OH}$ and $\text{O}_2\bullet/\text{HO}_2\bullet$ formation:



$\bullet\text{OH}$ can be generated from the first-order decay of organic hydroperoxides (ROOH) (R1).^{26, 98, 153} Krapf et al.¹²¹ provided molecular evidence of the unimolecular decomposition of labile hydroperoxides in the condensed phase through the cleavage of the weaker O-O bond which must lead to $\bullet\text{OH}$ formation. In addition, direct $\bullet\text{OH}$ formation has been observed from the decomposition of cumene hydroperoxide²⁶ (a common proxy of atmospheric ROOH) at room temperature and a recent study¹⁵⁴ demonstrated that the implementation of R1 in the aqueous chemistry model CAPRAM would account for an important source of aqueous $\bullet\text{OH}$ formation from HOM. Note that $\bullet\text{OH}$ formation in R1 results from the decomposition of organic hydroperoxides without additional functionalities on the α -carbon, as the decomposition of α -hydroxyhydroperoxides leads to the formation of carbonyl and H_2O_2 instead of $\bullet\text{OH}$.¹⁴⁸ The generated $\bullet\text{OH}$ can abstract a hydrogen atom from α -carbon of primary or secondary alcohols to form α -hydroxyalkyl radicals ($\text{R}_1\text{R}_2\text{C}(\text{OH})\bullet$), which immediately combine with dissolved O_2 to form α -hydroxyperoxyl radicals ($\text{R}_1\text{R}_2\text{C}(\text{O}_2)\text{OH}\bullet$) (R2). These radicals can subsequently undergo unimolecular decomposition to form $\text{HO}_2\bullet$ (R3)^{140, 141}. Note that this reaction is known to occur also in the gas phase.¹²

Note that $\bullet\text{OH}$ formation can be promoted in the presence of transition metal ions via Fenton(-like) reactions.^{155, 156} To address this possible interference of metal contamination on radical formation, concentrations of Fe and Cu ions in the SOA extracts were measured using two highly sensitive spectrophotometric methods (ferrozine and bathocuproine methods¹³⁹, respectively). The results showed that they were both below the detection limits (10 ± 2 nM and 20 ± 5 nM for Fe and Cu ions, respectively). An additional control experiment was also conducted measuring ROS formation from SOA extracts with

and without a metal-chelating agent, diethylenetriaminepentaacetic acid (DTPA), showing no significant difference, confirming the negligible impacts of potential metal contamination.

The kinetic model also considers a number of other reactions including $\bullet\text{OH}$ loss via reactions with SOA components, ROS coupling reactions, radical trapping by BMPO, and decay of BMPO-radical adducts (Table A2). Molar fractions of ROOH and $\text{R}_1\text{R}_2\text{CHOH}$ contained in SOA were estimated using the Monte Carlo genetic algorithm (MCGA) to reproduce experimental data¹⁴². The decomposition rate of ROOH estimated in this study ($(0.9 - 6.5) \times 10^{-5} \text{ s}^{-1}$) is in agreement with previous studies,^{26, 136} and the lifetime of α -hydroxyperoxyl radicals ($0.002 - 0.06 \text{ s}$) is also consistent with the aqueous chemistry model CAPRAM 3.0 ($0.001 - 0.005 \text{ s}$).¹⁴⁰ As shown in Figure 2.3, the modeling results show good agreement with measurements within modeling uncertainties, indicating that the above reaction mechanisms are plausible for $\bullet\text{OH}$ and $\text{O}_2\bullet/\text{HO}_2\bullet$ formation as they can explain the temporal evolution of distinct radical profiles depending on precursors and oxidation pathways. It should be noted that the decomposition rates involving hydroperoxides could be pH-dependent according to a recent study by Qiu et al.¹⁵⁷ Therefore, future studies are still warranted for the pH effects on ROS formation from SOA in the aqueous phase, where acidification (representative of aerosol pH) and neutralization (representative of physiological pH) are of interest and could both play a role in affecting the profiles of radical production.

The model-estimated molar fractions of ROOH in isoprene, β -pinene, and d-limonene SOA_{O_3} are 6–25%, 7–35%, 2–12%, respectively (Table A3), which are comparable with the peroxide mass fractions reported by previous studies for the same types of SOA ($\sim 30\%$, $\sim 85\%$, $\sim 2\%$, respectively),^{8, 149, 158, 159} assuming that molar masses of peroxides and SOA components are the same. Note that the measured total peroxide contents include both organic peroxides (ROOR) and hydroperoxides (ROOH), which may explain the lower estimated fraction of ROOH in isoprene and β -pinene compared to literature values. In addition, it may imply that some ROOH may be more stable and do not decompose within the timescale of the experiment, as has been observed for isoprene hydroxyl hydroperoxide in a recent study¹⁶⁰. Significantly higher fractions of ROOH are estimated in isoprene and β -pinene SOA_{O_3} compared to their corresponding

SOA_{OH} (3 – 5% and 1 – 3%), leading to the major contribution of •OH formation in SOA_{O₃}. The molar fractions of R₁R₂CH(OH) in d-limonene SOA are estimated to be higher compared to ROOH, contributing to the O₂•⁻/HO₂•-dominated profile for both d-limonene SOA_{O₃} and SOA_{OH}. Significant amounts of R₁R₂CH(OH) are predicted in most SOA (34 – 74%). Primary and secondary alcohols are generated via multigenerational gas-phase oxidation as shown in a number of previous experimental and theoretical studies as summarized in review papers.^{12, 161} α-terpineol SOA_{O₃} is estimated to contain a very small fraction of R₁R₂CH(OH) (0.1 – 1%), leading to suppression of the O₂•⁻/HO₂• formation. This is likely caused by the specific position of hydroxy groups in α-terpineol: tertiary alcohol without α-H for abstraction and subsequently no formation of peroxy radicals. The predicted very low fraction of R₁R₂CH(OH) in α-terpineol SOA_{O₃} is consistent with previous experimental measurements,¹⁶² showing that the primary products (>90%) from α-terpineol ozonolysis only contain tertiary alcohols.

2.5 Implications

This work elucidates ROS generation pathways from aqueous reactions of biogenic SOA as presented in Figure 2.4. Multi-generational atmospheric oxidation and autoxidation of biogenic VOCs by •OH and O₃ lead to the formation of highly functionalized and extremely low volatility organic compounds, HOM and ELVOC.^{108, 109} Most of these compounds contain alcohol and hydroperoxide functional groups. After condensation into the particle phase, a fraction of organic hydroperoxides (ROOH) decomposes to form •OH, which can act as an ignition step for a cascade of ROS formation pathways. The e-folding times for the ROOH decomposition are estimated to be 4 – 30 hours, which represent average lifetimes for different ROOH compounds; some of them may have shorter timescales,^{121, 122} while others may be very stable.^{163, 164} This decomposition process can be accelerated by photolysis^{151, 152} and Fenton-like reactions of transition metal ions.^{26, 136, 160} We acknowledge a caveat of this work that the particle mass concentrations in the PAM reactor are much higher compared to ambient conditions, leading to more prominent condensation of semi-volatile organic compounds. However, a recent study¹⁶⁴ found that the PAM-reactor-generated α-pinene SOA contain substantial amounts of particle-phase HOM, which is consistent with the

gas-phase measurements in previous studies.^{109, 165, 166} While this study serves as a proof of concept and provide mechanistic insights into possible mechanisms of ROS formation, future studies are definitively warranted to investigate the ROS formation from SOA generated under conditions with lower oxidant and particle concentrations.

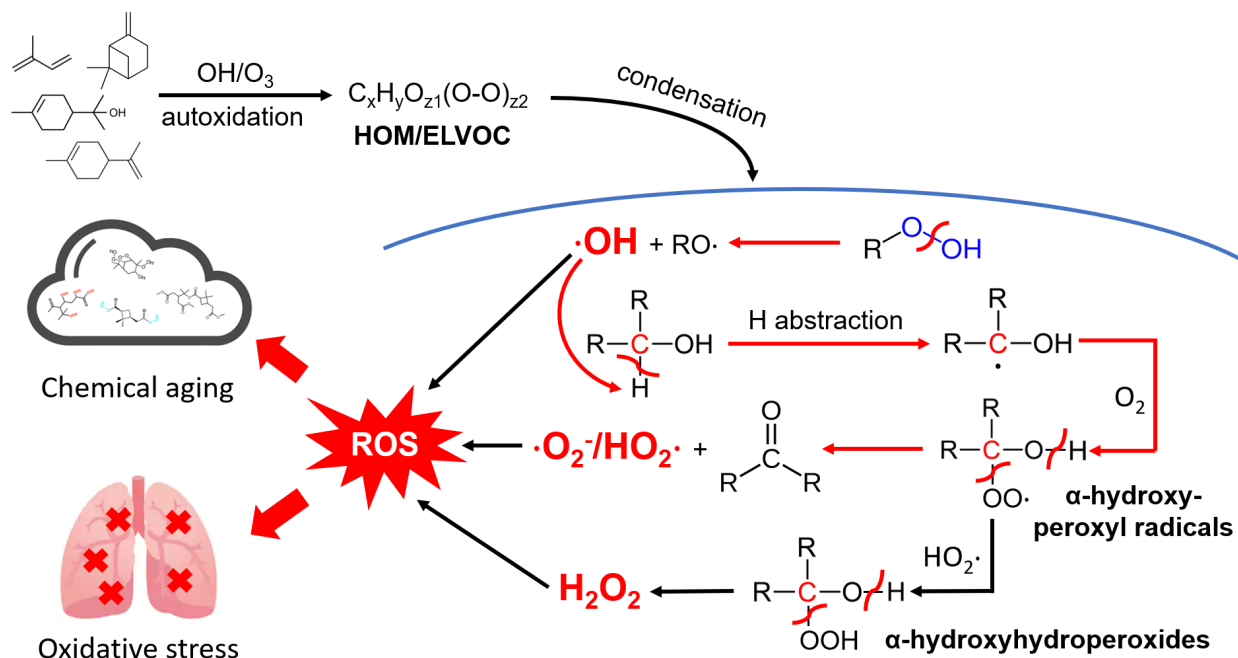


Figure 2.4. Implications of ROS formation by aqueous reactions of biogenic SOA. Highly oxygenated organic molecules (HOM) and extremely low volatility organic compounds (ELVOC) are generated by gas-phase oxidation and autoxidation. After condensation, ROS including $\cdot\text{OH}$, $\text{O}_2^-/\text{HO}_2\cdot$ and H_2O_2 can be generated via decomposition of organic hydroperoxides, $\cdot\text{OH}$ oxidation of primary or secondary alcohols, and unimolecular decomposition of α -hydroxyperoxyl radicals and α -hydroxyperoxyhydroperoxides in the aqueous phase. This process has significant implications for chemical aging of SOA in the atmosphere and oxidative stress upon respiratory deposition of SOA particles.

The $\cdot\text{OH}$ radicals released during SOA decomposition can abstract hydrogen from primary or secondary alcohols ($\text{R}_1\text{R}_2\text{CH}(\text{OH})$) to form α -hydroxyalkyl radicals, which quickly react with dissolved oxygen to form α -hydroxyperoxyl radicals. Within milliseconds α -hydroxyperoxyl radicals can undergo unimolecular decomposition to form $\text{O}_2^-/\text{HO}_2\cdot$ radicals. Through $\text{HO}_2\cdot$ termination, α -hydroxyperoxyl radicals form α -hydroxyalkyl hydroperoxides, which can decompose to generate H_2O_2 , another important

ROS.^{148, 167} Note that α -hydroxyalkyl hydroperoxides can form a stable complex with a water molecule, so the -O-OH group is unlikely to be cleaved to yield \bullet OH radicals.^{148, 168} Other feasible pathways of H₂O₂ formation by SOA have also been discussed in the literature including hydrolysis of diacyl peroxides or peroxy acids¹⁶⁹ and the relative contributions of different H₂O₂ sources still warrant further studies.

Our findings demonstrate the importance of the interplay among different functionalities in determining radical production in the aqueous phase. The relative abundance of ROOH and R₁R₂CH(OH) can largely affect the compositions of \bullet OH, O₂ \bullet^- /HO₂ \bullet , H₂O₂ and organic radicals. It has been established that ROS play a central role in chemical transformation of organic and inorganic compounds in aqueous particles. Sources, sinks and concentrations of ROS in atmospheric waters are still uncertain and it is still challenging to accurately predict their concentrations in atmospheric aqueous chemistry models.^{124, 170} Implementation of molar yields of ROS by SOA determined in this study into models should improve quantification of ROS in aqueous droplets, which can then be compared with traditional ROS sources such as gaseous HO_x uptake and Fenton reactions to evaluate relative importance of different ROS formation pathways.

α -terpineol and d-limonene are known as important indoor-relevant VOC. α -terpineol is a significant component of liquid cleaner/disinfectant and air freshener and can be emitted by some molds in the indoor environment, whereas d-limonene has been found in floor wax, all-purpose cleaners and personal care products¹⁷¹. These terpenes are found in higher concentrations in indoor environments compared to outdoors and their oxidation can lead to substantial SOA formation indoors.¹⁷² These compounds can also be transported to the outdoors, affecting ozone and SOA formation in the atmosphere.¹⁷³ α -terpineol SOA_{O₃} and d-limonene SOA_{OH} show the highest formation efficiencies in aqueous generation of \bullet OH and O₂ \bullet^- /HO₂ \bullet , respectively. Quantification of different types of ROS by SOA should be helpful for a better understanding of the aqueous-phase processing of chemical compounds in indoor and outdoor processes. Upon inhalation and respiratory deposition of SOA particles, O₂ \bullet^- can be generated via redox reactions with lung antioxidants or can be released by macrophages after phagocytosis of inhaled particles in the lung

lining fluid.^{174, 175} The antioxidant defense system can counteract ROS, however, excessive production of ROS can overwhelm antioxidant defenses and trigger or enhance oxidative stress, cell death, and biological aging.^{110, 176} As direct measurements of ROS in the lung lining fluid are challenging, implementation of formation efficiency of $O_2^{\bullet-}$ into the lung model^{111, 137} will improve quantification of ROS in the lung lining fluid for better evaluation of the impact of biogenic SOA on oxidative stress and adverse health effects including asthma, allergies and other respiratory diseases.

2.6 Chapter 2 Appendix

2.6.1 SOA chemistry

There are numerous reactions involving SOA components with other reactive functionalities,¹² but it is very challenging to make an exhaustive list with all possible reactions. The main focus of kinetic modeling is on reactions leading to the ROS formation, with the rest of reactions either lumped or omitted in the kinetic model. The termination reaction of α -hydroperoxyl radicals by HO_2^\bullet (R7 in Table A2) and $^\bullet\text{OH}$ oxidation of other SOA components represents the lumped reactions with other reactive functionalities, such as aldehydes and ketones. Even at the diffusion-limited rate of $10^{-11} \text{ cm}^3 \text{ s}^{-1}$,¹⁷⁷ the sensitivity analysis indicates that these reactions have negligible impacts on the formation of radicals and BMPO adducts. For the potential reactions of aldehyde and ROOH, Marteau et al.¹⁷⁸ demonstrated that they only act as a minor pathway for the initiation of a $\text{R}(\text{CO})^\bullet$ radical and subsequent autoxidation, while the major pathways are through UV irradiation, transition metal catalysis (not present in our system) and O_2 oxidation (more probable). Furthermore, due to the relatively slow reaction rates of ROOH with ketones/aldehydes¹⁷⁹ ($k \ll 1.0 \times 10^{-20} \text{ cm}^3 \text{ s}^{-1}$), the aldehyde-ROOH reaction is unlikely to be competitive with the unimolecular decomposition of ROOH (R1 in Table A2, $k_1 \sim 10^{-5} \text{ s}^{-1}$). Given that no $^\bullet\text{OH}$ or $\text{O}_2^\bullet/\text{HO}_2^\bullet$ would be generated through this reaction¹⁷⁸, we did not treat it in the kinetic model. A recent study by Peng and Jimenez⁵¹ discussed the potential formation of organic trioxide (ROOOH) from $\text{RO}_2^\bullet + ^\bullet\text{OH}$ in the PAM chamber, however, it is unlikely that ROOOH would contribute substantially to ROS formation in the aqueous phase as observed in this study. The $\text{ROOOH} + ^\bullet\text{OH}$ reaction by the H abstraction from the -OOOH is expected to be very fast at a near diffusion-controlled rate ($\sim 10^{-11} \text{ cm}^3 \text{ s}^{-1}$) to form ROOO^\bullet , which rapidly decomposes to RO^\bullet , leading to carbonyl production. Thus, the condensation of ROOOH into the particle phase may not be significant as it should either be decomposed or reacted away prior to or shortly after partitioning. In addition, we compared the ROS formation from SOA samples collected freshly versus the ones stored in a

freezer (-20°C) for one month, which showed no statistically significant difference indicating that the compounds responsible for ROS formation in the SOA particles should be relatively stable.

2.6.2 H₂O₂ fluorometric assay

The H₂O₂ reactions with •OH and HO₂• (R8, R12 in Table A2) are unlikely to cause noticeable interference in ROS quantification. Specifically, H₂O₂ reacts with both •OH and HO₂• relatively slowly (5.5×10^{-14} and 5.0×10^{-21} cm³ s⁻¹, respectively). Sensitivity analysis indicates that these reactions are negligible pathways for the loss of •OH and HO₂• compared to BMPO trapping. On the other hand, the H₂O₂ probe (i.e., red peroxidase substrate) is in excess when performing H₂O₂ analysis and reacts with H₂O₂ relatively fast compared to the H₂O₂-•OH and H₂O₂-HO₂• reactions. This probe is very sensitive and specific to H₂O₂ analysis as it does not yield fluorescence other than from its reaction with H₂O₂. Therefore, it is unlikely that other oxidants interfere with the H₂O₂ analysis. On a related issue, we note that the control experiment showed no EPR signal from BMPO + H₂O₂, indicating no inference of H₂O₂ in the EPR measurement.

Table A1. H₂O₂ yields of aqueous reactions of SOA_{O3} and SOA_{OH}.

Precursor	H ₂ O ₂ yield of SOA _{O3} , %	H ₂ O ₂ yield of SOA _{OH} , %
isoprene	4.2 ± 0.7	4.3 ± 0.4
β-pinene	1.8 ± 0.3	0.2 ± 0.05
α-terpineol	3.2 ± 0.7	0.4 ± 0.1
d-limonene	4.0 ± 0.5	0.3 ± 0.07

Table A2. Chemical reactions and parameters included in the kinetic model to simulate ROS formation from aqueous reactions of SOA. In the third column, the first row denotes the uncertainty range, while the second row denotes values for best fits for SOA_{O3} and SOA_{OH} (dashed lines in Figure 2.3), respectively. The units of k_1 , k_3 , k_{17} and k_{20} are s⁻¹, while the others are cm³ s⁻¹.

Reaction number	Reaction	Rate coefficient, best fit and uncertainty range	Refence or comment
-----------------	----------	--	--------------------

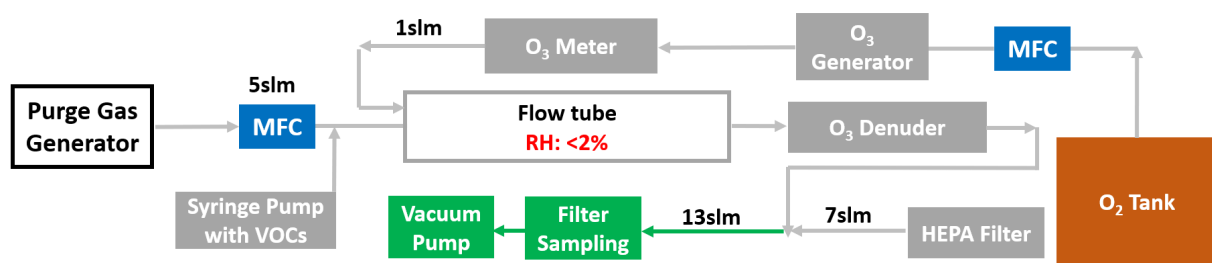
SOA chemistry			
R1	$\text{ROOH} \rightarrow \text{RO} + \text{OH}$	$k_1 = (0.9 - 6.5) \times 10^{-5}$ $1.1 \times 10^{-5}, 5.2 \times 10^{-5}$	Determined from MCGA
R2	$\text{R}_1\text{R}_2\text{CHOH} + \text{OH} \xrightarrow{\text{O}_2} c_1 \text{R}_1\text{R}_2\text{C}(\text{O}_2)\text{OH}$	$k_2 = (0.4 - 2.0) \times 10^{-11}$ $0.9 \times 10^{-11}, 2.0 \times 10^{-11}$ $c_1 = 0.16 - 0.30$ 0.28, 0.30	Determined from MCGA
R3	$\text{R}_1\text{R}_2\text{C}(\text{O}_2)\text{OH} \rightarrow \text{R}_1\text{C}(\text{O})\text{R}_2 + \text{HO}_2$	$k_3 = 17 - 595$ 456, 492	Determined from MCGA
R4	$\text{OH} + \text{ROOH} \rightarrow \text{RO}_2 + \text{H}_2\text{O}$	$k_4 = k_8$	Assumed to be same as R8
R5	$\text{R}_1\text{R}_2\text{C}(\text{O}_2)\text{OH} + \text{OH} \rightarrow \text{products}$	10^{-11} (insensitive)	
R6	$\text{SOA} + \text{OH} \rightarrow \text{SOA}'$	$k_6 = (0.7 - 9.9) \times 10^{-12}$ $1.5 \times 10^{-12}, 9.8 \times 10^{-12}$	Determined from MCGA
R7	$\text{R}_1\text{R}_2\text{C}(\text{O}_2)\text{OH} + \text{HO}_2 \rightarrow \text{products}$	10^{-13} (insensitive)	
ROS chemistry			
R8	$\text{O}_2^- + \text{OH} \rightarrow \text{O}_2 + \text{OH}^-$	$k_7 = 1.3 \times 10^{-11}$	180
R9	$\text{H}_2\text{O}_2 + \text{OH} \rightarrow \text{H}_2\text{O} + \text{HO}_2$	$k_8 = 5.5 \times 10^{-14}$	181
R10	$\text{OH} + \text{OH} \rightarrow \text{H}_2\text{O}_2$	$k_9 = 8.6 \times 10^{-12}$	182
R11	$\text{OH} + \text{HO}_2 \rightarrow \text{H}_2\text{O} + \text{O}_2$	$k_{10} = 1.2 \times 10^{-11}$	182
R12	$\text{HO}_2 + \text{HO}_2 \rightarrow \text{H}_2\text{O}_2 + \text{O}_2$	$k_{11} = 1.4 \times 10^{-15}$	183
R13	$\text{H}_2\text{O}_2 + \text{HO}_2 \rightarrow \text{H}_2\text{O} + \text{O}_2 + \text{OH}$	$k_{12} = 5.0 \times 10^{-21}$	184
R14	$\text{HO}_2 + \text{O}_2^- \rightarrow \text{H}_2\text{O}_2 + \text{OH}^- + \text{O}_2$	$k_{13} = 1.7 \times 10^{-13}$	183
R15	$\text{H}^+ + \text{O}_2^- \rightarrow \text{HO}_2$	$k_{14} = 2.9 \times 10^{-11}$	185
R16	$\text{HO}_2 \rightarrow \text{H}^+ + \text{O}_2^-$	$k_{15} = 2.3 \times 10^5$	185
BMPO chemistry			
R17	$\text{BMPO} + \text{OH} \rightarrow \text{BMPO-OH}$	$k_{16} = (0.1 - 1.3) \times 10^{-12}$ $0.5 \times 10^{-12}, 0.2 \times 10^{-12}$	Determined from MCGA
R18	$\text{BMPO-OH} \rightarrow \text{products}$	$k_{17} = (4.8 - 8.0) \times 10^{-4}$ $7.5 \times 10^{-4}, 7.6 \times 10^{-4}$	Determined from MCGA

R19	$\text{BMPO} + \text{O}_2^- + \text{H}^+ \rightarrow \text{BMPO-OOH}$	$k_{18} = (0.1 - 7.0) \times 10^{-14}$ $4.0 \times 10^{-14}, 3.0 \times 10^{-14}$	Determined from MCGA
R20	$\text{BMPO} + \text{HO}_2 \rightarrow \text{BMPO-OOH}$	$k_{19} = (0.1 - 7.0) \times 10^{-14}$ $2.5 \times 10^{-14}, 6.8 \times 10^{-14}$	Determined from MCGA
R21	$\text{BMPO-OOH} \rightarrow \text{products}$	$k_{20} = (0.8 - 2.0) \times 10^{-3}$ $1.3 \times 10^{-3}, 0.8 \times 10^{-3}$	Determined from MCGA

Table A3. Molar fractions (in percent) of ROOH and $\text{R}_1\text{R}_2\text{CHOH}$ in isoprene, β -pinene, α -terpineol and d-limonene SOA_{O_3} and SOA_{OH} . The values indicate best fit values with uncertainty ranges in brackets.

Functionality in SOA and reaction yield	SOA_{O_3}	SOA_{OH}
%ROOH – isoprene	10 (6 – 25)	3 (3 – 5)
%ROOH – β -pinene	12 (7 – 35)	2 (1 – 3)
%ROOH – α -terpineol	9 (6 – 14)	1 (1 – 3)
%ROOH – d-limonene	5 (2 – 12)	3 (2 – 4)
% $\text{R}_1\text{R}_2\text{CHOH}$ – isoprene	72 (45 – 74)	78 (40 – 78)
% $\text{R}_1\text{R}_2\text{CHOH}$ – β -pinene	40 (20 – 61)	72 (46 – 78)
% $\text{R}_1\text{R}_2\text{CHOH}$ – α -terpineol	0.2 (0.1 – 1)	74 (34 – 74)
% $\text{R}_1\text{R}_2\text{CHOH}$ – d-limonene	78 (57 – 79)	69 (43 – 73)

(a) Ozonolysis



(b) OH oxidation

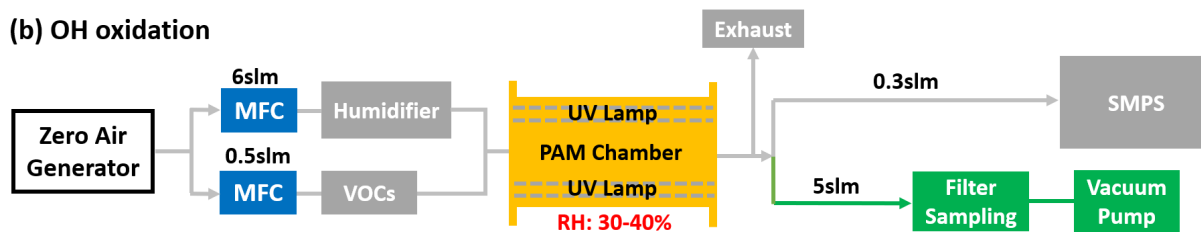


Figure A1. Schematics of (a) dark ozonolysis in the flow tube and (b) $\cdot\text{OH}$ photooxidation in the PAM reactor for generating SOA particles. MFC represents mass flow controller.

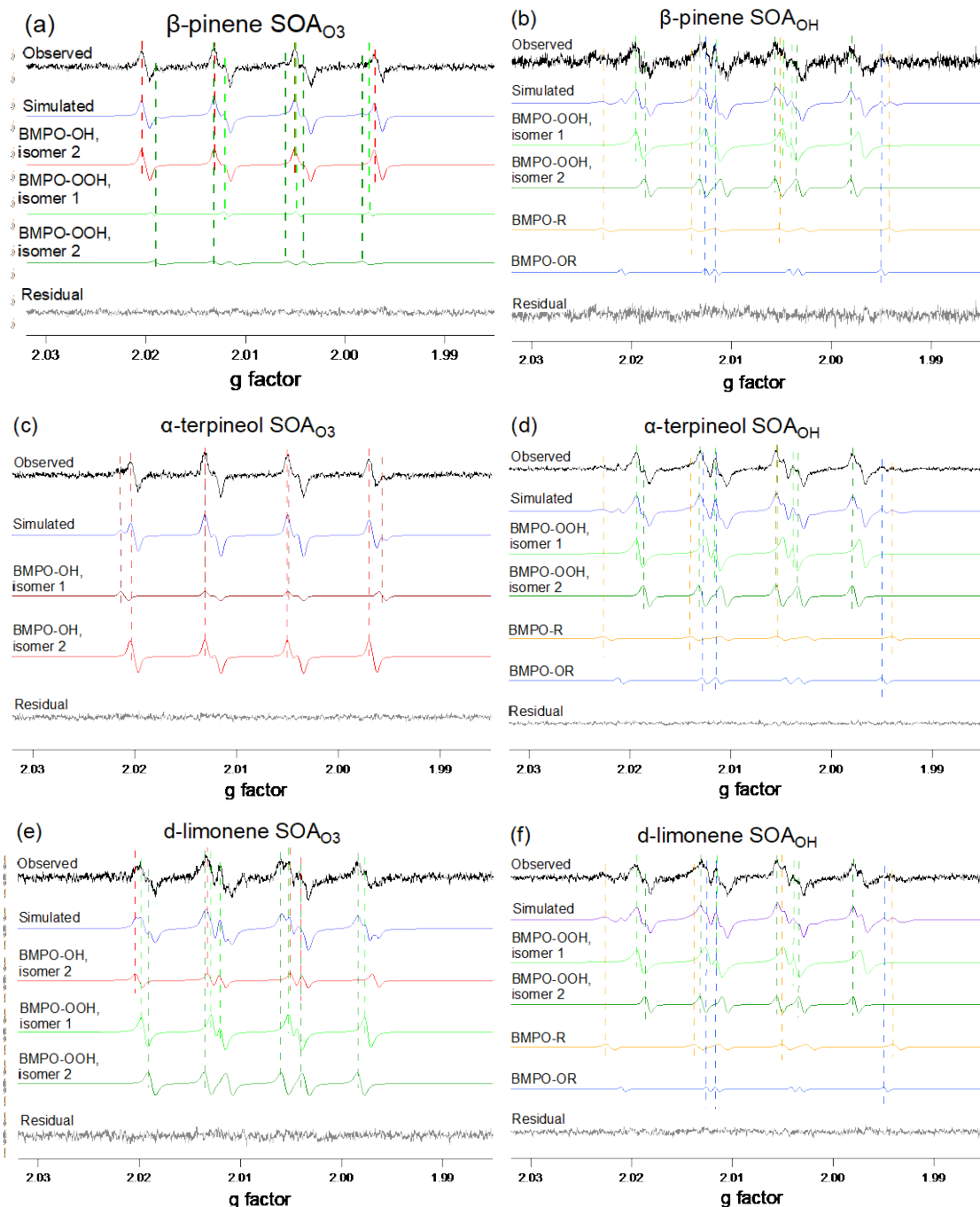


Figure A2. EPR spectra of sample solutions mixed with the spin-trapping agent BMPO: (a) β -pinene SOA_{O_3} , (b) β -pinene SOA_{OH} , (c) α -terpineol SOA_{O_3} , (d) α -terpineol SOA_{OH} , (e) d-limonene SOA_{O_3} , (f) d-limonene SOA_{OH} . The observed spectra (black) are simulated (purple) and deconvoluted into BMPO-OH isomer 1 (brown), BMPO-OH isomer 2 (red), BMPO-OOH isomer 1 (light green), BMPO-OOH isomer 2 (dark green), BMPO-R (yellow), BMPO-OR (blue), and residual (grey).

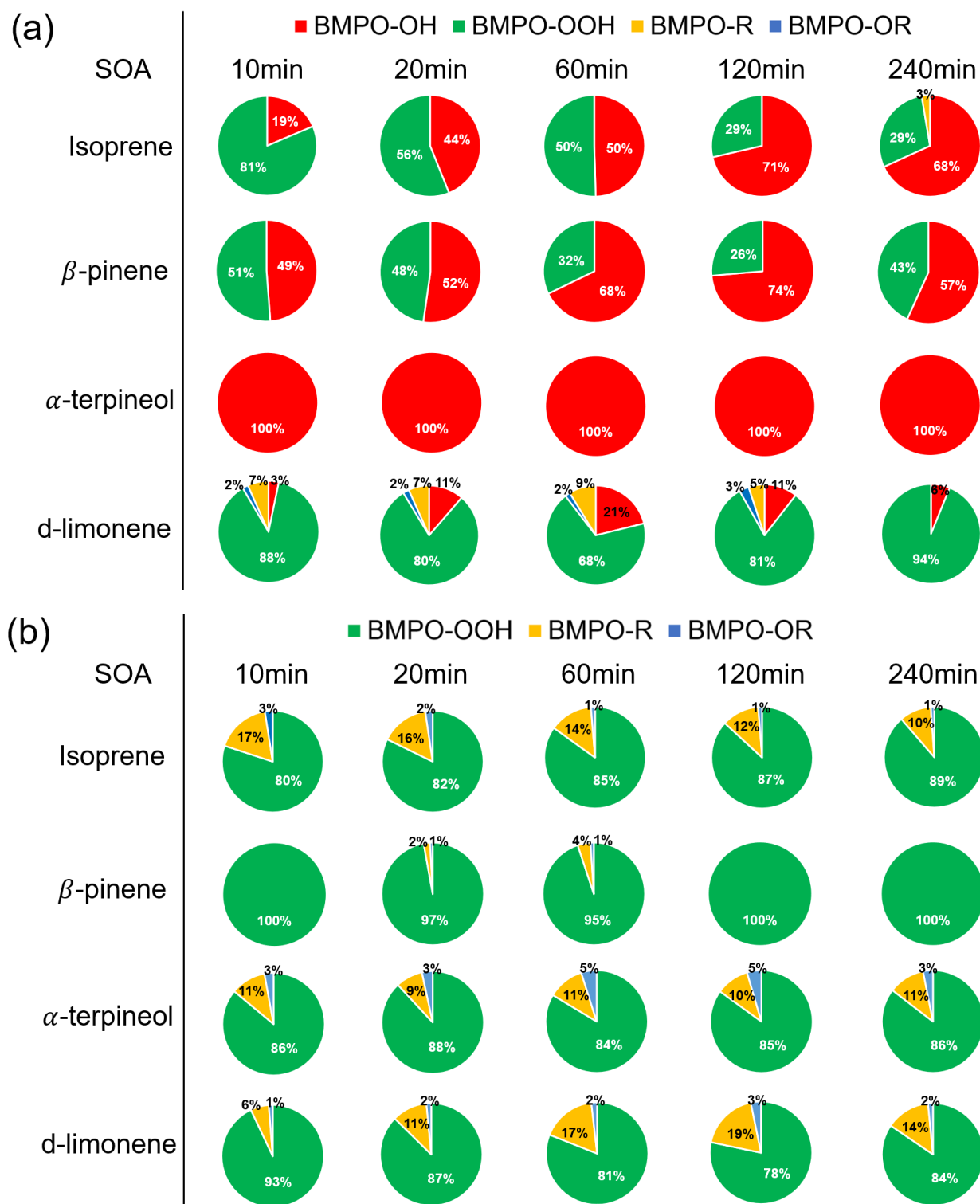


Figure A3. Temporal evolution of relative yields of BMPO- radical adduct from aqueous reactions of SOA generated by (a) ozonolysis versus (b) $\cdot\text{OH}$ photooxidation of isoprene, β -pinene, α -terpineol and d-limonene.

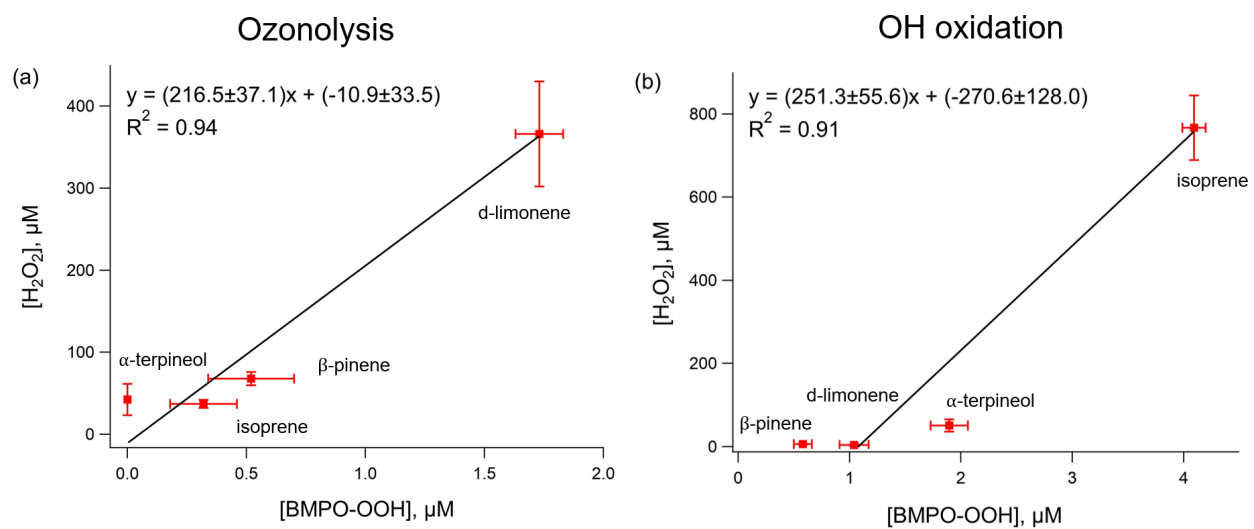


Figure A4. Correlation of BMPO-OOH and H₂O₂ concentrations in aqueous reactions of (a) SOA_{O₃} and (b) SOA_{OH}.

Chapter 3: Effects of Acidity on Reactive Oxygen Species Formation from Secondary Organic Aerosols

This chapter was published in ACS Environmental Au in 2022:

Wei, J.; Fang, T.; Shiraiwa, M., Effects of Acidity on Reactive Oxygen Species Formation from Secondary Organic Aerosols. *ACS Environmental Au* **2022**.

<https://doi.org/10.1021/acsenvironau.2c00018>

3.1 Abstract

Reactive oxygen species (ROS) play a critical role in the chemical transformation of atmospheric secondary organic aerosols (SOA) and aerosol health effects by causing oxidative stress *in vivo*. Acidity is an important physicochemical property of atmospheric aerosols, but its effects on the ROS formation from SOA have been poorly characterized. By applying the electron paramagnetic resonance spin-trapping technique and the Diogenes chemiluminescence assay, we find highly distinct radical yields and composition at different pH in the range of 1 – 7.4 from SOA generated by oxidation of isoprene, α -terpineol, α -pinene, β -pinene, toluene and naphthalene. We observe that isoprene SOA have substantial hydroxyl radical ($\bullet\text{OH}$) and organic radical yields at neutral pH, which are 1.5 – 2 times higher compared to acidic conditions in total radical yields. Superoxide ($\text{O}_2^{\bullet-}$) is found to be the dominant species generated by all types of SOA at lower pH. At neutral pH, α -terpineol SOA exhibit a substantial yield of carbon-centered organic radicals, while no radical formation is observed by aromatic SOA. Further experiments with model compounds show that the decomposition of organic peroxide leading to radical formation may be suppressed at lower pH due to acid-catalyzed rearrangement of peroxides. We also observe 1.5 – 3 times higher molar yields of hydrogen peroxide (H_2O_2) in acidic conditions compared to neutral pH by biogenic and aromatic SOA, likely due to enhanced decomposition of α -hydroxyhydroperoxides and quinone redox cycling, respectively. These findings are critical to bridge the gap in understanding ROS formation mechanisms and kinetics in atmospheric and physiological environments.

3.2 Introduction

Secondary organic aerosols (SOA) account for a substantial fraction of atmospheric particulate matter (PM) and play a critical role in climate, air quality and public health.^{8, 9} SOA originate from the multigenerational oxidation of volatile organic compounds (VOCs), followed by nucleation and condensation of the oxidation products.¹² Acidity is a key physicochemical property of atmospheric PM and droplets, influencing numerous atmospheric and environmental processes, including gas-particle partitioning,¹⁸⁶ organic aerosol composition and reactivity,^{10, 187} cloud processing,¹⁸⁸ and nutrient availability in terrestrial and marine ecosystems.^{189, 190} The atmospheric aerosols and droplets exhibit a wide range of pH, ranging from highly acidic (-1 – 2) in sulfate-rich aerosols¹⁹¹⁻¹⁹³ to near-neutral (5 – 7) in sea-salt particles, dust and cloud droplets.¹⁹⁴⁻¹⁹⁶ Acidity impacts multiphase chemical processes in atmospheric waters including the uptake of acidic or basic compounds and the phase partitioning and composition of aerosols.¹⁹⁷ Several studies have shown the link between acidic aerosols and adverse health effects such as respiratory symptoms,¹⁹⁸ pulmonary dysfunction¹⁹⁹ and other epidemiological outcomes.²⁰⁰

Reactive oxygen species (ROS), including hydroxyl radicals ($\bullet\text{OH}$), superoxide/hydroperoxyl radicals ($\text{O}_2\bullet/\text{HO}_2\bullet$), hydrogen peroxide (H_2O_2) and organic radicals play a central role in multiphase chemistry of atmospheric and physiological processes.²⁰¹ Decomposition of organic hydroperoxides²⁶ and peracids¹³¹ can lead to the formation of $\bullet\text{OH}$, the most reactive form of ROS. The subsequent reactions of $\bullet\text{OH}$ with primary or secondary alcohols can lead to the generation of superoxide via decomposition of α -hydroxyperoxy radicals.²⁰² Limited studies have investigated effects of pH on ROS formation. Enami²⁰³ reported that lower pH promotes the decomposition of α -hydroxyhydroperoxides leading to the formation of H_2O_2 . Tong et al.¹³⁶ showed significant enhancements in radical formation with highly acidic (pH 0 – 1) conditions in the mixtures of isoprene SOA and mineral dust, which could be due to enhanced Fenton(-like) reactions in the presence of transition metals in the dust. Our recent study demonstrated substantial formation of organic radicals from iron-facilitated decomposition of organic peroxides contained in SOA in surrogate epithelial lining fluid with pH of 7.4.²⁰⁴ As there has been little systematic investigations of pH

effects on ROS formation, it is still highly uncertain how different pH would affect ROS formation from SOA and the underlying chemical mechanism is poorly understood.

In this study, we characterized ROS formation from laboratory-generated SOA under three pH range(s): highly acidic (1.0), moderately acidic (2.5 – 3.5) and neutral (7.4) conditions. We observed that pH impacts yields and composition of ROS depending on SOA types: isoprene and α -terpineol SOA are found with significantly higher ROS formation at neutral pH; toluene and naphthalene SOA generate more superoxide in acidic conditions; α -pinene and β -pinene SOA may generate comparable amounts of radicals at different pH. Further, we revealed using model compounds that the radical generation by organic peroxide decomposition can be suppressed under lower pH. In contrast, acidic conditions consistently promote H_2O_2 yields from biogenic and aromatic SOA, likely due to the enhanced decomposition of α -hydroxyhydroperoxides and redox cycling by quinone-type compounds, respectively. This work presents the detailed characterization and mechanistic discussion of ROS formation from SOA under different pH, which have significant implications on atmospheric aerosol processes and oxidative stress.

3.3 Materials and Methods

3.3.1 Preparation of SOA and Model Compounds

A potential aerosol mass (PAM) reactor⁵⁸ was used to generate SOA particles from $\bullet\text{OH}$ photooxidation of isoprene (Sigma-Aldrich, $\geq 99\%$), α -terpineol (Arcos Organics, $\geq 97\%$), α -pinene (Sigma-Aldrich, 98%), β -pinene (Sigma-Aldrich, $\geq 99\%$), toluene (Alfa Aesar, $\geq 99.7\%$) and naphthalene (Sigma-Aldrich, $\geq 99\%$). Detailed procedures of SOA formation can be found in our recent studies.^{202, 204} While the PAM reactor applies high levels of oxidants (i.e., $\text{OH}\bullet$ concentration of $\sim 10^{10} \text{ cm}^{-3}$)⁵⁹ with short reaction time, the PAM-generated SOA have been found to have similar characteristic with ambient and chamber-generated SOA in terms of mass yield, oxidation state, hygroscopicity, and chemical composition with similar mass spectra measured by an Aerodyne ToF AMS.⁶⁶⁻⁶⁸ The relative humidity in the PAM reactor was 40 – 50%. A scanning mobility particle sizer (SMPS, Grimm Aerosol Technik) was used to record the particle size distribution. SOA particles were collected on 47 mm polytetrafluoro-

ethylene (PTFE) filters (Millipore FGLP04700, 0.2 μm pore size) for 60 – 120 min with average mass loadings of 0.45 ± 0.04 mg, 1.19 ± 0.26 mg, 0.73 ± 0.20 mg, 0.67 ± 0.10 mg, 2.52 ± 0.50 mg and 0.43 ± 0.12 mg for isoprene, α -terpineol, α -pinene, β -pinene, toluene and naphthalene SOA, respectively. The filter samples were extracted into 1 mL of 10 mM spin-trap solutions with pre-adjusted pH (1.0, 2.5 – 3.5, 7.4) for 7 min. The filters after extraction were dried under nitrogen flow for 10 – 20 min. The mass difference before and after the extraction was considered as the amount of SOA dissolved in the solution, and an average molar mass of 200 g mol^{-1} ²⁶ was assumed to calculate the SOA molar concentrations in filter extracts. SOA concentrations were in the range of 1.9 – 2.5 mM, 4.8 – 7.8 mM, 2.6 – 5.2 mM, 2.6 – 4.0 mM, 9.2 – 15.7 mM, and 1.2 – 2.5 mM for isoprene, α -terpineol, α -pinene, β -pinene, toluene and naphthalene SOA, respectively. Two SOA samples were prepared for each pH for the quantification of radicals. The radical formation under different pH was also quantified using several model compounds including cumene hydroperoxide (Alfa Aesar, 80%), *tert*-butyl hydroperoxide (Sigma-Aldrich, 70%), 5-hydroxy-1,4-naphthoquinone (5-H-1,4-NQ, Sigma-Aldrich, 97%), and ascaridole (MuseChem, > 98%).

3.3.2 pH Control

The SOA extracted solutions were maintained at highly acidic (pH = 1.0), moderately acidic (pH = 2.5 – 3.5) or neutral (pH = 7.4) conditions. The highly acidic condition mimics the ambient internally-mixed particles of sulfate and organics.¹⁹² pH was adjusted to 1.0 by adding sulfuric acid (VWR, 95 – 98%) in the spin trap solution. The moderately acidic condition is in line with aerosols containing lower amount of sulfate, biomass burning aerosols,²⁰⁵ and the lower end of cloud/fog water droplets.¹⁹⁶ The original pH of the SOA extracts varied from 2.5 – 3.5, representing the moderately acidic condition. The neutral pH is of interest for cloud droplets as well as the physiological environment upon inhalation and respiratory deposition of SOA.¹⁹⁶ A phosphate buffer saline (PBS, Corning, 10 \times) was used to adjust the pH at 7.4 in the SOA extracts. SOA particles were extracted into a spin-trap solution with pre-adjusted pH. The pH of the model compounds was maintained the same way for the highly acidic (sulfuric acid) and neutral (PBS)

conditions, while smaller amount of sulfuric acid was used to reach the moderately acidic condition (pH = 3.0). A pH meter (VWR sympHony) was used to measure the pH of the reagents.

3.3.3 EPR Analysis

A continuous-wave electron paramagnetic resonance (CW-EPR) spectrometer (Bruker, Germany) coupled with a spin-trapping technique was applied to quantify the free radical formation in the aqueous phase. The free radicals were captured by a spin-trapping agent 5-*tert*-Butoxycarbonyl-5-methyl-1-pyrroline-N-oxide (BMPO) (Enzo Life Sciences, $\geq 99\%$). After particle extraction into 1 mL of 10 mM BMPO solutions, a 50 μ L aliquot of the SOA extracts was loaded into a 50 μ L capillary tube (VWR) and inserted in the resonator of the EPR spectrometer at 10, 20, 60, 90 and 120 min from the start of aqueous reactions. The parameters for EPR measurements are as follows: a center field of 3515.0 G, a sweep width of 100.0 G, a receiver gain of 30 dB, a modulation amplitude of 1.0 G, a scan number of 10 – 50, attenuation of 12 dB, a microwave power of 12.6 mW, a modulation frequency of 100 kHz, a microwave frequency of 9.86 GHz and a conversion time and time constant of 5.12 ms. After obtaining the EPR spectra, SpinFit and SpinCount methods embedded in the Bruker Xenon software were applied to quantify BMPO-radical adducts at each time point.²⁶

In addition, an *in-situ* UV irradiation system (ER203UV, Bruker, Germany) equipped with a 100 W Hg lamp was used with EPR to characterize the radical formation upon illumination. The lamp was usually warmed up for roughly 10 min before the start of any irradiation experiments. A safety shutter between the lamp and the resonator was used to control the start and stop of irradiation. A liquid light guide focused the light to the EPR resonator where samples were exposed to UV to visible light with a wavelength range of 220 – 600 nm. To test the pH effect on BMPO trapping efficiencies, 1 mM H₂O₂ was mixed with 10 mM BMPO at pH 7.4, 3.0 and 1.0 and then placed into the irradiation system where H₂O₂ can be photolyzed to form \bullet OH. The background spectrum was recorded at the starting point, with the shutter raised after the first EPR measurement was finished (\sim 1 min). Temporal measurements were then conducted every minute for 10 minutes to monitor the change of BMPO-OH concentrations over time.

3.3.4 H₂O₂ Measurement

A modified protocol¹³⁹ was applied for the H₂O₂ measurement using a fluorometric H₂O₂ assay kit (MAK165, Sigma-Aldrich). Detailed procedures of assay preparation can be found in our previous study.²⁰² The H₂O₂ formation was quantified within two hours from the preparation of working solutions due to the instability of the probe. A calibration was performed using H₂O₂ standard solutions with concentrations ranging from 0.05 – 1.5 μ M in PBS to maintain pH at 7.4 (Figure A5). The reaction vials consisted of 2.94 mL sample (Milli-Q water + filter extracts + PBS) and 60 μ L working solution. The dilution factors were adjusted for different SOA samples so that the final H₂O₂ concentrations would be below 1.5 μ M. All H₂O₂ measurements were conducted with a filter blank with the same dilution factor as the samples. The addition of working solution to the samples was considered as the start of reaction and the measurement was conducted after the reaction vials were incubated at the room temperature of 298 K for 15 min. A spectrofluorophotometer (RF-6000, Shimadzu) was used to measure the fluorescence of the reagents at excitation and emission wavelengths of 540 and 590 nm, respectively.

3.3.5 Diogenes Chemiluminescence Assay

A Diogenes chemiluminescence assay was applied to quantify the superoxide formation from SOA at neutral pH of 7.4. The reaction products between the Diogenes probe and O₂^{•-} emit flash chemiluminescence signal proportional to the O₂^{•-} production rate.²⁰⁶ A Microplate Reader (Promega, GloMax®) was used to measure the chemiluminescence in relative light unit (RLU). To convert RLU to O₂^{•-} production rate, the Diogenes assay was calibrated by the EPR spectrometer using a standardized cell-free O₂^{•-} generation system – the hypoxanthine (HX) and xanthine oxidase (XO) system. The oxidation process of HX catalyzed by XO can pass electrons to dissolved oxygen to form O₂^{•-}.²⁰⁷ A spin probe CMH (1-Hydroxy-3-methoxycarbonyl-2,2,5,5-tetramethylpyrrolidine. HCl, Enzo Life Sciences, \geq 99%) was used to react with O₂^{•-} to form nitroxides radical CM[•] that can be quantified by EPR.²⁰⁸ Concentrations of O₂^{•-} at different time points were obtained by simulating the CM[•] spectra and then used to calculate the O₂^{•-}

production rate. The detail of the calibration is provided in SI and the calibration curve is shown in Figure A6. The O_2^{\bullet} production rates from six SOA were measured using the Diogenes method. The SOA samples were directly extracted in 1 mL PBS, after which 135 μ L of the SOA extracts were added to Diogenes to initiate the reaction. Two samples were used for each SOA, while a filter blank was used for blank correction. The chemiluminescence measurement was conducted from 1 to 10 minutes after the extraction was completed. The first data points with the reaction time up to 2 min were used to calculate initial O_2^{\bullet} production rates. The chemiluminescence signals were observed to decrease over 10 min and we integrated O_2^{\bullet} production rates to estimate the cumulative O_2^{\bullet} production.

3.4 Results and Discussion

3.4.1 Radical Formation from SOA at Different pH

Figures 3.1(a) and 3.1(b) show the observed EPR spectra of the aqueous extracts of isoprene SOA and α -terpineol SOA at different pH. Each EPR spectrum is composed of several overlapped lines, originating from different radical forms of ROS. Dashed lines indicate the positions of each peak for each type of trapped radicals, including OH (red), superoxide (green), carbon-centered (orange) and oxygen-centered organic radicals (blue). The observed spectra were simulated and deconvoluted to derive the radical yields and relative abundance of different BMPO radical adducts. As shown in Figure A7, the simulated EPR spectra reproduced the observed spectra very well with small residuals. The solid color bars in Figure 3.2 shows the relative abundance and BMPO-radical yields from SOA generated from six different precursors. As shown in Figure 3.2(a) and 3.2(b), the BMPO-radical adduct yields from isoprene and α -terpineol SOA at neutral pH are significantly enhanced to 0.10% and 0.035% from <0.05% and <0.02% at acidic conditions, respectively. Isoprene SOA at neutral pH generates substantial amounts of \bullet OH (45%) and carbon-centered organic radicals (44%) with a very minor contribution from oxygen-centered organic radicals (8%), while α -terpineol SOA shows dominant carbon-centered radical formation at neutral pH. In comparison, both isoprene and α -terpineol SOA produce O_2^{\bullet} / HO_2^{\bullet} (50 – 60%) predominantly in acidic

conditions, while $\bullet\text{OH}$ (10 – 20%) and organic radicals (15 – 33%) only constitute minor fractions, as consistent with our recent study.²⁰⁴ It should be noted that the highly acidic condition (pH = 1.0) does not lead to notable differences in radicals yields and relative abundance compared to the original SOA extracts with moderately acidic conditions (pH = 3.0 – 3.5).

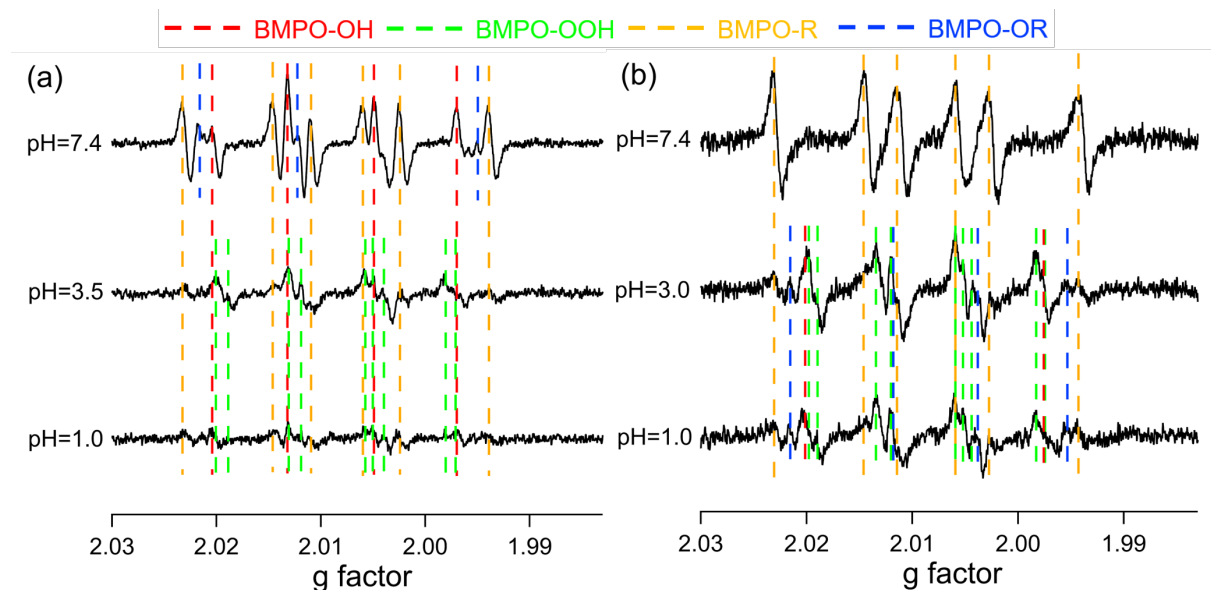


Figure 3.1. EPR spectra of aqueous extracts of (a) isoprene SOA and (b) α -terpineol SOA at different pH (7.4, 3.0, and 1.0) in the presence of the spin-trapping agent BMPO. The dashed vertical lines represent different BMPO-radical adducts including OH (red), superoxide (green), and carbon- (orange) and oxygen-centered (blue) organic radicals.

In addition, we characterized radical formation from α -pinene, β -pinene, toluene and naphthalene SOA (Figure 3.2(c)-(f)) at different pH, with the observed EPR spectra shown in Figure A8. α -pinene and β -pinene SOA (Figure 3.2(c), (d)) show an inverse trend to isoprene and α -terpineol SOA, with substantially lower BMPO-radical yields at neutral pH (< 0.01%) compared to acidic conditions (0.02 – 0.04%). At neutral pH, α -pinene and β -pinene SOA mainly generate low amounts of organic radicals, while the dominant formation of $\text{O}_2^{\bullet-}/\text{HO}_2^{\bullet}$ (> 60%) are observed at pH 1.0 and 3.0, similar to isoprene and α -terpineol SOA. For aromatic (toluene and naphthalene) SOA (Figure 3.2 (e), (f)), we observed dominant superoxide formation (90 – 100%) in acidic solutions, whereas no radicals above detection limit were found at neutral pH.

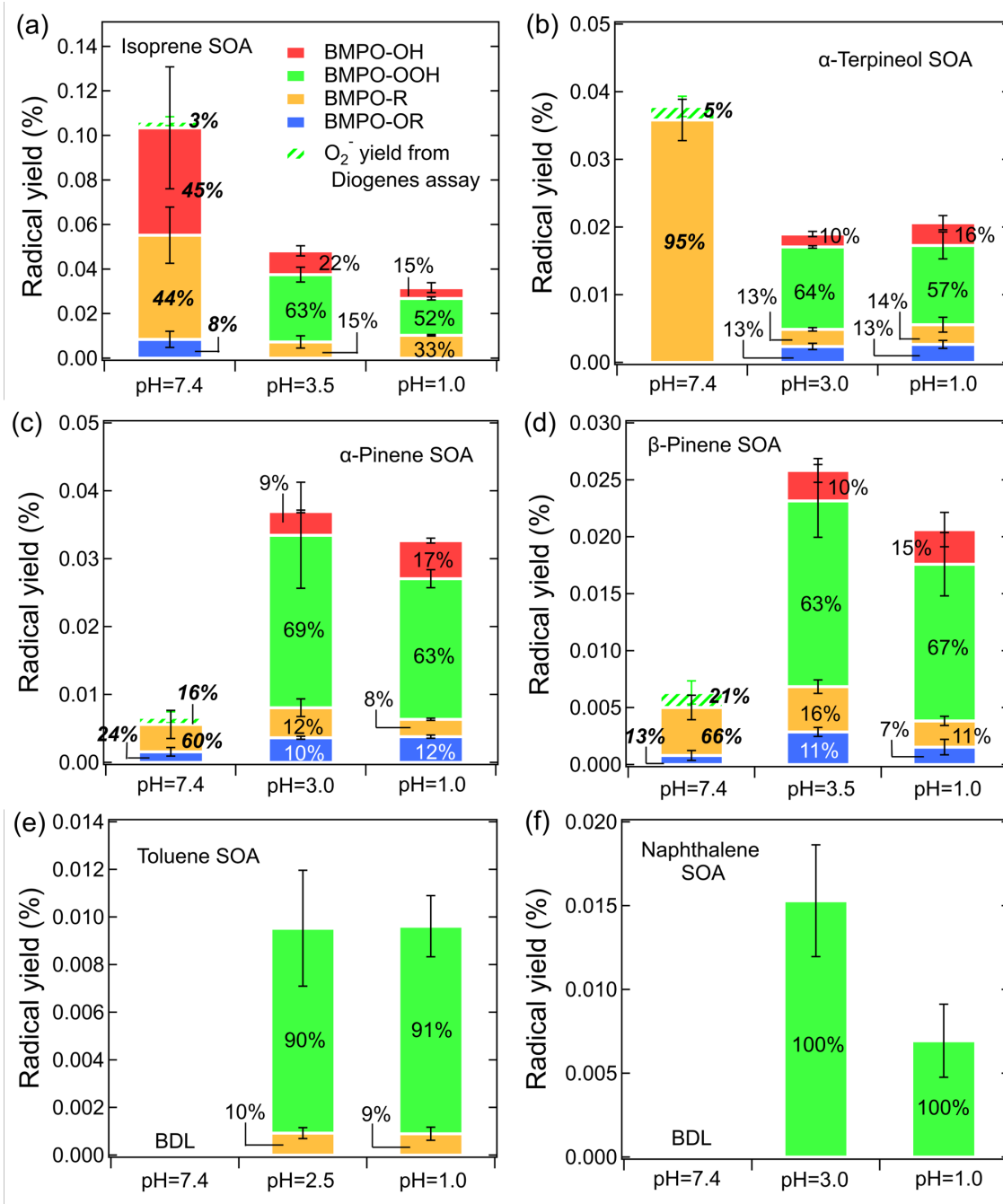


Figure 3.2. Yields and relative abundance of different radical species from (a) isoprene SOA, (b) α-terpineol SOA, (c) α-pinene SOA, (d) β-pinene SOA, (e) toluene SOA and (f) naphthalene SOA at different pH in the presence of BMPO. The solid-colored bars represent BMPO-radical adducts measured by EPR, while the green dashed bars represent superoxide yields estimated from the Diogenes assay. Note the italic bold numbers at pH 7.4 are calculated combining the results of EPR and the Diogenes assay. The error bars represent the error propagation from the two duplicates in EPR measurements or the Diogenes assay with the uncertainty in SOA mass measurements.

An interesting result as observed from Figure 3.2 is that no BMPO-OOH (green solid bars) was detected at pH 7.4 for all SOA, raising a question if the EPR-spin trap method with BMPO can detect superoxide efficiently at neutral pH. Given the pKa of HO_2^\bullet (4.88), the predominant form of superoxide in acidic conditions (pH 3.0 and 1.0) should be HO_2^\bullet , whereas it is $\text{O}_2^{\bullet-}$ at neutral pH.²⁰⁹ It has been reported that a nitron spin trap can react with HO_2^\bullet very efficiently (e.g., $\text{BMPO} + \text{HO}_2^\bullet \rightarrow \text{BMPO-OOH}$), while the trapping of $\text{O}_2^{\bullet-}$ is a two-step process via initial addition of $\text{O}_2^{\bullet-}$ to BMPO to form the BMPO-O_2^- adduct followed by protonation by water (or other acidic sources) to form BMPO-OOH.²¹⁰ As a consequence, the overall rate of $\text{O}_2^{\bullet-}$ trapping in neutral conditions can be an order of magnitude slower compared to HO_2^\bullet trapping in acidic conditions.²¹¹ Hence, we applied the Diogenes chemiluminescence assay which is more sensitive in superoxide measurements at neutral pH (see SI text and Figure A9). Figure 3.3 shows the measured initial $\text{O}_2^{\bullet-}/\text{HO}_2^\bullet$ production rates by SOA at neutral pH. All biogenic (isoprene, α -terpineol, α -pinene and β -pinene) SOA show positive superoxide production rates, varying from 0.005 – 0.013 $\mu\text{M min}^{-1}$. In contrast, toluene and naphthalene SOA do not generate $\text{O}_2^{\bullet-}/\text{HO}_2^\bullet$ above detection limit, as consistent with the EPR-spin trap method (Figure 3.2 (e), (f)).

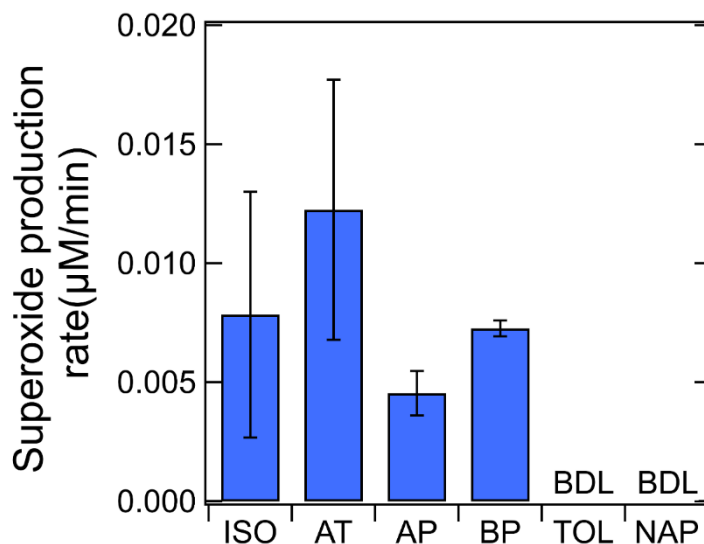


Figure 3.3. Initial superoxide production rates from SOA generated by isoprene, α -terpineol, α -pinene, β -pinene, toluene and naphthalene measured by Diogenes chemiluminescence assay at pH 7.4. The error bars represent uncertainties from the two duplicates of SOA in chemiluminescence measurements.

Overall, the cross-validation by the Diogenes assay suggests that the superoxide yields at neutral pH may be underestimated by BMPO trapping. Therefore, we estimated the total superoxide production yields by the Diogenes assay at neutral pH, which are added as green dashed bars in Figure 3.2. For isoprene and α -terpineol SOA, the additional $O_2^{\bullet-}$ formation at pH 7.4 can further increase the enhancement factors compared to acidic conditions, while the radical yields from α -pinene and β -pinene SOA are still much lower at neutral pH even after considering $O_2^{\bullet-}$ formation. Both methods confirm that superoxide formation is below detection limit from toluene and naphthalene SOA at pH 7.4, consolidating that aromatic SOA containing quinone-type compounds mediate redox cycling and $O_2^{\bullet-}$ formation in a pH-dependent manner favoring stronger acidity.²¹²

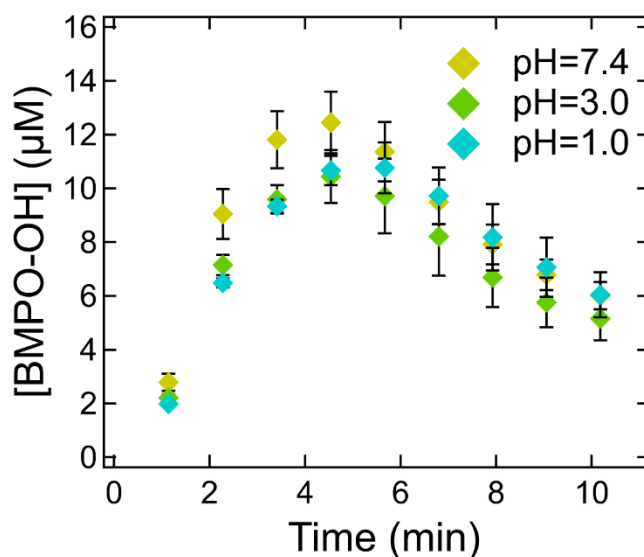


Figure 3.4. Temporal evolution of concentrations of BMPO-OH adducts from UV-vis irradiation of the mixture of 1 mM H_2O_2 and 10 mM BMPO at different pH. The light was switched on 1 minute after the starting point. The error bars represent the uncertainties from the two duplicates in EPR measurements.

We also investigated if pH affects the BMPO trapping efficiency of $^{\bullet}OH$ in the mixtures of 1 mM H_2O_2 and 10 mM BMPO under UV-vis irradiation at different pH. Due to the nature of H_2O_2 photolysis, the $^{\bullet}OH$ yields should be solely determined by the photon intensity without being affected by pH.²¹³ We note that the Fenton reaction ($H_2O_2 + Fe^{2+}$), the most common standard system for $^{\bullet}OH$ generation, is unsuitable for the assessment of pH effects on BMPO trapping efficiencies as this reaction is known to be

intrinsically affected by pH with higher acidity favoring $\bullet\text{OH}$ formation.²¹⁴ Figure 3.4 shows the temporal evolution of BMPO-OH concentrations. For all pH conditions, significant BMPO-OH formation ($> 10\ \mu\text{M}$) was observed within 5 min minutes after introducing the irradiation, indicating effective photolysis of H_2O_2 and efficient trapping of $\bullet\text{OH}$ by BMPO. The sharp decline in [BMPO-OH] after 5 min is likely due to photolytic decay of BMPO-OH. Only marginal differences ($< 20\%$) were observed in BMPO-OH concentrations over the course of reactions for different pH conditions, confirming that acidity has minor to negligible effects on the BMPO trapping of $\bullet\text{OH}$. We also speculate that pH effects on BMPO trapping $\text{R}\bullet$ and $\text{RO}\bullet$ should be trivial as no H^+ is involved in the reactions. This investigation of the potential pH effects on the trapping efficiencies of BMPO should elicit precaution for future studies using the EPR-spin trap method especially for detecting superoxide at neutral pH.

3.4.2 Reaction Mechanisms

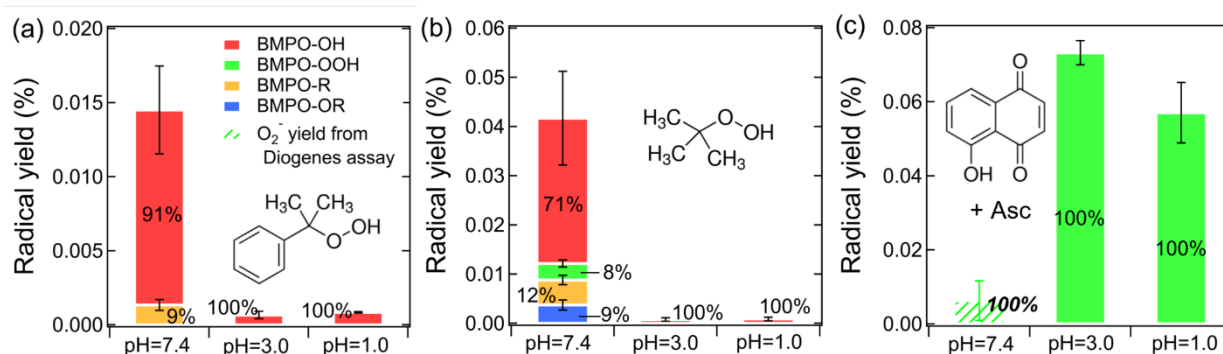


Figure 3.5. Yields and relative abundance of different radical species from (a) 10 mM cumene hydroperoxide, (b) 10 mM *tert*-butyl hydroperoxide and (c) the mixture of 0.2 mM 5-Hydroxy-1,4-naphthoquinone and 0.2 mM ascorbate (Asc) at different pH in the presence of BMPO. The solid bars represent BMPO-radical adducts measured by EPR, while the green dashed bars represent superoxide yields estimated from the Diogenes assay. The error bars represent the uncertainties from the two duplicates in EPR measurements.

To better understand the pH effects on ROS formation mechanism from SOA, we measured radical formation from commercially available organic hydroperoxides at different pH. Figure 3.5 (a) and (b) show predominant $\bullet\text{OH}$ formation (70 – 90%) from 10 mM cumene hydroperoxide (CHP) and *tert*-butyl

hydroperoxides at neutral pH, with total radical yields up to 0.014% and 0.04%, respectively. The unimolecular decomposition of labile organic hydroperoxides can lead to $\bullet\text{OH}$ formation through the cleavage of the weaker O-O bond.^{121, 154} In acidic solutions (pH 3.0 and 1.0), however, both organic hydroperoxides generate much lower $\bullet\text{OH}$ (radical yields < 0.0009%). While the first-order decomposition of peroxides should be a thermal process depending on temperature instead of pH, it may be suppressed at higher acidity due to the acid-catalyzed rearrangement of alkyl hydroperoxides.^{215, 216} Levin et al.²¹⁷ also characterized the kinetics of acid-catalyzed cleavage of CHP leading to phenol and acetone formation, which can take place at or even below the room temperature in the presence of sulfuric acid. Further, their study²¹⁷ provides thermodynamic evidence that the thermal decomposition of CHP forming phenol/acetone follows a combined linear-exponential function of sulfuric acid concentration (i.e., $\text{pH} \leq 2.7$) at the room temperature. This alternative decomposition pathway would lead to alcohol and ketone formation as the end products, involving no radical formation.²¹⁸ A similar mechanism has also been shown for aliphatic alkyl hydroperoxides including *tert*-butyl hydroperoxide.²¹⁹ Therefore, it may partially account for the decreased radical formation by isoprene and α -terpineol SOA at lower pH (Figure 3.2 (a), (b)), although the complex and multi-functionalized nature of organic hydroperoxides in SOA may not be accurately represented by cumene or *tert*-butyl hydroperoxides. The major contribution from $\bullet\text{OH}$ by isoprene SOA is likely be due to its higher fraction of organic hydroperoxides (3 – 5%) compared to α -terpineol SOA (1 – 3%) as predicted by kinetic modeling in our previous study.²⁰²

Further, the decomposition of organic hydroperoxides is unlikely to account for the exclusive formation of organic radicals by α -terpineol SOA as measured by EPR. Iyer et al.²²⁰ recently proposed that rapid autoxidation during α -pinene ozonolysis may lead to the formation of endoperoxides through ring-opening and hydrogen shift reactions. While common organic peroxides (e.g. *tert*-butyl peroxybenzoate) can be stable under the room temperature and do not decompose into organic radicals,²⁰⁴ the radical formation from endoperoxides has not been investigated. The decay of ROOR may potentially serve as a plausible channel, as the $\text{RO}\bullet$ generated from O-O cleavage can rapidly undergo isomerization or

decomposition to form R^\bullet .^{155, 221} Therefore, we characterized the ROS formation from a commercially available endoperoxide, ascaridole. However, we observed no radicals above detection limit (Figure A10c), indicating that endoperoxides are not responsible for the organic radical formation from α -terpineol SOA, or the reactivity of ascaridole is lower compared to endoperoxides contained in α -terpineol SOA. Meanwhile, it may be possible that $\bullet OH$ can abstract H from the tertiary alcohol group in α -terpineol SOA to form RO^\bullet , which undergoes β -scission to form R^\bullet .²²¹ While this mechanism has been demonstrated for the tertiary alcohol group in citric acid,²²² further studies are warranted as $\bullet OH$ oxidation of monoterpene alcohol has been rarely studied.

Quinones often contained in aromatic SOA are well known to induce superoxide formation: in the presence of electron donor, quinones can be reduced to semiquinone radicals which can further react with dissolved oxygen to form superoxide.^{86, 135} The pH dependence of the quinone redox cycling has been rarely discussed in the context of ambient PM, so we measured radical formation in the mixture of 0.2 mM 5-Hydroxy-1,4-naphthoquinone (5-H-1,4-NQ) and 0.2 mM ascorbate. Note that 5-H-1,4-NQ alone did not generate radicals above detection limit. Figure 3.5(c) shows significantly higher superoxide production at lower pH. It has been demonstrated that the quinone/hydroquinone couple has a redox potential dependent on pH in a straightforward Nernstian manner,²¹² which follows that increasing pH causes a decrease in the redox potential.²²³ This provides a thermodynamic explanation on favoring $O_2^{\bullet -}/HO_2^\bullet$ formation through stronger quinone redox cycling in acidic conditions compared to neutral pH (Figure 3.2 (e), (f)). It has been shown that hydroquinones can be unstable at physiological pH, undergoing autoxidation to form semiquinone radicals and quinones with concomitant generation of $O_2^{\bullet -}$ and H_2O_2 .²²⁴ Further studies are necessary to evaluate the relevance of such pathways especially for SOA generated from phenolics such as catechol and cresol.^{225, 226}

3.4.3 H_2O_2 Formation from SOA at Different pH

In addition to radicals, we characterized H_2O_2 yields from all SOA at different pH as shown in Figure 3.6. Overall, higher H_2O_2 yields are consistently observed for all SOA as pH decreases from 7.4 to

1.0, with the enhancement factors varying from 1.5 to 3. This is in good agreement with Wang et al.,¹²⁹ who observed that H₂O₂ generation by α -pinene, β -pinene and toluene SOA increased by a factor of 1.5, 2.4 and 1.75, respectively, when pH decreased from 7.5 to 3.5. Isoprene SOA shows significantly higher yields of H₂O₂ (4.0 – 6.6%) compared to other SOA (< 2.0%) with the H₂O₂ level (4.2%) in the original extract (pH 3.5) in excellent consistency with our previous study ($4.3 \pm 0.4\%$).²⁰² Naphthalene SOA shows the second highest H₂O₂ yields (1.4 – 2.0%), which is comparable with Liu et al.⁹⁵ (1.9 – 2.5%). Qiu et al.¹⁵⁷ recently proposed that the decomposition of α -hydroxyalkyl-hydroperoxides (α -HHs) is a proton-catalyzed process associated with H₂O₂ formation, which is a highly plausible mechanism accounting for the elevated H₂O₂ yields from biogenic SOA. They showed that the decay rates of α -HHs derived from α -terpineol increase drastically from $0.29 \times 10^{-3} \text{ s}^{-1}$ to $12 \times 10^{-3} \text{ s}^{-1}$ when pH decreases from 5.7 to 3.3.¹⁵⁷ For toluene and naphthalene SOA, the enhanced superoxide formation with higher acidity may subsequently lead to H₂O₂ yields because O₂^{•-} is known as an important precursor of H₂O₂.¹¹³ Given the low O₂^{•-} formation (Figure 3.2 (f)) but high H₂O₂ yields from naphthalene SOA, additional H₂O₂ sources could be important including decomposition of hydroxyhydroperoxides,⁹⁵ which may account for significant fractions in naphthalene SOA.²²⁷

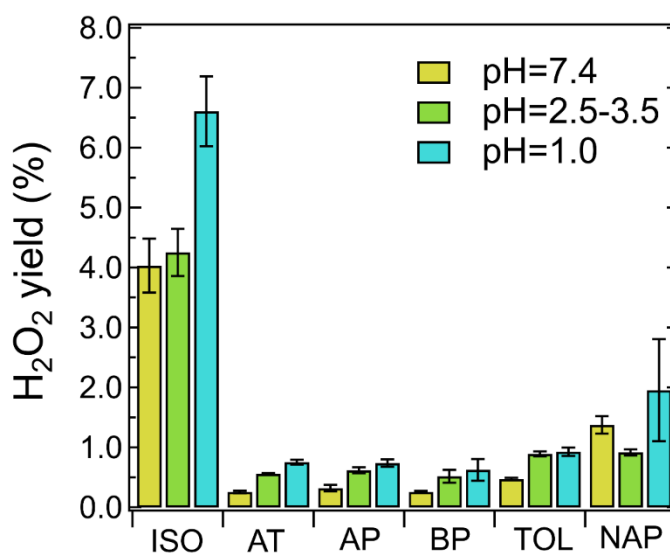


Figure 3.6. H₂O₂ yields from aqueous reactions of isoprene SOA (ISO), α -terpineol SOA (AT), α -pinene SOA (AP), β -pinene SOA (BP), toluene SOA (TOL) and naphthalene SOA (NAP) at different pH. The

actual pH of each SOA in the 2.5 – 3.5 range corresponds to those in Figure 3.2. The error bars represent the error propagation from the two duplicates in fluorescence measurements and the uncertainty in SOA mass measurements.

3.5 Implications

This work provides the detailed characterization of pH effects on ROS formation from various SOA and probes into the underlying mechanisms in acidic versus physiological pH. In atmospheric aerosols, the acidity plays a critical role in chemical transformation and composition by regulating acid-catalyzed particle-phase reactions. A primary mechanism is through acid-catalyzed aldehyde and carbonyl reactions including protonation, hydration and addition of alcohol,²²⁸ which can contribute to high aerosol yields due to oligomerization and aldol condensation.^{229, 230} It has also been well studied that higher acidity can enhance isoprene SOA concentrations by triggering ring opening of epoxydiols followed by the nucleophilic addition of inorganic sulfate.^{231, 232} In comparison, acid-catalyzed reactions of organic peroxides have been less discussed despite their significance in aqueous-phase radical formation. A recent study demonstrated that carboxylic acid can catalyze the reaction between hydroperoxides and aldehydes to form peroxyhemiacetals.²³³ In addition, Hu et al.²³⁴ reported that the decomposition of α -alkoxyalkyl-hydroperoxides can be enhanced at lower pH involving no radical formation. Thus, the complex nature of SOA can alter the ROS formation capacity of organic peroxides under acidic conditions. These aspects should be considered along with the acid-catalyzed rearrangement of hydroperoxides to better understand ROS formation from SOA.

By analogy to ROOH (e.g., CHP), α -HHs undergo acid-catalyzed decomposition forming carbonyls and H₂O₂, as shown by substantially higher H₂O₂ yields in acidic conditions observed in this work. α -HHs can originate from hydrolysis of Criegee intermediates¹⁵⁷ or \bullet OH oxidation of alcohols to form α -hydroxyalkyl radicals followed by O₂ addition and HO₂ \bullet termination.²³⁵ A recent study indicated dominant contribution of decomposition/hydrolysis of organic peroxides to the condensed-phase H₂O₂, whereas the partitioning of the gas-phase H₂O₂ was negligible.²³⁶ In the presence of transition metals, H₂O₂

can be further converted to much more reactive $\bullet\text{OH}$ and induce the formation of highly oxygenated species and chemical aging.¹⁰² Recent field measurements revealed that elevated H_2O_2 concentrations are associated with haze events and H_2O_2 oxidation may act as the primary pathway for sulfate formation.^{237, 238} Therefore, our work highlights the importance of acidity in altering the ROS formation yield and composition and the acidity should be considered for further investigations of ROS formation from SOA.

Inhalation and deposition of organic aerosols can lead to oxidative stress by the formed ROS at physiological pH. H_2O_2 yields from SOA are shown to be 25 – 100 times and 5 – 8 times higher than the total radical yields in acidic and neutral conditions, respectively, which indicates H_2O_2 as the most abundant exogenous ROS in ambient PM especially considering its much longer lifetime. Under neutral conditions organic hydroperoxides can preferably undergo unimolecular decomposition to generate highly reactive $\bullet\text{OH}$ radicals, which can initiate a cascade of reactions to propagate further radical formation¹⁰² as well as directly attack biological components to induce pathological processes such as lipid peroxidation.²³⁹ The formed organic radicals can be persistent even in the presence of antioxidants,²⁰⁴ although their capacity in causing oxidative potential still warrants further studies. While this study used the PAM reactor to generate SOA, further experiments are necessary with SOA generated in an environmental chamber that applies lower VOC and oxidant concentrations as well as with organic particles collected from the ambient atmosphere to consolidate the atmospheric and health relevance of acidity effects on ROS formation by SOA.

3.6 Chapter 3 Appendix

3.6.1 Calibration of Diogenes Chemiluminescence Assay

We used the HX/XO system to perform the calibration of the Diogenes chemiluminescence assay. The concentration of HX was fixed at 250 μM and XO was varied from 0 – 1.0 mU mL^{-1} (U as the enzyme unit in $\mu\text{mol min}^{-1}$). First, XO and probe (either 50 μL Diogenes or 15 μL 3 mM CMH in 200 μL reaction vials) were mixed in PBS, which generated negligible chemiluminescence or CM^\bullet signal. Next, HX was added to initiate the reaction to produce $\text{O}_2^{\bullet-}$. Chemiluminescence and EPR measurements were then conducted within 1 to 6 minutes of reaction. In control groups, 15 μL superoxide dismutase (SOD) was used to suppress the signals to below detection limit, suggesting that the signals without SOD were due to $\text{O}_2^{\bullet-}$ formation. The sample data were corrected with the SOD groups, which involves the propagation of standard deviation. Figure A6 shows a linear relationship ($R^2 = 0.97$) between $\text{O}_2^{\bullet-}$ production rates calculated from the EPR-CMH method and RLU from chemiluminescence. The slope from the linear regressions was used to convert the Diogenes chemiluminescence signals to $\text{O}_2^{\bullet-}$ production rates in the unit of $\mu\text{M min}^{-1}$.

3.6.2 Superoxide Measurement at Neutral pH by EPR and Chemiluminescence

Using the same standard system of superoxide generation – HX/XO, we compared the sensitivities of the EPR-spin trapping technique and the Diogenes assay at neutral pH. Figure A15 shows the accumulation of BMPO-OOH adducts from 250 μM HX and 1.0 munit/mL XO, reaching 1.37 μM in 60 minutes. The XO concentration of 1.0 munit/mL corresponds to the highest point in Figure A12, which translates into a superoxide production rate of $\sim 0.3 \mu\text{M/min}$. Thus, it can be roughly estimated that the total superoxide produced over 60 minutes should be $\sim 18 \mu\text{M}$, which is more than one order of magnitude greater compared to the results of the EPR-BMPO method (1.37 μM). In addition, the Diogenes assay is capable of superoxide measurements at neutral pH for biogenic SOA (Figure 3.3), while we observed no superoxide above detection limit from the EPR-BMPO method (Figure 3.2(a)-(d)). Therefore, it can be

concluded that the Diogenes assay is substantially more sensitive by about one order of magnitude in superoxide measurements compared to the EPR-BMPO method at neutral pH.

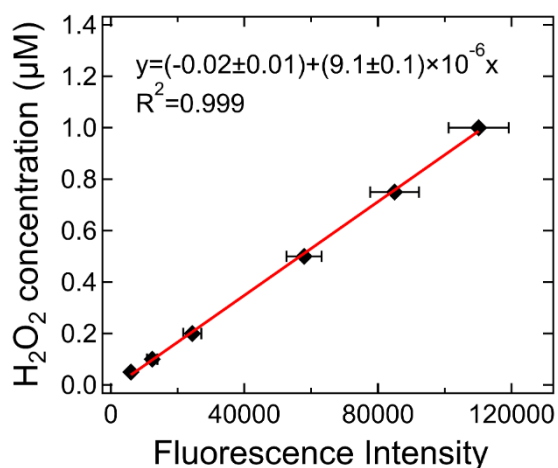


Figure A5. Calibration of the flurometric H₂O₂ assay with 0.05 – 1.5 μM H₂O₂ in phosphate buffer saline (PBS). The fluorescence data were shown as the mean values of two independent experiments.

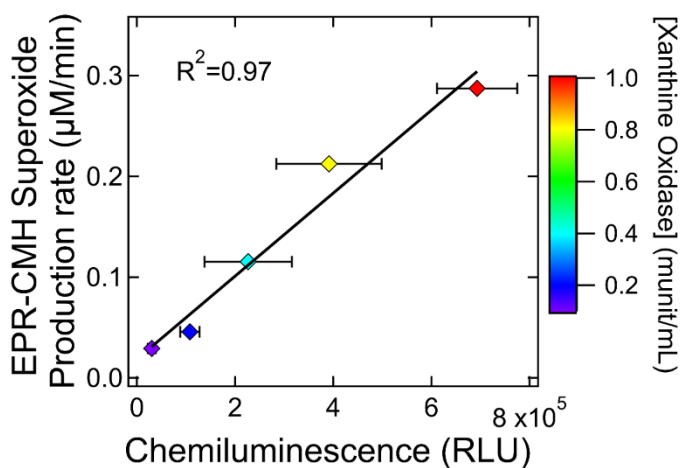


Figure A6. Calibration of Diogenes chemiluminescence by the superoxide production rate determined from the EPR-spin probe method with 250 μM HX and 0 – 1.0 munit/mL XO. The chemiluminescence data were shown as the mean values of two independent experiments.

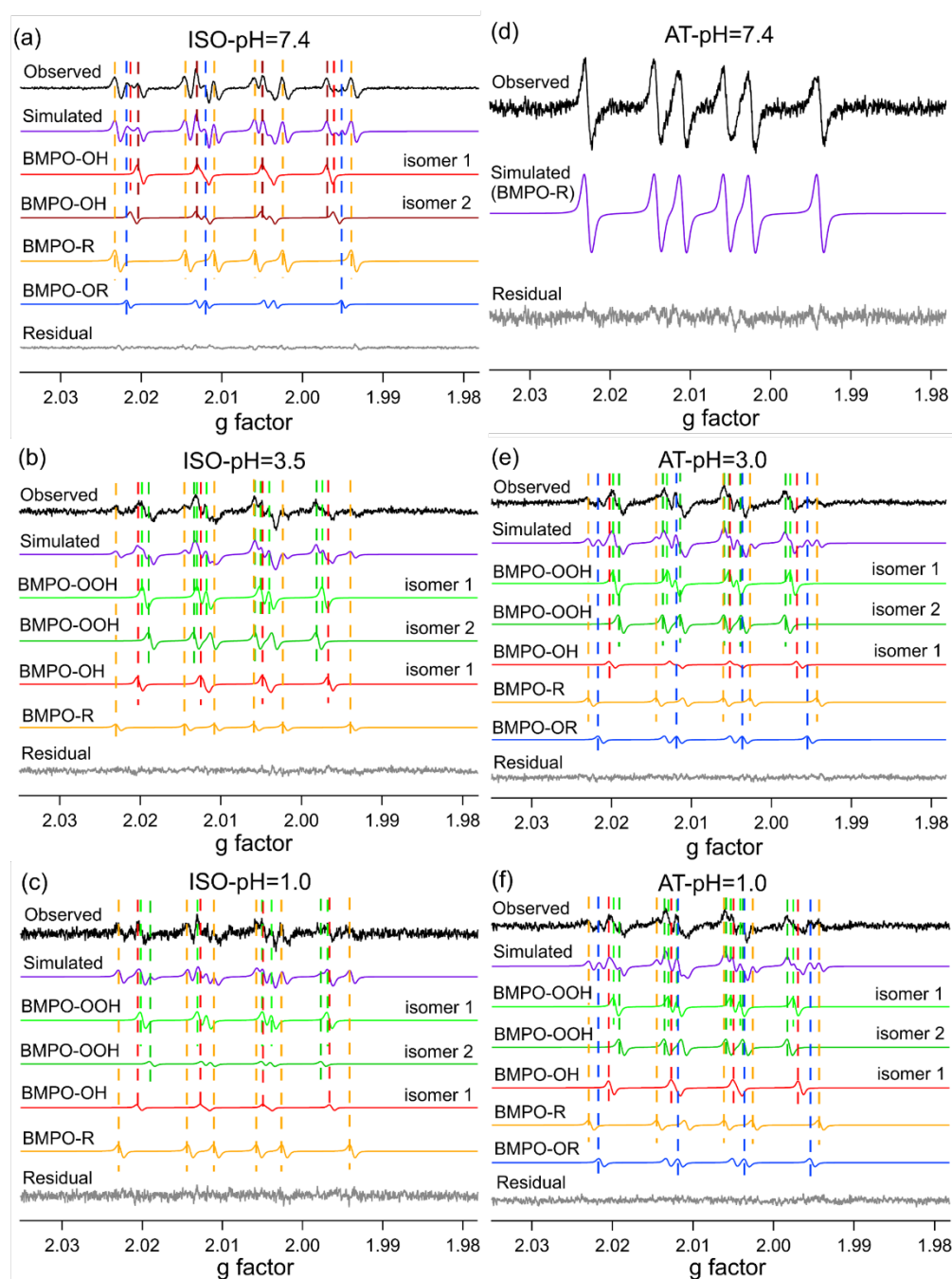


Figure A7. EPR-spectra of BMPO-radical adducts from aqueous reactions of isoprene SOA with (a) pH = 7.4, (b) pH = 3.5, (c) pH = 1.0 and α -terpineol SOA with (d) pH = 7.4, (e) pH = 3.0 and (f) pH = 1.0. The observed spectra (black) are simulated (purple) and deconvoluted into BMPO-OH isomer 1 (red), BMPO-OH isomer 2 (brown), BMPO-OOH isomer 1 (light green), BMPO-OOH isomer 2 (dark green), BMPO-R (yellow), and BMPO-OR (blue). Residual (grey) denotes the difference of observed and simulated spectra. The two isomers of BMPO-OH and BMPO-OOH represent the trans of cis structures of the -OH and -OOH groups, respectively.

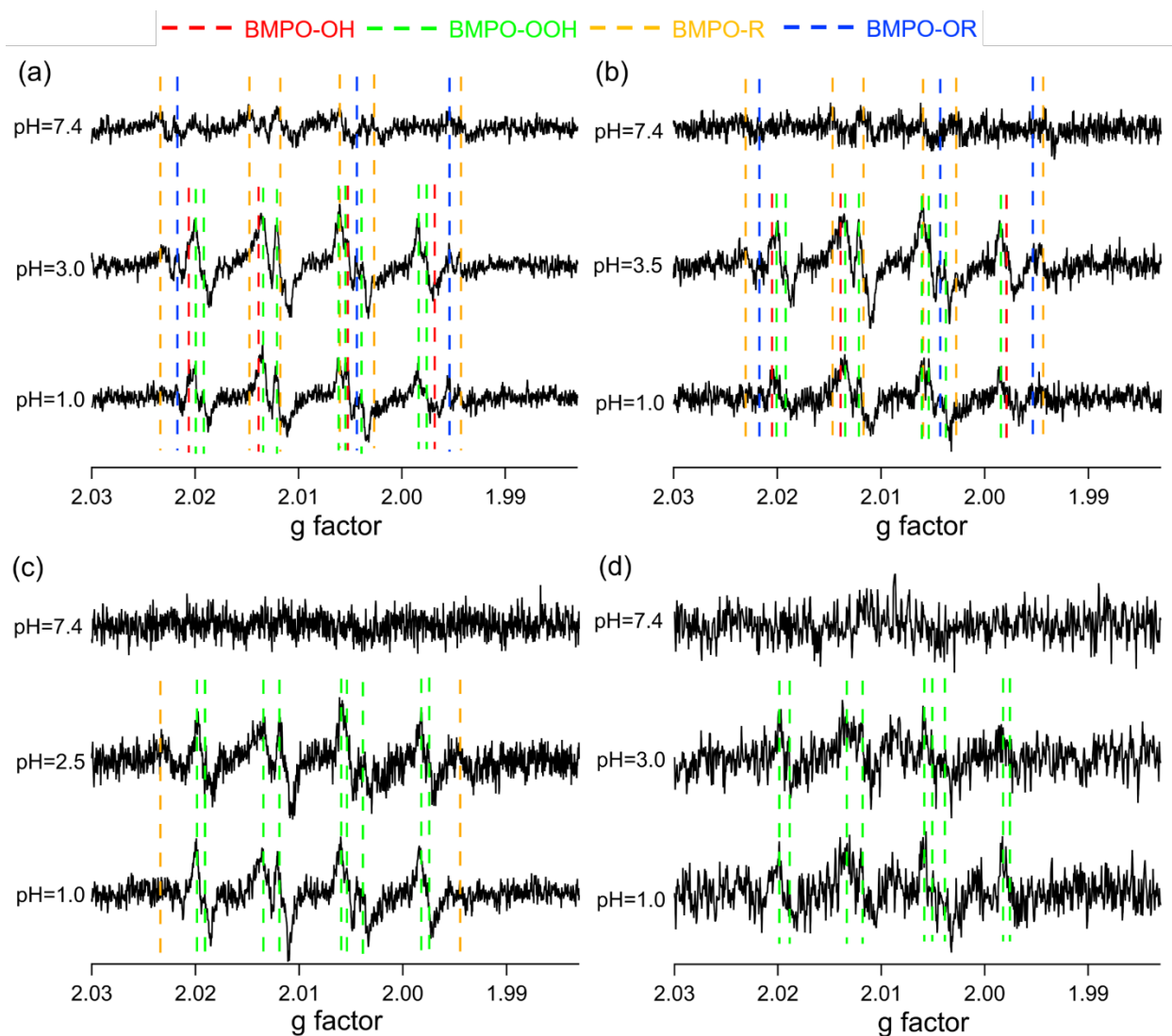


Figure A8. EPR spectra of (a) α -pinene SOA, (b) β -pinene SOA, (c) toluene SOA and (d) naphthalene SOA at different pH in the presence of spin-trapping agent BMPO. The dashed vertical lines represent different BMPO-radical adducts.

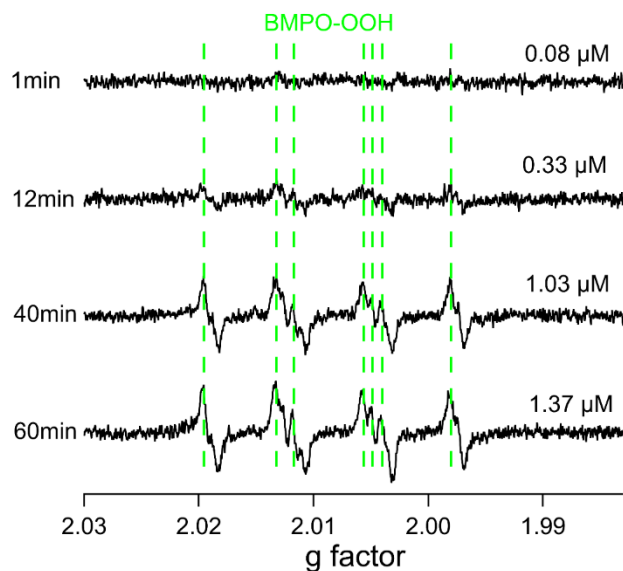


Figure A9. EPR spectra from the mixture of 250 μM HX, 1.0 unit/mL XO and 10 mM BMPO in phosphate buffer saline (PBS) over different time points. The numbers to the right of each spectrum denote the concentrations of BMPO-OOH at each time point. Note that the BMPO-OOH concentrations after the addition of SOD are below detection limit; thus their EPR spectra are not shown here.

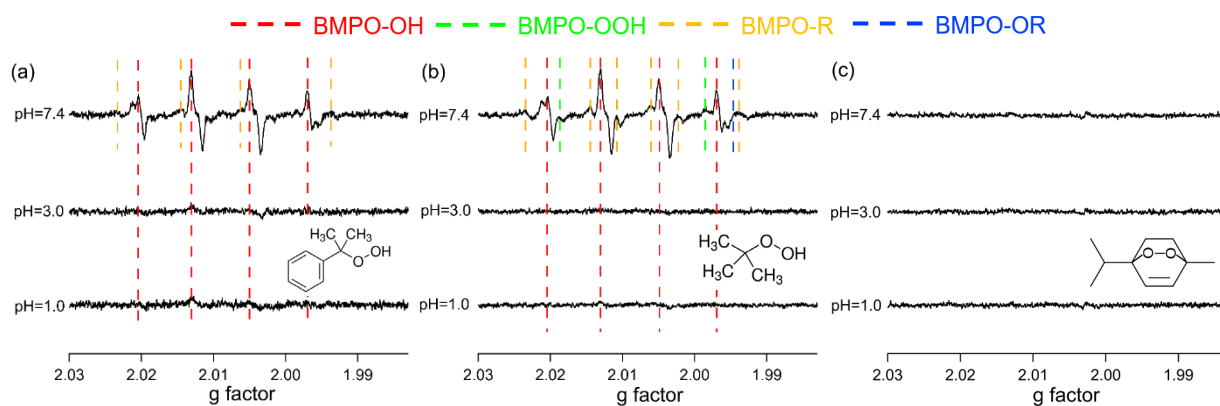


Figure A10. EPR spectra of 10 mM (a) cumene hydroperoxide, (b) *tert*-butyl hydroperoxide and (c) ascaridole at different pH(s) in the presence of BMPO. The dashed vertical lines represent different BMPO-radical adducts.

Chapter 4: Iron-facilitated Organic Radical Formation from Secondary Organic Aerosols in Surrogate Lung Fluid

This chapter was published in *Environmental Science & Technology* in 2021:

Wei, J.; Fang, T.; Lakey, P. S. J.; Shiraiwa, M., Iron-Facilitated Organic Radical Formation from Secondary Organic Aerosols in Surrogate Lung Fluid. *Environ Sci Technol* **2021**.

<https://doi.org/10.1021/acs.est.1c04334>

4.1 Abstract

Respiratory deposition of secondary organic aerosols (SOA) and iron may lead to the generation of reactive oxygen species and free radicals in lung fluid to cause oxidative stress, but their underlying mechanism and formation kinetics are not well understood. Here we demonstrate substantial formation of organic radicals in surrogate lung fluid (SLF) by mixtures of Fe^{2+} and SOA generated from photooxidation of isoprene, α -terpineol and toluene. The molar yields of organic radicals by SOA are measured to be 0.03 – 0.5% in SLF, which are 5 – 10 times higher than in water. We observe that Fe^{2+} enhances organic radical yields dramatically by a factor of 20 – 80, which can be attributed to Fe^{2+} -facilitated decomposition of organic peroxides, in consistency with a positive correlation between peroxide contents and organic radical yields. Ascorbate mediates redox cycling of iron ions to sustain organic peroxide decomposition, as supported by kinetic modeling reproducing time- and concentration-dependence of organic radical formation as well as additional experiments observing the formation of Fe^{2+} and ascorbate radicals in mixtures of ascorbate and Fe^{3+} . $\cdot\text{OH}$ and superoxide are found to be scavenged by antioxidants efficiently. These findings have implications on the role of organic radicals in oxidative damage and lipid peroxidation.

4.2 Introduction

Secondary organic aerosols (SOA) represent a substantial fraction of ambient particulate matter (PM) and play a significant role in air quality and public health.⁷⁻⁹ SOA are generated from oxidation of anthropogenic and biogenic volatile organic compounds (VOCs) followed by nucleation and condensation

of semi- and low-volatile oxidation products.¹² Transition metals are also important for aerosol health effects and iron is regarded as being especially important due to its strong redox activity. Iron is emitted from anthropogenic and crustal sources such as diesel emissions, non-exhaust emissions, and resuspension of dust.^{240, 241} In atmospheric aerosol particles the water-soluble fractions of iron are reported to be up to about 20%^{242, 243} with majority (> 60%) in the form of Fe (III), while significantly greater fractions (up to 90%) of Fe (II) can be found in fog and cloud water.^{243, 244} Mineral dust can take up organic compounds to facilitate particle formation and growth and to become internally mixed with organics.²⁴⁵⁻²⁴⁷

Inhalation and respiratory deposition of redox-active PM components can lead to the formation of reactive oxygen species including hydroxyl radicals ($\bullet\text{OH}$), superoxide/hydroperoxyl radicals ($\text{O}_2\bullet^-/\text{HO}_2\bullet$), hydrogen peroxide (H_2O_2) and organic radicals, which may cause oxidative stress. PM oxidative potential is related to ROS formation and it has been suggested to be an emerging indicator of aerosol health effects in addition to PM mass concentrations.^{90, 248, 249} While substantial efforts have been made to advance our understanding of toxicity and oxidative potential of SOA and metals, the underlying mechanism of oxidative stress and linkage to ROS formation by PM in lung fluid are still poorly established.⁸

SOA contain a number of oxidized products such as alcohols, carboxylic acids, and highly oxygenated organic molecules (HOMs) with multiple peroxide functionalities.^{108, 109, 121} Organic hydroperoxides^{26, 132} and peracids¹³¹ can decompose to form $\bullet\text{OH}$, which can be enhanced with Fenton-like interactions of ferrous iron ions.^{26, 27} Subsequent $\bullet\text{OH}$ oxidation of primary or secondary alcohols can lead to the formation of $\text{O}_2\bullet^-/\text{HO}_2\bullet$.²⁰² A recent study demonstrated the formation and stabilization of carbon-centered radicals in organic aerosols containing Fe ions.²⁵⁰ Despite recent progress, the chemical mechanism of ROS formation induced by SOA and transition metals is highly uncertain, especially in lung fluid.

In this study, we characterized radical formation from laboratory-generated SOA and Fe^{2+} in water and in surrogate lung fluid (SLF). We observed major formation of $\bullet\text{OH}$ and $\text{O}_2\bullet^-/\text{HO}_2\bullet$ in water, but dominant formation of organic radicals in SLF with significant enhancement effects by Fe^{2+} . Kinetic

modeling elucidated that the substantial formation of organic radicals is due to Fe^{2+} -facilitated decomposition of organic peroxides and subsequent aqueous reactions, which is further enhanced by antioxidants through $\text{Fe}^{3+}/\text{Fe}^{2+}$ redox cycling. We found that $\bullet\text{OH}$ and $\text{O}_2\bullet^-/\text{HO}_2\bullet$ can be effectively scavenged by lung antioxidants, while some organic radicals can persist due to relatively longer lifetimes and low reactivity with antioxidants. This work provides the mechanistic explanation for organic radical formation in lung fluid by SOA and Fe^{2+} with significant implications on oxidative stress.

4.3 Materials and Methods

4.3.1 SOA formation, collection and extraction

SOA particles were generated from $\bullet\text{OH}$ photooxidation of isoprene (Sigma-Aldrich, $\geq 99\%$), α -terpineol (Arcos Organics, $\geq 97\%$) and toluene (Alfa Aesar, $\geq 99.7\%$) using a potential aerosol mass (PAM) reactor.⁵⁸ We selected isoprene and toluene because they are among the most heavily emitted biogenic¹⁵ and anthropogenic¹⁴ VOCs, respectively. α -terpineol was selected as an important biogenic and indoor-relevant VOC, which is a significant component of liquid cleaner/disinfectants and air fresheners.¹⁷¹ Detailed procedures of SOA formation can be found in our recent study.²⁰² Despite high $\bullet\text{OH}$ concentrations ($\sim 10^{10} \text{ cm}^{-3}$) compared to ambient levels ($\sim 10^6 \text{ cm}^{-3}$), previous studies have shown that the PAM reactor can generate SOA highly relevant to that from ambient and chamber conditions in terms of mass yield, oxidation state, hygroscopicity, and chemical composition with similar mass spectra measured by an Aerodyne ToF AMS.⁶⁶⁻⁶⁸ Additional advantages of the PAM reactor include efficient generation of SOA mass in shortened experimental timescales, ability to reach long photochemical ages, and minimized wall losses.^{60, 68, 251} Nevertheless, lifetimes of peroxy radicals in OFR are much shorter compared to typical ambient conditions and the reaction regime with high radical concentrations would affect SOA chemistry;⁶⁸ thus, future studies with ambient SOA or SOA generated with low concentrations would be warranted.

A scanning mobility particle sizer (SMPS, Grimm Aerosol Technik) was used to monitor the number concentrations and size distributions of PAM-generated SOA. Particle sampling was initiated after

the number concentrations stabilized. The SOA particles were collected on 47 mm polytetrafluoroethylene (PTFE) filters (Millipore FGLP04700, 0.2 μm pore size) for 30 – 60 min with average mass loadings of 0.35 ± 0.06 mg, 2.18 ± 0.15 mg and 1.04 ± 0.16 mg for isoprene, toluene and α -terpineol SOA, respectively. The filter samples were extracted in 1 mL spin-trap solution (10 mM) containing Fe^{2+} salt $((\text{NH}_4)_2\text{Fe}(\text{SO}_4)_2$, Sigma-Aldrich, 99%, 0 – 0.8 mM) in water or in buffered SLF (pH = 7.4). SLF is an artificial solution containing naturally occurring lung antioxidants including L-ascorbic acid (Asc, 200 μM , Sigma-Aldrich, 99%), L-glutathione reduced (GSH, 100 μM , Sigma-Aldrich, >98%) and uric acid (100 μM , UA, Sigma-Aldrich, >99%).¹¹⁴ It also contains citric acid (CA, 300 μM , Sigma-Aldrich, >99.5%), mimicking metal-binding proteins *in vivo*.²⁵² A phosphate buffer saline (PBS, Corning, 10 \times) was used to maintain the physiological pH at 7.4 in SLF. The mass difference before and after the extraction was regarded as the amount of SOA dissolved in reagents, and an average molar mass of 200 g mol^{-1} was assumed for the calculation of SOA molar concentrations in filter extracts. SOA concentrations were in the range of 1.2 – 2.1 mM, 2.0 – 3.9 mM and 5.6 – 9.9 mM for isoprene, α -terpineol and toluene SOA, respectively. The pH of the SOA extracts in water varied between 4 and 6. Two SOA samples were prepared for each Fe^{2+} concentration for the analysis of radical formation. More detailed procedures of SOA formation, collection and extraction can be found in our previous study.²⁰²

Experiments were also conducted using the model compounds of ROOR and ROOH including *tert*-butyl peroxybenzoate (Sigma-Aldrich, 98%), *tert*-butyl peracetate (Sigma-Aldrich, 50 wt%), cumene hydroperoxide (Alfa Aesar, 80%), benzoyl peroxide (Sigma-Aldrich, $\geq 98\%$) and dicumyl peroxide (Sigma-Aldrich, 98%). 0.1 mM Fe^{2+} and 10 mM peroxides were mixed with 10 mM BMPO in water and SLF, respectively, followed by EPR measurements.

4.3.2 EPR Measurements

A continuous-wave electron paramagnetic resonance (CW-EPR) spectrometer (Bruker, Germany) coupled with a spin-trapping technique was used for free radical quantification. The spin-trapping agent 5-*tert*-Butoxycarbonyl-5-methyl-1-pyrroline-N-oxide (BMPO) (Enzo, $\geq 99\%$) was used to capture free

radicals generated upon aqueous reactions of SOA. After particle extraction from a filter, the extracts were incubated at a room temperature of 20 °C. A 50 μ L aliquot was loaded into a 50 μ L capillary tube (VWR) and inserted in the resonator of the EPR spectrometer at 10, 20, 60, 120, 180 and 240 min from the start of aqueous reactions. The parameters for EPR measurements are as follows: a center field of 3515.0 G, a sweep width of 100.0 G, a receiver gain of 30 dB, a modulation amplitude of 1.0 G, a scan number of 10 – 50, attenuation of 12 dB, a microwave power of 12.6 mW, a modulation frequency of 100 kHz, a microwave frequency of 9.86 GHz and a conversion time and time constant of 5.12 ms. After obtaining the EPR spectra, SpinFit and SpinCount methods embedded in the Bruker Xenon software were applied to quantify BMPO-radical adducts²⁶ at each time point. In consistency with our previous study,²⁰² the detection limits for all BMPO-radical adducts are around 50 – 80 nM. The radical yield was calculated by normalizing the concentrations of BMPO adducts with SOA concentrations in the aqueous extracts.

4.3.3 Fe²⁺ Measurement

Fe²⁺ measurements were performed using the ferrozine method.¹³⁹ The stock solution of 2.55 mg/mL ferrozine (3-(2-Pyridyl)-5,6-diphenyl-1,2,4-triazine-p,p'-disulfonic acid monosodium salt hydrate, Sigma-Aldrich, 97%) was prepared. 100 μ L of this solution was added to 10 mL samples containing Fe³⁺ or Fe³⁺ + ascorbate, and the magenta-colored ligand formed by Fe²⁺ and ferrozine was quantified by an online miniature spectrophotometer (Ocean Optics) at a characteristic wavelength of 562 nm. The calibration was conducted using Fe²⁺ standard solutions (Figure A11). Note that the control experiments show that Fe³⁺ or ascorbate alone with ferrozine do not generate Fe²⁺ signal above detection limit (4 nM).

4.3.4 Total Peroxide Measurement

The total peroxide measurements were conducted using a modified iodometric-spectrophotometric method.¹⁴⁹ Peroxides in all forms (ROOH, ROOR, HOOH) can oxidize I⁻ to form I₂, which combines with the excess I⁻ to form I₃⁻ with characteristic absorbance peaks at wavelengths 289 nm and 350 nm²⁵³ and the absorbance at 350 nm was measured in this study. Isoprene, α -terpineol and toluene SOA were extracted in

1 mL Milli-Q water for 7 min, after which 100 μ L of the SOA extracts were mixed with 700 μ L ethyl acetate (Sigma-Aldrich, 99.8%) to obtain 800 μ L diluted extracts. Then the 800 μ L diluted extracts were mixed with 1200 μ L reagents consisting of 636 μ L acetic acid (Sigma-Aldrich, $\geq 99\%$), 324 μ L chloroform (Sigma-Aldrich, $\geq 99.5\%$) and 240 μ L water (acetic acid:chloroform:water = v:v 0.53:0.27:0.20). Note that the dilution factor of SOA extracts in the reagents (i.e., 100 μ L in 2000 μ L) was determined when different reagents were completely miscible so that the solution was homogeneous. The 2000 μ L diluted SOA extracts with reagents were then purged with a flow of 15 ccm N_2 for 1 min to exclude dissolved oxygen that can also oxidize I $^-$. Next, 20 mg of potassium iodide (KI, Sigma-Aldrich, $\geq 99\%$) was added into each sample, after which the vials were capped and allowed to stand for 1 h. Lastly, the solution was further diluted in water by a factor of 200 (25 μ L in 5000 μ L) and the absorbance at 350 nm was measured using an online miniature spectrophotometer (Ocean Optics). The calibration was performed using 0.2 – 2 μ M benzoyl peroxide (Sigma-Aldrich, $\geq 98\%$) and the calibration curve is shown in Figure A12. Blank (water instead of SOA extracts or benzoyl peroxide) correction was always performed and the measurements were repeated twice for each SOA sample.

4.3.5 DTT assay

The dithiothreitol (DTT) assay was performed following the protocol in Fang et al.²⁵⁴ Briefly, the consumption rate of DTT is considered as an indicator of the oxidative potential. To perform this assay, a 1 mL reaction vial was prepared consisting of 0.7 mL samples or blank, 0.2 mL phosphate buffer (0.5 M KH_2PO_4 and K_2HPO_4 , Sigma-Aldrich) and 0.1 mL of 1 mM DTT (Sigma-Aldrich, $\geq 99\%$). The reaction starts with the addition of DTT, and a 100 μ L aliquot was withdrawn from the reaction vial at 0, 5, 10, 15, and 20 min and added to 1 mL of TCA (trichloroacetic acid, LabChem, 1% w/v) to quench the reaction. The reaction vials were incubated at 37 $^{\circ}C$ in a thermo mixer (Eppendorf). Next, 2 mL Tris buffer (0.08 M Trizma base, Sigma-Aldrich, $\geq 99.9\%$ with pH adjusted to 8.9 by hydrochloric acid (LabChem, 10 M)) and 0.5 mL DTNB (0.2 mM, 5,5'-Dithiobis-(2-nitrobenzoic acid, Sigma-Aldrich, $\geq 98\%$) were added to the quenched aliquot. The mixture was then diluted 10 times and immediately measured by the absorbance of

412 nm using an online miniature spectrophotometer (Ocean Optics). Note, a blank control (Milli-Q water) was always performed in each experiment. For the SOA extracts, isoprene and α -terpineol SOA were diluted 10 times while toluene SOA was diluted 20 times to obtain linear DTT consumption rate within the timescale of the experiment. The $[\text{Fe}^{2+}]/[\text{SOA}]$ molar ratios in the reaction vials were maintained consistent with those in EPR measurement.

4.3.6 Kinetic modeling

A kinetic model was applied to simulate the radical formation by aqueous reactions of isoprene SOA with Fe^{2+} in SLF using the reactions listed in Table A4. The reactions include radical chemistry involving SOA (R1 – R31), ROS coupling (R32 – R41), reactions of Fe ions (R42 – R51), reactions involving antioxidants (R52 – R63), and BMPO chemistry (R64 – R84). The mechanisms of $\bullet\text{OH}$ and $\bullet\text{O}_2^-/\text{HO}_2\bullet$ formation from SOA (R1, R3 and R4) were explicitly addressed in our previous study,²⁰² with the addition of Fe^{2+} -catalyzed ROOH decomposition (R2).^{26, 255} The $\text{RO}\bullet$ formation originates from Fe^{2+} -catalyzed decomposition of ROOR (R5) and ROOH (R10, branching of R2), which can be further converted to $\text{R}\bullet$ through isomerization (R12),²⁵⁶ decomposition (R13)²⁵⁷ and bimolecular reactions (R14 – R16).²²¹ Note that the rate coefficients involving SOA chemistry were assumed to be independent of the structures of R groups contained in isoprene SOA, representing a major model assumption. The variations in rate coefficients depending on R structures were reflected in the uncertainties shown in Table A4.

The rate coefficients of ROS coupling reactions were obtained from literature values. For Fe-oxidant interaction (R42 – R45), we also consider potential impacts of Fe-citrate ligand on the rate coefficients as demonstrated by Gonzalez et al.²⁵⁸ The rate coefficients of antioxidants with radicals and Fe ions were also adopted from literature, except that the scavenging of $\text{R}\bullet$ and $\text{RO}\bullet$ by ascorbate (R56 and R57) were assumed to be a few orders of magnitude slower than that of $\bullet\text{OH}$ and $\bullet\text{O}_2^-/\text{HO}_2\bullet$ (R52 and R55). This is in line with the experimental results showing BMPO-OH and BMPO-OOH below the detection limit, in contrast to the significant formation of BMPO-R and BMPO-OR in SLF. The redox cycling of $\text{Fe}^{3+}/\text{Fe}^{2+}$ by ascorbate is also considered (R63). The unknown rate coefficients and molar fractions of

ROOH, R_1R_2CHOH and ROOR contained in isoprene SOA were determined using the Monte Carlo genetic algorithm (MCGA) to reproduce experimental data.¹⁴² In the Monte Carlo search, input parameters were varied randomly within individual bounds: the boundaries of all reaction rate constants were generally constrained to within two or three orders of magnitude based on literature values, while the ROOH/ R_1R_2CHOH /ROOR molar fractions were constrained to between 0.1 – 80%. The uncertainty of the rate coefficients in Table A4 and the ROOH/ R_1R_2CHOH /ROOR fractions in Table A5 were obtained by running the MCGA numerous times (> 100), among which 40 parameter sets were selected which reasonably captured the temporal trends of the experimental data.

4.4 Results and Discussion

4.4.1 Radical formation from SOA and Fe^{2+} in water and SLF

Figure 4.1 (a) shows the observed EPR spectra of isoprene SOA in water and SLF in the absence of Fe^{2+} or in the presence of 0.4 mM Fe^{2+} . The simulations and deconvolution of EPR spectra (Figure A13) allows us to quantify the absolute radical yields and relative abundance of different types of BMPO radical adducts including $\bullet OH$, $O_2\bullet^-/HO_2\bullet$, and carbon- and oxygen-centered organic radicals. As shown in Figure 4.1 (b), we find striking enhancements in the observed total radical yields with Fe^{2+} addition in both water (from 0.07% to 0.57%) and SLF (from 0.005% to 0.42%) with large changes in radical composition. Isoprene SOA in water leads to the predominant formation of superoxide (64%) with a minor contribution from $\bullet OH$ and carbon-centered radicals; upon the addition of 0.4 mM Fe^{2+} , the radical profile becomes dominated by $\bullet OH$ (77%) with contributions from $O_2\bullet^-/HO_2\bullet$ (15%) and carbon-centered radicals (8%) (Figure 4.1 (b)). In the presence of antioxidants in SLF without Fe^{2+} , only carbon-centered radicals are observed, while a minor contribution from oxygen-centered organic radicals (16%) is also observed with 0.4 mM Fe^{2+} . $\bullet OH$ and $O_2\bullet^-/HO_2\bullet$ radicals are not observed in SLF, indicating effective scavenging of these highly reactive species by antioxidants, which is consistent with the formation of ascorbate radicals ($Asc\bullet^-$)²⁵⁹ in Figure 4.1 (a). Note that the detected organic radical formation in SLF should be attributed to

isoprene SOA with negligible contributions from $\text{Asc}^{\bullet-}$ trapping by BMPO, as $\bullet\text{OH}$ radicals formed by the Fenton reaction ($\text{Fe}^{2+} + \text{H}_2\text{O}_2$) are effectively scavenged in the SLF by ascorbate forming $\text{Asc}^{\bullet-}$ without the formation of organic radical adducts (Figure A14).

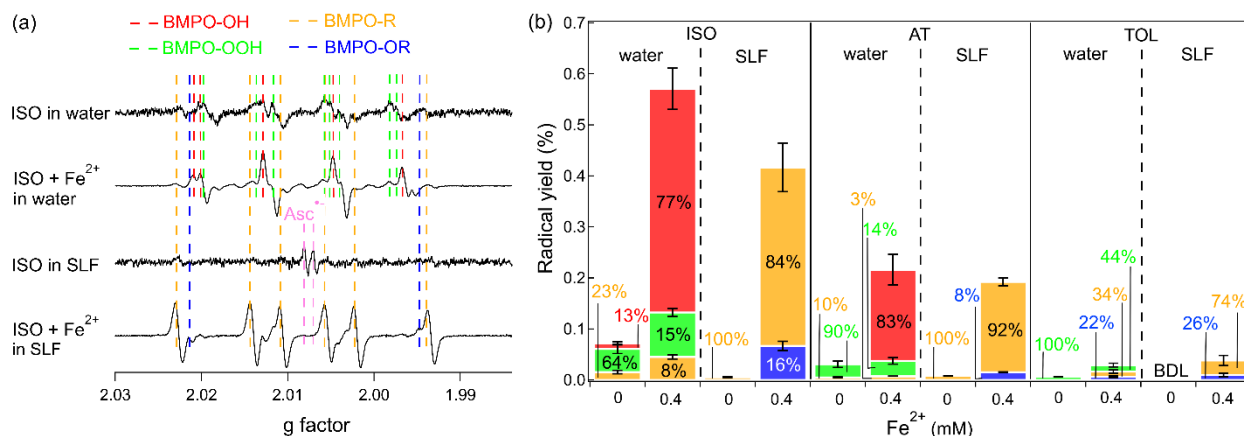


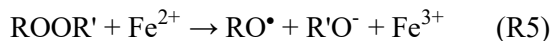
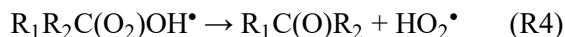
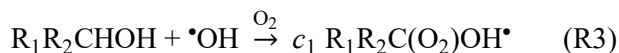
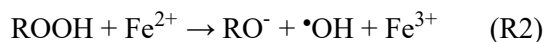
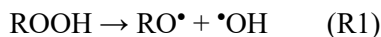
Figure 4.1. (a) EPR spectra of isoprene SOA with 0 or 0.4 mM Fe^{2+} in water and SLF in the presence of spin-trapping agent BMPO. The dashed vertical lines represent different BMPO-radical adducts and ascorbate radicals ($\text{Asc}^{\bullet-}$). (b) Yields and relative abundance of different radical species including BMPO-OH (red), BMPO-OOH (green), BMPO-R (yellow) and BMPO-OR (blue) from isoprene (ISO), α -terpineol (AT) and toluene (TOL) SOA in water and SLF with 0 or 0.4 mM Fe^{2+} . Radical yields peaked and thus selected to show at reaction time of 20 min in water and 60 min in SLF, respectively. The error bars represent the error propagation from the two duplicates in EPR measurement and the uncertainty in SOA mass measurements.

In addition to isoprene SOA, α -terpineol and toluene SOA are also characterized for the radical yields in water and SLF, with the observed EPR spectra shown in Figure A15. In water, α -terpineol and toluene SOA alone consistently generate radicals dominated by $\text{O}_2^{\bullet-}/\text{HO}_2^{\bullet}$ (> 90%). The total radical yields are elevated by a factor of 4 – 8 upon Fe^{2+} addition: α -terpineol SOA exhibits dominant (83%) $\bullet\text{OH}$ formation which is similar to isoprene SOA (77%), while we observe no $\bullet\text{OH}$ above the detection limit from toluene SOA + Fe^{2+} in water. In SLF, Figure 14b shows consistent enhancement effects by Fe^{2+} in organic radical formation, with radical yields increasing substantially from 0.008% to 0.19% for α -terpineol SOA and from below the detection limit (BDL) to 0.04% for toluene SOA, respectively. Carbon-centered radicals are the dominant species for α -terpineol (92%) and toluene (74%) SOA with minor contributions

from oxygen-centered organic radicals (8% and 26%, respectively). Overall, we observe the highest radical yields and strongest enhancement effects of Fe^{2+} (by a factor up to ~ 80) from isoprene SOA followed by α -terpineol and toluene SOA.

4.4.2 Reaction Mechanisms

To elucidate the chemical mechanisms of organic radical formation by SOA and Fe^{2+} , we developed and applied a kinetic model to simulate the temporal evolution of R^\bullet and RO^\bullet radicals. The following reactions were implemented into the kinetic model for radical formation from isoprene SOA and Fe^{2+} based on previous studies:



SOA contain organic hydroperoxides (ROOH), which can undergo thermal decomposition to yield $\bullet\text{OH}$ radicals (R1), which can be drastically promoted by Fe^{2+} with the Fenton-like reaction leading to enhanced formation of $\bullet\text{OH}$ (R2).²⁶ Note that R1 occurs for ROOH without additional functionalities on the α -carbon, as the decomposition of α -hydroxyhydroperoxides leads to the formation of carbonyl and H_2O_2 .^{148, 203} HO_2^\bullet is formed subsequently by $\bullet\text{OH}$ oxidation of primary or secondary alcohols ($\text{R}_1\text{R}_2\text{CHOH}$) followed by fast addition of dissolved oxygen (R3) and unimolecular decomposition of α -hydroxyperoxyl radicals (R4).¹⁴⁰ Our recent study showed that this mechanism can explain the dominated $\text{O}_2^\bullet/\text{HO}_2^\bullet$ formation from the aqueous reactions of isoprene and terpene SOA in the absence of Fe^{2+} .²⁰² While organic peroxides (ROOR') are thermally stable, they are known to be reactive towards Fe^{2+} , releasing RO^\bullet radicals (R5) in analogy to R2.^{260, 261}

To confirm Fe^{2+} -facilitated decomposition of organic peroxides, we measured radical formation in mixtures of Fe^{2+} and commercially available organic hydroperoxides and peroxides in water and SLF. As shown in Figure 4.2, *tert*-butyl peroxybenzoate, *tert*-butyl peracetate (ROOR) and cumene hydroperoxide (ROOH) produce various radicals via Fenton-like reactions of Fe^{2+} in water; note that organic radicals are below detection limit without Fe^{2+} . Benzoyl peroxide and dicumyl peroxide (not shown) are found to be unreactive with Fe^{2+} within the timescale of our experiments, indicating that some organic peroxides are very stable. In SLF, only R^\bullet was formed and other radicals ($^\bullet\text{OH}$, O_2^\bullet , RO^\bullet) were hardly observed. It indicates efficient scavenging of reactive radicals by antioxidants and rapid conversion of RO^\bullet to R^\bullet .

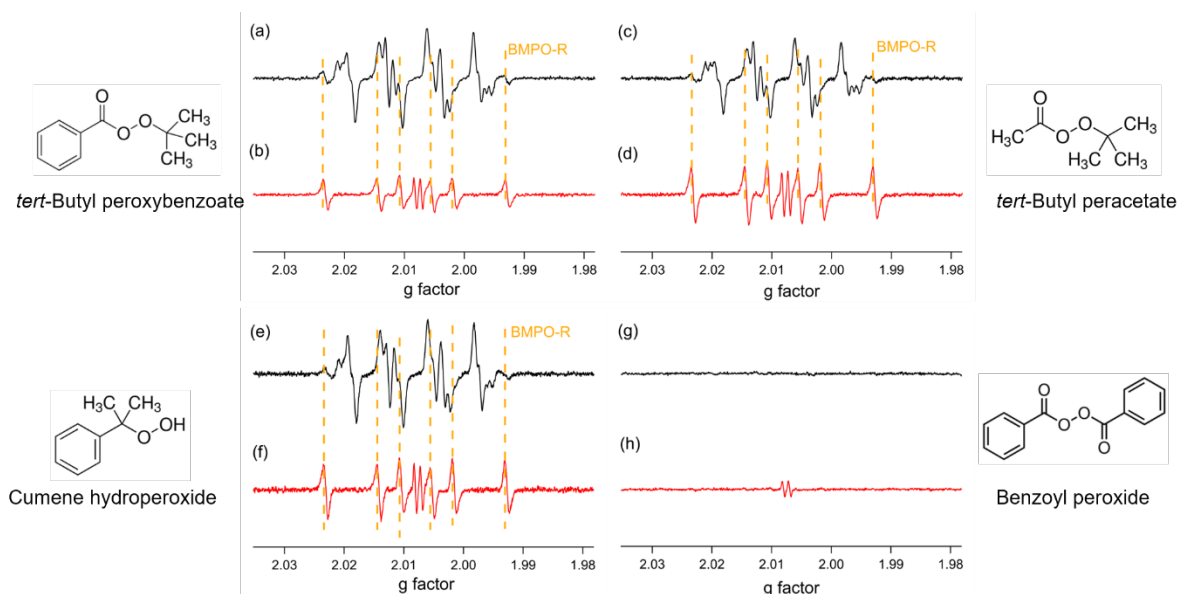


Figure 4.2. EPR spectra of mixtures of 0.1 mM Fe^{2+} with 10 mM (a, b) *tert*-butyl peroxybenzoate, (c, d) *tert*-butyl peracetate, (e, f) cumene hydroperoxide and (g, h) benzoyl peroxide in water (black) or SLF (red).

Indeed, we observed significantly higher formation of R^\bullet than RO^\bullet from isoprene SOA in both water and SLF (Figure 4.1 (b)), most likely due to the rapid conversion of RO^\bullet to R^\bullet via isomerization (R12 in Table A4), decomposition (R13) and a bimolecular reaction resulting in H abstraction (R14).²⁶² Note that the R groups in R^\bullet than RO^\bullet should be different. While the isomerization and decomposition of RO^\bullet are established in the gas phase, these pathways can also occur in the aqueous phase.¹⁵⁵ Our model sensitivity analysis suggested that R12 and R13 contribute to over 99% of the total BMPO-R formation,

consistent with Carrasquillo et al.²²¹ showing that a bimolecular reaction as a negligible channel in the condensed phase. Isomerization and decomposition rates of RO^\bullet are comparable in forming R^\bullet given the fitted rate coefficients ($(0.05 - 6.4) \times 10^6 \text{ s}^{-1}$ and $(0.1 - 9.6) \times 10^5 \text{ s}^{-1}$, respectively), which are in line with literature values ($< 10^7 \text{ s}^{-1}$ ²⁵⁶ and $< 1.4 \times 10^6 \text{ s}^{-1}$ ²⁵⁷, respectively).

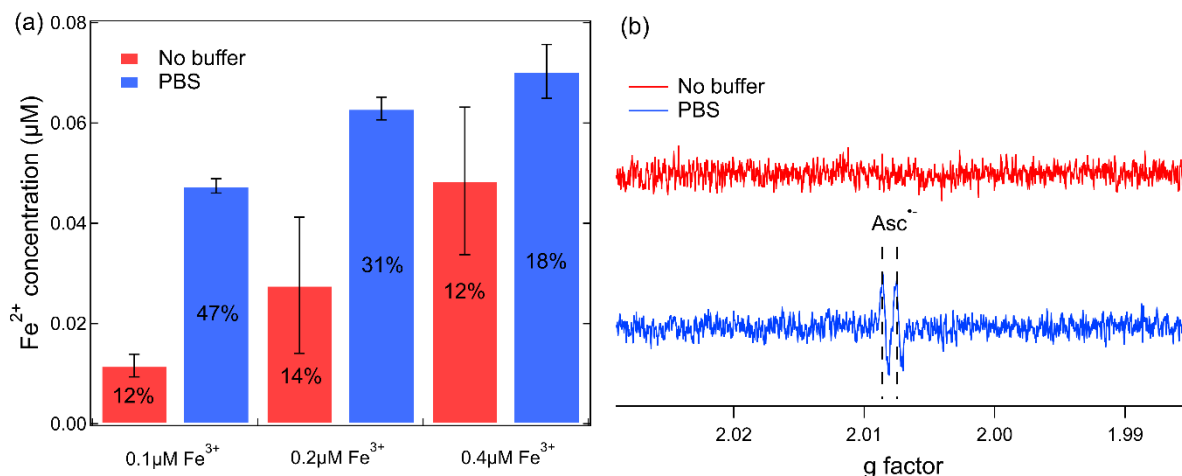


Figure 4.3. (a) Concentrations of Fe^{2+} formed in the mixtures of ascorbate (10 μM) with Fe^{3+} (0.1, 0.2 and 0.4 μM) with and without PBS. The number on each bar represents the percentage of Fe^{3+} that gets reduced by ascorbate. (b) EPR spectra of 0.1 mM Fe^{3+} and 0.2 mM ascorbate with and without PBS. The pH is 4 – 5 without PBS in the mixtures.

The significantly higher formation of organic radicals in SLF than in water can be attributed to redox cycling of $\text{Fe}^{3+}/\text{Fe}^{2+}$ mediated by antioxidants (R63): $\text{Fe}^{3+} + \text{AscH}^- \rightarrow \text{Fe}^{2+} + \text{H}^+ + \text{Asc}^\bullet$. Fe^{3+} can be reduced rapidly to regenerate Fe^{2+} by ascorbate anions,^{111, 263-265} maintaining reaction rates of R5 and R10 to sustain organic radical formation. The model sensitivity analysis revealed that such recycling of Fe^{2+} contribute to 5 – 10 times higher organic radical formation in the SLF than in water. Note that a very recent study suggested that Fe^{3+} and ascorbate reactions are catalytic rather than redox reactions:²⁶⁶ $\text{Fe}^{3+} + \text{Asc} + \text{O}_2 \rightarrow \text{Fe}^{3+} + \text{dehydroascorbic acid (DHA)} + \text{H}_2\text{O}_2$. To further investigate the nature of the Fe^{3+} -ascorbate reaction, we measured Fe^{2+} in the mixtures of Fe^{3+} and ascorbate in water or PBS solutions. Figure 4.3 (a) shows that 12 – 14% of Fe^{3+} can be reduced to form Fe^{2+} in water, which can be further enhanced when buffered by PBS (18 – 47%). In addition, EPR measurements show that Asc^\bullet is formed in the Fe^{3+} -Asc mixtures when buffered by PBS (Figure 4.3 (b)), which is only generated by redox instead of catalytic

reactions. Interestingly, both Fe^{2+} and $\text{Asc}^{\bullet-}$ measurements indicate that Fe^{3+} -Asc redox reactions are highly pH-dependent and more prominent when buffered by PBS. We also conducted sensitive analysis in the model, showing that the redox reactions remain the dominant channel of Fe^{3+} -Asc interaction even if the catalytic reactions are considered (see details in SI). Future studies are required to elucidate the relative importance of catalytic and redox reactions between Fe^{3+} and ascorbate particularly under different pH.

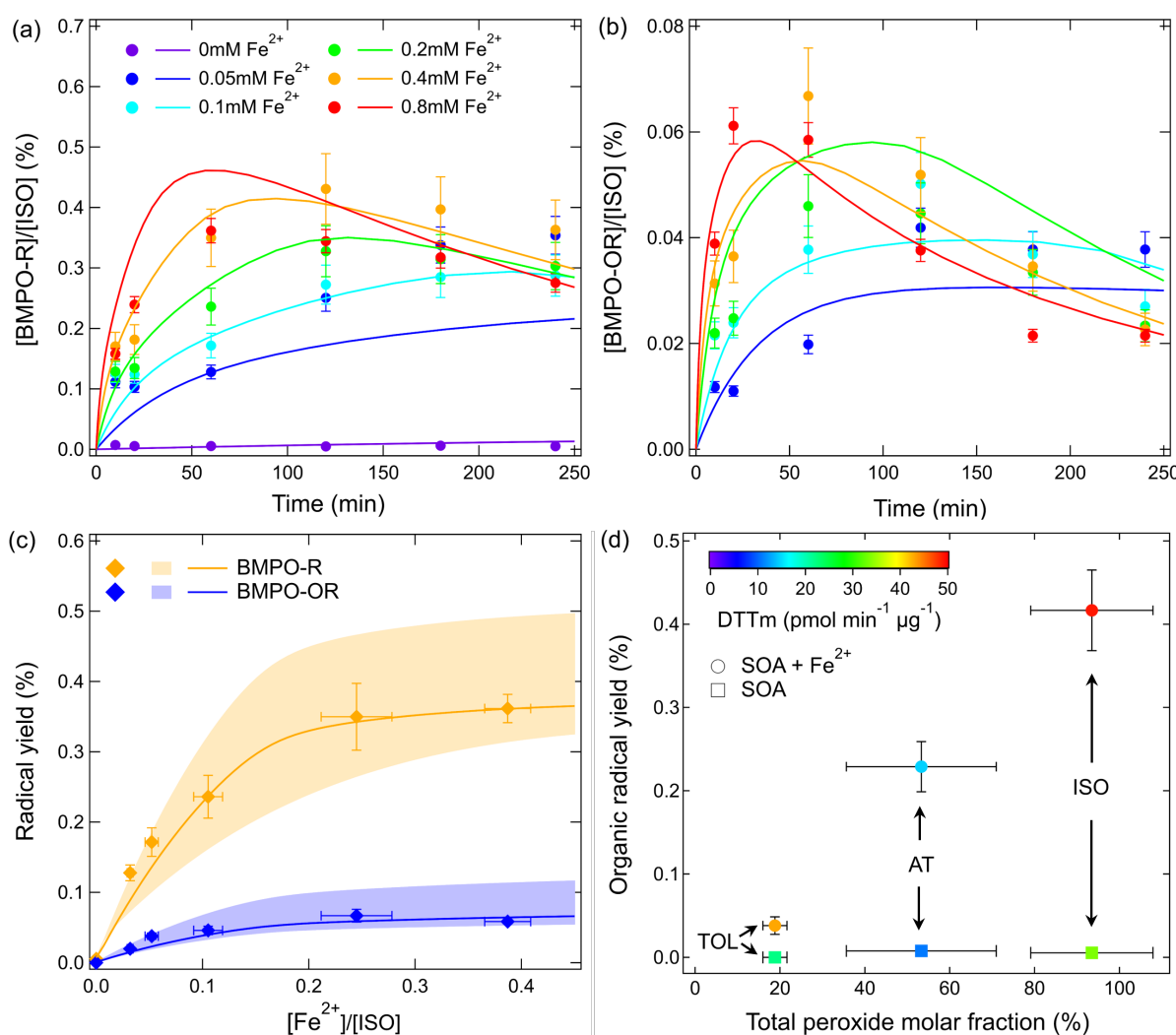


Figure 4.4. (a) Temporal evolution of molar yields of (a) BMPO-R and (b) BMPO-OR from aqueous reactions of isoprene SOA and Fe^{2+} (0 – 0.8 mM) in SLF. (c) Yields of carbon- (yellow) and oxygen-centered (blue) organic radicals from isoprene SOA in SLF as a function of $[\text{Fe}^{2+}]/[\text{ISO}]$ molar ratios. The markers are experimental data. The solid lines represent the best fits of the kinetic model and the shaded areas represent the modeling uncertainties. (d) Organic radical yields (BMPO-R + BMPO-OR) versus total peroxide molar fractions in isoprene, α -terpineol and toluene SOA with 0 (square) or 0.4 mM (circle) Fe^{2+} .

The color scale represents the DTT consumption rate normalized by SOA mass (DTTm). The error bars in all panels represent the error propagation from the two duplicates in EPR measurement or total peroxide measurement and the uncertainty in SOA mass measurements.

Overall, the implemented mechanisms successfully reproduce the time dependence of organic radical formation (Figure 4.4 (a), (b)) as well as the concentration dependence (Figure 4.4 (c)), demonstrating the consistency of model simulations with experiments. We measured peroxide molar fractions in SOA, showing a positive correlation with organic radical yields by SOA in the presence of Fe^{2+} (circles in Figure 4.4 (d)). It indicates that peroxides ($\text{ROOR} + \text{ROOH}$) are highly probable sources of aqueous organic radical formation. This is in line with a very recent study showing that the total ROS production from cooking SOA can be enhanced substantially through atmospheric aging, coinciding with the elevation in peroxide contents.¹⁰⁰ Isoprene SOA is measured to have high peroxide content ($\sim 97\%$) compared to Surratt et al.²⁶⁷ ($\sim 61\%$, from a Teflon chamber); this difference may be due to excess RO_2^\bullet chemistry in the PAM reactor, inducing more production of peroxides through termination steps such as $\text{RO}_2^\bullet + \text{HO}_2^\bullet \rightarrow \text{ROOH} + \text{O}_2$ and $\text{RO}_2^\bullet + \text{RO}_2^\bullet \rightarrow \text{ROOR} + \text{O}_2$.¹² Toluene SOA has the lowest peroxide content with 18%, which is consistent with a previous study,²⁶⁸ leading to a lower organic radical yield.

To investigate the linkage between organic radical formation and oxidative potential, we performed the DTT assay on mixtures of SOA and Fe^{2+} and the results are shown by the color scale in Figure 4.4 (d) (see also Table A6). The DTT consumption rates normalized by SOA mass (DTTm) for isoprene SOA ($33.4 \pm 6.2 \text{ pmol min}^{-1} \mu\text{g}^{-1}$) and toluene SOA ($22.3 \pm 2.5 \text{ pmol min}^{-1} \mu\text{g}^{-1}$) are consistent with previous studies.^{93, 269} With Fe^{2+} addition, clear enhancements of DTTm are observed for all types of SOA. Due to the moderate DTT activity from Fe^{2+} alone (Figure A16), SOA and Fe^{2+} demonstrate a strong synergistic effect in causing oxidative potential (Table A6). Figure 4.4 (d) shows no clear association between organic radical yields and DTTm. Despite the lowest organic radical yields from mixtures of toluene SOA and Fe^{2+} , they induce relatively high DTTm ($42.8 \pm 0.4 \text{ pmol min}^{-1} \mu\text{g}^{-1}$), which is comparable with mixtures of isoprene SOA and Fe^{2+} ($49.0 \pm 11.2 \text{ pmol min}^{-1} \mu\text{g}^{-1}$). Tu et al.²³ reported generally higher DTT activities from anthropogenic SOA than biogenic SOA, although the interactions of SOA and transition metals in

oxidative potential are still understudied. Dedicated studies are necessary to further elucidate the link between ROS formation and oxidative potential from SOA.

4.5 Implications

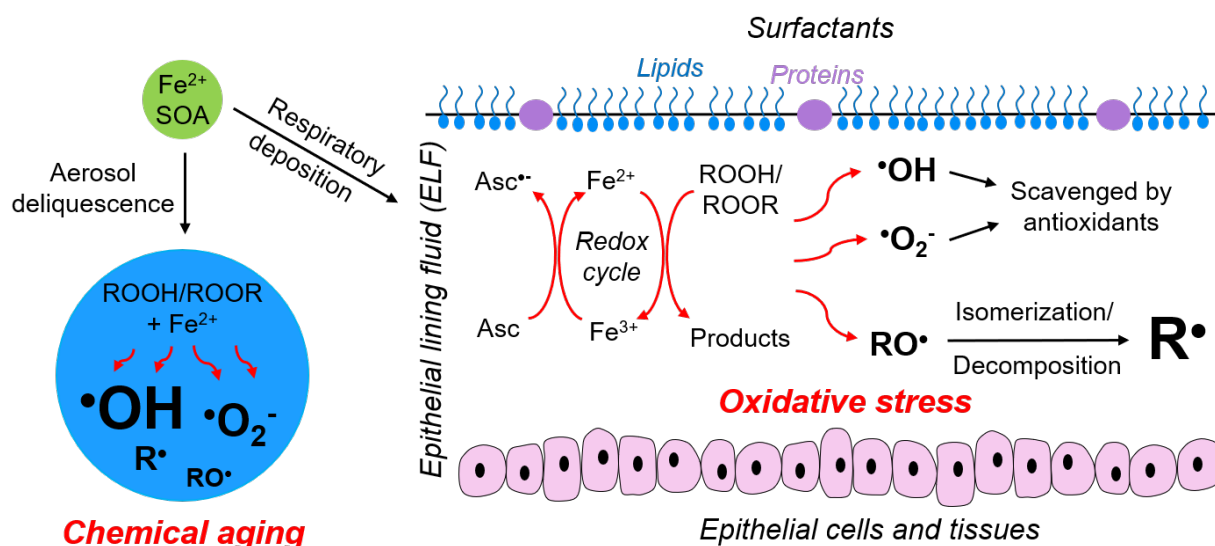


Figure 4.5. Implications of free radical formation by SOA and Fe^{2+} in water and epithelial lining fluid. Ambient aerosol particles containing SOA and Fe^{2+} can undergo deliquescence and release ROS dominated by $\bullet\text{OH}$ and $\text{O}_2^{\bullet-}/\text{HO}_2^{\bullet}$ through Fe^{2+} -facilitated decomposition of organic hydroperoxides and subsequent aqueous reactions. Upon respiratory deposition, various radical species can be generated by interactions of ROOH/ROOR , Fe^{2+} , and antioxidants. $\bullet\text{OH}$ and $\text{O}_2^{\bullet-}/\text{HO}_2^{\bullet}$ can be effectively scavenged by antioxidants, which may contribute to antioxidant depletion. The organic radical formation dominated by $\text{R}\bullet$ with relatively long lifetimes may trigger lipid peroxidation to cause oxidative stress.

This work establishes the mechanisms driving organic radical formation by the interactions among SOA, Fe^{2+} in SLF as shown in Figure 4.5. In liquid droplets formed through aerosol deliquescence, the decomposition of organic hydroperoxides in SOA can be promoted by Fe^{2+} , leading to enhanced formation of $\bullet\text{OH}$ and $\text{O}_2^{\bullet-}/\text{HO}_2^{\bullet}$ with a minor contribution from organic radicals ($\text{R1} - \text{R4}$). These aqueous-phase processes involving ROS formation are efficient pathways for the chemical aging of SOA,^{124, 125} which may lead to the change of particle properties such as cloud condensation nuclei activity¹²⁶ and optical properties.¹²⁷

Upon respiratory deposition of aerosol particles, SOA and Fe^{2+} may interact and release various radical species in epithelial lining fluid (ELF). While organic peroxides are thermally stable under physiological temperature,²⁷⁰ the chemical lifetimes of organic peroxides with respect to Fe^{2+} reactions are calculated to be 0.3 – 46 hours depending on Fe^{2+} concentrations in the experimental range of 0.05 – 0.8 mM. Meanwhile, the antioxidant defense system can counteract ROS formation: for example, ascorbate efficiently scavenges $\cdot\text{OH}$ and $\text{O}_2\cdot^-/\text{HO}_2\cdot$ with relatively fast rate constants of $\sim 1.8 \times 10^{11} \text{ cm}^3 \text{ s}^{-1}$ and $\sim 3.6 \times 10^{16} \text{ cm}^3 \text{ s}^{-1}$, respectively.^{271, 272} In comparison, organic radicals, especially $\text{R}\cdot$, react with ascorbate more slowly by multiple orders of magnitude, leading to much longer lifetimes.²⁶³ A recent study characterized that the reaction rates of ascorbate and glutathione with alkyl radicals are too slow to protect proteins from peroxidation.²⁷³ The rapid redox cycling of $\text{Fe}^{3+}/\text{Fe}^{2+}$ maintained by ascorbate can further facilitate the ROOR decomposition and subsequent organic radical formation (R5, R10 – R14, R63). Note that $\text{Fe}^{3+}/\text{Fe}^{2+}$ redox cycles can also be mediated by ROS such as superoxide,^{258, 274} which can be hindered by the addition of antioxidants through direct scavenging of ROS. Antioxidants play a reciprocal role by depleting short-lived reactive radicals while amplifying organic radical formation.

Epithelial cell membranes contain phospholipid bilayers and $\cdot\text{OH}$ and $\text{HO}_2\cdot$ are known to initiate a cascade of propagation reactions lipid peroxidation,^{116, 275} which may alter the membrane fluidity and trigger the inactivation of membrane-embedded proteins functioning as ion channels and receptors.²⁷⁶ Our results on persistency of organic radicals even in the presence of antioxidants imply that organic radicals may also participate in radical chain reactions to be involved in lipid peroxidation. Despite the significance in numerous pathological processes, lipid peroxidation has not been linked mechanistically to radical formation from organic aerosols and transition metals, which underlines the need of future studies. Overall, our experimental and modeling results demonstrate the central role of Fe^{2+} in inducing organic radical formation by facilitating ROOR decomposition in lung fluid, highlighting the significance of the interactions among redox-active components in ambient PM in potentially causing oxidative stress.

4.6 Chapter 4 Appendix

4.6.1 Additional discussion on reaction mechanisms

In the kinetic model, we include the established mechanisms involving aqueous RO_2^\bullet chemistry (R3, R4, R6, R7, R16 – R23). To investigate the impact of RO_2^\bullet chemistry, we performed a sensitivity analysis showing that the interconversion of RO_2^\bullet with R^\bullet or RO^\bullet (e.g., R17 and R18) have negligible ($\pm <1\%$) contribution to the overall R^\bullet and RO^\bullet formation.

In the presence of antioxidants, Gonzalez et al.²⁵⁸ demonstrated the enhancement effect of Fe-Cit ligands on the rate coefficients of Fe^{2+} oxidation by O_2 , $\text{O}_2^{\bullet-}$ and H_2O_2 (R42 – R45). Thus, we consider this potential effect by simulating the rates of R42 – R45 using the rates of free Fe^{2+} and Fe^{2+} -Cit ligands as lower and upper boundaries in the Monte Carlo Genetic Algorithm (MCGA)¹⁴², respectively. The sensitivity analysis again indicates negligible impacts of the ligands on R^\bullet and RO^\bullet formation.

The kinetic model provides the simulated rate coefficient of organic peroxides reacting with Fe^{2+} (R5 in Table A4): $k_5 = (0.06 - 1.9) \times 10^{-21} \text{ cm}^3 \text{ s}^{-1}$. The first-order loss rate of organic peroxides towards Fe^{2+} reactions were then calculated using the $k_5 \times [\text{Fe}^{2+}]$ (0.05 – 0.8 mM), and its inverse would be the corresponding lifetimes of 0.3 – 46 hours.

The simulated rate coefficients of BMPO chemistry with $^\bullet\text{OH}$ and $\text{O}_2^{\bullet-}/\text{HO}_2^\bullet$ (R64 – R70) are consistent with previous studies.^{26, 98, 202} The rates of BMPO trapping R^\bullet and RO^\bullet ($(0.1 - 9.5) \times 10^{-13} \text{ cm}^3 \text{ s}^{-1}$ and $(0.2 - 7.5) \times 10^{-13} \text{ cm}^3 \text{ s}^{-1}$, respectively) are also in good agreement with Tong et al.¹³⁶ ($1.5 \times 10^{-13} \text{ cm}^3 \text{ s}^{-1}$ and $7.7 \times 10^{-13} \text{ cm}^3 \text{ s}^{-1}$, respectively). In addition, the simulated lifetime of BMPO-R (2.0 – 6.0 hrs) is around twice as long than BMPO-OR (1.0 – 2.5 hrs), which is in line with the overall sharper decreasing trend by BMPO-OR in Figure 4.4b.

The best fit out of these 40 parameter sets was used for plotting the solid lines in Figure 4.4 (a)-(c). The 40 parameter sets were also used to plot 40 traces in Figure 4.4(c), and the highest and lowest traces were selected as the upper and lower boundaries of the shaded areas. Note that these boundaries do not

necessarily correspond to the boundaries of each parameter in Table A4 and A5. There is still relatively large uncertainty in the actual values of some parameters, as shown by the parameter ranges in Table A4; further measurements to quantify organic hydroperoxides and alcohols as well as dedicated kinetic studies would be required for determination of these parameters.

A recent study suggested that the catalytic reactions dominate between Fe^{3+} and ascorbate rather than redox reactions:²⁶⁶ $\text{Fe}^{3+} + \text{AscH}^- + \text{O}_2 \rightarrow \text{Fe}^{3+} + \text{dehydroascorbic acid (DHA)} + \text{H}_2\text{O}_2$. We performed sensitive analysis for the feasibility of this hypothesis. By adopting the catalytic rate coefficient in their study and assuming the dissolved oxygen concentration ($\sim 10^{17} \text{ cm}^{-3}$), the rate coefficient of Fe^{3+} -ascorbate catalytic reaction is calculated to be one order of magnitude smaller compared to the redox reaction (R63). Therefore, the redox reaction remains the dominant source of Fe^{2+} regeneration and thus enhancement in R^\bullet formation in SLF, while we do not exclude the possibility of Fe^{3+} reduction by other reactions such as Fe^{3+} -peroxides.^{26, 258}

For measurements of Fe^{2+} in the mixtures of Fe^{3+} and ascorbate, Fe^{2+} should be generated from $\text{Fe}^{3+} + \text{Asc}$ but not from $\text{Fe}^{3+} + \bullet\text{O}_2^-$ as the concentration of $\bullet\text{O}_2^-$ would be extremely low. In this simple system, the source of $\bullet\text{O}_2^-$ would be R42 in Table A4: $\text{Fe}^{2+} + \text{O}_2 \rightarrow \text{Fe}^{3+} + \bullet\text{O}_2^-$ with a relatively slow rate ($\sim 10^{-21} \text{ cm}^3 \text{ s}^{-1}$) compared to $\text{Fe}^{3+} + \text{Asc}$ reaction rate (R63, $\sim 10^{-19} \text{ cm}^3 \text{ s}^{-1}$). Moreover, the system does not contain any Fe^{2+} initially, which should be generated only through the reduction of Fe^{3+} by Asc.

4.6.2 Peroxide measurements

The measured total peroxide molar fraction from isoprene SOA is $93 \pm 14\%$, which is consistent with the result of near 100% reported by Tong et al.⁹⁸ However, this is in contrast with the simulated fractions of (ROOR+ROOH) (2 – 23%) from the kinetic model as shown in Table A5. On the one hand, we acknowledge that there is still relatively large uncertainty in the fitting values of the kinetic model. On the other hand, it should be noted that these fitted results represent the fractions that can effectively react with Fe^{2+} within the timescales of our experiments, while in reality there could be larger fractions of organic peroxides that are stable enough and do not induce ROS formation. This is further supported by the standard

compound (benzoyl peroxide) used for the calibration of the total peroxide measurement, which yields no radicals above the detection limit when mixed with Fe^{2+} in water or SLF as shown by Figure 4.2 (g) and (h). An additional explanation for the difference could be due to the H_2O_2 generated by aqueous reactions of SOA, although our recent study²⁰² reports $\sim 4\%$ in H_2O_2 molar yield from isoprene SOA, accounting for a minor contribution to the total peroxide measurement at most. Nevertheless, Figure 4.4(d) shows the tight correlation between organic radical formation and total peroxide fractions among different SOA, indicating the latter as a significant source of aqueous RO^\bullet and R^\bullet formation.

4.6.3 Additional information on experiments

The quantification of radicals from SOA by EPR requires high SOA mass. To keep the $[\text{Fe}^{2+}]/[\text{SOA}]$ molar ratios relevant to the ambient conditions, we selected Fe^{2+} concentrations to be 0.05 – 0.8 mM. In a typical urban area with $\sim 10 \mu\text{g m}^{-3}$ $\text{PM}_{2.5}$, the SOA mass concentrations would be $\sim 5 \mu\text{g m}^{-3}$ by assuming 50% of ambient $\text{PM}_{2.5}$ as SOA. As the soluble Fe concentrations typically vary between 10 – 50 ng m^{-3} ,²⁴² the $[\text{Fe}^{2+}]/[\text{SOA}]$ ratio would be 0.008 – 0.05. In our study, the $[\text{Fe}^{2+}]/[\text{SOA}]$ is 0.01 – 0.4 with the selected $[\text{Fe}^{2+}]$. The higher end of this range would be representative of areas with heavier transition metal pollution and less SOA formation.

Filter collection of SOA particles usually took 30 – 60 min, while the extraction and analysis were performed between hours to days after the collection. The filters were stored in a freezer (-20°C) before the analysis. Note that we have conducted control experiments showing consistent results by filters analyzed immediately after collection versus that stored in a freezer for one week. This indicates that the ROS-inducing compounds in the SOA should be stable within this time frame.

Table A4. Chemical reactions and parameters included in the kinetic model to simulate ROS formation from aqueous reactions of isoprene SOA and Fe²⁺ in SLF. In the third column, the first row denotes the uncertainty range, while the second row denotes values for best fits (solid lines in Figure 4.4). The reaction rates with uncertainties are all simulated in MCGA, while the rates without uncertainties are obtained from literature or fixed due to their insensitivity. The units of k_1 , k_4 , k_{11} , k_{12} , k_{13} , k_{41} , k_{65} , k_{69} , k_{72} and k_{75} are s⁻¹, while the others are cm³ s⁻¹.

Reaction number	Reaction	Rate coefficient, uncertainty range and best fit	Reference or comment
Radical chemistry involving SOA			
R1	ROOH → RO• + •OH	$k_1 = (0.1 - 3.2) \times 10^{-5}$ 0.5×10^{-5}	$(0.1 - 4) \times 10^{-5}$ 26, 202
R2	ROOH + Fe ²⁺ → RO• + •OH + Fe ³⁺	$k_2 = (0.03 - 9.5) \times 10^{-17}$ 0.2×10^{-17}	$(1.0 - 6.0) \times 10^{17}$ 26
R3	R ₁ R ₂ CHOH + •OH $\xrightarrow{O_2}$ c ₁ R ₁ R ₂ C•(O ₂)OH	$k_3 = (1.0 - 9.9) \times 10^{-12}$ 3.0×10^{-12} c ₁ = 0.03 – 0.30 0.09	$(0.4 - 2.0) \times 10^{-11}$ $(0.06 - 0.30)^{202}$
R4	R ₁ R ₂ C•(O ₂)OH → R ₁ R ₂ C(O) + HO ₂ •	$k_4 = 15 - 914$ 914	17 – 595 ²⁰²
R5	ROOR' + Fe ²⁺ → RO• + R'O• + Fe ³⁺	$k_9 = (0.06 - 1.9) \times 10^{-21}$ 0.2×10^{-21}	Comparable to R10
R6	•OH + ROOH → RO ₂ • + H ₂ O	$k_5 = (0.1 - 9.9) \times 10^{-14}$ 0.8×10^{-14}	5.5×10^{-14} 26
R7	R ₁ R ₂ C•(O ₂)OH + •OH → products	$k_6 = (0.1 - 7.6) \times 10^{-12}$ 4.0×10^{-12}	Insensitive ²⁰²
R8	SOA + •OH → SOA'	$k_7 = (0.2 - 5.7) \times 10^{-12}$ 1.0×10^{-12}	$(0.7 - 9.9) \times 10^{-12}$ 202
R9	Carbonyls + •OH → products	$k_8 = 1.0 \times 10^{-12}$	Insensitive
R10	ROOH + Fe ²⁺ → RO• + OH• + Fe ³⁺	$k_{10} = (0.05 - 9.5) \times 10^{-21}$ 0.4×10^{-21}	< 10 ⁻²⁰ 26

R11	$\text{ROOR}' \rightarrow \text{RO}\cdot + \cdot\text{OR}'$	$k_{11} = (1.0 - 6.8) \times 10^{-7}$ 2.1×10^{-7}	> 1 order slower than R3
R12	$\text{RO}\cdot + \text{H}_2\text{O} \rightarrow \cdot\text{R}'\text{OH} + \text{H}_2\text{O}$	$k_{12} = (0.05 - 6.4) \times 10^6$ 0.2×10^6	$< 10^7 \text{ s}^{-1}$ 256
R13	$\text{RO}\cdot \rightarrow \text{R}'\cdot + \text{carbonyls}$	$k_{13} = (0.1 - 9.6) \times 10^5$ 6.4×10^5	$< 1.4 \times 10^6$ 257
R14	$\text{RO}\cdot + \text{RH} \rightarrow \text{ROH} + \text{R}\cdot$	$k_{14} = (0.002 - 9.6) \times 10^{-13}$ 0.2×10^{-13}	221, 262
R15	$\text{R}_1\cdot + \text{R}_2\text{H} \rightarrow \text{R}_1\text{H} + \text{R}_2\cdot$	$k_{15} = (0.002 - 8.0) \times 10^{-13}$ 0.05×10^{-13}	In analogy to R14
R16	$\text{RO}_2\cdot + \text{RH} \rightarrow \text{ROOH} + \text{R}\cdot$	$k_{16} = (0.001 - 9.0) \times 10^{-13}$ 0.06×10^{-13}	262
R17	$\text{R}\cdot + \text{O}_2 \rightarrow \text{RO}_2\cdot$	$k_{17} = (0.5 - 4.6) \times 10^{-12}$ 0.8×10^{-12}	$\sim 10^{-12}$ 277
R18	$\text{RO}_2\cdot + \text{RO}_2\cdot \rightarrow 2\text{RO}\cdot + \text{O}_2$	$k_{18} = (1.0 - 9.6) \times 10^{-13}$ 1.4×10^{-13}	$< 10^{-12}$ 155
R19	$\text{RO}_2\cdot + \text{RO}_2\cdot \rightarrow \text{products}$ (carbonyls/alcohols)	$k_{19} = (1.0 - 9.9) \times 10^{-13}$ 6.3×10^{-13}	$\sim 10^{-12}$ 155
R20	$\text{RO}_2\cdot + \text{HO}_2\cdot \rightarrow \text{ROOH} + \text{O}_2$	$k_{20} = (0.1 - 5.7) \times 10^{-13}$ 0.2×10^{-13}	$< 10^{-12}$ 278 (insensitive)
R21	$\text{RO}_2\cdot + \cdot\text{OH} \rightarrow \text{products}$	$k_{21} = (0.1 - 8.3) \times 10^{-12}$ 1.2×10^{-12}	(insensitive)
R22	$\text{RO}_2\cdot + \text{R}\cdot \rightarrow \text{products}$	$k_{22} = (0.03 - 6.4) \times 10^{-13}$ 0.2×10^{-13}	(insensitive)
R23	$\text{RO}_2\cdot + \text{RO}\cdot \rightarrow \text{products}$	$k_{23} = (0.01 - 7.8) \times 10^{-13}$ 0.3×10^{-13}	(insensitive)
R24	$\text{R}\cdot + \cdot\text{OH} \rightarrow \text{products}$	$k_{24} = (0.1 - 8.2) \times 10^{-12}$ 0.6×10^{-12}	(insensitive)
R25	$\text{RO}\cdot + \cdot\text{OH} \rightarrow \text{products}$	$k_{25} = (0.1 - 9.8) \times 10^{-13}$ 1.6×10^{-12}	(insensitive)
R26	$\text{RO}\cdot + \text{O}_2 \rightarrow \text{HO}_2\cdot + \text{products (carbonyls)}$	$k_{26} = (0.1 - 9.5) \times 10^{-14}$	$(0.1 - 1.0) \times 10^{-14}$

		5.4×10^{-14}	279
R27	$R^\bullet + HO_2^\bullet \rightarrow \text{products}$	$k_{27} = (0.1 - 9.3) \times 10^{-13}$ 3.5×10^{-13}	(insensitive)
R28	$RO^\bullet + HO_2^\bullet \rightarrow \text{products}$	$k_{28} = (0.1 - 9.8) \times 10^{-13}$ 0.9×10^{-13}	(insensitive)
R29	$R^\bullet + R^\bullet \rightarrow \text{products}$	$k_{29} = (0.01 - 9.4) \times 10^{-13}$ 0.2×10^{-13}	(insensitive)
R30	$RO^\bullet + RO^\bullet \rightarrow \text{products}$	$k_{30} = (0.01 - 6.7) \times 10^{-13}$ 0.03×10^{-13}	(insensitive)
R31	$R^\bullet + RO^\bullet \rightarrow \text{products}$	$k_{31} = (0.02 - 7.1) \times 10^{-13}$ 0.4×10^{-13}	(insensitive)
ROS coupling			
R32	$\bullet O_2^- + \bullet OH \rightarrow O_2 + OH^-$	$k_{32} = 1.3 \times 10^{-11}$	180
R33	$H_2O_2 + \bullet OH \rightarrow H_2O + HO_2^\bullet$	$k_{33} = 5.5 \times 10^{-14}$	181
R34	$\bullet OH + \bullet OH \rightarrow H_2O_2$	$k_{34} = 8.6 \times 10^{-12}$	182
R35	$\bullet OH + HO_2^\bullet \rightarrow H_2O + O_2$	$k_{35} = 1.2 \times 10^{-11}$	182
R36	$HO_2^\bullet + HO_2^\bullet \rightarrow H_2O_2 + O_2$	$k_{36} = 1.4 \times 10^{-15}$	183
R37	$\bullet O_2^- + \bullet O_2^- + 2H^+ \rightarrow H_2O_2 + O_2$	$k_{37} = 3.0 \times 10^{-16}$	280
R38	$H_2O_2 + HO_2^\bullet \rightarrow H_2O + O_2 + \bullet OH$	$k_{38} = 5.0 \times 10^{-21}$	184
R39	$HO_2^\bullet + \bullet O_2^- \rightarrow H_2O_2 + OH^- + O_2$	$k_{39} = 1.7 \times 10^{-13}$	183
R40	$H^+ + \bullet O_2^- \rightarrow HO_2^\bullet$	$k_{40} = 2.9 \times 10^{-11}$	185
R41	$HO_2^\bullet \rightarrow H^+ + \bullet O_2^-$	$k_{41} = 2.3 \times 10^5$	185
Fe-oxidant interaction			
R42	$Fe^{2+} + O_2 \rightarrow Fe^{3+} + \bullet O_2^-$	$k_{42} = (0.1 - 3.7) \times 10^{-21}$	$(0.2 - 5.0) \times 10^{-21}$
	$Cit-Fe^{2+} + O_2 \rightarrow Cit-Fe^{3+} + \bullet O_2^-$	1.1×10^{-21}	258
R43	$Fe^{2+} + \bullet O_2^- + 2H^+ \rightarrow Fe^{3+} + H_2O_2$	$k_{43} = (0.001 - 7.4) \times 10^{-16}$	$(0.003 - 1.0) \times 10^{-15}$ 258
	$Cit-Fe^{2+} + \bullet O_2^- + 2H^+ \rightarrow Cit-Fe^{3+} + H_2O_2$	0.02×10^{-16}	
R44	$Fe^{3+} + \bullet O_2^- \rightarrow Fe^{2+} + O_2$	$k_{44} = (0.06 - 4.8) \times 10^{-13}$	$(0.01 - 2.5) \times 10^{-13}$ 258
	$Cit-Fe^{3+} + \bullet O_2^- \rightarrow Cit-Fe^{2+} + O_2$	1.7×10^{-13}	
R45	$Fe^{2+} + H_2O_2 \rightarrow Fe^{3+} + OH^- + \bullet OH$	$k_{45} = (0.1 - 1.0) \times 10^{-17}$	$(0.03 - 1.0) \times$

	$\text{Cit-Fe}^{2+} + \text{H}_2\text{O}_2 \rightarrow \text{Cit-Fe}^{3+} + \text{OH}^- + \bullet\text{OH}$	0.5×10^{-17}	10^{-17} 26, 258
R46	$\text{Fe}^{2+} + \bullet\text{OH} \rightarrow \text{Fe}^{3+} + \text{OH}^-$	$k_{46} = 0.01 - 1.0 \times 10^{-11}$	281
R47	$\text{Fe}^{2+} + \text{HO}_2\bullet \rightarrow \text{Fe}^{3+} + \text{HO}_2^-$	$k_{47} = 1.6 \times 10^{-15}$	258
R48	$\text{Fe}^{2+} + \bullet\text{O}_2^- \rightarrow \text{Fe}^{3+} + \text{O}_2^{2-}$	$k_{48} = 1.3 \times 10^{-14}$	258
R49	$\text{Fe}^{3+} + \text{H}_2\text{O}_2 \rightarrow \text{Fe}^{2+} + \text{HO}_2\bullet + \text{H}^+$	$k_{49} < 10^{-23}$	26, 258
R50	$\text{Fe}^{3+} + \text{HO}_2\bullet \rightarrow \text{Fe}^{2+} + \text{O}_2 + \text{H}^+$	$k_{50} = 3.3 \times 10^{-18}$	183
R51	$\text{Fe}^{3+} + \text{R}\bullet \rightarrow \text{Fe}^{2+} + \text{products (carbonyls)}$	$k_{51} = (0.1 - 5.8) \times 10^{-13}$ 4.2×10^{-13}	$< 6.0 \times 10^{-13}$ 155
SLF-radical/Fe interaction			
R52	$\text{AscH}^- + \bullet\text{OH} \rightarrow \text{Asc}\bullet^- + \text{H}_2\text{O}$	$k_{52} = 1.8 \times 10^{-11}$	271
R53	$\text{UAH}^- + \bullet\text{OH} \rightarrow \text{UA}^- + \text{products}$	$k_{53} = 1.2 \times 10^{-11}$	282
R54	$\text{GSH} + \bullet\text{OH} \rightarrow \text{GSSG} + \text{products}$	$k_{54} = 1.7 \times 10^{-11}$	283
R55	$\text{AscH}^- + \bullet\text{O}_2^- + 2\text{H}^+ \rightarrow \text{Asc}\bullet^- + \text{H}_2\text{O}_2$	$k_{55} = 0.5 - 3.6 \times 10^{-16}$	26, 258
R56	$\text{AscH}^- + \text{R}\bullet \rightarrow \text{products}$	$k_{56} = (0.001 - 9.0) \times 10^{-17}$ 0.009×10^{-17}	
R57	$\text{AscH}^- + \text{RO}\bullet \rightarrow \text{products}$	$k_{57} = (0.001 - 8.5) \times 10^{-14}$ 0.4×10^{-14}	$< 10^{-13}$ 263
R58	$\text{Asc}\bullet^- + \text{Asc}\bullet^- + \text{H}^+ \rightarrow \text{AscH}^- + \text{DHA}$	$k_{58} = 5.0 \times 10^{-16}$	284
R59	$\text{AscH}^- + \text{GSSG} \rightarrow \text{GSH} + \text{Asc}\bullet^-$	$k_{59} = 1.0 \times 10^{-12}$	263
R60	$\text{AscH}^- + \text{UA}^- \rightarrow \text{UAH}^- + \text{Asc}\bullet^-$	$k_{60} = 1.7 \times 10^{-15}$	263
R61	$\text{UAH}^- + \text{GSSG} \rightarrow \text{GSH} + \text{UA}^-$	$k_{61} = 5.0 \times 10^{-14}$	285
R62	$\text{Cit}^{3+} + \bullet\text{OH} \rightarrow \text{Cit}_{\text{ox}}$	$k_{62} = 1.7 \times 10^{-13}$	258
R63	$\text{Fe}^{3+} + \text{AscH}^- \rightarrow \text{Fe}^{2+} + \text{H}^+ + \text{Asc}\bullet^-$	$k_{63} = 1.7 \times 10^{-19}$	115, 263
BMPO chemistry			
R64	$\text{BMPO} + \bullet\text{OH} \rightarrow \text{BMPO-OH}$	$k_{64} = (0.5 - 4.6) \times 10^{-12}$ 1.1×10^{-12}	$(0.1 - 1.3) \times 10^{-12}$ 202
R65	$\text{BMPO-OH} \rightarrow \text{products}$	$k_{65} = (3.0 - 3.6) \times 10^{-4}$ 3.3×10^{-4}	$\sim 3.8 \times 10^{-4}$ $(\tau_{1/2} \sim 30\text{min})^{144}$
R66	$\text{BMPO-OH} + \bullet\text{OH} \rightarrow \text{products}$	$k_{66} = (0.1 - 8.3) \times 10^{-12}$ 0.2×10^{-12}	$(0.1 - 8.0) \times 10^{-12}$ 26

R67	$\text{BMPO} + \text{HO}_2^\bullet \rightarrow \text{BMPO-OOH}$	$k_{67} = (0.1 - 8.7) \times 10^{-14}$ 1.9×10^{-14}	$(0.1 - 7.0) \times 10^{-14}$ 202
R68	$\text{BMPO} + \text{O}_2^- + \text{H}^+ \rightarrow \text{BMPO-OOH}$	$k_{68} = (0.1 - 8.7) \times 10^{-14}$ 0.3×10^{-14}	$(0.1 - 7.0) \times 10^{-14}$ 202
R69	$\text{BMPO-OOH} \rightarrow \text{products}$	$k_{69} = 5.0 \times 10^{-4}$	$(\tau_{1/2} = 23\text{min})^{146}$
R70	$\text{BMPO-OOH} + \bullet\text{OH} \rightarrow \text{products}$	$k_{70} = (0.1 - 9.7) \times 10^{-12}$ 3.3×10^{-12}	
R71	$\text{BMPO} + \text{R}^\bullet \rightarrow \text{BMPO-R}$	$k_{71} = (0.1 - 9.5) \times 10^{-13}$ 1.8×10^{-13}	1.5×10^{-13} 136
R72	$\text{BMPO-R} \rightarrow \text{products}$	$k_{72} = (3.2 - 9.8) \times 10^{-5}$ 5.0×10^{-5}	$\tau_{1/2} = 2.0 - 6.0 \text{ hr}$
R73	$\text{BMPO-R} + \bullet\text{OH} \rightarrow \text{products}$	$k_{73} = (0.1 - 7.4) \times 10^{-12}$ 0.2×10^{-12}	
R74	$\text{BMPO} + \text{RO}^\bullet \rightarrow \text{BMPO-OR}$	$k_{74} = (0.2 - 7.5) \times 10^{-13}$ 0.6×10^{-13}	7.7×10^{-13} 136
R75	$\text{BMPO-OR} \rightarrow \text{products}$	$k_{75} = (0.8 - 2.0) \times 10^{-4}$ 1.0×10^{-4}	$\tau_{1/2} = 1.0 - 2.5 \text{ hr}$ Faster than R72
R76	$\text{BMPO-OR} + \bullet\text{OH} \rightarrow \text{products}$	$k_{76} = (0.2 - 9.0) \times 10^{-12}$ 7.2×10^{-12}	
R77	$\text{BMPO-OH} + \text{Fe}^{2+} \rightarrow \text{Fe}^{3+} + \text{products}$	$k_{77} = (0.1 - 1.5) \times 10^{-18}$ 0.1×10^{-18}	$(0.1 - 1.0) \times 10^{-19}$ 26
R78	$\text{BMPO-OH} + \text{Fe}^{3+} \rightarrow \text{Fe}^{2+} + \text{products}$	$k_{78} = (0.1 - 9.0) \times 10^{-21}$ 6.0×10^{-21}	$< 10^{-20}$ 26
R79	$\text{BMPO-OOH} + \text{Fe}^{2+} \rightarrow \text{Fe}^{3+} + \text{products}$	$k_{79} = (0.1 - 5.3) \times 10^{-18}$ 1.0×10^{-18}	
R80	$\text{BMPO-OOH} + \text{Fe}^{3+} \rightarrow \text{Fe}^{2+} + \text{products}$	$k_{80} = (0.1 - 9.7) \times 10^{-21}$ 3.3×10^{-21}	$< 10^{-20}$
R81	$\text{BMPO-R} + \text{Fe}^{2+} \rightarrow \text{Fe}^{3+} + \text{products}$	$k_{81} = (0.02 - 2.0) \times 10^{-21}$ 0.8×10^{-21}	
R82	$\text{BMPO-R} + \text{Fe}^{3+} \rightarrow \text{Fe}^{2+} + \text{products}$	$k_{82} = (0.1 - 3.0) \times 10^{-21}$ 0.1×10^{-21}	

R83	BMPO-OR + Fe ²⁺ → Fe ³⁺ + products	$k_{83} = (0.01 - 9.7) \times 10^{-21}$ 2.2×10^{-21}
R84	BMPO-OR + Fe ³⁺ → Fe ²⁺ + products	$k_{84} = (0.1 - 4.1) \times 10^{-21}$ 0.4×10^{-21}

Table A5. Molar fractions (in percent) of ROOH, R₁R₂CHOH and ROOR in isoprene SOA. The values indicate best fit values with uncertainty ranges in brackets.

	this study	Wei et al. (2021) ²⁰²
% ROOH	5 (1 – 12)	3 (3 – 5) ²⁰²
% R ₁ R ₂ CHOH	63 (21 – 76)	78 (40 – 78) ²⁰²
% ROOR	6 (1 – 11)	

Table A6. Mass normalized DTT consumption rate (DTTm) by SOA and SOA + Fe²⁺. The Fe²⁺ concentrations in the final reaction vials for DTT assay are 0.04 mM, 0.02 mM and 0.04 mM for isoprene, α-terpineol and toluene SOA, respectively.

DTTm (pmol min ⁻¹ μg ⁻¹)	SOA	SOA + Fe ²⁺
ISO	33.4 ± 6.2	49.0 ± 11.2
TOL	22.3 ± 2.5	42.8 ± 0.4
AT	10.8 ± 0.9	14.6 ± 1.7

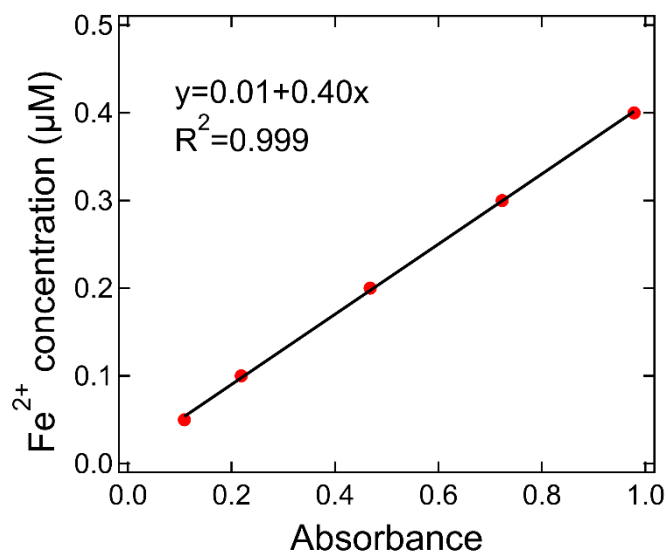


Figure A11. Calibration of the ferrozine method using Fe²⁺ standard solutions (0.05 – 0.4 μM).

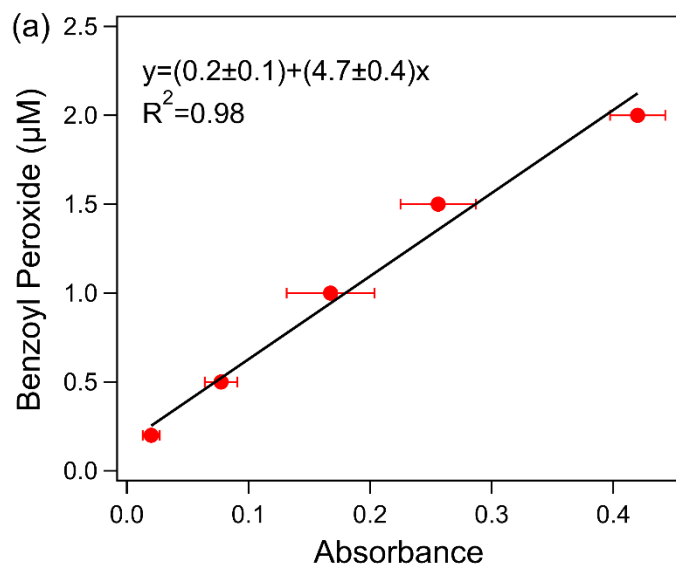


Figure A12. Calibration of total peroxide measurements using iodometric-spectrophotometric method. The error bars represent standard deviation of two duplicates.

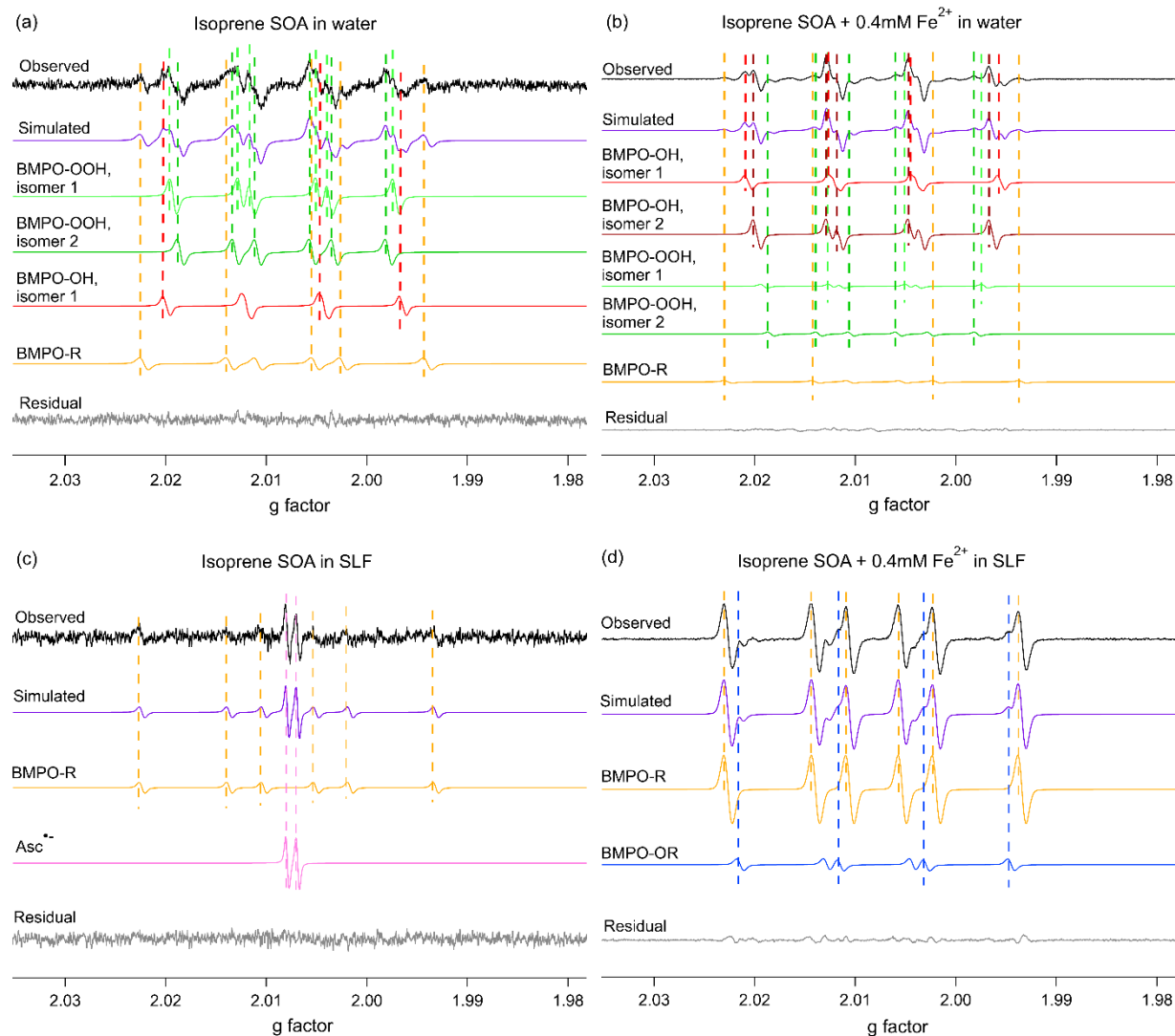


Figure A13. EPR-spectra of BMPO-radical adducts from aqueous reactions of isoprene SOA in (a) water and (c) SLF, and isoprene SOA + 0.4 mM Fe^{2+} in (b) water and (d) SLF. The observed spectra (black) are simulated (purple) and deconvoluted into BMPO-OH isomer 1 (red), BMPO-OH isomer 2 (brown), BMPO-OOH isomer 1 (light green), BMPO-OOH isomer 2 (dark green), BMPO-R (yellow), and BMPO-OR (blue). Residual (grey) denotes the difference of observed and simulated spectra. The ascorbate radicals ($\text{Asc}^{\bullet\bullet}$) are simulated independent of BMPO-radical adducts and shown in pink spectrum in panel (c). Note that the two isomers of BMPO-OH and BMPO-OOH represent the trans or cis structures of the -OH and -OOH groups, respectively.

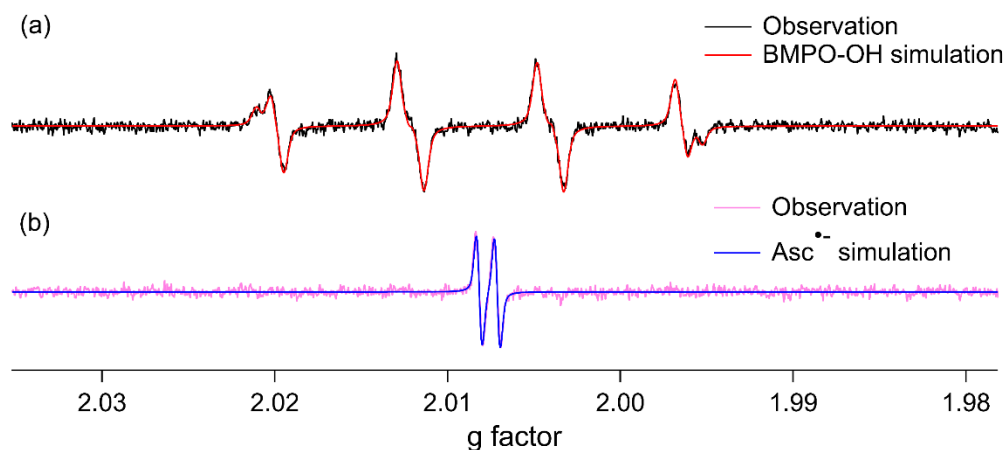


Figure A14. EPR spectra of mixtures of 0.1 mM Fe^{2+} and 0.1 mM H_2O_2 in (a) water and (b) SLF. Both solutions were buffered by PBS at pH 7.4.

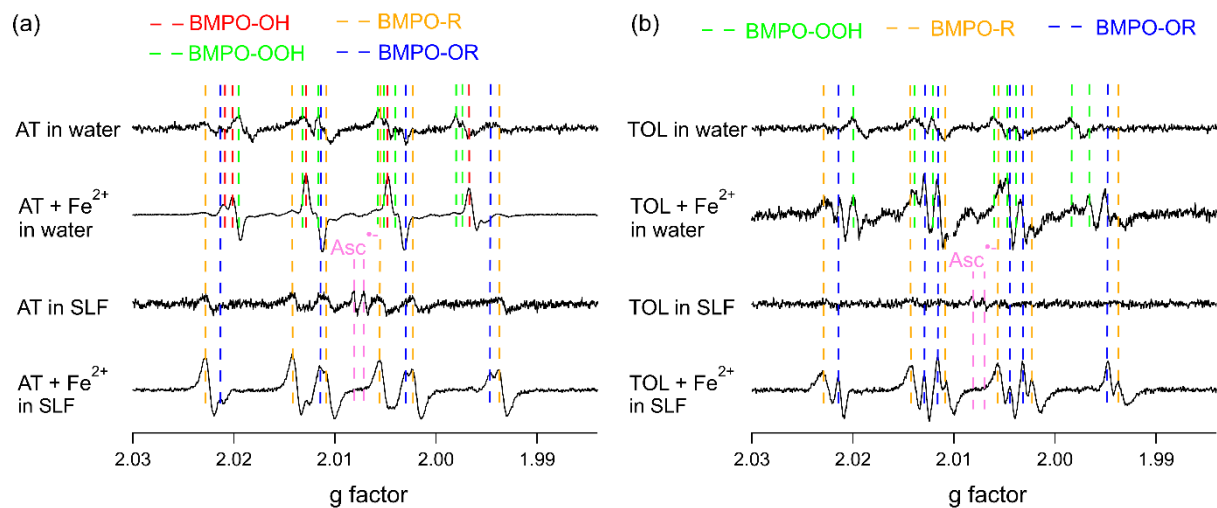


Figure A15. EPR spectra of (a) α -terpineol SOA and (b) toluene SOA in water and SLF with or without 0.4 mM Fe^{2+} in the presence of spin-trapping agent BMPO. The dashed vertical lines represent different BMPO-radical adducts and ascorbate radicals ($\text{Asc}^{\bullet-}$).

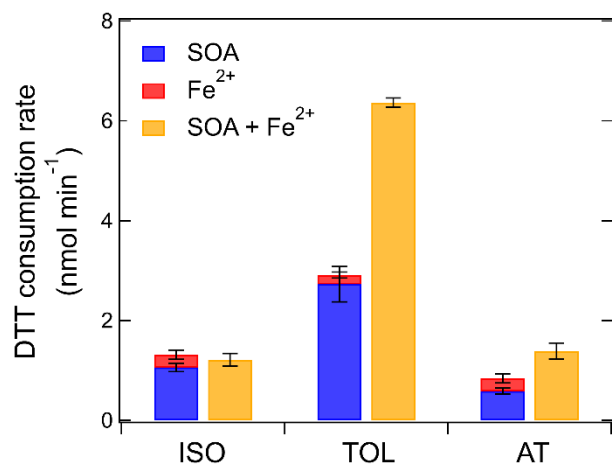


Figure A16. DTT consumption rates of SOA, Fe²⁺ and the mixtures of SOA and Fe²⁺. The Fe²⁺ concentrations for ISO, TOL and AT are 0.04 mM, 0.02 mM and 0.04 mM, respectively. ISO and AT are diluted 10 times from the filter extracts in the final reaction of DTT assay, while TOL is diluted 20 times.

Chapter 5: Impacts of Photoirradiation on Reactive Oxygen Species Generation by Secondary Organic Aerosols

5.1 Abstract

Photochemical aging is a key aging process for secondary organic aerosols (SOA), but its underlying mechanism involving free radical formation is not well understood. In this study, we combined an *in-situ* UV-Vis irradiation system with electron paramagnetic resonance (EPR) spectroscopy to characterize the photolytic formation of ROS from laboratory-generated SOA. We observed substantial organic radical formation upon irradiation, with enhancement factors up to ~ 100 compared to dark conditions. Total peroxide measurement reveals that organic peroxides can be an important source of the observed organic radicals, although additional sources may be necessary to fully account for the significant enhancement. High-resolution mass spectrometry elucidates the chemical composition of the organic radicals, indicating that photolysis of carbonyls or peroxides could be important to account for the organic radical formation. This study provides a first characterization of photolytic ROS formation from SOA involving different radical species and demonstrates that these processes have significant implications in the photoinduced aqueous chemistry of SOA.

5.2 Introduction

Secondary organic aerosols (SOA) are an important constituent of atmospheric particulate matter (PM), playing a critical role in climate, air quality and public health.^{8, 9} SOA originate from oxidation of anthropogenic and biogenic volatile organic compounds (VOCs), followed by nucleation and condensation of the oxidation products into the particle phase.¹² Upon formation, SOA can be transported through the atmosphere and participate in various aging processes which substantially change the physicochemical properties of SOA.²⁸⁶ Aging processes include heterogeneous oxidation by oxidants such as $\bullet\text{OH}$ and O_3 , uptake of gases by particles, cloud/fog processing of particulate compounds,^{286, 287} and a suite of condensed-phase reactions such as photochemical reactions, hydrolysis, and other particle-phase reactions.²⁸⁸⁻²⁹⁰

Photochemistry is at the core of many atmospheric aging processes. However, the photochemical aging of SOA is still not well understood, posing challenges to evaluate the environmental impacts of SOA.⁷

Photolysis reactions of SOA are initiated by photon absorption leading to excited-state molecules, which subsequently split into two fragments through covalent bond cleavage.²⁸⁶ The fragmentation of SOA leads to the formation of smaller, more volatile compounds, which can evaporate into the gas phase and cause mass loss in SOA.^{151, 288, 291, 292} Such mass loss could be due to evaporation of small gas molecules (e.g. CO, HCHO, HCOOH) and rapid loss of condensed-phase carbonyls.²⁹³⁻²⁹⁵ The bond cleavage of SOA components is often associated with free radical formation. Photolysis of atmospheric carbonyls can proceed via Norrish type-I or type-II mechanisms to form carbonyl ($\text{RC}\cdot(\text{O})$) and alkyl ($\text{R}\cdot$) radicals,^{159, 293} which subsequently form acyl peroxy ($\text{RC}(\text{O})\text{O}_2\cdot$) and alkyl peroxy radicals ($\text{RO}_2\cdot$) in the presence of dissolved oxygen. Direct photolysis of organic hydroperoxides (ROOH) leads to formation of alkoxy ($\text{RO}\cdot$) and $\cdot\text{OH}$ radicals by breaking the weak O-O bond.^{121, 159} $\cdot\text{OH}$ radicals can unselectively react with any molecules while alkoxy radicals may isomerize to form $\text{R}\cdot$ followed by oxygen addition to form $\text{RO}_2\cdot$.^{279, 296} $\text{RO}\cdot$ may also directly react with $\cdot\text{OH}$ to form H_2O and carbonyls.²⁹⁷ Despite these advances, it is unclear whether photochemical aging occurs through only primary photolysis reactions or secondary processes also take place which can be initiated by radical formation in a primary step.

Direct quantification of radical formation from SOA photolysis can be essential to understanding particle-phase chemistry and aqueous-phase processing of SOA. Limited studies characterized ROS formation from photochemical aging of SOA. Badali et al.²⁹⁸ directly quantified $\cdot\text{OH}$ radicals from photolysis of ROOH in SOA and reported 5 times faster rate of $\cdot\text{OH}$ formation compared to photolysis of H_2O_2 with equal concentrations of ROOH. Manfrin et al.¹³⁴ characterized singlet oxygen ($^1\text{O}_2$) formation from photosensitized reactions mediated by chromophoric components in aromatic SOA, although no free radicals were directly measured. Photolytic generation of organic radicals has been shown to contribute to SOA formation.^{299, 300} However, direct measurement of photoinduced organic radical formation from SOA has not been studied. In this study, we combined an *in-situ* UV-vis irradiation system with EPR spectroscopy to characterize the photolytic generation of free radicals from SOA generated by isoprene, α -

terpineol, α -pinene and toluene. We observe substantial formation of organic radicals (yields 0.02 – 1.5%) with enhancement factors up to ~ 100 compared to dark conditions. Total peroxide measurements elucidate that the peroxide fractions decrease by 50 – 70% after irradiation, indicating organic peroxides as a potential source of organic radical formation. We also applied high resolution mass spectrometry (HR-MS) to reveal the chemical identity of organic radicals formed during SOA photolysis. Our findings are critical to understanding the photoinduced aqueous-phase chemistry of SOA involving radical formation, which provide insights into the underlying mechanism of particle-phase processing.

5.3 Materials and Methods

5.3.1 Preparation of SOA

A potential aerosol mass (PAM) reactor⁵⁸ was used to generate SOA particles from $\bullet\text{OH}$ photooxidation of isoprene (Sigma-Aldrich, $\geq 99\%$), α -terpineol (Arcos Organics, $\geq 97\%$), α -pinene (Sigma-Aldrich, 98%), and toluene (Alfa Aesar, $\geq 99.7\%$). The relevance of PAM-generated SOA with ambient SOA has been discussed in previous chapters. The relative humidity in the PAM reactor was 40 – 50%. A scanning mobility particle sizer (SMPS, Grimm Aerosol Technik) was used to record the particle size distribution. SOA particles were collected on 47 mm polytetrafluoro-ethylene (PTFE) filters (Millipore FGLP04700, 0.2 μm pore size) for 60 – 120 min with average mass loadings of 0.41 ± 0.08 mg, 1.03 ± 0.23 mg, 0.64 ± 0.21 mg and 2.18 ± 0.56 mg for isoprene, α -terpineol, α -pinene, and toluene SOA, respectively. The filter samples were extracted into 1 mL of 10 mM spin-trap solutions with pre-adjusted pH (1.0, 2.5 – 3.5, 7.4) for 7 min. The filters after extraction were dried under nitrogen flow for 10 – 20 min. The mass difference before and after the extraction was considered as the amount of SOA dissolved in the solution, and an average molar mass of 200 g mol^{-1} ²⁶ was assumed to calculate the SOA molar concentrations in filter extracts. SOA concentrations were in the range of 1.7 – 2.5 mM, 4.0 – 6.3 mM, 2.3 – 4.3 mM and 8.1 – 13.7 mM for isoprene, α -terpineol, α -pinene, and toluene SOA, respectively. Two SOA samples were prepared for each pH for the quantification of radicals.

5.3.2 EPR Analysis

A continuous-wave electron paramagnetic resonance (CW-EPR) spectrometer (Bruker, Germany) coupled with a spin-trapping technique was applied to quantify the free radical formation in the aqueous phase. The free radicals were captured by a spin-trapping agent 5-*tert*-Butoxycarbonyl-5-methyl-1-pyrroline-N-oxide (BMPO) (Enzo Life Sciences, $\geq 99\%$). After particle extraction into 1 mL of 10 mM BMPO solutions, a 50 μ L aliquot of the SOA extracts was loaded into a 50 μ L capillary tube (VWR) and inserted in the resonator of the EPR spectrometer for temporal measurements over 75 minutes. To characterize the radical formation upon illumination, an *in-situ* UV irradiation system (ER203UV, Bruker, Germany) equipped with a 100 W Hg lamp was used with EPR. The lamp was usually warmed up for roughly 10 min before the start of any irradiation experiments. A safety shutter between the lamp and the resonator was used to control the start and stop of irradiation. A liquid light guide focused the light to the EPR resonator where samples were exposed to UV to visible light with a wavelength range of 300 – 600 nm (Figure 5.1). For the temporal measurement, the background spectrum was recorded at the starting point, with the shutter raised after the first EPR measurement was finished (~ 3 min). Temporal measurements were then conducted every 3 min for 75 min in total to monitor the change of BMPO-radical concentrations over time.

The operating parameters for EPR measurements are as follows: a center field of 3515.0 G, a sweep width of 100.0 G, a receiver gain of 30 dB, a modulation amplitude of 1.0 G, a scan number of 10 – 20, attenuation of 12 dB, a microwave power of 12.6 mW, a modulation frequency of 100 kHz, a microwave frequency of 9.86 GHz and a conversion time and time constant of 5.12 ms. After obtaining the EPR spectra, SpinFit and SpinCount methods embedded in the Bruker Xenon software were applied to quantify BMPO-radical adducts at each time point.²⁶

5.3.3 Characterization of spectral flux density

The spectral flux of the EPR *in-situ* irradiation system was characterized using a StellarNet radiometer. The TUV model (https://www.acom.ucar.edu/Models/TUV/Interactive_TUV/) was used to

obtain Los Angeles summer solstice maximum and the 24-hour average Los Angeles solar flux for comparison. The following parameters were used in the TUV calculator: latitude/longitude: 34°/-118°; date and time: June 30, 2021 – data from each hour in the day were acquired and averaged to obtain a 24-hour average spectral flux density or 19:00:00 GMT representing the summer solstice maximum; overhead ozone column: 300 du; surface albedo: 0.1; ground altitude: 0 km; measured altitude: 0 km; clouds optical depth/base/top: 0.00/4.00/5.00; aerosols optical depth/S-S albedo/alpha: 0.235/0.990/1.000; sunlight direct beam/diffuse down/diffuse up: 1.0/1.0/1.0. The unit of output of radiometer and TUV model is in $\text{W m}^{-2} \text{nm}^{-1}$ which was converted to photons $\text{cm}^{-2} \text{s}^{-1} \text{nm}^{-1}$.

5.3.4 Total peroxide measurement

The total peroxide measurements were conducted using a modified iodometric-spectrophotometric method.¹⁴⁹ Peroxides in all forms can oxidize I^- to form I_2 , which combines with the excess I^- to form I_3^- with characteristic absorbance peaks at wavelengths 289 nm and 350 nm²⁵³ and the absorbance at 350 nm was measured in this study. Isoprene, α -terpineol and toluene SOA were extracted in 1 mL Milli-Q water for 7 min. The SOA extracts were divided into three groups which were measured directly after extraction, 75 min after irradiation and 75 min under dark conditions, respectively. For the irradiated sample, 200 μL of SOA extracts were placed in a glass tube and then inserted into EPR resonator. The length of the liquid column in the glass tube can be entirely irradiated by the UV-vis light over 75 min. As a control group, the rest of SOA extracts were left under dark conditions for 75 min, after which the peroxide fractions were measured together with the irradiated sample.

To conduct the assay, 100 μL of the SOA extracts from the three groups were mixed with 700 μL ethyl acetate (Sigma-Aldrich, 99.8%) to obtain 800 μL diluted extracts. Then the 800 μL diluted extracts were mixed with 1200 μL reagents consisting of 636 μL acetic acid (Sigma-Aldrich, $\geq 99\%$), 324 μL chloroform (Sigma-Aldrich, $\geq 99.5\%$) and 240 μL water (acetic acid:chloroform:water = v:v 0.53:0.27:0.20). Note that the dilution factor of SOA extracts in the reagents (i.e., 100 μL in 2000 μL) was determined when different reagents were completely miscible so that the solution was homogeneous. The 2000 μL diluted

SOA extracts with reagents were then purged with a flow of 15 ccm N₂ for 1 min to exclude dissolved oxygen that can also oxidize I⁻. Next, 20 mg of potassium iodide (KI, Sigma-Aldrich, ≥ 99%) was added into each sample, after which the vials were capped and allowed to stand for 1 h. Lastly, the solution was further diluted in water by a factor of 200 (25 μL in 5000 μL) and the absorbance at 350 nm was measured using an online miniature spectrophotometer (Ocean Optics). The calibration was performed using 0.2 – 2 μM benzoyl peroxide (Sigma-Aldrich, ≥ 98%). Blank (water instead of SOA extracts or benzoyl peroxide) correction was always performed and the measurements were repeated twice for each SOA sample.

5.3.5 HR-MS analysis

A LTQ-Orbitrap mass spectrometer (Thermo Scientific) coupled with a modified electrospray ionization (ESI) source was used to characterize the chemical composition of the organic radicals formed upon SOA photolysis. The ESI-MS was operated at a mass resolving power of 1.4×10^5 in a positive ion mode at spray voltage of 3.5 kV.²⁸⁸ The analyte was prepared by mixing 400 μL SOA extracts with 400 μL acetonitrile with mass concentration of ~ 0.3 mg/mL. Peak positions and relative abundance were determined using the Decon2LS program (<https://omics.pnl.gov/software/decontoolsdecon2ls>). The peaks were assigned with 0.001 m/z accuracy with formulas of [C_xH_yO_z + Na]⁺ (sodium adduct formation as the dominant ionization form).²⁹⁰

5.4 Results and Discussion

5.4.1 Spectral flux of *in-situ* irradiation system

Figure 5.1 shows the spectral flux density from the EPR *in-situ* lamp as well as Los Angeles summer solstice maximum and the 24-hour average Los Angeles solar flux as obtained from the TUV model. The EPR *in-situ* lamp exhibits several prominent emission lines above 300 nm at 312 – 313nm, 334 nm, 365nm, 405 nm, 436 nm, 546 nm and 579 nm which is consistent with typical Hg lamp spectra.³⁰¹ In comparison, the ambient solar flux in summertime Los Angeles is substantially weaker in the UV range (300 – 380 nm) while stronger in the visible light range. Given the high photon flux ($3 - 4 \times 10^{14}$ photons

$\text{cm}^{-2} \text{s}^{-1} \text{nm}^{-1}$) in the UV range by Hg lamp compared to the ambient flux ($< 0.5 \times 10^{14} \text{ photons cm}^{-2} \text{s}^{-1} \text{nm}^{-1}$), it is reasonable to assume that the UV irradiation (300 – 380 nm) is primarily responsible for the aqueous chemistry and radical formation observed in this work. Therefore, we calculated the scaling factor (i.e. ratio of integrated spectral flux densities) of the Hg lamp to ambient solar flux in the UV range to be ~ 11 , indicating that 75 min of irradiation by the Hg lamp is approximately equivalent to ambient irradiation of 13.8 hours.

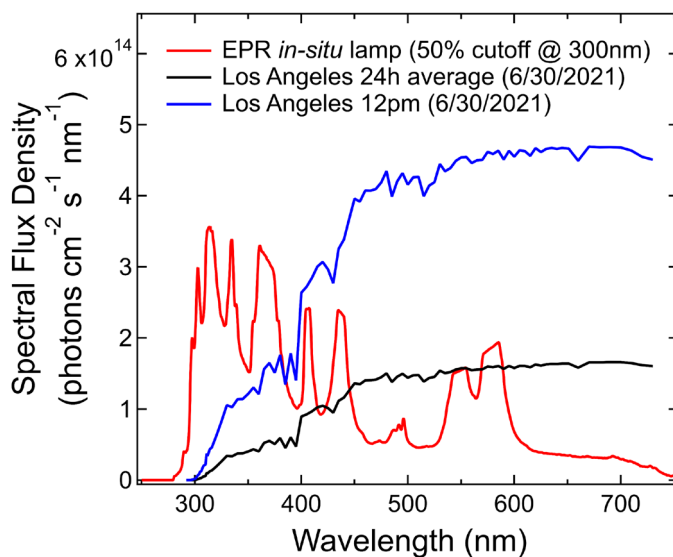


Figure 5.1. Spectral flux density of the 100 W Hg lamp (300 – 600 nm), Los Angeles summer solstice maximum, and the 24-hour average Los Angeles solar flux.

5.4.2 Photolytic generation of free radicals from SOA

Temporal radical formation was characterized using EPR-spin trap method from photolysis of isoprene, α -terpineol, α -pinene and toluene SOA. Figure 5.2 shows the temporal EPR spectra of BMPO-radical adducts from isoprene SOA photolysis. At $t = 0$, negligible radical formation is observed before the Hg lamp is switched on. The spectrum at $t = 3.1$ min represents the first measurement after the light is switched on, showing prominent superoxide formation with minor contributions from $\bullet\text{OH}$ and organic radicals. The $\text{O}_2\bullet$ keeps increasing through the second measurement ($t = 6.2$ min), although carbon- and oxygen-centered radicals take over after 15.4 min and reach maximum at ~ 46.0 min. The spectra at

t = 46.0 min and t = 76.6 min are very similar, indicating a plateau is reached after t = 46.0 min especially for organic radicals which dominate the radical formation.

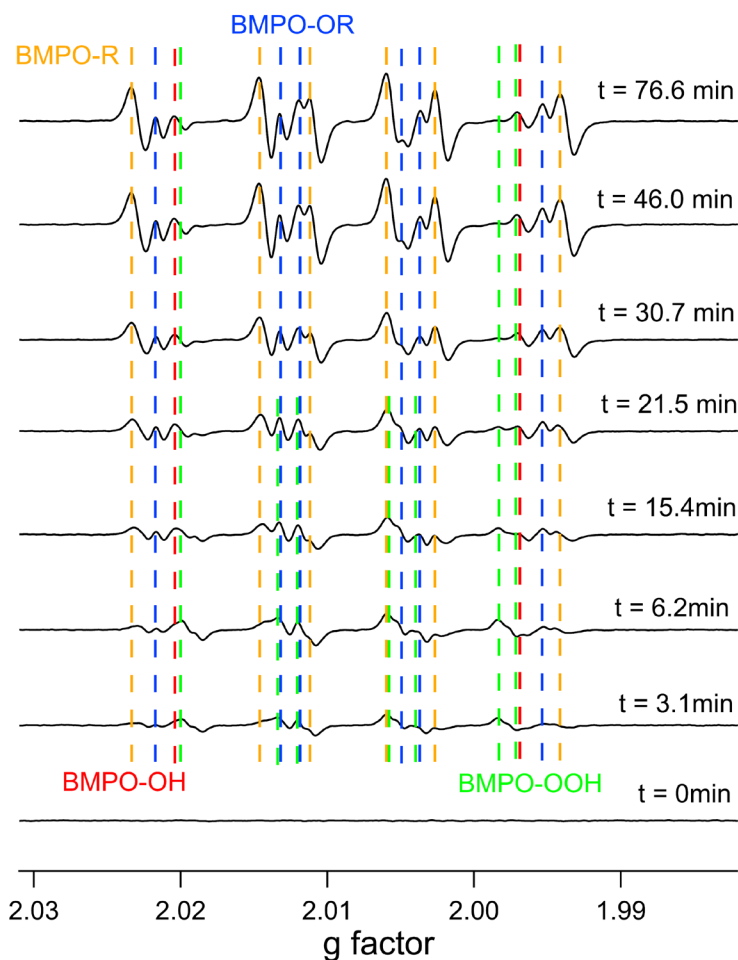


Figure 5.2. Temporal EPR spectra of BMPO-radical adducts from isoprene SOA with *in-situ* irradiation over 76.6 min. The dashed vertical lines represent different BMPO-radical adducts. Note, the measurement was taken every 3.1 min, while only 8 spectra are selected to show prominent changes over 76.6 min.

In addition to isoprene SOA, we further characterized ROS formation from α -terpineol, α -pinene and toluene SOA under irradiated versus dark conditions, and the temporal radical yields are shown in Figure 5.3. Apparently, all SOA (Figure 5.3 (a)-(d)) show substantial formation of organic radicals (carbon-centered and oxygen-centered) upon irradiation, with radical yields from 0.03 – 1.6% within 75 min. The total organic radical yield is found highest for isoprene SOA reaching 1.6%, followed by α -terpineol SOA

($\sim 0.7\%$), α -pinene SOA ($\sim 0.6\%$) and toluene SOA ($\sim 0.02\%$). Compared to dark conditions, UV-Vis irradiation significantly facilitate the organic radical formation, with enhancement factors of 60 – 100 for

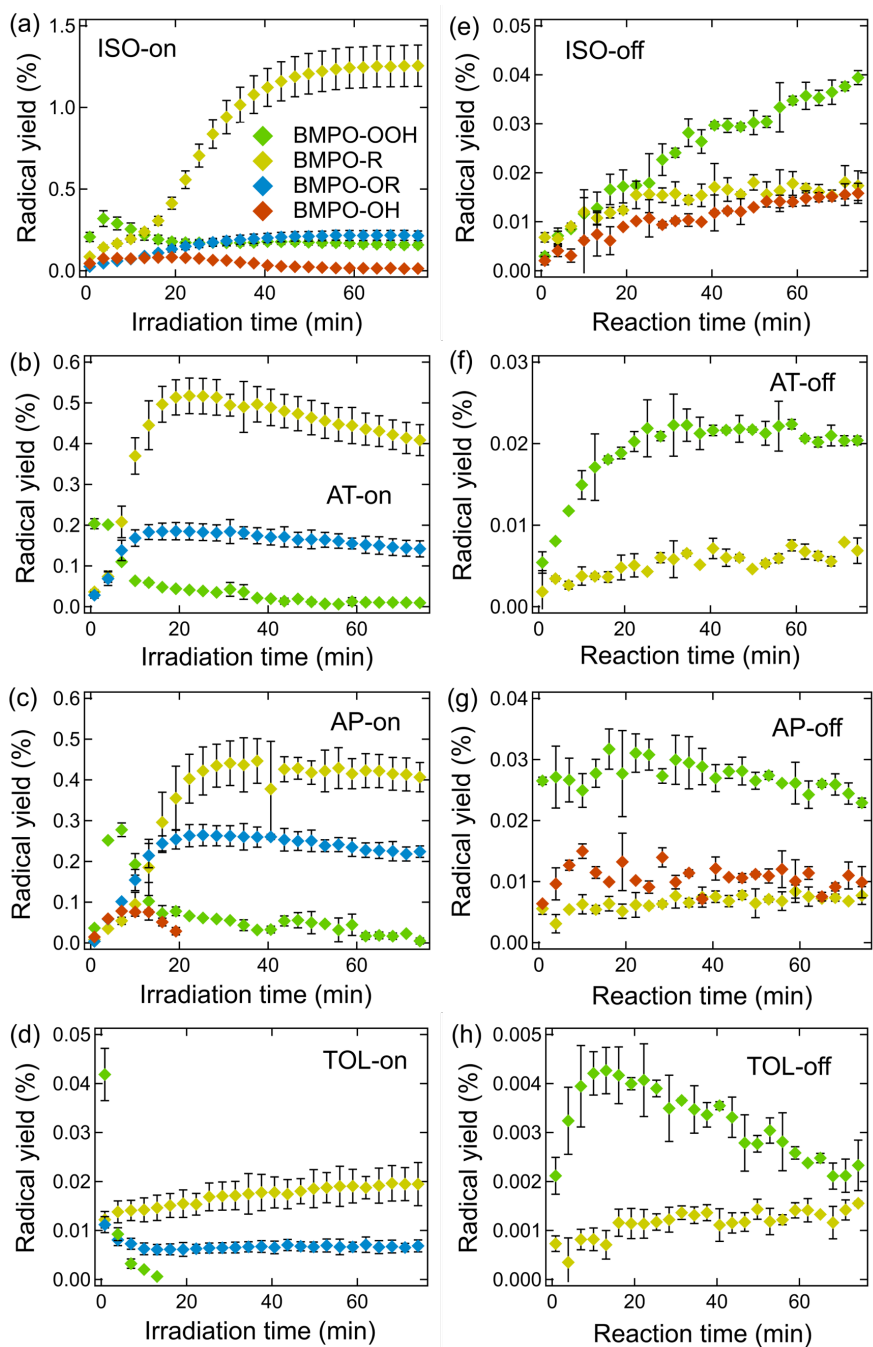


Figure 5.3. Temporal formation of BMPO-radical adducts from isoprene, α -terpineol, α -pinene and toluene SOA under UV-Vis irradiation (“on”) versus dark conditions (“off”). The error bars represent the error propagation from the two duplicates in EPR measurements with the uncertainty in SOA mass measurements.

species for all SOA. For biogenic SOA (Figure 5.3 (a)-(c)), an initial spike of $O_2^{\bullet-}$ formation is consistently observed as consistent with Figure 20, which drastically decreases within 10 – 20 min of irradiation. A possible mechanism for the initial $O_2^{\bullet-}$ burst could be due to photoinduced decomposition of ROOH leading to $\bullet OH$ biogenic (isoprene, α -terpineol and α -pinene) SOA and 20 for toluene SOA. Under dark conditions, total radical yields are found to be orders of magnitude lower with superoxide as the dominant (> 60%) radical formation,²⁹⁸ which subsequently initiate aqueous chemistry responsible for enhanced $O_2^{\bullet-}$ formation.²⁰² The sharp decrease within 20 min can be due to the self-decomposition as well as the direct photolysis of BMPO-OOH adducts as shown by our recent study.³⁰² Note, the substantial formation of carbon-centered radicals may be partially due to O_2 depletion in the reaction system, eliminating the fate of $R^{\bullet} + O_2$ as a competitive reaction for R^{\bullet} .

Interestingly, biogenic SOA upon irradiation consistently show an exponential increase in organic radical formation within 10 – 40 min for isoprene SOA and 0 – 20 min for α -terpineol and α -pinene SOA. Despite the lag in isoprene SOA, such a pattern is indicative of a similar mechanism driving the photoinduced organic radical formation from biogenic SOA. In contrast, organic radical formation from toluene SOA (Figure 5.3 (d)) shows moderate to negligible increase over 75 min, indicating a highly distinct mechanism compared to biogenic SOA. Overall, the organic radical formation plateaus or slightly decreases (α -terpineol SOA) within 75 min, indicating that the maximum capacity of radical formation can be reached with given irradiation, and that the sinks (i.e. self-decomposition and photolysis) of BMPO-organic-radical adducts become important beyond 1 hour of reaction.

5.4.3 Total peroxide fractions

Given the lability of organic hydroperoxides under photolysis, we performed total peroxide measurements for isoprene, α -pinene and toluene SOA as shown in Figure 5.4. The peroxide fractions in the original extracts are $101 \pm 16\%$, $47 \pm 29\%$ and $21 \pm 5\%$ for isoprene, α -pinene and toluene SOA, respectively, as consistent with our recent study.²⁰⁴ Under dark conditions, we observed significant decrease ($\sim 40\%$ for α -pinene and toluene SOA) in peroxide fraction over 75 min, which is consistent with the labile

nature of organic peroxides in aqueous phase.¹²¹ Upon irradiation, the peroxide fractions further decrease to $52\pm24\%$, $18\pm9\%$ and $5.1\pm1.7\%$ for isoprene, α -pinene and toluene SOA, respectively, equivalent to 50 – 75% decrease from the total peroxide fractions in the original extracts. The photoinduced decomposition of ROOH leads to simultaneous formation of RO^\bullet with $^\bullet OH$.²⁹⁸ In addition, Bateman et al.¹⁵⁹ discussed analogous fission of O-O bond in more complexed organic peroxides ($ROOR'$) forming two RO^\bullet radicals, although no direct measurement has been conducted for such organic radical formation. RO^\bullet can undergo rapid isomerization or β -scission to generate R^\bullet ,²²¹ which potentially explains the dominant R^\bullet formation over RO^\bullet as shown in Figure 5.2(a)-(d). However, the organic radicals formed under dark conditions (Figure 18(e)-(h)) are extremely low compared to irradiated samples, despite that the total peroxides already decompose to some extent (up to 40%) without irradiation. Therefore, photoinduced decomposition of peroxides may not be the sole source of organic radicals observed in this study.

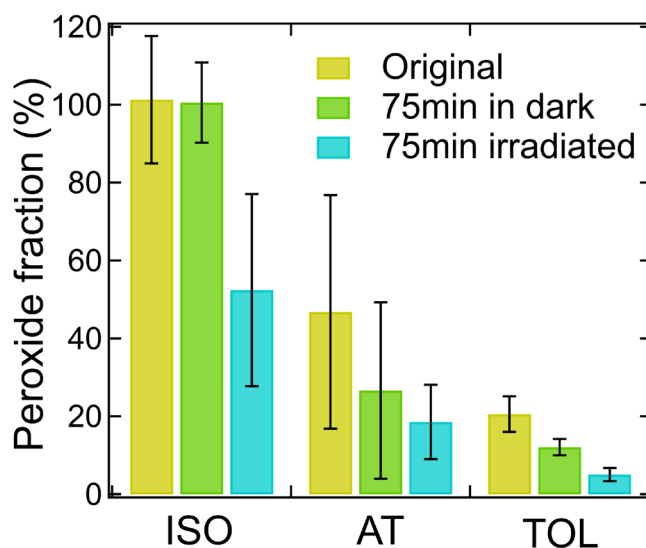


Figure 5.4. Total peroxide molar fractions from isoprene (ISO), α -pinene (AT) and toluene (TOL) SOA in original extracts, 75 min under dark conditions and 75 min under UV-Vis irradiation. The error bars represent the error propagation from the two duplicates in peroxide measurements with the uncertainty in SOA mass measurements.

5.4.4 Composition of organic radicals

Understanding the chemical identity of the observed organic radicals can be pivotal to unravelling their formation mechanisms. Thus, we applied HR-MS to elucidate the atomic composition of BMPO-organic-radical adducts. Figure 5.5 shows the comparison of ESI (+) mass spectra of α -pinene SOA with 10 mM BMPO under irradiated and dark conditions. Note the ESI-MS was operated at positive ion mode which more sensitive to BMPO and its radical adducts than negative ion mode. As SOA were generated under NO_x -free conditions, any analyte containing nitrogen should be BMPO ($\text{C}_{10}\text{H}_{17}\text{O}_3\text{N}$) or its radical adducts. Besides the original form, we identify that BMPO also appears in a fragmented form: $\text{C}_6\text{H}_9\text{O}_3\text{N}$. Considering the structure of BMPO, the fragmentation should take place on the *tert*-butyl group, removing a C_4H_8 group. Such fragmentation may result from both the in-situ EPR irradiation and ionization source of the HR-MS. Overall, the irradiated sample shows highly distinct spectrum compared to the dark sample with an apparent shift toward larger molar mass molecules, likely due to the trapping of organic radicals by BMPO and its fragment. The difference is particularly prominent in the neutral mass range of 300 – 400.

By subtracting the chemical formulas of BMPO and its fragments, we can obtain the composition of organic radicals as labeled in Figure 5.5 for some major peaks. For example, the organic radicals at neutral mass 357.185 and 387.195 are found to have the composition of $\text{C}_7\text{H}_{11}\text{O}_4$ and $\text{C}_8\text{H}_{13}\text{O}_5$, respectively. Based on the degree of unsaturation and number of O atoms, $\text{C}_7\text{H}_{11}\text{O}_4$ is predicted to contain 3 carbonyl groups and 1 hydroxy/ether group, whereas $\text{C}_8\text{H}_{13}\text{O}_5$ should contain 3 carbonyl groups and 2 hydroxy/ether groups. If these BMPO-radical adducts contain ether groups, it is probable that they are in the form of alkoxy radicals trapped by BMPO (BMPO-OR), given that ether groups are unlikely to be present in the monomers ($\text{C} \leq 10$) of monoterpene $\cdot\text{OH}$ oxidation products.⁵³ If these BMPO-radical adducts do not contain ether groups, instead they should be alkyl radicals trapped by BMPO (BMPO-R), with multiple carbonyl/carboxylate groups. Regardless of the types of organic radicals ($\text{RO}\cdot$ or $\text{R}\cdot$), $\text{C}_7\text{H}_{11}\text{O}_4$ and $\text{C}_8\text{H}_{13}\text{O}_5$ both contain 3 carbonyl groups, indicating that carbonyls could remain intact under the photolysis, or they can be formed through the conversion from $\text{RO}\cdot$ to $\text{R}\cdot$ (β -scission).²²¹ To test such hypothesis, future studies

should characterize photolytic ROS formation from model compounds with carbonyls and organic peroxides. The comparison between model compounds and SOA may provide critical insights into the mechanisms of photoinduced organic radical formation. It should be noted that current information from HR-MS is still limited, and the mechanisms discussed above are largely based on speculation. Future advances in isomer-resolved HR-MS techniques could be essential to better understand the nature of the organic radicals, and subsequently their formation mechanisms.

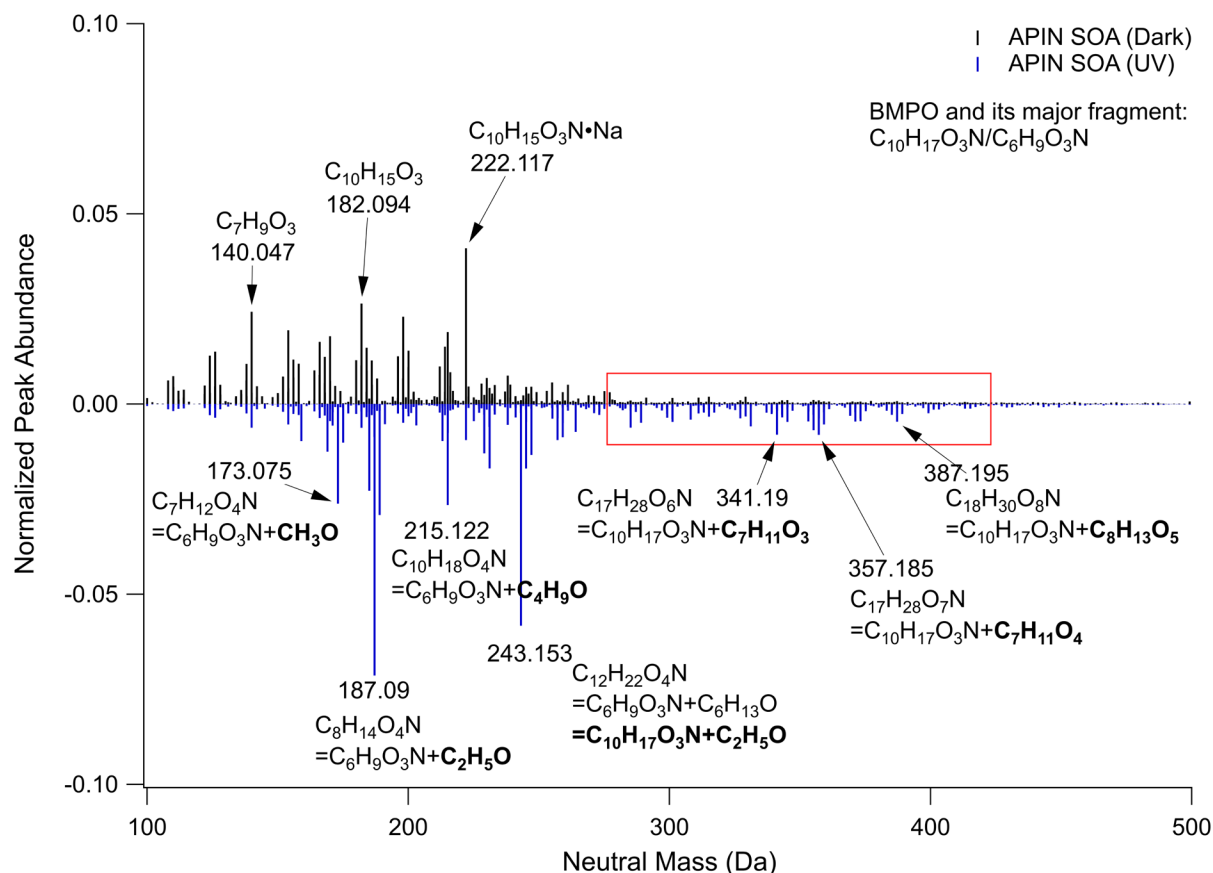


Figure 5.5. High-resolution ESI (+) mass spectra of α -pinene SOA with 10 mM BMPO under irradiated (blue) and dark (black) conditions. The peaks are normalized to the combined peak abundance. The dark condition data are inverted for comparison.

5.5 Conclusions

In this preliminary study, we combined an *in-situ* UV-Vis irradiation system with EPR to characterize the photolytic formation of ROS from laboratory-generated SOA. Substantial organic radical

formation is observed upon irradiation, with enhancement factors up to ~ 100 compared to dark conditions. Using total peroxide measurement, we show that organic peroxides can be an important source of the observed organic radicals, although additional sources may be necessary to fully account for the significant enhancement. High-resolution mass spectrometry elucidates the chemical composition of the organic radicals, indicating that photolysis of carbonyls or peroxides could be important to account for the organic radical formation. Further compositional studies are still necessary to fully understand the underlying mechanism of organic radical formation from photolysis of SOA.

Chapter 6: Conclusions, Limitations and Outlook

6.1 Conclusions

In this dissertation, we characterized ROS formation from aqueous reactions of SOA alone, SOA in reaction media with different pH, SOA with transition metals and lung antioxidants, as well as SOA under photolysis. Experimental evidence and model simulations reveal that organic (hydro)peroxides play a central role in aqueous ROS formation from SOA involving other redox-active components. This dissertation successfully establishes the superoxide formation mechanisms from biogenic SOA: ROOH can decompose under room temperature to form $\bullet\text{OH}$ which generate $\text{O}_2^{\bullet-}$ through subsequent mechanisms. Acidity can significantly alter the ROS formation patterns from SOA: neutral pH favors $\bullet\text{OH}$ and organic radical formation due to decomposition of organic (hydro)peroxides; acidic conditions favor $\text{O}_2^{\bullet-}$ and H_2O_2 formation due to enhanced quinone redox cycling and decomposition of α -hydroxyhydroperoxides. We observed substantial organic radical formation from Fe^{2+} -facilitated decomposition of organic peroxides. Through interactions among SOA, Fe^{2+} and antioxidants, we elucidated the reciprocal role of antioxidants to effectively scavenge $\bullet\text{OH}$ and $\text{O}_2^{\bullet-}$ while amplifying organic radical formation. Finally, we showed substantial formation of organic radicals from photoirradiation of SOA, which can be partially due to photolytic decomposition of organic peroxides. Overall, our work highlights the significant role of organic (hydro)peroxides when assessing the ROS formation capacity, which has implications on the health effects of SOA. Our findings also provide mechanistic insights into the chemical transformation of SOA involving oxidants in the atmosphere as well as under physiological conditions after respiratory deposition.

In Chapter 2, we demonstrate dominant formation of $\text{O}_2^{\bullet-}$ with molar yields of 0.01 – 0.03% from aqueous reactions of biogenic SOA generated by $\bullet\text{OH}$ photooxidation of isoprene, β -pinene, α -terpineol, and d-limonene. Meanwhile, biogenic SOA from dark ozonolysis primarily generate $\bullet\text{OH}$ via aqueous decomposition of ROOH, while $\text{O}_2^{\bullet-}$ only contributes to a minor fraction of total radical formation. The temporal evolution of $\bullet\text{OH}$ and $\text{O}_2^{\bullet-}$ formation is elucidated by kinetic modeling with a cascade of aqueous

reactions including the decomposition of ROOH, $\bullet\text{OH}$ oxidation of primary or secondary alcohols, and unimolecular decomposition of α -hydroxyperoxyl radicals. Relative yields of various types of ROS reflect relative abundance of organic hydroperoxides and alcohols contained in SOA, which can be significantly affected by oxidation pathways and different precursors. In Chapter 3, by applying the EPR spin-trapping technique and the Diogenes chemiluminescence assay, we find highly distinct radical yields and composition at different pH in the range of 1 – 7.4 from SOA generated by oxidation of isoprene, α -terpineol, α -pinene, β -pinene, toluene and naphthalene. We observe that isoprene SOA have substantial $\bullet\text{OH}$ and organic radical yields at neutral pH, which are 1.5 – 2 times higher compared to acidic conditions in total radical yields. Superoxide is found to be the dominant species generated by all types of SOA at lower pH. Further experiments with model compounds show that the decomposition of organic peroxide leading to radical formation may be suppressed at lower pH due to acid-catalyzed rearrangement of peroxides. We also observe 1.5 – 3 times higher molar yields of hydrogen peroxide in acidic conditions compared to neutral pH by biogenic and aromatic SOA, likely due to enhanced decomposition of α -hydroxyhydroperoxides and quinone redox cycling, respectively.

In Chapter 4, we demonstrate substantial formation of organic radicals in surrogate lung fluid by mixtures of Fe^{2+} and SOA generated from photooxidation of isoprene, α -terpineol and toluene. The molar yields of organic radicals by SOA are measured to be 0.03 – 0.5% in SLF, which are 5 – 10 times higher than in water. We observe that Fe^{2+} enhances organic radical yields dramatically by a factor of 20 – 80, which can be attributed to Fe^{2+} -facilitated decomposition of organic peroxides, in consistency with a positive correlation between peroxide contents and organic radical yields. Ascorbate mediates redox cycling of iron ions to sustain organic peroxide decomposition, as supported by kinetic modeling reproducing time- and concentration-dependence of organic radical formation as well as additional experiments observing the formation of Fe^{2+} and ascorbate radicals in mixtures of ascorbate and Fe^{3+} . $\bullet\text{OH}$ and superoxide are found to be scavenged by antioxidants efficiently. Therefore, we conclude a reciprocal role of antioxidants in scavenging $\bullet\text{OH}$ and $\text{O}_2\bullet$ efficiently, while amplifying organic radical formation. In Chapter 5, we

combined an *in-situ* UV-Vis irradiation system with EPR to characterize the photolytic formation of ROS from laboratory-generated SOA. We observed substantial organic radical formation upon irradiation, with enhancement factors up to ~ 100 compared to dark conditions. Total peroxide measurement reveals that organic peroxides can be an important source of the observed organic radicals, although additional sources may be necessary to fully account for the significant enhancement. High-resolution mass spectrometry elucidates the chemical composition of the organic radicals, which can be essential to understand the formation mechanisms. This study provides a first characterization of photolytic ROS formation from SOA involving different radical species and have significant implications in the photoinduced aqueous chemistry of SOA.

6.2 Contributions to co-authored papers

In addition to the first-authored papers mentioned in this dissertation, I have also contributed to three other co-authored papers. The first paper is “Environmentally Persistent Free Radicals, Reactive Oxygen Species Generation, and Oxidative Potential of Highway PM_{2.5}” by Hwang et al.³⁰³ published in *ACS Earth & Space Chemistry* in 2021. I contributed to roadside sampling of ambient PM using high volume sampler and MOUDI impactor, as well as data analysis and manuscript preparation. The second paper is “Cellular Superoxide Release Overwhelms Chemistry upon Lung Deposition of Particulate Matter” by Fang et al. which is currently under review. I contributed to SOA sampling, O₂^{•-} measurement from aqueous reactions of SOA, kinetic modeling for chemically generated O₂^{•-}, as well as data analysis and manuscript preparation. The third paper is “Nitrogen oxide influences on the production of reactive oxygen species from alpha-pinene and naphthalene secondary organic aerosols” by Edwards et al. which is currently in preparation. I contributed to SOA sampling, data analysis and manuscript preparation.

6.3 Limitations and Outlook

6.3.1 Complex nature of SOA

This work underscores the central role of organic peroxides in ROS formation including $\bullet\text{OH}$, $\text{O}_2\bullet^-$ and organic radicals through aqueous reactions involving transition metals, lung antioxidants and reactions media with different pH. Experimental evidence, along with kinetic modeling, provide insights into the reaction mechanisms and kinetic information of radical formation from SOA. However, it is still challenging to fully understand the ROS formation mechanisms due to the complex nature of SOA. In our kinetic model, a major assumption is that the reaction rate coefficients do not vary with the structures of R groups in ROOH , $\text{R}_1\text{R}_2\text{CHOH}$ and other compounds. Such assumption could be an oversimplification which induces uncertainty in model simulation, particularly when R groups contain other reactive functionalities such as aldehydes.

In addition, despite the similar results as obtained from model peroxide and quinone compounds in ROS formation with SOA, some differences are nontrivial and should be discussed. For example, the radical formation from commercially available organic peroxides and Fe^{2+} in water (Figure 4.2 (a), (c) and (e)) does not resemble that from SOA with Fe^{2+} in water (Figure 4.1 (a)), which is dominated by $\bullet\text{OH}$ radical formation. The EPR spectra in Figure 4.2 (a), (c) and (e) are still not fully resolved, indicating the presence of more complex radicals other than $\bullet\text{OH}$, $\text{O}_2\bullet^-$, $\text{R}\bullet$ and $\text{RO}\bullet$. Meanwhile, Figure 3.5 (a) and (b) show almost negligible radical formation from cumene and *tert*-butyl hydroperoxides in acidic conditions. Although suppressed at lower pH, isoprene and α -terpineol SOA still show noticeable amounts of radical formation (Figure 3.2 (a) and (b), 1/3 to 1/2 compared to neutral pH). This indicates the stronger capacity of SOA-contained peroxides at lower pH to induce radical formation compared to cumene and *tert*-butyl hydroperoxides. Furthermore, the toluene and naphthalene SOA (Figure 3.2 (e) and (f)) can generate $\text{O}_2\bullet^-$ in acidic conditions, while 5H-1,4-NQ alone does not lead to $\text{O}_2\bullet^-$ formation above detection limit but requires the assistance of ascorbate (Figure 3.5 (c)). Finally, no appropriate model compounds have been identified to represent the exclusive $\text{R}\bullet$ formation from α -terpineol SOA (Figure 3.2 (b)), and the suppressed

radical formation at neutral pH for α -pinene and β -pinene SOA (Figure 3.2 (c) and (d)). Therefore, these inconsistencies highlight the discrepancies between model compounds and SOA functionalities in reaction patterns and rates.

Given these discrepancies, further studies are encouraged to explore potential candidates of model compounds that can better represent the ROS formation patterns from SOA. The interaction among different functionalities should be considered, as well as different structures in adjacent R groups of these functionalities. Such advances may also provide valuable input to kinetic modeling, where the rate coefficients can be varied depending on the R structures to optimize the model. Besides OFR-generated SOA, SOA from environmental chambers or ambient should also be investigated for ROS formation, as no such comparison has been made for SOA generated by different tools. It is also highly recommended that future studies should attempt to directly link the ROS formation to the chemical composition and functional groups of SOA. Such studies should find it useful to employ chromatographic and mass spectrometric techniques. Zhao et al.³⁰⁴ and Yao et al.³⁰⁵ have recently developed isomer-resolved identification method of organic peroxides in monoterpene SOA using iodometry-assisted LC-MS. Advances in such techniques can be pivotal to bridge the chemical identities and ROS formation from SOA, considering the central role of organic peroxides.

6.3.2 Future directions in photolytic ROS formation of SOA

Chapter 4 presented the preliminary results of photolytic ROS formation of SOA. Despite the measurements in peroxide fractions and characterization with HR-MS, the sources of organic radical formation are still not well understood. Besides organic peroxides, the photolytic fission of carbonyl compounds is a potential source of organic (carbonyl and alkyl) radicals.¹⁵⁹ Thus, future studies are warranted to investigate the photolytic radical formation from model compounds such as organic peroxides and carbonyl compounds. Again, these experiments can be critical to connect the chemical composition and photochemical ROS formation from SOA.

6.3.3 Connecting exogenous ROS to endogenous ROS

This dissertation establishes a fundamental framework of ROS formation mechanisms including $\bullet\text{OH}$, $\text{O}_2\bullet^-$, and organic radicals from aqueous reactions of SOA. Upon inhalation and respiratory deposition of SOA and other redox-active PM components like transition metals, they may induce ROS formation in ELF through chemical reactions, which is considered as exogenous ROS. Meanwhile, another important mechanism of oxidative stress is through endogenous ROS formation, known as cell-released ROS when exposed to redox-active PM components.³⁰⁶ Such mechanisms include the activation of macrophages, mitochondria and ROS-producing enzymes like NADPH-oxidase.^{175, 176, 307} Therefore, understanding the relative importance of exogenous versus endogenous ROS is a pivotal step to link chemically generated ROS to the health effects of SOA. However, very limited studies have investigated this topic, which warrants future studies to bridge the gap between exogenous ROS and cellular oxidative stress.

In addition to experiments, kinetic modeling can be an alternative tool to predict exogenous ROS formation. Lakey et al.¹⁰¹ developed a kinetic multi-layer model of surface and bulk chemistry in the epithelial lining fluid (KM-SUB-ELF) to predict ROS concentrations resulting from redox-active PM components such as quinones and transition metals. Implementing the ROS formation mechanisms from SOA in this dissertation can potentially enhance the applicability of KM-SUB-ELF. In chapter 4, we demonstrate that $\bullet\text{OH}$ and $\text{O}_2\bullet^-$ can be efficiently scavenged by antioxidants, whereas organic radicals are relatively long-lived. These mechanisms and kinetic information can also be adopted to KM-SUB-ELF. The potential effects of organic radical in lipid peroxidation can be investigated by including reactions between organic radicals and phospholipids in ELF in the model. More experimental studies are encouraged to provide insights in such mechanisms and their applicability in KM-SUB-ELF.

References

1. Ezzati, M.; Lopez, A. D.; Rodgers, A.; Vander Hoorn, S.; Murray, C. J. L., Selected major risk factors and global and regional burden of disease. *The Lancet* **2002**, *360*, (9343), 1347-1360.
2. Kampa, M.; Castanas, E., Human health effects of air pollution. *Environmental Pollution* **2008**, *151*, (2), 362-367.
3. Hime, N. J.; Marks, G. B.; Cowie, C. T., A Comparison of the Health Effects of Ambient Particulate Matter Air Pollution from Five Emission Sources. *Int J Env Res Pub He* **2018**, *15*, (6).
4. Cohen, A. J.; Ross Anderson, H.; Ostro, B.; Pandey, K. D.; Krzyzanowski, M.; Künzli, N.; Gutschmidt, K.; Pope, A.; Romieu, I.; Samet, J. M.; Smith, K., The Global Burden of Disease Due to Outdoor Air Pollution. *Journal of Toxicology and Environmental Health, Part A* **2005**, *68*, (13-14), 1301-1307.
5. Kelly, F. J.; Fussell, J. C., Size, source and chemical composition as determinants of toxicity attributable to ambient particulate matter. *Atmospheric Environment* **2012**, *60*, 504-526.
6. Pandis, S. N.; Harley, R. A.; Cass, G. R.; Seinfeld, J. H., Secondary organic aerosol formation and transport. *Atmospheric Environment. Part A. General Topics* **1992**, *26*, (13), 2269-2282.
7. Shrivastava, M.; Cappa, C. D.; Fan, J. W.; Goldstein, A. H.; Guenther, A. B.; Jimenez, J. L.; Kuang, C.; Laskin, A.; Martin, S. T.; Ng, N. L.; Petaja, T.; Pierce, J. R.; Rasch, P. J.; Roldin, P.; Seinfeld, J. H.; Shilling, J.; Smith, J. N.; Thornton, J. A.; Volkamer, R.; Wang, J.; Worsnop, D. R.; Zaveri, R. A.; Zelenyuk, A.; Zhang, Q., Recent advances in understanding secondary organic aerosol: Implications for global climate forcing. *Rev Geophys* **2017**, *55*, (2), 509-559.
8. Shiraiwa, M.; Ueda, K.; Pozzer, A.; Lammel, G.; Kampf, C. J.; Fushimi, A.; Enami, S.; Arangio, A. M.; Frohlich-Nowoisky, J.; Fujitani, Y.; Furuyama, A.; Lakey, P. S. J.; Lelieveld, J.; Lucas, K.; Morino, Y.; Poschl, U.; Takaharna, S.; Takami, A.; Tong, H. J.; Weber, B.; Yoshino, A.; Sato, K., Aerosol Health Effects from Molecular to Global Scales. *Environ Sci Technol* **2017**, *51*, (23), 13545-13567.
9. Jimenez, J. L.; Canagaratna, M. R.; Donahue, N. M.; Prevot, A. S. H.; Zhang, Q.; Kroll, J. H.; DeCarlo, P. F.; Allan, J. D.; Coe, H.; Ng, N. L.; Aiken, A. C.; Docherty, K. S.; Ulbrich, I. M.; Grieshop, A. P.; Robinson, A. L.; Duplissy, J.; Smith, J. D.; Wilson, K. R.; Lanz, V. A.; Hueglin, C.; Sun, Y. L.; Tian, J.; Laaksonen, A.; Raatikainen, T.; Rautiainen, J.; Vaattovaara, P.; Ehn, M.; Kulmala, M.; Tomlinson, J. M.; Collins, D. R.; Cubison, M. J.; Dunlea, E. J.; Huffman, J. A.; Onasch, T. B.; Alfarra, M. R.; Williams, P. I.; Bower, K.; Kondo, Y.; Schneider, J.; Drewnick, F.; Borrmann, S.; Weimer, S.; Demerjian, K.; Salcedo, D.; Cottrell, L.; Griffin, R.; Takami, A.; Miyoshi, T.; Hatakeyama, S.; Shimono, A.; Sun, J. Y.; Zhang, Y. M.; Dzepina, K.; Kimmel, J. R.; Sueper, D.; Jayne, J. T.; Herndon, S. C.; Trimborn, A. M.; Williams, L. R.; Wood, E. C.; Middlebrook, A. M.; Kolb, C. E.; Baltensperger, U.; Worsnop, D. R., Evolution of Organic Aerosols in the Atmosphere. *Science* **2009**, *326*, (5959), 1525-1529.
10. Zhang, Q.; Jimenez, J. L.; Worsnop, D. R.; Canagaratna, M., A Case Study of Urban Particle Acidity and Its Influence on Secondary Organic Aerosol. *Environ Sci Technol* **2007**, *41*, (9), 3213-3219.
11. De Gouw, J.; Jimenez, J. L., Organic Aerosols in the Earth's Atmosphere. *Environ Sci Technol* **2009**, *43*, (20), 7614-7618.
12. Ziemann, P. J.; Atkinson, R., Kinetics, products, and mechanisms of secondary organic aerosol formation. *Chemical Society Reviews* **2012**, *41*, (19), 6582-6605.
13. Atkinson, R.; Arey, J., Atmospheric Degradation of Volatile Organic Compounds. *Chem Rev* **2003**, *103*, (12), 4605-4638.
14. Piccot, S. D.; Watson, J. J.; Jones, J. W., A global inventory of volatile organic compound emissions from anthropogenic sources. *Journal of Geophysical Research: Atmospheres* **1992**, *97*, (D9), 9897-9912.
15. Guenther, A. B.; Jiang, X.; Heald, C. L.; Sakulyanontvittaya, T.; Duhl, T.; Emmons, L. K.; Wang, X., The Model of Emissions of Gases and Aerosols from Nature version 2.1 (MEGAN2.1): an extended and updated framework for modeling biogenic emissions. *Geosci Model Dev* **2012**, *5*, (6), 1471-1492.
16. Guenther, A.; Hewitt, C. N.; Erickson, D.; Fall, R.; Geron, C.; Graedel, T.; Harley, P.; Klinger, L.; Lerdau, M.; McKay, W. A.; Pierce, T.; Scholes, B.; Steinbrecher, R.; Tallamraju, R.; Taylor, J.;

Zimmerman, P., A global model of natural volatile organic compound emissions. *Journal of Geophysical Research: Atmospheres* **1995**, *100*, (D5), 8873-8892.

17. Kanakidou, M.; Seinfeld, J. H.; Pandis, S. N.; Barnes, I.; Dentener, F. J.; Facchini, M. C.; Van Dingenen, R.; Ervens, B.; Nenes, A.; Nielsen, C. J.; Swietlicki, E.; Putaud, J. P.; Balkanski, Y.; Fuzzi, S.; Horth, J.; Moortgat, G. K.; Winterhalter, R.; Myhre, C. E. L.; Tsigaridis, K.; Vignati, E.; Stephanou, E. G.; Wilson, J., Organic aerosol and global climate modelling: a review. *Atmos. Chem. Phys.* **2005**, *5*, (4), 1053-1123.

18. Cruz, C. N.; Pandis, S. N., A study of the ability of pure secondary organic aerosol to act as cloud condensation nuclei. *Atmospheric Environment* **1997**, *31*, (15), 2205-2214.

19. Zhang, H. F.; Yee, L. D.; Lee, B. H.; Curtis, M. P.; Worton, D. R.; Isaacman-VanWertz, G.; Offenberg, J. H.; Lewandowski, M.; Kleindienst, T. E.; Beaver, M. R.; Holder, A. L.; Lonneman, W. A.; Docherty, K. S.; Jaoui, M.; Pye, H. O. T.; Hu, W. W.; Day, D. A.; Campuzano-Jost, P.; Jimenez, J. L.; Guo, H. Y.; Weber, R. J.; de Gouw, J.; Koss, A. R.; Edgerton, E. S.; Brune, W.; Mohr, C.; Lopez-Hilfiker, F. D.; Lutz, A.; Kreisberg, N. M.; Spielman, S. R.; Hering, S. V.; Wilson, K. R.; Thornton, J. A.; Goldstein, A. H., Monoterpenes are the largest source of summertime organic aerosol in the southeastern United States. *P Natl Acad Sci USA* **2018**, *115*, (9), 2038-2043.

20. Sartelet, K. N.; Couvidat, F.; Seigneur, C.; Roustan, Y., Impact of biogenic emissions on air quality over Europe and North America. *Atmospheric Environment* **2012**, *53*, 131-141.

21. Chen, Q.; Farmer, D. K.; Schneider, J.; Zorn, S. R.; Heald, C. L.; Karl, T. G.; Guenther, A.; Allan, J. D.; Robinson, N.; Coe, H.; Kimmel, J. R.; Pauliquevis, T.; Borrmann, S.; Pöschl, U.; Andreae, M. O.; Artaxo, P.; Jimenez, J. L.; Martin, S. T., Mass spectral characterization of submicron biogenic organic particles in the Amazon Basin. *Geophys Res Lett* **2009**, *36*, (20).

22. Shrivastava, M.; Andreae, M. O.; Artaxo, P.; Barbosa, H. M. J.; Berg, L. K.; Brito, J.; Ching, J.; Easter, R. C.; Fan, J.; Fast, J. D.; Feng, Z.; Fuentes, J. D.; Glasius, M.; Goldstein, A. H.; Alves, E. G.; Gomes, H.; Gu, D.; Guenther, A.; Jathar, S. H.; Kim, S.; Liu, Y.; Lou, S.; Martin, S. T.; McNeill, V. F.; Medeiros, A.; de Sá, S. S.; Shilling, J. E.; Springston, S. R.; Souza, R. A. F.; Thornton, J. A.; Isaacman-VanWertz, G.; Yee, L. D.; Ynoue, R.; Zaveri, R. A.; Zelenyuk, A.; Zhao, C., Urban pollution greatly enhances formation of natural aerosols over the Amazon rainforest. *Nat Commun* **2019**, *10*, (1), 1046.

23. Tuet, W. Y.; Chen, Y. L.; Xu, L.; Fok, S.; Gao, D.; Weber, R. J.; Ng, N. L., Chemical oxidative potential of secondary organic aerosol (SOA) generated from the photooxidation of biogenic and anthropogenic volatile organic compounds. *Atmos Chem Phys* **2017**, *17*, (2), 839-853.

24. Tuet, W. Y.; Chen, Y.; Fok, S.; Champion, J. A.; Ng, N. L., Inflammatory responses to secondary organic aerosols (SOA) generated from biogenic and anthropogenic precursors. *Atmos. Chem. Phys.* **2017**, *17*, (18), 11423-11440.

25. Baltensperger, U.; Dommen, J.; Alfarra, M. R.; Duplissy, J.; Gaeggeler, K.; Metzger, A.; Facchini, M. C.; Decesari, S.; Finessi, E.; Reinnig, C.; Schott, M.; Warnke, J.; Hoffmann, T.; Klatzer, B.; Puxbaum, H.; Geiser, M.; Savi, M.; Lang, D.; Kalberer, M.; Geiser, T., Combined Determination of the Chemical Composition and of Health Effects of Secondary Organic Aerosols: The POLYSOA Project. *J Aerosol Med Pulm D* **2008**, *21*, (1), 145-154.

26. Tong, H.; Arangio, A. M.; Lakey, P. S. J.; Berkemeier, T.; Liu, F. B.; Kampf, C. J.; Brune, W. H.; Poschl, U.; Shiraiwa, M., Hydroxyl radicals from secondary organic aerosol decomposition in water. *Atmos Chem Phys* **2016**, *16*, (3), 1761-1771.

27. Tuet, W. Y.; Chen, Y.; Fok, S.; Gao, D.; Weber, R. J.; Champion, J. A.; Ng, N. L., Chemical and cellular oxidant production induced by naphthalene secondary organic aerosol (SOA): effect of redox-active metals and photochemical aging. *Scientific Reports* **2017**, *7*, (1), 15157.

28. Brown, S. S.; Stutz, J., Nighttime radical observations and chemistry. *Chemical Society Reviews* **2012**, *41*, (19), 6405-6447.

29. Riva, M.; Budisulistiorini, S. H.; Zhang, Z.; Gold, A.; Surratt, J. D., Chemical characterization of secondary organic aerosol constituents from isoprene ozonolysis in the presence of acidic aerosol. *Atmospheric Environment* **2016**, *130*, 5-13.

30. Wennberg, P. O.; Bates, K. H.; Crounse, J. D.; Dodson, L. G.; McVay, R. C.; Mertens, L. A.; Nguyen, T. B.; Praske, E.; Schwantes, R. H.; Smarte, M. D.; St Clair, J. M.; Teng, A. P.; Zhang, X.; Seinfeld, J. H., Gas-Phase Reactions of Isoprene and Its Major Oxidation Products. *Chem Rev* **2018**, *118*, (7), 3337-3390.
31. Koch, S.; Winterhalter, R.; Uherek, E.; Kolloff, A.; Neeb, P.; Moortgat, G. K., Formation of new particles in the gas-phase ozonolysis of monoterpenes. *Atmospheric Environment* **2000**, *34*, (23), 4031-4042.
32. Larsen, B. R.; Di Bella, D.; Glasius, M.; Winterhalter, R.; Jensen, N. R.; Hjorth, J., Gas-Phase OH Oxidation of Monoterpenes: Gaseous and Particulate Products. *J Atmos Chem* **2001**, *38*, (3), 231-276.
33. Bonn, B.; Moortgat, G. K., Sesquiterpene ozonolysis: Origin of atmospheric new particle formation from biogenic hydrocarbons. *Geophys Res Lett* **2003**, *30*, (11).
34. Fu, P.; Kawamura, K.; Chen, J.; Barrie, L. A., Isoprene, Monoterpene, and Sesquiterpene Oxidation Products in the High Arctic Aerosols during Late Winter to Early Summer. *Environ Sci Technol* **2009**, *43*, (11), 4022-4028.
35. Ji, Y.; Zhao, J.; Terazono, H.; Misawa, K.; Levitt Nicholas, P.; Li, Y.; Lin, Y.; Peng, J.; Wang, Y.; Duan, L.; Pan, B.; Zhang, F.; Feng, X.; An, T.; Marrero-Ortiz, W.; Secrest, J.; Zhang Annie, L.; Shibuya, K.; Molina Mario, J.; Zhang, R., Reassessing the atmospheric oxidation mechanism of toluene. *Proceedings of the National Academy of Sciences* **2017**, *114*, (31), 8169-8174.
36. Chan, A. W. H.; Kautzman, K. E.; Chhabra, P. S.; Surratt, J. D.; Chan, M. N.; Crounse, J. D.; Kürten, A.; Wennberg, P. O.; Flagan, R. C.; Seinfeld, J. H., Secondary organic aerosol formation from photooxidation of naphthalene and alkylnaphthalenes: implications for oxidation of intermediate volatility organic compounds (IVOCs). *Atmos. Chem. Phys.* **2009**, *9*, (9), 3049-3060.
37. Kroll, J. H.; Lim, C. Y.; Kessler, S. H.; Wilson, K. R., Heterogeneous Oxidation of Atmospheric Organic Aerosol: Kinetics of Changes to the Amount and Oxidation State of Particle-Phase Organic Carbon. *The Journal of Physical Chemistry A* **2015**, *119*, (44), 10767-10783.
38. Varutbangkul, V.; Brechtel, F. J.; Bahreini, R.; Ng, N. L.; Keywood, M. D.; Kroll, J. H.; Flagan, R. C.; Seinfeld, J. H.; Lee, A.; Goldstein, A. H., Hygroscopicity of secondary organic aerosols formed by oxidation of cycloalkenes, monoterpenes, sesquiterpenes, and related compounds. *Atmos. Chem. Phys.* **2006**, *6*, (9), 2367-2388.
39. Lambe, A. T.; Onasch, T. B.; Massoli, P.; Croasdale, D. R.; Wright, J. P.; Ahern, A. T.; Williams, L. R.; Worsnop, D. R.; Brune, W. H.; Davidovits, P., Laboratory studies of the chemical composition and cloud condensation nuclei (CCN) activity of secondary organic aerosol (SOA) and oxidized primary organic aerosol (OPOA). *Atmos. Chem. Phys.* **2011**, *11*, (17), 8913-8928.
40. DeRieux, W. S. W.; Li, Y.; Lin, P.; Laskin, J.; Laskin, A.; Bertram, A. K.; Nizkorodov, S. A.; Shiraiwa, M., Predicting the glass transition temperature and viscosity of secondary organic material using molecular composition. *Atmos. Chem. Phys.* **2018**, *18*, (9), 6331-6351.
41. Lambe, A. T.; Cappa, C. D.; Massoli, P.; Onasch, T. B.; Forestieri, S. D.; Martin, A. T.; Cummings, M. J.; Croasdale, D. R.; Brune, W. H.; Worsnop, D. R.; Davidovits, P., Relationship between Oxidation Level and Optical Properties of Secondary Organic Aerosol. *Environ Sci Technol* **2013**, *47*, (12), 6349-6357.
42. Haagen-Smit, A. J., Chemistry and physiology of Los Angeles smog. *Industrial & Engineering Chemistry* **1952**, *44*, (6), 1342-1346.
43. Atkinson, R., Kinetics and mechanisms of the gas-phase reactions of the hydroxyl radical with organic compounds under atmospheric conditions. *Chem Rev* **1986**, *86*, (1), 69-201.
44. Cocker, D. R.; Flagan, R. C.; Seinfeld, J. H., State-of-the-Art Chamber Facility for Studying Atmospheric Aerosol Chemistry. *Environ Sci Technol* **2001**, *35*, (12), 2594-2601.
45. Carter, W. P. L.; Cocker, D. R.; Fitz, D. R.; Malkina, I. L.; Bumiller, K.; Sauer, C. G.; Pisano, J. T.; Bufalino, C.; Song, C., A new environmental chamber for evaluation of gas-phase chemical mechanisms and secondary aerosol formation. *Atmospheric Environment* **2005**, *39*, (40), 7768-7788.

46. Liu, X.; Day, D. A.; Krechmer, J. E.; Brown, W.; Peng, Z.; Ziemann, P. J.; Jimenez, J. L., Direct measurements of semi-volatile organic compound dynamics show near-unity mass accommodation coefficients for diverse aerosols. *Communications Chemistry* **2019**, *2*, (1), 98.
47. Wang, J.; Doussin, J. F.; Perrier, S.; Perraudin, E.; Katrib, Y.; Pangui, E.; Picquet-Varrault, B., Design of a new multi-phase experimental simulation chamber for atmospheric photosmog, aerosol and cloud chemistry research. *Atmos. Meas. Tech.* **2011**, *4*, (11), 2465-2494.
48. Kirkby, J.; Curtius, J.; Almeida, J.; Dunne, E.; Duplissy, J.; Ehrhart, S.; Franchin, A.; Gagné, S.; Ickes, L.; Kürten, A.; Kupc, A.; Metzger, A.; Riccobono, F.; Rondo, L.; Schobesberger, S.; Tsagkogeorgas, G.; Wimmer, D.; Amorim, A.; Bianchi, F.; Breitenlechner, M.; David, A.; Dommen, J.; Downard, A.; Ehn, M.; Flagan, R. C.; Haider, S.; Hansel, A.; Hauser, D.; Jud, W.; Junninen, H.; Kreissl, F.; Kvashin, A.; Laaksonen, A.; Lehtipalo, K.; Lima, J.; Lovejoy, E. R.; Makhmurov, V.; Mathot, S.; Mikkilä, J.; Minginette, P.; Mogo, S.; Nieminen, T.; Onnela, A.; Pereira, P.; Petäjä, T.; Schnitzhofer, R.; Seinfeld, J. H.; Sipilä, M.; Stozhkov, Y.; Stratmann, F.; Tomé, A.; Vanhanen, J.; Viisanen, Y.; Vrtala, A.; Wagner, P. E.; Walther, H.; Weingartner, E.; Wex, H.; Winkler, P. M.; Carslaw, K. S.; Worsnop, D. R.; Baltensperger, U.; Kulmala, M., Role of sulphuric acid, ammonia and galactic cosmic rays in atmospheric aerosol nucleation. *Nature* **2011**, *476*, (7361), 429-433.
49. Möhler, O.; Stetzer, O.; Schaeffers, S.; Linke, C.; Schnaiter, M.; Tiede, R.; Saathoff, H.; Krämer, M.; Mangold, A.; Budz, P.; Zink, P.; Schreiner, J.; Mauersberger, K.; Haag, W.; Kärcher, B.; Schurath, U., Experimental investigation of homogeneous freezing of sulphuric acid particles in the aerosol chamber AIDA. *Atmos. Chem. Phys.* **2003**, *3*, (1), 211-223.
50. Mao, J.; Ren, X.; Brune, W. H.; Olson, J. R.; Crawford, J. H.; Fried, A.; Huey, L. G.; Cohen, R. C.; Heikes, B.; Singh, H. B.; Blake, D. R.; Sachse, G. W.; Diskin, G. S.; Hall, S. R.; Shetter, R. E., Airborne measurement of OH reactivity during INTEX-B. *Atmos. Chem. Phys.* **2009**, *9*, (1), 163-173.
51. Peng, Z.; Jimenez, J. L., Radical chemistry in oxidation flow reactors for atmospheric chemistry research. *Chemical Society Reviews* **2020**.
52. Matsunaga, A.; Ziemann, P. J., Gas-Wall Partitioning of Organic Compounds in a Teflon Film Chamber and Potential Effects on Reaction Product and Aerosol Yield Measurements. *Aerosol Science and Technology* **2010**, *44*, (10), 881-892.
53. Zhang, X.; McVay Renee, C.; Huang Dan, D.; Dalleska Nathan, F.; Aumont, B.; Flagan Richard, C.; Seinfeld John, H., Formation and evolution of molecular products in α -pinene secondary organic aerosol. *Proceedings of the National Academy of Sciences* **2015**, *112*, (46), 14168-14173.
54. St. Clair, J. M.; Rivera-Rios, J. C.; Crounse, J. D.; Praske, E.; Kim, M. J.; Wolfe, G. M.; Keutsch, F. N.; Wennberg, P. O.; Hanisco, T. F., Investigation of a potential HCHO measurement artifact from ISOPOOH. *Atmos. Meas. Tech.* **2016**, *9*, (9), 4561-4568.
55. McMurry, P. H.; Grosjean, D., Gas and aerosol wall losses in Teflon film smog chambers. *Environ Sci Technol* **1985**, *19*, (12), 1176-1182.
56. Bones, D. L.; Henricksen, D. K.; Mang, S. A.; Gonsior, M.; Bateman, A. P.; Nguyen, T. B.; Cooper, W. J.; Nizkorodov, S. A., Appearance of strong absorbers and fluorophores in limonene-O₃ secondary organic aerosol due to NH₄⁺-mediated chemical aging over long time scales. *Journal of Geophysical Research: Atmospheres* **2010**, *115*, (D5).
57. George, I. J.; Vlasenko, A.; Slowik, J. G.; Broekhuizen, K.; Abbatt, J. P. D., Heterogeneous oxidation of saturated organic aerosols by hydroxyl radicals: uptake kinetics, condensed-phase products, and particle size change. *Atmos. Chem. Phys.* **2007**, *7*, (16), 4187-4201.
58. Kang, E.; Root, M. J.; Toohey, D. W.; Brune, W. H., Introducing the concept of Potential Aerosol Mass (PAM). *Atmos. Chem. Phys.* **2007**, *7*, (22), 5727-5744.
59. Kang, E.; Toohey, D. W.; Brune, W. H., Dependence of SOA oxidation on organic aerosol mass concentration and OH exposure: experimental PAM chamber studies. *Atmos Chem Phys* **2011**, *11*, (4), 1837-1852.
60. Brune, W. H., The Chamber Wall Index for Gas-Wall Interactions in Atmospheric Environmental Enclosures. *Environ Sci Technol* **2019**, *53*, (7), 3645-3652.

61. Palm, B. B.; Campuzano-Jost, P.; Ortega, A. M.; Day, D. A.; Kaser, L.; Jud, W.; Karl, T.; Hansel, A.; Hunter, J. F.; Cross, E. S.; Kroll, J. H.; Peng, Z.; Brune, W. H.; Jimenez, J. L., In situ secondary organic aerosol formation from ambient pine forest air using an oxidation flow reactor. *Atmos. Chem. Phys.* **2016**, *16*, (5), 2943-2970.
62. Ortega, A. M.; Hayes, P. L.; Peng, Z.; Palm, B. B.; Hu, W. W.; Day, D. A.; Li, R.; Cubison, M. J.; Brune, W. H.; Graus, M.; Warneke, C.; Gilman, J. B.; Kuster, W. C.; de Gouw, J.; Gutierrez-Montes, C.; Jimenez, J. L., Real-time measurements of secondary organic aerosol formation and aging from ambient air in an oxidation flow reactor in the Los Angeles area. *Atmos Chem Phys* **2016**, *16*, (11), 7411-7433.
63. Nault, B. A.; Campuzano-Jost, P.; Day, D. A.; Schroder, J. C.; Anderson, B.; Beyersdorf, A. J.; Blake, D. R.; Brune, W. H.; Choi, Y.; Corr, C. A.; de Gouw, J. A.; Dibb, J.; DiGangi, J. P.; Diskin, G. S.; Fried, A.; Huey, L. G.; Kim, M. J.; Knote, C. J.; Lamb, K. D.; Lee, T.; Park, T.; Pusede, S. E.; Scheuer, E.; Thornhill, K. L.; Woo, J. H.; Jimenez, J. L., Secondary organic aerosol production from local emissions dominates the organic aerosol budget over Seoul, South Korea, during KORUS-AQ. *Atmos. Chem. Phys.* **2018**, *18*, (24), 17769-17800.
64. Tkacik, D. S.; Lambe, A. T.; Jathar, S.; Li, X.; Presto, A. A.; Zhao, Y.; Blake, D.; Meinardi, S.; Jayne, J. T.; Croteau, P. L.; Robinson, A. L., Secondary Organic Aerosol Formation from in-Use Motor Vehicle Emissions Using a Potential Aerosol Mass Reactor. *Environ Sci Technol* **2014**, *48*, (19), 11235-11242.
65. Watne, Å. K.; Psychoudaki, M.; Ljungström, E.; Le Breton, M.; Hallquist, M.; Jerksjö, M.; Fallgren, H.; Jutterström, S.; Hallquist, Å. M., Fresh and Oxidized Emissions from In-Use Transit Buses Running on Diesel, Biodiesel, and CNG. *Environ Sci Technol* **2018**, *52*, (14), 7720-7728.
66. Lambe, A. T.; Chhabra, P. S.; Onasch, T. B.; Brune, W. H.; Hunter, J. F.; Kroll, J. H.; Cummings, M. J.; Brogan, J. F.; Parmar, Y.; Worsnop, D. R.; Kolb, C. E.; Davidovits, P., Effect of oxidant concentration, exposure time, and seed particles on secondary organic aerosol chemical composition and yield. *Atmos Chem Phys* **2015**, *15*, (6), 3063-3075.
67. Lambe, A. T.; Ahern, A. T.; Williams, L. R.; Slowik, J. G.; Wong, J. P. S.; Abbatt, J. P. D.; Brune, W. H.; Ng, N. L.; Wright, J. P.; Croasdale, D. R.; Worsnop, D. R.; Davidovits, P.; Onasch, T. B., Characterization of aerosol photooxidation flow reactors: heterogeneous oxidation, secondary organic aerosol formation and cloud condensation nuclei activity measurements. *Atmos. Meas. Tech.* **2011**, *4*, (3), 445-461.
68. Peng, Z.; Jimenez, J. L., Radical chemistry in oxidation flow reactors for atmospheric chemistry research. *Chem. Soc. Rev.* **2020**, *49*, (9), 2570-2616.
69. Burkholder, J.; Sander, S.; Abbatt, J.; Barker, J.; Cappa, C.; Crounse, J.; Dibble, T.; Huie, R.; Kolb, C.; Kurylo, M. *Chemical kinetics and photochemical data for use in atmospheric studies; evaluation number 19*; Pasadena, CA: Jet Propulsion Laboratory, National Aeronautics and Space ...: 2020.
70. Schlesinger, R. B.; Kunzli, N.; Hidy, G. M.; Gotschi, T.; Jerrett, M., The Health Relevance of Ambient Particulate Matter Characteristics: Coherence of Toxicological and Epidemiological Inferences. *Inhal Toxicol* **2006**, *18*, (2), 95-125.
71. Du, Y.; Xu, X.; Chu, M.; Guo, Y.; Wang, J., Air particulate matter and cardiovascular disease: the epidemiological, biomedical and clinical evidence. *J Thorac Dis* **2016**, *8*, (1), E8-E19.
72. Schwarze, P. E.; Øvreivik, J.; Låg, M.; Refsnes, M.; Nafstad, P.; Hetland, R. B.; Dybing, E., Particulate matter properties and health effects: consistency of epidemiological and toxicological studies. *Human & Experimental Toxicology* **2006**, *25*, (10), 559-579.
73. Peters, A., Particulate matter and heart disease: Evidence from epidemiological studies. *Toxicology and Applied Pharmacology* **2005**, *207*, (2, Supplement), 477-482.
74. Chowdhury, S.; Pozzer, A.; Haines, A.; Klingmüller, K.; Münzel, T.; Paasonen, P.; Sharma, A.; Venkataraman, C.; Lelieveld, J., Global health burden of ambient PM_{2.5} and the contribution of anthropogenic black carbon and organic aerosols. *Environment International* **2022**, *159*, 107020.
75. Pye, H. O. T.; Ward-Caviness, C. K.; Murphy, B. N.; Appel, K. W.; Seltzer, K. M., Secondary organic aerosol association with cardiorespiratory disease mortality in the United States. *Nat Commun* **2021**, *12*, (1), 7215.

76. McDonald, J. D.; Doyle-Eisele, M.; Campen, M. J.; Seagrave, J.; Holmes, T.; Lund, A.; Surratt, J. D.; Seinfeld, J. H.; Rohr, A. C.; Knipping, E. M., Cardiopulmonary response to inhalation of biogenic secondary organic aerosol. *Inhal Toxicol* **2010**, *22*, (3), 253-265.
77. McDonald, J. D.; Doyle-Eisele, M.; Kracko, D.; Lund, A.; Surratt, J. D.; Hersey, S. P.; Seinfeld, J. H.; Rohr, A. C.; Knipping, E. M., Cardiopulmonary response to inhalation of secondary organic aerosol derived from gas-phase oxidation of toluene. *Inhal Toxicol* **2012**, *24*, (11), 689-697.
78. Lund, A. K.; Doyle-Eisele, M.; Lin, Y.-H.; Arashiro, M.; Surratt, J. D.; Holmes, T.; Schilling, K. A.; Seinfeld, J. H.; Rohr, A. C.; Knipping, E. M.; McDonald, J. D., The effects of α -pinene versus toluene-derived secondary organic aerosol exposure on the expression of markers associated with vascular disease. *Inhal Toxicol* **2013**, *25*, (6), 309-324.
79. Win-Shwe, T.-T.; Fujitani, Y.; Kyi-Tha-Thu, C.; Furuyama, A.; Michikawa, T.; Tsukahara, S.; Nitta, H.; Hirano, S., Effects of Diesel Engine Exhaust Origin Secondary Organic Aerosols on Novel Object Recognition Ability and Maternal Behavior in BALB/C Mice. *Int J Env Res Pub He* **2014**, *11*, (11).
80. Win-Shwe, T.-T.; Kyi-Tha-Thu, C.; Moe, Y.; Fujitani, Y.; Tsukahara, S.; Hirano, S., Exposure of BALB/c Mice to Diesel Engine Exhaust Origin Secondary Organic Aerosol (DE-SOA) during the Developmental Stages Impairs the Social Behavior in Adult Life of the Males. *Frontiers in Neuroscience* **2016**, *9*.
81. Lin, Y.-H.; Arashiro, M.; Martin, E.; Chen, Y.; Zhang, Z.; Sexton, K. G.; Gold, A.; Jaspers, I.; Fry, R. C.; Surratt, J. D., Isoprene-Derived Secondary Organic Aerosol Induces the Expression of Oxidative Stress Response Genes in Human Lung Cells. *Environmental Science & Technology Letters* **2016**, *3*, (6), 250-254.
82. Eaves, L. A.; Smeester, L.; Hartwell, H. J.; Lin, Y.-H.; Arashiro, M.; Zhang, Z.; Gold, A.; Surratt, J. D.; Fry, R. C., Isoprene-Derived Secondary Organic Aerosol Induces the Expression of MicroRNAs Associated with Inflammatory/Oxidative Stress Response in Lung Cells. *Chemical Research in Toxicology* **2020**, *33*, (2), 381-387.
83. Khan, F.; Kwapiszewska, K.; Zhang, Y.; Chen, Y.; Lambe, A. T.; Kołodziejczyk, A.; Jalal, N.; Rudzinski, K.; Martínez-Romero, A.; Fry, R. C.; Surratt, J. D.; Szmigielski, R., Toxicological Responses of α -Pinene-Derived Secondary Organic Aerosol and Its Molecular Tracers in Human Lung Cell Lines. *Chemical Research in Toxicology* **2021**, *34*, (3), 817-832.
84. Ito, T.; Bekki, K.; Fujitani, Y.; Hirano, S., The toxicological analysis of secondary organic aerosol in human lung epithelial cells and macrophages. *Environmental Science and Pollution Research* **2019**, *26*, (22), 22747-22755.
85. Leni, Z.; Cassagnes, L. E.; Daellenbach, K. R.; El Haddad, I.; Vlachou, A.; Uzu, G.; Prévôt, A. S. H.; Jaffrezo, J.-L.; Baumlin, N.; Salathe, M.; Baltensperger, U.; Dommen, J.; Geiser, M., Oxidative stress-induced inflammation in susceptible airways by anthropogenic aerosol. *Plos One* **2020**, *15*, (11), e0233425.
86. Bates, J. T.; Fang, T.; Verma, V.; Zeng, L.; Weber, R. J.; Tolbert, P. E.; Abrams, J. Y.; Sarnat, S. E.; Klein, M.; Mulholland, J. A.; Russell, A. G., Review of Acellular Assays of Ambient Particulate Matter Oxidative Potential: Methods and Relationships with Composition, Sources, and Health Effects. *Environ Sci Technol* **2019**, *53*, (8), 4003-4019.
87. Cho, A. K.; Sioutas, C.; Miguel, A. H.; Kumagai, Y.; Schmitz, D. A.; Singh, M.; Eiguren-Fernandez, A.; Froines, J. R., Redox activity of airborne particulate matter at different sites in the Los Angeles Basin. *Environmental Research* **2005**, *99*, (1), 40-47.
88. Verma, V.; Ning, Z.; Cho, A. K.; Schauer, J. J.; Shafer, M. M.; Sioutas, C., Redox activity of urban quasi-ultrafine particles from primary and secondary sources. *Atmospheric Environment* **2009**, *43*, (40), 6360-6368.
89. Strak, M.; Janssen Nicole, A. H.; Godri Krystal, J.; Gosens, I.; Mudway Ian, S.; Cassee Flemming, R.; Lebre, E.; Kelly Frank, J.; Harrison Roy, M.; Brunekreef, B.; Steenhof, M.; Hoek, G., Respiratory Health Effects of Airborne Particulate Matter: The Role of Particle Size, Composition, and Oxidative Potential—The RAPTES Project. *Environ Health Persp* **2012**, *120*, (8), 1183-1189.
90. Daellenbach, K. R.; Uzu, G.; Jiang, J.; Cassagnes, L.-E.; Leni, Z.; Vlachou, A.; Stefanelli, G.; Canonaco, F.; Weber, S.; Segers, A.; Kuenen, J. J. P.; Schaap, M.; Favez, O.; Albinet, A.; Aksoyoglu, S.;

- Dommen, J.; Baltensperger, U.; Geiser, M.; El Haddad, I.; Jaffrezo, J.-L.; Prévôt, A. S. H., Sources of particulate-matter air pollution and its oxidative potential in Europe. *Nature* **2020**, 587, (7834), 414-419.
91. Kramer, A. J.; Rattanavaraha, W.; Zhang, Z.; Gold, A.; Surratt, J. D.; Lin, Y.-H., Assessing the oxidative potential of isoprene-derived epoxides and secondary organic aerosol. *Atmospheric Environment* **2016**, 130, 211-218.
 92. Jiang, H.; Jang, M., Dynamic Oxidative Potential of Atmospheric Organic Aerosol under Ambient Sunlight. *Environ Sci Technol* **2018**, 52, (13), 7496-7504.
 93. Jiang, H.; Jang, M.; Sabo-Attwood, T.; Robinson, S. E., Oxidative potential of secondary organic aerosols produced from photooxidation of different hydrocarbons using outdoor chamber under ambient sunlight. *Atmospheric Environment* **2016**, 131, 382-389.
 94. Wang, S.; Ye, J.; Soong, R.; Wu, B.; Yu, L.; Simpson, A. J.; Chan, A. W. H., Relationship between chemical composition and oxidative potential of secondary organic aerosol from polycyclic aromatic hydrocarbons. *Atmos. Chem. Phys.* **2018**, 18, (6), 3987-4003.
 95. Liu, F.; Saavedra, M. G.; Champion, J. A.; Griendling, K. K.; Ng, N. L., Prominent Contribution of Hydrogen Peroxide to Intracellular Reactive Oxygen Species Generated upon Exposure to Naphthalene Secondary Organic Aerosols. *Environmental Science & Technology Letters* **2020**, 7, (3), 171-177.
 96. Zhang, Z. H.; Hartner, E.; Uttinger, B.; Gfeller, B.; Paul, A.; Sklorz, M.; Czech, H.; Yang, B. X.; Su, X. Y.; Jakobi, G.; Orasche, J.; Schnelle-Kreis, J.; Jeong, S.; Gröger, T.; Pardo, M.; Hohaus, T.; Adam, T.; Kiendler-Scharr, A.; Rudich, Y.; Zimmermann, R.; Kalberer, M., Are reactive oxygen species (ROS) a suitable metric to predict toxicity of carbonaceous aerosol particles? *Atmos. Chem. Phys.* **2022**, 22, (3), 1793-1809.
 97. Dellinger, B.; Pryor, W. A.; Cueto, R.; Squadrito, G. L.; Hegde, V.; Deutsch, W. A., Role of Free Radicals in the Toxicity of Airborne Fine Particulate Matter. *Chemical Research in Toxicology* **2001**, 14, (10), 1371-1377.
 98. Tong, H.; Lakey, P. S. J.; Arangio, A. M.; Socorro, J.; Shen, F. X.; Lucas, K.; Brune, W. H.; Poschl, U.; Shiraiwa, M., Reactive Oxygen Species Formed by Secondary Organic Aerosols in Water and Surrogate Lung Fluid. *Environ Sci Technol* **2018**, 52, (20), 11642-11651.
 99. Chowdhury, P. H.; He, Q. F.; Carmieli, R.; Li, C. L.; Rudich, Y.; Pardo, M., Connecting the Oxidative Potential of Secondary Organic Aerosols with Reactive Oxygen Species in Exposed Lung Cells. *Environ Sci Technol* **2019**, 53, (23), 13949-13958.
 100. Wang, S.; Takhar, M.; Zhao, Y.; Al Rashdi, L. N. S.; Chan, A. W. H., Dynamic Oxidative Potential of Organic Aerosol from Heated Cooking Oil. *Acs Earth Space Chem* **2021**, 5, (5), 1150-1162.
 101. Lakey, P. S.; Berkemeier, T.; Tong, H.; Arangio, A. M.; Lucas, K.; Poschl, U.; Shiraiwa, M., Chemical exposure-response relationship between air pollutants and reactive oxygen species in the human respiratory tract. *Sci Rep* **2016**, 6, 32916.
 102. Gligorovski, S.; Strekowski, R.; Barbati, S.; Vione, D., Environmental Implications of Hydroxyl Radicals ($\bullet\text{OH}$). *Chem Rev* **2015**, 115, (24), 13051-13092.
 103. Halliwell, B.; Gutteridge, J. M., Formation of a thiobarbituric-acid-reactive substance from deoxyribose in the presence of iron salts: the role of superoxide and hydroxyl radicals. *FEBS letters* **1981**, 128, (2), 347-352.
 104. Balasubramanian, B.; Pogozelski Wendy, K.; Tullius Thomas, D., DNA strand breaking by the hydroxyl radical is governed by the accessible surface areas of the hydrogen atoms of the DNA backbone. *Proceedings of the National Academy of Sciences* **1998**, 95, (17), 9738-9743.
 105. Ni, Y.; Zhao, B.; Hou, J.; Xin, W., Preventive effect of Ginkgo biloba extract on apoptosis in rat cerebellar neuronal cells induced by hydroxyl radicals. *Neuroscience Letters* **1996**, 214, (2), 115-118.
 106. Baek, S. M.; Kwon, C. H.; Kim, J. H.; Woo, J. S.; Jung, J. S.; Kim, Y. K., Differential roles of hydrogen peroxide and hydroxyl radical in cisplatin-induced cell death in renal proximal tubular epithelial cells. *Journal of Laboratory and Clinical Medicine* **2003**, 142, (3), 178-186.
 107. Kroll, J. H.; Seinfeld, J. H., Chemistry of secondary organic aerosol: Formation and evolution of low-volatility organics in the atmosphere. *Atmospheric Environment* **2008**, 42, (16), 3593-3624.

108. Bianchi, F.; Kurten, T.; Riva, M.; Mohr, C.; Rissanen, M. P.; Roldin, P.; Berndt, T.; Crounse, J. D.; Wennberg, P. O.; Mentel, T. F.; Wildt, J.; Junninen, H.; Jokinen, T.; Kulmala, M.; Worsnop, D. R.; Thornton, J. A.; Donahue, N.; Kjaergaard, H. G.; Ehn, M., Highly Oxygenated Organic Molecules (HOM) from Gas-Phase Autoxidation Involving Peroxy Radicals: A Key Contributor to Atmospheric Aerosol. *Chem Rev* **2019**, *119*, (6), 3472-3509.
109. Ehn, M.; Thornton, J. A.; Kleist, E.; Sipila, M.; Junninen, H.; Pullinen, I.; Springer, M.; Rubach, F.; Tillmann, R.; Lee, B.; Lopez-Hilfiker, F.; Andres, S.; Acir, I. H.; Rissanen, M.; Jokinen, T.; Schobesberger, S.; Kangasluoma, J.; Kontkanen, J.; Nieminen, T.; Kurten, T.; Nielsen, L. B.; Jorgensen, S.; Kjaergaard, H. G.; Canagaratna, M.; Dal Maso, M.; Berndt, T.; Petaja, T.; Wahner, A.; Kerminen, V. M.; Kulmala, M.; Worsnop, D. R.; Wildt, J.; Mentel, T. F., A large source of low-volatility secondary organic aerosol. *Nature* **2014**, *506*, (7489), 476-479.
110. Nel, A., Air pollution-related illness: Effects of particles. *Science* **2005**, *308*, (5723), 804-806.
111. Lakey, P. S. J.; Berkemeier, T.; Tong, H. J.; Arangio, A. M.; Lucas, K.; Poschl, U.; Shiraiwa, M., Chemical exposure-response relationship between air pollutants and reactive oxygen species in the human respiratory tract. *Scientific Reports* **2016**, *6*, 1-6.
112. McCord, J. M., The evolution of free radicals and oxidative stress. *Am J Med* **2000**, *108*, (8), 652-659.
113. Hayyan, M.; Hashim, M. A.; AlNashef, I. M., Superoxide Ion: Generation and Chemical Implications. *Chem Rev* **2016**, *116*, (5), 3029-3085.
114. Charrier, J. G.; Anastasio, C., Rates of Hydroxyl Radical Production from Transition Metals and Quinones in a Surrogate Lung Fluid. *Environ Sci Technol* **2015**, *49*, (15), 9317-9325.
115. Buettner, G. R., The Pecking Order of Free Radicals and Antioxidants: Lipid Peroxidation, α -Tocopherol, and Ascorbate. *Archives of Biochemistry and Biophysics* **1993**, *300*, (2), 535-543.
116. Yin, H.; Xu, L.; Porter, N. A., Free Radical Lipid Peroxidation: Mechanisms and Analysis. *Chemical Reviews* **2011**, *111*, (10), 5944-5972.
117. Wikipedia Electron paramagnetic resonance. https://en.wikipedia.org/wiki/Electron_paramagnetic_resonance (5/26),
118. Pöschl, U.; Martin, S. T.; Sinha, B.; Chen, Q.; Gunthe, S. S.; Huffman, J. A.; Borrmann, S.; Farmer, D. K.; Garland, R. M.; Helas, G.; Jimenez, J. L.; King, S. M.; Manzi, A.; Mikhailov, E.; Pauliquevis, T.; Petters, M. D.; Prenni, A. J.; Roldin, P.; Rose, D.; Schneider, J.; Su, H.; Zorn, S. R.; Artaxo, P.; Andreae, M. O., Rainforest aerosols as biogenic nuclei of clouds and precipitation in the Amazon. *Science* **2010**, *329*, (5998), 1513-1516.
119. Huang, R.-J.; Zhang, Y.; Bozzetti, C.; Ho, K.-F.; Cao, J.-J.; Han, Y.; Daellenbach, K. R.; Slowik, J. G.; Platt, S. M.; Canonaco, F.; Zotter, P.; Wolf, R.; Pieber, S. M.; Bruns, E. A.; Crippa, M.; Ciarelli, G.; Piazzalunga, A.; Schwikowski, M.; Abbaszade, G.; Schnelle-Kreis, J.; Zimmermann, R.; An, Z.; Szidat, S.; Baltensperger, U.; Haddad, I. E.; Prevot, A. S. H., High secondary aerosol contribution to particulate pollution during haze events in China. *Nature* **2014**, *514*, (7521), 218-222.
120. Carlton, A. G.; de Gouw, J.; Jimenez, J. L.; Ambrose, J. L.; Attwood, A. R.; Brown, S.; Baker, K. R.; Brock, C.; Cohen, R. C.; Edgerton, S.; Farkas, C. M.; Farmer, D.; Goldstein, A. H.; Gratz, L.; Guenther, A.; Hunt, S.; Jaeglé, L.; Jaffe, D. A.; Mak, J.; McClure, C.; Nenes, A.; Nguyen, T. K.; Pierce, J. R.; de Sa, S.; Selin, N. E.; Shah, V.; Shaw, S.; Shepson, P. B.; Song, S.; Stutz, J.; Surratt, J. D.; Turpin, B. J.; Warneke, C.; Washenfelder, R. A.; Wennberg, P. O.; Zhou, X., Synthesis of the Southeast Atmosphere Studies: Investigating Fundamental Atmospheric Chemistry Questions. *Bull. Amer. Meteorol. Soc.* **2018**, *99*, (3), 547-567.
121. Krapf, M.; El Haddad, I.; Bruns, E. A.; Molteni, U.; Daellenbach, K. R.; Prevot, A. S. H.; Baltensperger, U.; Dommen, J., Labile Peroxides in Secondary Organic Aerosol. *Chem-Us* **2016**, *1*, (4), 603-616.
122. Pospisilova, V.; Lopez-Hilfiker, F. D.; Bell, D. M.; El Haddad, I.; Mohr, C.; Huang, W.; Heikkinen, L.; Xiao, M.; Dommen, J.; Prevot, A. S. H.; Baltensperger, U.; Slowik, J. G., On the fate of oxygenated organic molecules in atmospheric aerosol particles. *Sci Adv* **2020**, *6*, (11), 1-11.

123. Ervens, B.; Turpin, B. J.; Weber, R. J., Secondary organic aerosol formation in cloud droplets and aqueous particles (aqSOA): a review of laboratory, field and model studies. *Atmos Chem Phys* **2011**, *11*, (21), 11069-11102.
124. Herrmann, H.; Schaefer, T.; Tilgner, A.; Styler, S. A.; Weller, C.; Teich, M.; Otto, T., Tropospheric Aqueous-Phase Chemistry: Kinetics, Mechanisms, and Its Coupling to a Changing Gas Phase. *Chem Rev* **2015**, *115*, (10), 4259-4334.
125. McNeill, V. F., Aqueous Organic Chemistry in the Atmosphere: Sources and Chemical Processing of Organic Aerosols. *Environ Sci Technol* **2015**, *49*, (3), 1237-1244.
126. Farmer, D. K.; Cappa, C. D.; Kreidenweis, S. M., Atmospheric Processes and Their Controlling Influence on Cloud Condensation Nuclei Activity. *Chem Rev* **2015**, *115*, (10), 4199-4217.
127. Laskin, A.; Laskin, J.; Nizkorodov, S. A., Chemistry of Atmospheric Brown Carbon. *Chem Rev* **2015**, *115*, (10), 4335-4382.
128. Poschl, U.; Shiraiwa, M., Multiphase Chemistry at the Atmosphere-Biosphere Interface Influencing Climate and Public Health in the Anthropocene. *Chem Rev* **2015**, *115*, (10), 4440-4475.
129. Wang, Y.; Kim, H.; Paulson, S. E., Hydrogen peroxide generation from α - and β -pinene and toluene secondary organic aerosols. *Atmospheric Environment* **2011**, *45*, (18), 3149-3156.
130. Gallimore, P. J.; Mahon, B. M.; Wragg, F. P. H.; Fuller, S. J.; Giorio, C.; Kourtchev, I.; Kalberer, M., Multiphase composition changes and reactive oxygen species formation during limonene oxidation in the new Cambridge Atmospheric Simulation Chamber (CASC). *Atmos Chem Phys* **2017**, *17*, (16), 9853-9868.
131. Paulson, S. E.; Gallimore, P. J.; Kuang, X. B. M.; Chen, J. R.; Kalberer, M.; Gonzalez, D. H., A light-driven burst of hydroxyl radicals dominates oxidation chemistry in newly activated cloud droplets. *Sci Adv* **2019**, *5*, (5), 1-7.
132. Tong, H. J.; Zhang, Y.; Filippi, A.; Wang, T.; Li, C. P.; Liu, F. B.; Leppla, D.; Kourtchev, I.; Wang, K.; Keskinen, H. M.; Levula, J. T.; Arangio, A. M.; Shen, F. X.; Ditas, F.; Martin, S. T.; Artaxo, P.; Godoi, R. H. M.; Yamamoto, C. I.; de Souza, R. A. F.; Huang, R. J.; Berkemeier, T.; Wang, Y. S.; Su, H.; Cheng, Y. F.; Pope, F. D.; Fu, P. Q.; Yao, M. S.; Pohlker, C.; Petaja, T.; Kulmala, M.; Andreae, M. O.; Shiraiwa, M.; Poschl, U.; Hoffmann, T.; Kalberer, M., Radical Formation by Fine Particulate Matter Associated with Highly Oxygenated Molecules. *Environ Sci Technol* **2019**, *53*, (21), 12506-12518.
133. Kaur, R.; Anastasio, C., Light absorption and the photoformation of hydroxyl radical and singlet oxygen in fog waters. *Atmos. Environ.* **2017**, *164*, (Supplement C), 387-397.
134. Manfrin, A.; Nizkorodov, S. A.; Malecha, K. T.; Getzinger, G. J.; McNeill, K.; Borduas-Dedekind, N., Reactive Oxygen Species Production from Secondary Organic Aerosols: The Importance of Singlet Oxygen. *Environ Sci Technol* **2019**, *53*, (15), 8553-8562.
135. McWhinney, R. D.; Zhou, S.; Abbatt, J. P. D., Naphthalene SOA: redox activity and naphthoquinone gas-particle partitioning. *Atmos. Chem. Phys.* **2013**, *13*, (19), 9731-9744.
136. Tong, H.; Lakey, P. S. J.; Arangio, A. M.; Socorro, J.; Kampf, C. J.; Berkemeier, T.; Brune, W. H.; Poschl, U.; Shiraiwa, M., Reactive oxygen species formed in aqueous mixtures of secondary organic aerosols and mineral dust influencing cloud chemistry and public health in the Anthropocene. *Faraday Discuss* **2017**, *200*, 251-270.
137. Fang, T.; Lakey, P. S. J.; Weber, R. J.; Shiraiwa, M., Oxidative Potential of Particulate Matter and Generation of Reactive Oxygen Species in Epithelial Lining Fluid. *Environ Sci Technol* **2019**, *53*, (21), 12784-12792.
138. Kelly, F. J., Oxidative stress: Its role in air pollution and adverse health effects. *Occup Environ Med* **2003**, *60*, (8), 612-616.
139. Wei, J.; Yu, H.; Wang, Y.; Verma, V., Complexation of Iron and Copper in Ambient Particulate Matter and Its Effect on the Oxidative Potential Measured in a Surrogate Lung Fluid. *Environ Sci Technol* **2019**, *53*, (3), 1661-1671.
140. Herrmann, H.; Tilgner, A.; Barzaghi, P.; Majdik, Z.; Gligorovski, S.; Poulain, L.; Monod, A., Towards a more detailed description of tropospheric aqueous phase organic chemistry: CAPRAM 3.0. *Atmospheric Environment* **2005**, *39*, (23-24), 4351-4363.

141. Bothe, E.; Schuchmann, M. N.; Schultefrohlinde, D.; Vonsonntag, C., HO₂ Elimination from Alpha-Hydroxyalkylperoxyl Radicals in Aqueous-Solution. *Photochem Photobiol* **1978**, *28*, (4-5), 639-644.
142. Berkemeier, T.; Ammann, M.; Krieger, U. K.; Peter, T.; Spichtinger, P.; Pschl, U.; Shiraiwa, M.; Huisman, A. J., Technical note: Monte Carlo genetic algorithm (MCGA) for model analysis of multiphase chemical kinetics to determine transport and reaction rate coefficients using multiple experimental data sets. *Atmos Chem Phys* **2017**, *17*, (12), 8021-8029.
143. Tresp, H.; Hammer, M. U.; Winter, J.; Weltmann, K. D.; Reuter, S., Quantitative detection of plasma-generated radicals in liquids by electron paramagnetic resonance spectroscopy. *Journal of Physics D: Applied Physics* **2013**, *46*, (43), 1-8.
144. Biller, J. R.; Tseitlin, M.; Mitchell, D. G.; Yu, Z.; Buchanan, L. A.; Elajaili, H.; Rosen, G. M.; Kao, J. P. Y.; Eaton, S. S.; Eaton, G. R., Improved Sensitivity for Imaging Spin Trapped Hydroxyl Radical at 250 MHz. *ChemPhysChem* **2015**, *16*, (3), 528-531.
145. Mitchell, D. G.; Rosen, G. M.; Tseitlin, M.; Symmes, B.; Eaton, S. S.; Eaton, G. R., Use of Rapid-Scan EPR to Improve Detection Sensitivity for Spin-Trapped Radicals. *Biophys J* **2013**, *105*, (2), 338-342.
146. Twahir, U. T.; Stedwell, C. N.; Lee, C. T.; Richards, N. G. J.; Polfer, N. C.; Angerhofer, A., Observation of superoxide production during catalysis of *Bacillus subtilis* oxalate decarboxylase at pH 4. *Free Radic Biol Med* **2015**, *80*, 59-66.
147. Hasson, A. S.; Ho, A. W.; Kuwata, K. T.; Paulson, S. E., Production of stabilized Criegee intermediates and peroxides in the gas phase ozonolysis of alkenes 2. Asymmetric and biogenic alkenes. *J Geophys Res-Atmos* **2001**, *106*, (D24), 34143-34153.
148. Qiu, J.; Liang, Z.; Tonokura, K.; Colussi, A. J.; Enami, S., Stability of Monoterpene-Derived α -Hydroxyalkyl-Hydroperoxides in Aqueous Organic Media: Relevance to the Fate of Hydroperoxides in Aerosol Particle Phases. *Environ Sci Technol* **2020**, *54*, (7), 3890-3899.
149. Docherty, K. S.; Wu, W.; Lim, Y. B.; Ziemann, P. J., Contributions of organic peroxides to secondary aerosol formed from reactions of monoterpenes with O₃. *Environ Sci Technol* **2005**, *39*, (11), 4049-4059.
150. Mertes, P.; Pfaffenberger, L.; Dommen, J.; Kalberer, M.; Baltensperger, U., Development of a sensitive long path absorption photometer to quantify peroxides in aerosol particles (Peroxide-LOPAP). *Atmos. Meas. Tech.* **2012**, *5*, (10), 2339-2348.
151. Epstein, S. A.; Blair, S. L.; Nizkorodov, S. A., Direct Photolysis of α -Pinene Ozonolysis Secondary Organic Aerosol: Effect on Particle Mass and Peroxide Content. *Environ Sci Technol* **2014**, *48*, (19), 11251-11258.
152. Badali, K. M.; Zhou, S.; Aljawhary, D.; Antiñolo, M.; Chen, W. J.; Lok, A.; Mungall, E.; Wong, J. P. S.; Zhao, R.; Abbatt, J. P. D., Formation of hydroxyl radicals from photolysis of secondary organic aerosol material. *Atmos. Chem. Phys.* **2015**, *15*, 7831-7840.
153. Chen, Q.; Liu, Y.; Donahue, N. M.; Shilling, J. E.; Martin, S. T., Particle-Phase Chemistry of Secondary Organic Material: Modeled Compared to Measured O:C and H:C Elemental Ratios Provide Constraints. *Environ Sci Technol* **2011**, *45*, (11), 4763-4770.
154. Tilgner, A.; Herrmann, H., Tropospheric Aqueous-Phase OH Oxidation Chemistry: Current Understanding, Uptake of Highly Oxidized Organics and Its Effects. In *Multiphase Environmental Chemistry in the Atmosphere*, American Chemical Society: 2018; Vol. 1299, pp 49-85.
155. Chevallier, E.; Jolibois, R. D.; Meunier, N.; Carlier, P.; Monod, A., "Fenton-like" reactions of methylhydroperoxide and ethylhydroperoxide with Fe²⁺ in liquid aerosols under tropospheric conditions. *Atmos. Environ.* **2004**, *38*, (6), 921-933.
156. Nam, W.; Han, H. J.; Oh, S.-Y.; Lee, Y. J.; Choi, M.-H.; Han, S.-Y.; Kim, C.; Woo, S. K.; Shin, W., New Insights into the Mechanisms of O-O Bond Cleavage of Hydrogen Peroxide and tert-Alkyl Hydroperoxides by Iron(III) Porphyrin Complexes. *J Am Chem Soc* **2000**, *122*, (36), 8677-8684.
157. Qiu, J.; Tonokura, K.; Enami, S., Proton-Catalyzed Decomposition of α -Hydroxyalkyl-Hydroperoxides in Water. *Environ Sci Technol* **2020**, *54*, (17), 10561-10569.

158. Nguyen, T. B.; Bateman, A. P.; Bones, D. L.; Nizkorodov, S. A.; Laskin, J.; Laskin, A., High-resolution mass spectrometry analysis of secondary organic aerosol generated by ozonolysis of isoprene. *Atmospheric Environment* **2010**, *44*, (8), 1032-1042.
159. Bateman, A. P.; Nizkorodov, S. A.; Laskin, J.; Laskin, A., Photolytic processing of secondary organic aerosols dissolved in cloud droplets. *Phys Chem Chem Phys* **2011**, *13*, (26), 12199-12212.
160. Fang, T.; Lakey, P. S. J.; Rivera-Rios, J. C.; Keutsch, F. N.; Shiraiwa, M., Aqueous-Phase Decomposition of Isoprene Hydroxy Hydroperoxide and Hydroxyl Radical Formation by Fenton-Like Reactions with Iron Ions. *J. Phys. Chem. A* **2020**, *124*, (25), 5230–5236.
161. Vereecken, L.; Francisco, J. S., Theoretical studies of atmospheric reaction mechanisms in the troposphere. *Chem. Soc. Rev.* **2012**, *41*, (19), 6259-6293.
162. Levis, D. H.; Van Ry, D. A.; Hinrichs, R. Z., Multiphase Ozonolysis of Aqueous α -Terpineol. *Environ Sci Technol* **2016**, *50*, (21), 11698-11705.
163. Kenseth, C. M.; Huang, Y.; Zhao, R.; Dalleska, N. F.; Hethcox, J. C.; Stoltz, B. M.; Seinfeld, J. H., Synergistic O₃ + OH oxidation pathway to extremely low-volatility dimers revealed in β -pinene secondary organic aerosol. *Proceedings of the National Academy of Sciences* **2018**, *115*, (33), 8301.
164. Zhang, X.; Lambe, A. T.; Upshur, M. A.; Brooks, W. A.; Gray Bé, A.; Thomson, R. J.; Geiger, F. M.; Surratt, J. D.; Zhang, Z.; Gold, A.; Graf, S.; Cubison, M. J.; Groessl, M.; Jayne, J. T.; Worsnop, D. R.; Canagaratna, M. R., Highly Oxygenated Multifunctional Compounds in α -Pinene Secondary Organic Aerosol. *Environ Sci Technol* **2017**, *51*, (11), 5932-5940.
165. Ehn, M.; Kleist, E.; Junninen, H.; Petaja, T.; Lonn, G.; Schobesberger, S.; Dal Maso, M.; Trimborn, A.; Kulmala, M.; Worsnop, D. R.; Wahner, A.; Wildt, J.; Mentel, T. F., Gas phase formation of extremely oxidized pinene reaction products in chamber and ambient air. *Atmos Chem Phys* **2012**, *12*, (11), 5113-5127.
166. Kirkby, J.; Duplissy, J.; Sengupta, K.; Frege, C.; Gordon, H.; Williamson, C.; Heinritzi, M.; Simon, M.; Yan, C.; Almeida, J.; Trostl, J.; Nieminen, T.; Ortega, I. K.; Wagner, R.; Adamov, A.; Amorim, A.; Bernhammer, A. K.; Bianchi, F.; Breitenlechner, M.; Brilke, S.; Chen, X. M.; Craven, J.; Dias, A.; Ehrhart, S.; Flagan, R. C.; Franchin, A.; Fuchs, C.; Guida, R.; Hakala, J.; Hoyle, C. R.; Jokinen, T.; Junninen, H.; Kangasluoma, J.; Kim, J.; Krapf, M.; Kurten, A.; Laaksonen, A.; Lehtipalo, K.; Makhmutov, V.; Mathot, S.; Molteni, U.; Onnela, A.; Perakyla, O.; Piel, F.; Petaja, T.; Praplan, A. P.; Pringle, K.; Rap, A.; Richards, N. A. D.; Riipinen, I.; Rissanen, M. P.; Rondo, L.; Sarnela, N.; Schobesberger, S.; Scott, C. E.; Seinfeld, J. H.; Sipila, M.; Steiner, G.; Stozhkov, Y.; Stratmann, F.; Tome, A.; Virtanen, A.; Vogel, A. L.; Wagner, A. C.; Wagner, P. E.; Weingartner, E.; Wimmer, D.; Winkler, P. M.; Ye, P. L.; Zhang, X.; Hansel, A.; Dommen, J.; Donahue, N. M.; Worsnop, D. R.; Baltensperger, U.; Kulmala, M.; Carslaw, K. S.; Curtius, J., Ion-induced nucleation of pure biogenic particles. *Nature* **2016**, *533*, (7604), 521-526.
167. Sauer, F.; Schafer, C.; Neeb, P.; Horie, O.; Moortgat, G. K., Formation of hydrogen peroxide in the ozonolysis of isoprene and simple alkenes under humid conditions. *Atmospheric Environment* **1999**, *33*, (2), 229-241.
168. Kumar, M.; Busch, D. H.; Subramaniam, B.; Thompson, W. H., Role of Tunable Acid Catalysis in Decomposition of α -Hydroxyalkyl Hydroperoxides and Mechanistic Implications for Tropospheric Chemistry. *J. Phys. Chem. A* **2014**, *118*, (41), 9701-9711.
169. Ziemann, P. J., Evidence for Low-Volatility Diacyl Peroxides as a Nucleating Agent and Major Component of Aerosol Formed from Reactions of O₃ with Cyclohexene and Homologous Compounds. *The Journal of Physical Chemistry A* **2002**, *106*, (17), 4390-4402.
170. Arakaki, T.; Anastasio, C.; Kuroki, Y.; Nakajima, H.; Okada, K.; Kotani, Y.; Handa, D.; Azechi, S.; Kimura, T.; Tshuhako, A.; Miyagi, Y., A General Scavenging Rate Constant for Reaction of Hydroxyl Radical with Organic Carbon in Atmospheric Waters. *Environ. Sci. Technol.* **2013**, *47*, (15), 8196-8203.
171. Nazaroff, W. W.; Weschler, C. J., Cleaning products and air fresheners: exposure to primary and secondary air pollutants. *Atmospheric Environment* **2004**, *38*, (18), 2841-2865.
172. Waring, M. S., Secondary organic aerosol in residences: predicting its fraction of fine particle mass and determinants of formation strength. *Indoor Air* **2014**, *24*, (4), 376-389.

173. McDonald, B. C.; de Gouw, J. A.; Gilman, J. B.; Jathar, S. H.; Akherati, A.; Cappa, C. D.; Jimenez, J. L.; Lee-Taylor, J.; Hayes, P. L.; McKeen, S. A.; Cui, Y. Y.; Kim, S.-W.; Gentner, D. R.; Isaacman-VanWertz, G.; Goldstein, A. H.; Harley, R. A.; Frost, G. J.; Roberts, J. M.; Ryerson, T. B.; Trainer, M., Volatile chemical products emerging as largest petrochemical source of urban organic emissions. *Science* **2018**, *359*, (6377), 760.
174. Kleinman, M. T.; Sioutas, C.; Chang, M. C.; Boere, A. J. F.; Cassee, F. R., Ambient fine and coarse particle suppression of alveolar macrophage functions. *Toxicol. Lett.* **2003**, *137*, (3), 151-158.
175. Becker, S.; Soukup, J. M.; Gilmour, M. I.; Devlin, R. B., Stimulation of Human and Rat Alveolar Macrophages by Urban Air Particulates: Effects on Oxidant Radical Generation and Cytokine Production. *Toxicology and Applied Pharmacology* **1996**, *141*, (2), 637-648.
176. Winterbourn, C. C., Reconciling the chemistry and biology of reactive oxygen species. *Nature Chem. Biol.* **2008**, *4*, (5), 278-286.
177. Arangio, A. M.; Slade, J. H.; Berkemeier, T.; Pöschl, U.; Knopf, D. A.; Shiraiwa, M., Multiphase Chemical Kinetics of OH Radical Uptake by Molecular Organic Markers of Biomass Burning Aerosols: Humidity and Temperature Dependence, Surface Reaction and Bulk Diffusion. *J. Phys. Chem. A* **2015**, *119*, (19), 4533-4544.
178. Marteau, C.; Ruyffelaere, F.; Aubry, J. M.; Penverne, C.; Favier, D.; Nardello-Rataj, V., Oxidative degradation of fragrant aldehydes. Autoxidation by molecular oxygen. *Tetrahedron* **2013**, *69*, (10), 2268-2275.
179. Denisov, E. T.; Afanas'ev, I. B., *Oxidation and antioxidants in organic chemistry and biology*. CRC press: 2005.
180. Buxton, G. V.; Greenstock, C. L.; Helman, W. P.; Ross, A. B., Critical-Review of Rate Constants for Reactions of Hydrated Electrons, Hydrogen-Atoms and Hydroxyl Radicals ($\cdot\text{OH}/\text{O}\cdot$) in Aqueous-Solution. *J Phys Chem Ref Data* **1988**, *17*, (2), 1-21.
181. Christensen, H.; Sehested, K.; Corfitzen, H., Reactions of Hydroxyl Radicals with Hydrogen-Peroxide at Ambient and Elevated-Temperatures. *J Phys Chem-Us* **1982**, *86*, (9), 1588-1590.
182. Sehested, K.; Rasmussen, O. L.; Fricke, H., Rate Constants of OH with HO_2 , $\text{O}_2\cdot$ and H_2O_2^+ from Hydrogen Peroxide Formation in Pulse-Irradiated Oxygenated Water. *J Phys Chem-Us* **1968**, *72*, (2), 626-631.
183. Rush, J. D.; Bielski, B. H. J., Pulse radiolytic studies of the reaction of perhydroxyl/superoxide $\text{O}_2\cdot$ with iron(II)/iron(III) ions. The reactivity of $\text{HO}_2/\text{O}_2\cdot$ with ferric ions and its implication on the occurrence of the Haber-Weiss reaction. *The Journal of Physical Chemistry* **1985**, *89*, (23), 5062-5066.
184. Koppenol, W. H.; Butler, J.; Leeuwen, J. W. v., THE HABER-WEISS CYCLE. *Photochem Photobiol* **1978**, *28*, (4-5), 655-658.
185. Thornton, J. A.; Jaeglé, L.; McNeill, V. F., Assessing known pathways for HO_2 loss in aqueous atmospheric aerosols: Regional and global impacts on tropospheric oxidants. *Journal of Geophysical Research: Atmospheres* **2008**, *113*, (D5), 1-15.
186. Guo, H.; Liu, J.; Froyd, K. D.; Roberts, J. M.; Veres, P. R.; Hayes, P. L.; Jimenez, J. L.; Nenes, A.; Weber, R. J., Fine particle pH and gas-particle phase partitioning of inorganic species in Pasadena, California, during the 2010 CalNex campaign. *Atmos. Chem. Phys.* **2017**, *17*, (9), 5703-5719.
187. Surratt, J. D.; Lewandowski, M.; Offenberg, J. H.; Jaoui, M.; Kleindienst, T. E.; Edney, E. O.; Seinfeld, J. H., Effect of acidity on secondary organic aerosol formation from isoprene. *Environ Sci Technol* **2007**, *41*, (15), 5363-5369.
188. Kerminen, V.-M.; Hillamo, R.; Teinilä, K.; Pakkanen, T.; Allegrini, I.; Sparapani, R., Ion balances of size-resolved tropospheric aerosol samples: implications for the acidity and atmospheric processing of aerosols. *Atmospheric Environment* **2001**, *35*, (31), 5255-5265.
189. Bougiatioti, A.; Nikolaou, P.; Stavroulas, I.; Kouvarakis, G.; Weber, R.; Nenes, A.; Kanakidou, M.; Mihalopoulos, N., Particle water and pH in the eastern Mediterranean: source variability and implications for nutrient availability. *Atmos. Chem. Phys.* **2016**, *16*, (7), 4579-4591.
190. Baker Alex, R.; Kanakidou, M.; Nenes, A.; Myriokefalitakis, S.; Croot Peter, L.; Duce Robert, A.; Gao, Y.; Guieu, C.; Ito, A.; Jickells Tim, D.; Mahowald Natalie, M.; Middag, R.; Perron Morgane, M. G.;

- Sarin Manmohan, M.; Shelley, R.; Turner David, R., Changing atmospheric acidity as a modulator of nutrient deposition and ocean biogeochemistry. *Sci Adv* **2021**, 7, (28), 1-9.
191. Nah, T.; Guo, H. Y.; Sullivan, A. P.; Chen, Y. L.; Tanner, D. J.; Nenes, A.; Russell, A.; Ng, N. L.; Huey, L. G.; Weber, R. J., Characterization of aerosol composition, aerosol acidity, and organic acid partitioning at an agriculturally intensive rural southeastern US site. *Atmos Chem Phys* **2018**, 18, (15), 11471-11491.
192. Weber, R. J.; Guo, H. Y.; Russell, A. G.; Nenes, A., High aerosol acidity despite declining atmospheric sulfate concentrations over the past 15 years. *Nat Geosci* **2016**, 9, (4), 282-286.
193. Ault, A. P., Aerosol Acidity: Novel Measurements and Implications for Atmospheric Chemistry. *Accounts Chem Res* **2020**, 53, (9), 1703-1714.
194. Shi, Z.; Krom, M. D.; Bonneville, S.; Benning, L. G., Atmospheric Processing Outside Clouds Increases Soluble Iron in Mineral Dust. *Environ Sci Technol* **2015**, 49, (3), 1472-1477.
195. Saxena, V. K.; Lin, N. H., Cloud chemistry measurements and estimates of acidic deposition on an above cloudbase coniferous forest. *Atmospheric Environment. Part A. General Topics* **1990**, 24, (2), 329-352.
196. Pye, H. O. T.; Nenes, A.; Alexander, B.; Ault, A. P.; Barth, M. C.; Clegg, S. L.; Collett Jr, J. L.; Fahey, K. M.; Hennigan, C. J.; Herrmann, H.; Kanakidou, M.; Kelly, J. T.; Ku, I. T.; McNeill, V. F.; Riemer, N.; Schaefer, T.; Shi, G.; Tilgner, A.; Walker, J. T.; Wang, T.; Weber, R.; Xing, J.; Zaveri, R. A.; Zuend, A., The acidity of atmospheric particles and clouds. *Atmos. Chem. Phys.* **2020**, 20, (8), 4809-4888.
197. Tilgner, A.; Schaefer, T.; Alexander, B.; Barth, M.; Collett Jr, J. L.; Fahey, K. M.; Nenes, A.; Pye, H. O. T.; Herrmann, H.; McNeill, V. F., Acidity and the multiphase chemistry of atmospheric aqueous particles and clouds. *Atmos. Chem. Phys.* **2021**, 21, (17), 13483-13536.
198. Dockery, D. W.; Cunningham, J.; Damokosh, A. I.; Neas, L. M.; Spengler, J. D.; Koutrakis, P.; Ware, J. H.; Raizenne, M.; Speizer, F. E., Health effects of acid aerosols on North American children: respiratory symptoms. *Environ Health Persp* **1996**, 104, (5), 500-505.
199. Raizenne, M.; Neas, L. M.; Damokosh, A. I.; Dockery, D. W.; Spengler, J. D.; Koutrakis, P.; Ware, J. H.; Speizer, F. E., Health effects of acid aerosols on North American children: pulmonary function. *Environ Health Persp* **1996**, 104, (5), 506-514.
200. Brauer, M.; Dumyahn, T. S.; Spengler, J. D.; Gutschmidt, K.; Heinrich, J.; Wichmann, H. E., Measurement of acidic aerosol species in eastern Europe: implications for air pollution epidemiology. *Environ Health Persp* **1995**, 103, (5), 482-488.
201. Pöschl, U.; Shiraiwa, M., Multiphase Chemistry at the Atmosphere–Biosphere Interface Influencing Climate and Public Health in the Anthropocene. *Chem. Rev.* **2015**, 115, (10), 4440–4475.
202. Wei, J.; Fang, T.; Wong, C.; Lakey, P. S. J.; Nizkorodov, S. A.; Shiraiwa, M., Superoxide Formation from Aqueous Reactions of Biogenic Secondary Organic Aerosols. *Environ Sci Technol* **2021**, 55, (1), 260-270.
203. Enami, S., Fates of Organic Hydroperoxides in Atmospheric Condensed Phases. *The Journal of Physical Chemistry A* **2021**, 125, (21), 4513-4523.
204. Wei, J.; Fang, T.; Lakey, P. S. J.; Shiraiwa, M., Iron-Facilitated Organic Radical Formation from Secondary Organic Aerosols in Surrogate Lung Fluid. *Environ Sci Technol* **2021**.
205. Cai, J.; Zhi, G.; Yu, Z.; Nie, P.; Gligorovski, S.; Zhang, Y.; Zhu, L.; Guo, X.; Li, P.; He, T.; He, Y.; Sun, J.; Zhang, Y., Spectral changes induced by pH variation of aqueous extracts derived from biomass burning aerosols: Under dark and in presence of simulated sunlight irradiation. *Atmospheric Environment* **2018**, 185, 1-6.
206. Yamazaki, T.; Kawai, C.; Yamauchi, A.; Kuribayashi, F., A highly sensitive chemiluminescence assay for superoxide detection and chronic granulomatous disease diagnosis. *Tropical Medicine and Health* **2011**, 39, (2), 41-45.
207. McCord, J. M., Oxygen-derived free radicals in postischemic tissue injury. *New England Journal of Medicine* **1985**, 312, (3), 159-163.
208. Dikalov, S. I.; Kirilyuk, I. A.; Voinov, M.; Grigor'ev, I. A., EPR detection of cellular and mitochondrial superoxide using cyclic hydroxylamines. *Free Radical Research* **2011**, 45, (4), 417-430.

209. Gutteridge, J., Lipid peroxidation and antioxidants as biomarkers of tissue damage. *Clinical chemistry* **1995**, *41*, (12), 1819-1828.
210. Villamena, F. A.; Merle, J. K.; Hadad, C. M.; Zweier, J. L., Superoxide radical anion adduct of 5,5-dimethyl-1-pyrroline N-oxide (DMPO). 1. The thermodynamics of formation and its acidity. *J Phys Chem A* **2005**, *109*, (27), 6083-6088.
211. Tsai, P.; Ichikawa, K.; Mailer, C.; Pou, S.; Halpern, H. J.; Robinson, B. H.; Nielsen, R.; Rosen, G. M., Esters of 5-Carboxyl-5-methyl-1-pyrroline N-Oxide: A Family of Spin Traps for Superoxide. *The Journal of Organic Chemistry* **2003**, *68*, (20), 7811-7817.
212. Guin, P. S.; Das, S.; Mandal, P. C., Electrochemical Reduction of Quinones in Different Media: A Review. *International Journal of Electrochemistry* **2011**, *2011*, 816202.
213. Baxendale, J.; Wilson, J., The photolysis of hydrogen peroxide at high light intensities. *Transactions of the Faraday Society* **1957**, *53*, 344-356.
214. Kremer, M. L., The Fenton Reaction. Dependence of the Rate on pH. *The Journal of Physical Chemistry A* **2003**, *107*, (11), 1734-1741.
215. Anderson, G. H.; Smith, J. G., Acid-catalyzed rearrangement of hydroperoxides. II. Phenylcycloalkyl hydroperoxides. *Canadian Journal of Chemistry* **1968**, *46*, (9), 1561-1570.
216. Walling, C., Chemistry of the Organic Peroxides. *Radiation Research Supplement* **1963**, *3*, 3-16.
217. Levin, M. E.; Gonzales, N. O.; Zimmerman, L. W.; Yang, J., Kinetics of acid-catalyzed cleavage of cumene hydroperoxide. *Journal of Hazardous Materials* **2006**, *130*, (1), 88-106.
218. Yaremenko, I. A.; Vil', V. A.; Demchuk, D. V.; Terent'ev, A. O., Rearrangements of organic peroxides and related processes. *Beilstein Journal of Organic Chemistry* **2016**, *12*, 1647-1748.
219. Deno, N. C.; Billups, W. E.; Kramer, K. E.; Lastomirsky, R. R., Rearrangement of aliphatic primary, secondary, and tertiary alkyl hydroperoxides in strong acid. *The Journal of Organic Chemistry* **1970**, *35*, (9), 3080-3082.
220. Iyer, S.; Rissanen, M. P.; Valiev, R.; Barua, S.; Krechmer, J. E.; Thornton, J.; Ehn, M.; Kurtén, T., Molecular mechanism for rapid autoxidation in α -pinene ozonolysis. *Nat Commun* **2021**, *12*, (1), 878.
221. Carrasquillo, A. J.; Daumit, K. E.; Kroll, J. H., Radical Reactivity in the Condensed Phase: Intermolecular versus Intramolecular Reactions of Alkoxy Radicals. *The Journal of Physical Chemistry Letters* **2015**, *6*, (12), 2388-2392.
222. Liu, M. J.; Wiegel, A. A.; Wilson, K. R.; Houle, F. A., Aerosol Fragmentation Driven by Coupling of Acid-Base and Free-Radical Chemistry in the Heterogeneous Oxidation of Aqueous Citric Acid by OH Radicals. *The Journal of Physical Chemistry A* **2017**, *121*, (31), 5856-5870.
223. Walczak, M. M.; Dryer, D. A.; Jacobson, D. D.; Foss, M. G.; Flynn, N. T., pH Dependent Redox Couple: An Illustration of the Nernst Equation. *J Chem Educ* **1997**, *74*, (10), 1195.
224. Yuan, X.; Miller, C. J.; Pham, A. N.; Waite, T. D., Kinetics and mechanism of auto- and copper-catalyzed oxidation of 1,4-naphthohydroquinone. *Free Radical Bio Med* **2014**, *71*, 291-302.
225. Schwantes, R. H.; Schilling, K. A.; McVay, R. C.; Lignell, H.; Coggon, M. M.; Zhang, X.; Wennberg, P. O.; Seinfeld, J. H., Formation of highly oxygenated low-volatility products from cresol oxidation. *Atmos. Chem. Phys.* **2017**, *17*, (5), 3453-3474.
226. Hoffmann, E. H.; Tilgner, A.; Wolke, R.; Böge, O.; Walter, A.; Herrmann, H., Oxidation of substituted aromatic hydrocarbons in the tropospheric aqueous phase: kinetic mechanism development and modelling. *Phys Chem Chem Phys* **2018**, *20*, (16), 10960-10977.
227. Kautzman, K. E.; Surratt, J. D.; Chan, M. N.; Chan, A. W. H.; Hersey, S. P.; Chhabra, P. S.; Dalleska, N. F.; Wennberg, P. O.; Flagan, R. C.; Seinfeld, J. H., Chemical Composition of Gas- and Aerosol-Phase Products from the Photooxidation of Naphthalene. *The Journal of Physical Chemistry A* **2010**, *114*, (2), 913-934.
228. Freedman, M. A.; Ott, E.-J. E.; Marak, K. E., Role of pH in Aerosol Processes and Measurement Challenges. *The Journal of Physical Chemistry A* **2019**, *123*, (7), 1275-1284.
229. Jang, M.; Carroll, B.; Chandramouli, B.; Kamens, R. M., Particle Growth by Acid-Catalyzed Heterogeneous Reactions of Organic Carbonyls on Preexisting Aerosols. *Environ Sci Technol* **2003**, *37*, (17), 3828-3837.

230. Hallquist, M.; Wenger, J. C.; Baltensperger, U.; Rudich, Y.; Simpson, D.; Claeys, M.; Dommen, J.; Donahue, N. M.; George, C.; Goldstein, A. H.; Hamilton, J. F.; Herrmann, H.; Hoffmann, T.; Iinuma, Y.; Jang, M.; Jenkin, M. E.; Jimenez, J. L.; Kiendler-Scharr, A.; Maenhaut, W.; McFiggans, G.; Mentel, T. F.; Monod, A.; Prevot, A. S. H.; Seinfeld, J. H.; Surratt, J. D.; Szmigielski, R.; Wildt, J., The formation, properties and impact of secondary organic aerosol: current and emerging issues. *Atmos Chem Phys* **2009**, 9, (14), 5155-5236.
231. Surratt, J. D.; Chan, A. W. H.; Eddingsaas, N. C.; Chan, M. N.; Loza, C. L.; Kwan, A. J.; Hersey, S. P.; Flagan, R. C.; Wennberg, P. O.; Seinfeld, J. H., Reactive intermediates revealed in secondary organic aerosol formation from isoprene. *P Natl Acad Sci USA* **2010**, 107, (15), 6640-6645.
232. Lin, Y.-H.; Zhang, Z.; Docherty, K. S.; Zhang, H.; Budisulistiorini, S. H.; Rubitschun, C. L.; Shaw, S. L.; Knipping, E. M.; Edgerton, E. S.; Kleindienst, T. E.; Gold, A.; Surratt, J. D., Isoprene Epoxydiols as Precursors to Secondary Organic Aerosol Formation: Acid-Catalyzed Reactive Uptake Studies with Authentic Compounds. *Environ Sci Technol* **2012**, 46, (1), 250-258.
233. Bakker-Arkema, J. G.; Ziemann, P. J., Measurements of Kinetics and Equilibria for the Condensed Phase Reactions of Hydroperoxides with Carbonyls to Form Peroxyhemiacetals. *Acs Earth Space Chem* **2020**, 4, (3), 467-475.
234. Hu, M.; Qiu, J.; Tonokura, K.; Enami, S., Aqueous-phase fates of α -alkoxyalkyl-hydroperoxides derived from the reactions of Criegee intermediates with alcohols. *Phys Chem Chem Phys* **2021**, 23, (8), 4605-4614.
235. Capouet, M.; Peeters, J.; Nozière, B.; Müller, J. F., Alpha-pinene oxidation by OH: simulations of laboratory experiments. *Atmos. Chem. Phys.* **2004**, 4, (9/10), 2285-2311.
236. Xuan, X.; Chen, Z.; Gong, Y.; Shen, H.; Chen, S., Partitioning of hydrogen peroxide in gas-liquid and gas-aerosol phases. *Atmos. Chem. Phys.* **2020**, 20, (9), 5513-5526.
237. Ye, C.; Liu, P.; Ma, Z.; Xue, C.; Zhang, C.; Zhang, Y.; Liu, J.; Liu, C.; Sun, X.; Mu, Y., High H₂O₂ Concentrations Observed during Haze Periods during the Winter in Beijing: Importance of H₂O₂ Oxidation in Sulfate Formation. *Environmental Science & Technology Letters* **2018**, 5, (12), 757-763.
238. Ye, C.; Chen, H.; Hoffmann, E. H.; Mettke, P.; Tilgner, A.; He, L.; Mutzel, A.; Brüggemann, M.; Poulain, L.; Schaefer, T.; Heinold, B.; Ma, Z.; Liu, P.; Xue, C.; Zhao, X.; Zhang, C.; Zhang, F.; Sun, H.; Li, Q.; Wang, L.; Yang, X.; Wang, J.; Liu, C.; Xing, C.; Mu, Y.; Chen, J.; Herrmann, H., Particle-Phase Photoreactions of HULIS and TMIs Establish a Strong Source of H₂O₂ and Particulate Sulfate in the Winter North China Plain. *Environ Sci Technol* **2021**, 55, (12), 7818-7830.
239. Yin, H. Y.; Xu, L. B.; Porter, N. A., Free Radical Lipid Peroxidation: Mechanisms and Analysis. *Chem Rev* **2011**, 111, (10), 5944-5972.
240. de Kok, T. M. C. M.; Driess, H. A. L.; Hogervorst, J. G. F.; Briedé, J. J., Toxicological assessment of ambient and traffic-related particulate matter: A review of recent studies. *Mutation Research/Reviews in Mutation Research* **2006**, 613, (2), 103-122.
241. Grigoratos, T.; Martini, G., Brake wear particle emissions: a review. *Environmental Science and Pollution Research* **2015**, 22, (4), 2491-2504.
242. Fang, T.; Guo, H.; Verma, V.; Peltier, R. E.; Weber, R. J., PM_{2.5} water-soluble elements in the southeastern United States: automated analytical method development, spatiotemporal distributions, source apportionment, and implications for health studies. *Atmos Chem Phys* **2015**, 15, (20), 11667-11682.
243. Majestic, B. J.; Schauer, J. J.; Shafer, M. M., Application of synchrotron radiation for measurement of iron red-ox speciation in atmospherically processed aerosols. *Atmos. Chem. Phys.* **2007**, 7, (10), 2475-2487.
244. Kieber, R. J.; Skrabal, S. A.; Smith, B. J.; Willey, J. D., Organic Complexation of Fe(II) and Its Impact on the Redox Cycling of Iron in Rain. *Environ Sci Technol* **2005**, 39, (6), 1576-1583.
245. Usher, C. R.; Michel, A. E.; Grassian, V. H., Reactions on Mineral Dust. *Chem. Rev.* **2003**, 103, (12), 4883-4940.
246. Nie, W.; Ding, A.; Wang, T.; Kerminen, V.-M.; George, C.; Xue, L.; Wang, W.; Zhang, Q.; Petäjä, T.; Qi, X., Polluted dust promotes new particle formation and growth. *Sci. Rep.* **2014**, 4, 6634.

247. Bondy, A. L.; Bonanno, D.; Moffet, R. C.; Wang, B.; Laskin, A.; Ault, A. P., The diverse chemical mixing state of aerosol particles in the southeastern United States. *Atmos. Chem. Phys.* **2018**, *18*, (16), 12595-12612.
248. Steenhof, M.; Gosens, I.; Strak, M.; Godri, K. J.; Hoek, G.; Cassee, F. R.; Mudway, I. S.; Kelly, F. J.; Harrison, R. M.; Lebre, E.; Brunekreef, B.; Janssen, N. A. H.; Pieters, R. H. H., In vitro toxicity of particulate matter (PM) collected at different sites in the Netherlands is associated with PM composition, size fraction and oxidative potential - the RAPTES project. *Part Fibre Toxicol* **2011**, *8*.
249. Saffari, A.; Daher, N.; Shafer, M. M.; Schauer, J. J.; Sioutas, C., Global Perspective on the Oxidative Potential of Airborne Particulate Matter: A Synthesis of Research Findings. *Environ Sci Technol* **2014**, *48*, (13), 7576-7583.
250. Alpert, P. A.; Dou, J.; Corral Arroyo, P.; Schneider, F.; Xto, J.; Luo, B.; Peter, T.; Huthwelker, T.; Borca, C. N.; Henzler, K. D.; Schaefer, T.; Herrmann, H.; Raabe, J.; Watts, B.; Krieger, U. K.; Ammann, M., Photolytic radical persistence due to anoxia in viscous aerosol particles. *Nat Commun* **2021**, *12*, (1), 1769.
251. Peng, Z.; Day, D. A.; Ortega, A. M.; Palm, B. B.; Hu, W. W.; Stark, H.; Li, R.; Tsigaridis, K.; Brune, W. H.; Jimenez, J. L., Non-OH chemistry in oxidation flow reactors for the study of atmospheric chemistry systematically examined by modeling. *Atmos Chem Phys* **2016**, *16*, (7), 4283-4305.
252. Charrier, J. G.; Anastasio, C., Impacts of antioxidants on hydroxyl radical production from individual and mixed transition metals in a surrogate lung fluid. *Atmospheric Environment* **2011**, *45*, (40), 7555-7562.
253. Awtrey, A. D.; Connick, R. E., The Absorption Spectra of I₂, I₃⁻, I⁻, IO₃⁻, S₄O₆⁼ and S₂O₃⁼. Heat of the Reaction I₃⁻ = I₂ + I⁻. *J Am Chem Soc* **1951**, *73*, (4), 1842-1843.
254. Fang, T.; Verma, V.; Guo, H.; King, L. E.; Edgerton, E. S.; Weber, R. J., A semi-automated system for quantifying the oxidative potential of ambient particles in aqueous extracts using the dithiothreitol (DTT) assay: results from the Southeastern Center for Air Pollution and Epidemiology (SCAPE). *Atmos. Meas. Tech.* **2015**, *8*, (1), 471-482.
255. Goldstein, S.; Meyerstein, D., Comments on the mechanism of the "Fenton like" reaction. *Accounts Chem Res* **1999**, *32*, (7), 547-550.
256. Gilbert, B. C.; Holmes, R. G.; Laue, H. A.; Norman, R. O., Electron spin resonance studies. Part L. Reactions of alkoxyl radicals generated from alkyl hydroperoxides and titanium (III) ion in aqueous solution. *Journal of the Chemical Society, Perkin Transactions 2* **1976**, (9), 1047-1052.
257. Erben-Russ, M.; Michel, C.; Bors, W.; Saran, M., Absolute rate constants of alkoxyl radical reactions in aqueous solution. *The Journal of Physical Chemistry* **1987**, *91*, (9), 2362-2365.
258. Gonzalez, D. H.; Cala, C. K.; Peng, Q.; Paulson, S. E., HULIS Enhancement of Hydroxyl Radical Formation from Fe(II): Kinetics of Fulvic Acid-Fe(II) Complexes in the Presence of Lung Antioxidants. *Environ Sci Technol* **2017**, *51*, (13), 7676-7685.
259. Buettner, G. R.; Jurkiewicz, B. A., Ascorbate free radical as a marker of oxidative stress: An EPR study. *Free Radical Bio Med* **1993**, *14*, (1), 49-55.
260. Denisov, E. T.; Tumanov, V. E., Estimation of the bond dissociation energies from the kinetic characteristics of liquid-phase radical reactions. *Russian Chemical Reviews* **2005**, *74*, (9), 825-858.
261. Eames, J.; Watkinson, M., Catalytic Allylic Oxidation of Alkenes Using an Asymmetric Kharasch-Sosnovsky Reaction. *Angewandte Chemie International Edition* **2001**, *40*, (19), 3567-3571.
262. Studer, A.; Curran, D. P., Catalysis of Radical Reactions: A Radical Chemistry Perspective. *Angewandte Chemie International Edition* **2016**, *55*, (1), 58-102.
263. Buettner, G. R.; Jurkiewicz, B. A., Catalytic metals, ascorbate and free radicals: combinations to avoid. *Radiation research* **1996**, *145*, (5), 532-541.
264. Sun, H.; Xie, G.; He, D.; Zhang, L., Ascorbic acid promoted magnetite Fenton degradation of alachlor: Mechanistic insights and kinetic modeling. *Applied Catalysis B: Environmental* **2020**, *267*, 118383.
265. Valko, M.; Morris, H.; Cronin, M. T. D., Metals, toxicity and oxidative stress. *Current medicinal chemistry* **2005**, *12*, (10), 1161-1208.

266. Shen, J.; Griffiths, P. T.; Campbell, S. J.; Utinger, B.; Kalberer, M.; Paulson, S. E., Ascorbate oxidation by iron, copper and reactive oxygen species: review, model development, and derivation of key rate constants. *Scientific Reports* **2021**, *11*, (1), 7417.
267. Surratt, J. D.; Murphy, S. M.; Kroll, J. H.; Ng, N. L.; Hildebrandt, L.; Sorooshian, A.; Szmigielski, R.; Vermeylen, R.; Maenhaut, W.; Claeys, M., Chemical composition of secondary organic aerosol formed from the photooxidation of isoprene. *The Journal of physical chemistry A* **2006**, *110*, (31), 9665-9690.
268. Sato, K.; Hatakeyama, S.; Imamura, T., Secondary Organic Aerosol Formation during the Photooxidation of Toluene: NO_x Dependence of Chemical Composition. *The Journal of Physical Chemistry A* **2007**, *111*, (39), 9796-9808.
269. Fujitani, Y.; Furuyama, A.; Tanabe, K.; Hirano, S., Comparison of Oxidative Abilities of PM_{2.5} Collected at Traffic and Residential Sites in Japan. Contribution of Transition Metals and Primary and Secondary Aerosols. *Aerosol and Air Quality Research* **2017**, *17*, (2), 574-587.
270. Sanchez, J.; Myers, T. N., Peroxides and peroxide compounds, organic peroxides. *Kirk-Othmer encyclopedia of chemical technology* **2000**, 1-86.
271. Adams, G.; Boag, J.; Currant, J.; Michael, B., *Absolute rate constants for the reaction of the hydroxyl radical with organic compounds*. Academic Press: New York: 1965; p 13.
272. Nadezhdin, A. D.; Dunford, H. B., The oxidation of ascorbic acid and hydroquinone by perhydroxyl radicals. A flash photolysis study. *Canadian Journal of Chemistry* **1979**, *57*, (23), 3017-3022.
273. Nauser, T.; Gebicki, J. M., Reaction rates of glutathione and ascorbate with alkyl radicals are too slow for protection against protein peroxidation in vivo. *Archives of Biochemistry and Biophysics* **2017**, *633*, 118-123.
274. Voelker, B. M.; Sedlak, D. L., Iron reduction by photoproduced superoxide in seawater. *Marine Chemistry* **1995**, *50*, (1), 93-102.
275. Ayala, A.; Muñoz, M. F.; Argüelles, S., Lipid Peroxidation: Production, Metabolism, and Signaling Mechanisms of Malondialdehyde and 4-Hydroxy-2-Nonenal. *Oxidative Medicine and Cellular Longevity* **2014**, *2014*, 360438.
276. Los, D. A.; Murata, N., Membrane fluidity and its roles in the perception of environmental signals. *Biochimica et Biophysica Acta (BBA) - Biomembranes* **2004**, *1666*, (1), 142-157.
277. Marchaj, A.; Kelley, D. G.; Bakac, A.; Espenson, J. H., Kinetics of the reactions between alkyl radicals and molecular oxygen in aqueous solution. *The Journal of Physical Chemistry* **1991**, *95*, (11), 4440-4441.
278. Boyd, A. A.; Flaud, P.-M.; Daugey, N.; Lesclaux, R., Rate Constants for RO₂ + HO₂ Reactions Measured under a Large Excess of HO₂. *The Journal of Physical Chemistry A* **2003**, *107*, (6), 818-821.
279. Atkinson, R., Rate constants for the atmospheric reactions of alkoxy radicals: An updated estimation method. *Atmospheric Environment* **2007**, *41*, (38), 8468-8485.
280. Pham, A. N.; Waite, T. D., Modeling the Kinetics of Fe(II) Oxidation in the Presence of Citrate and Salicylate in Aqueous Solutions at pH 6.0–8.0 and 25 °C. *The Journal of Physical Chemistry A* **2008**, *112*, (24), 5395-5405.
281. Stuglik, Z.; PawełZagórski, Z., Pulse radiolysis of neutral iron(II) solutions: oxidation of ferrous ions by OH radicals. *Radiation Physics and Chemistry (1977)* **1981**, *17*, (4), 229-233.
282. Masuda, T.; Shinohara, H.; Kondo, M., Reactions of Hydroxyl Radicals with Nucleic Acid Bases and the Related Compounds in Gamma-irradiated Aqueous Solution. *Journal of Radiation Research* **1975**, *16*, (3), 153-161.
283. Liphard, M.; Bothe, E.; Schulte-Frohlinde, D., The Influence of Glutathione on Single-strand Breakage in Single-stranded DNA Irradiated in Aqueous Solution in the Absence and Presence of Oxygen. *International Journal of Radiation Biology* **1990**, *58*, (4), 589-602.
284. Packer, L., *Vitamin C in health and disease*. CRC Press: 1997; Vol. 4.
285. Ford, E.; Hughes, M. N.; Wardman, P., Kinetics of the reactions of nitrogen dioxide with glutathione, cysteine, and uric acid at physiological pH. *Free Radical Bio Med* **2002**, *32*, (12), 1314-1323.
286. George, C.; Ammann, M.; D'Anna, B.; Donaldson, D. J.; Nizkorodov, S. A., Heterogeneous Photochemistry in the Atmosphere. *Chem Rev* **2015**, *115*, (10), 4218-4258.

287. Rudich, Y.; Donahue, N. M.; Mentel, T. F., Aging of Organic Aerosol: Bridging the Gap Between Laboratory and Field Studies. *Annu Rev Phys Chem* **2007**, *58*, (1), 321-352.
288. Baboamian, V. J.; Gu, Y.; Nizkorodov, S. A., Photodegradation of Secondary Organic Aerosols by Long-Term Exposure to Solar Actinic Radiation. *Acs Earth Space Chem* **2020**, *4*, (7), 1078-1089.
289. Donahue, N. M.; Robinson, A. L.; Trump, E. R.; Riipinen, I.; Kroll, J. H., Volatility and Aging of Atmospheric Organic Aerosol. In *Atmospheric and Aerosol Chemistry*, McNeill, V. F.; Ariya, P. A., Eds. Springer Berlin Heidelberg: Berlin, Heidelberg, 2012; pp 97-143.
290. Klodt, A. L.; Romonosky, D. E.; Lin, P.; Laskin, J.; Laskin, A.; Nizkorodov, S. A., Aqueous Photochemistry of Secondary Organic Aerosol of α -Pinene and α -Humulene in the Presence of Hydrogen Peroxide or Inorganic Salts. *Acs Earth Space Chem* **2019**, *3*, (12), 2736-2746.
291. Henry, K. M.; Donahue, N. M., Photochemical Aging of α -Pinene Secondary Organic Aerosol: Effects of OH Radical Sources and Photolysis. *The Journal of Physical Chemistry A* **2012**, *116*, (24), 5932-5940.
292. Wong, J. P. S.; Zhou, S.; Abbatt, J. P. D., Changes in Secondary Organic Aerosol Composition and Mass due to Photolysis: Relative Humidity Dependence. *The Journal of Physical Chemistry A* **2015**, *119*, (19), 4309-4316.
293. Mang, S. A.; Henricksen, D. K.; Bateman, A. P.; Andersen, M. P. S.; Blake, D. R.; Nizkorodov, S. A., Contribution of Carbonyl Photochemistry to Aging of Atmospheric Secondary Organic Aerosol. *The Journal of Physical Chemistry A* **2008**, *112*, (36), 8337-8344.
294. Walser, M. L.; Park, J.; Gomez, A. L.; Russell, A. R.; Nizkorodov, S. A., Photochemical Aging of Secondary Organic Aerosol Particles Generated from the Oxidation of d-Limonene. *The Journal of Physical Chemistry A* **2007**, *111*, (10), 1907-1913.
295. Donahue, N. M.; Henry, K. M.; Mentel, T. F.; Kiendler-Scharr, A.; Spindler, C.; Bohn, B.; Brauers, T.; Dorn, H. P.; Fuchs, H.; Tillmann, R.; Wahner, A.; Saathoff, H.; Naumann, K. H.; Mohler, O.; Leisner, T.; Muller, L.; Reinnig, M. C.; Hoffmann, T.; Salo, K.; Hallquist, M.; Frosch, M.; Bilde, M.; Tritscher, T.; Barmet, P.; Praplan, A. P.; DeCarlo, P. F.; Dommen, J.; Prevot, A. S.; Baltensperger, U., Aging of biogenic secondary organic aerosol via gas-phase OH radical reactions. *Proc Natl Acad Sci U S A* **2012**, *109*, (34), 13503-8.
296. Monod, A.; Chevallier, E.; Durand Jolibois, R.; Doussin, J. F.; Picquet-Varrault, B.; Carlier, P., Photooxidation of methylhydroperoxide and ethylhydroperoxide in the aqueous phase under simulated cloud droplet conditions. *Atmospheric Environment* **2007**, *41*, (11), 2412-2426.
297. Kamboures, M. A.; Nizkorodov, S. A.; Gerber, R. B., Ultrafast photochemistry of methyl hydroperoxide on ice particles. *Proceedings of the National Academy of Sciences* **2010**, *107*, (15), 6600-6604.
298. Badali, K. M.; Zhou, S.; Aljawhary, D.; Antiñolo, M.; Chen, W. J.; Lok, A.; Mungall, E.; Wong, J. P. S.; Zhao, R.; Abbatt, J. P. D., Formation of hydroxyl radicals from photolysis of secondary organic aerosol material. *Atmos. Chem. Phys.* **2015**, *15*, (14), 7831-7840.
299. Kessler, S. H.; Nah, T.; Carrasquillo, A. J.; Jayne, J. T.; Worsnop, D. R.; Wilson, K. R.; Kroll, J. H., Formation of Secondary Organic Aerosol from the Direct Photolytic Generation of Organic Radicals. *The Journal of Physical Chemistry Letters* **2011**, *2*, (11), 1295-1300.
300. Healy, R. M.; Chen, Y.; Kourtchev, I.; Kalberer, M.; O'Shea, D.; Wenger, J. C., Rapid Formation of Secondary Organic Aerosol from the Photolysis of 1-Nitronaphthalene: Role of Naphthoxy Radical Self-reaction. *Environ Sci Technol* **2012**, *46*, (21), 11813-11820.
301. Davidson, M. W. <https://zeiss-campus.magnet.fsu.edu/articles/lightsources/mercuryarc.html>
302. Wei, J.; Fang, T.; Shiraiwa, M., Effects of Acidity on Reactive Oxygen Species Formation from Secondary Organic Aerosols. *ACS Environmental Au* **2022**.
303. Hwang, B.; Fang, T.; Pham, R.; Wei, J.; Gronstal, S.; Lopez, B.; Frederickson, C.; Galeazzo, T.; Wang, X.; Jung, H.; Shiraiwa, M., Environmentally Persistent Free Radicals, Reactive Oxygen Species Generation, and Oxidative Potential of Highway PM2.5. *Acs Earth Space Chem* **2021**, *5*, (8), 1865-1875.

304. Zhao, R.; Kenseth, C. M.; Huang, Y.; Dalleska, N. F.; Seinfeld, J. H., Iodometry-Assisted Liquid Chromatography Electrospray Ionization Mass Spectrometry for Analysis of Organic Peroxides: An Application to Atmospheric Secondary Organic Aerosol. *Environ Sci Technol* **2018**, *52*, (4), 2108-2117.
305. Yao, M.; Li, Z.; Li, C.; Xiao, H.; Wang, S.; Chan, A. W. H.; Zhao, Y., Isomer-Resolved Reactivity of Organic Peroxides in Monoterpene-Derived Secondary Organic Aerosol. *Environ Sci Technol* **2022**, *56*, (8), 4882-4893.
306. Sarniak, A.; Lipińska, J.; Tytman, K.; Lipińska, S., Endogenous mechanisms of reactive oxygen species (ROS) generation. *Postepy Hig Med Dosw (Online)* **2016**, *70*, (0), 1150-1165.
307. Zorov, D. B.; Juhaszova, M.; Sollott, S. J., Mitochondrial ROS-induced ROS release: An update and review. *Biochimica et Biophysica Acta (BBA) - Bioenergetics* **2006**, *1757*, (5), 509-517.